

Editorial corner – a personal view

The new challenge of green tires for the electric vehicles

Shipeng Wen*

State Key Laboratory of Organic-Inorganic Composites, Beijing University of Chemical Technology, 100029 Beijing 100029, China

The fast development of electric vehicles (EVs) is attracting more and more attention. Many countries plan to ban conventional petrol cars within the next twenty years. Public opinion supports these policies because they gradually reduce greenhouse gas emissions. Unlike gasoline cars, EVs have higher acceleration and less noise pollution from the engine but increased weight from the battery (<https://doi.org/10.1016/j.tej.2015.11.011>). Accordingly, new challenges to EV tires are emerging. The high instantaneous torque of EVs leads to higher tread wear. Long travel distances require low rolling resistance and lower tire weight. In addition, EV tires require low road noise.

To meet these new requirements of EV tires, we need to adjust the tire structure and materials. Reinforcement layers: traditional cars mainly use steel cords for the reinforcement layers. These steel cords are much heavier than rubber composites. Organic fibers with high strength, such as aramid and polyimide fibers (<https://doi.org/10.1002/app.49733>), can be partially used in the belt layer and carcass layer to reduce tire weight. The adhesive strength of fiber/rubber composites also should be enhanced. The light tires provide more driving ranges for EVs. Tread patterns: the tread patterns' improvement is more important than that in tread rubbers to reduce road noise (<https://doi.org/10.1016/j.apacoust.2020.107617>). The novel patterns can be designed according to the acoustic theory. Rolling and abrasion resistance: it is challenging to balance these two

properties. The traditional method for improving abrasion resistance is to increase the tensile strength and modulus of the tread rubber, but this leads to an increase in rolling resistance. Therefore, researchers need to rationalize the rubber formula and manufacturing process. In addition, some novel fillers, such as graphene and carbon nanotubes, significantly increase the modulus of rubber composites. A reasonable combination of different fillers can balance these two properties (<https://doi.org/10.5254/rct.21.79928>). The fine dispersion of the hybrid fillers and the strong interface between novel fillers and rubber molecules should be ensured during the manufacturing process. In my opinion, these novel technologies have the potential to be realized in EV tires and contribute to making transport more environmentally friendly.



Prof. Dr. Shipeng Wen
Member of the International Advisory Board

*Corresponding author, e-mail: wensp@mail.buct.edu.cn
© BME-PT

Research article

Effect of graphene oxide and ionic liquid on the sliding wear and abrasion resistance of injection molded PMMA nanocomposites

Luis-Francisco Minguez-Enkovaara, Francisco-Jose Carrión-Vilches, María-Dolores Avilés, María-Dolores Bermúdez*

Grupo de Ciencia de Materiales e Ingeniería Metalúrgica Universidad Politécnica de Cartagena. Campus de la Muralla del Mar, 30202 Cartagena, Spain

Received 12 May 2022; accepted in revised form 26 September 2022

Abstract. New polymethylmethacrylate (PMMA) nanocomposites containing 0.5 wt% graphene oxide (GO), or 1.5 wt% graphene oxide modified with the ionic liquid (IL) 1-octyl-3-methylimidazolium tetrafluoroborate (GOIL) have been processed by extrusion and injection molding to obtain PMMA+GO and PMMA+GOIL, respectively. Raman microscopy and mapping show that the additives align parallel to the flow close to the exterior surfaces, with an almost perpendicular orientation in the central core region. Reciprocating sliding tests have been carried out on the exterior surfaces and also on the surface of core sections of the injected parts. GO prevents surface damage, showing negligible wear on both section surfaces under sliding parallel and perpendicular to the injection flow. In contrast, the performance of PMMA+GOIL depends on the sliding direction. Under multiple scratching, both GO and GOIL reduced residual depth values and increased the viscoelastic recovery of PMMA, thus reducing permanent surface damage. PMMA+GOIL shows the highest viscoelastic recovery and the lowest complex viscosity values. Wear mechanisms are discussed as a function of materials properties, nanofiller type, and orientation and sliding direction.

Keywords: nanocomposites, nanomaterials, graphene oxide, ionic liquid, material testing

1. Introduction

One of the technological purposes in the research and development of new polymer nanocomposites is the reduction of energy loss and material damage due to friction and wear in sliding applications and of surface damage produced by abrasion [1, 2]. Carbon nanophases are studied as reinforcements of different polymer matrices aimed at reducing friction coefficients and material loss. Sun and Du [3] have recently reviewed the state of the tribological studies of graphene nanocomposites.

Polymethylmethacrylate (PMMA) parts are manufactured for applications in many structural, industrial, transport, and even biomedical applications for

which tribological performance is critical. PMMA composites [4] are easily manufactured by melt processing techniques, such as extrusion and injection molding, but their wear and scratch resistance need to be improved [5]. Carbon nanophase fillers such as nanotubes, graphene, and graphene oxide have been added to a PMMA matrix [6–12]. The resistance to damage of the surfaces of the final parts is influenced by nanophase distribution and orientation with respect to the melt flow. A very recent review [13] on fiber-reinforced polymer composites containing graphene reported that they exhibit higher wear resistance than the corresponding materials without graphene.

*Corresponding author, e-mail: mdolores.bermudez@upct.es
© BME-PT

Song *et al.* [14] described the preparation of PMMA nanocomposites by in-situ polymerization, containing up to 1 wt% of graphene oxide (GO) with respect to the monomer. A reduction of the running-in friction coefficient was described for GO content higher than 0.8 wt% to reach the same steady-state friction coefficient as pure PMMA after a short sliding distance. They proposed that the good compatibility between the functional groups of GO and PMMA enhances interfacial strength and improves the tribological performance.

Ionic liquids (ILs), salts that are in liquid state at room temperature, have found many applications in tribology and materials science, including polymer technology [15]. ILs possess a unique combination of outstanding properties, such as their high thermal stability in the fluid state; their ability to act as solvents and surfactants; their plasticizing effect towards thermoplastic polymers; and their curing effect in the case of thermosets.

The plasticizing effect of imidazolium ILs for PMMA, when added in very high proportions (50 vol% ILs), was described by Scott and coworkers [16, 17]. Zhao *et al.*, [18] described the multiple roles of 1-butyl-3-methylimidazolium hexafluorophosphate, which not only acts as a plasticizer and processing aid additive, but also improves the dispersion of multiwalled carbon nanotubes in a PMMA matrix. Recently, 2 wt% ILs have been added to PMMA [19], to improve its resistance to deformation, but no tribological studies were conducted.

Graphene-ionic liquid nanohybrid lubricants have received much attention in recent times [20–22]. The synergistic effect between carbon nanophases and ionic liquids [23, 24] has been demonstrated in lubrication [22], both as neat lubricants and as lubricant additives, and also in the reduction of friction and wear of polymers [3, 25]. IL functionalized GO reduced the friction and wear of epoxy resin [25]. Thin lubricant films formed by graphene dispersed in octylmethylimidazolium ILs have been reported recently [26].

The ionic liquid selected in the present study has previously shown its ability to modify carbon nanophases, in particular carbon nanotubes, to develop new thermoplastic nanocomposites [27, 28] with improved abrasive wear resistance.

The most commonly used processing conditions for these nanocomposites require the use of solvents in order to disperse the additives. However, for practical

applications with a reduced environmental impact, melt processing is an adequate route. A recently published precedent of the present work is the preparation, characterization, and optimization of extrusion parameters for extruded PMMA nanocomposites with graphene oxide and graphene oxide modified by ionic liquid [29].

In the present work, PMMA nanocomposites containing graphene oxide (GO) or graphene oxide previously modified by ionic liquid (GOIL) have been melt-processed by extrusion followed by injection molding, avoiding the use of organic solvents. The main objectives are to study the wear resistance of the new materials under different sliding conditions and to relate the results with variables such as injection flow, nanophase type, and distribution. The main novelty with respect to previous works is the study of the different tribological behavior of different regions of nanocomposite injected parts.

2. Experimental

Injection molding grade polymethylmethacrylate (PMMA) (8N; Evonik AG, Germany) was selected for the present study. Graphene oxide (GO) (lateral size (LD50): 40 μm ; average thickness: 1–2 nm; oxygen content (determined by X-ray photoelectron spectroscopy, XPS): 30% Brunauer-Emmett-Teller (BET) specific surface area: approx. 400 m^2/g ; average number of layers 1–2) was purchased from Avanzare S.L., Spain. The ionic liquid (IL) used in the present study was 1-octyl-3-methylimidazolium tetrafluoroborate (Iolitec GmbH, Germany) (>99% purity). Graphene oxide modified by ionic liquid (GOIL) was obtained following a general procedure similar to that previously described [29]. The first step was the mechanical mixing of GO and IL (in a 1:2 weight proportion) in an agate mortar. After 10 minutes, the mixture was sonicated for 1 hour, and the solid residue was then washed repeatedly with acetonitrile and dried in a vacuum oven for 32 hours at 70 °C.

PMMA pellets were milled using an ultracentrifuge mill (ZM200; Retsch, Germany) and dried in a vacuum oven. A TwinLab 10 mm co-rotating twin-screw micro-extruder (TwinTech Extrusion Ltd, U.K.) was used for the first processing step of PMMA and the new nanocomposites, under a temperature profile between 205 and 245 °C and a specific mechanical energy of 1800 kJ/kg. Extrusion processing parameters were selected according to previous optimization

works [29]. The extruded materials were then cooled to 70 °C and pelletized before injection molding in a DEU (Spain) 250 H55 mini VP machine at 245 °C, under an injection pressure of 120 MPa, with a mold temperature of 65 °C and an injection speed of 10 cm³/s. The injection molding parameters are those recommended for PMMA.

In order to observe the presence of the nanofillers inside the injected parts, images of 1 mm thick sections were taken with a digital camera and edited using GIMP image editing software.

Materials were characterized using a Leica DMRX optical microscope, a Hitachi S-3500N Scanning electron microscope (SEM), (Hitachi, Tokyo, Japan) was used to obtain energy dispersive X-ray (EDX) spectra, and Raman microscopy WiTec Access 300 equipment with a 532 nm laser. X-ray photoelectron spectroscopy (XPS) was determined by means of a VG-Microtech Multilab 3000. JEOL JEM 2100 equipment was used to obtain transmission electron microscopic (TEM) micrographs and a Bruker D-8 Advance diffractometer was used to record X-ray diffraction (XRD) peaks. Thermal characterization was performed with a DSC-822e type differential scanning calorimeter (DSC), between 0 and 140 °C, at a heating rate of 10 °C/min. TGA 1 HT type thermogravimetric analyzer (TGA) (Mettler-Toledo, USA) was used under a nitrogen atmosphere (50 ml/min) at a heating rate of 10 °C/min, under a nitrogen atmosphere (50 ml/min). Q800 (TA Instruments, USA) equipment was used for dynamic mechanical analysis (DMA), under the single cantilever configuration, in the temperature range between 30 and 145 °C, at a heating rate of 3 °C/min, with a frequency of 1 Hz, in ambient atmosphere.

Surface roughness and wear volumes were determined by means of a Talysurf CLI 500 (Taylor Hobson, U.K.) profilometer. Reciprocating sliding tribological tests with AISI 316L balls (1.6 mm diameter) against PMMA injected parts were carried out using a TRB tribometer (Anton Paar, Switzerland), under a normal applied load of 1 N, with a sliding frequency of 2 Hz, and a stroke length of 5 mm. Coefficients of friction were continuously recorded during each test. Tests were carried out on both the exterior and core surfaces under sliding directions parallel or perpendicular to the melt flow. Average friction coefficient and wear values were calculated after at least three tests.

Abrasion tests under multiple scratching were carried out according to ASTM D7027-05, using an MTR 3/50-50/Ni microscratch (Microtest S.A., Spain) tester, with a diamond indenter (200 nm sphere radius) being used for multiple scratch (15 successive scratches) abrasive wear tests, under a normal applied load of 10 N, at a sliding velocity of 5 mm/min, with a sliding distance of 5 mm. Average instantaneous penetration (Pd), residual depth (Rd), and viscoelastic recovery values were calculated after at least three tests. All tribological tests were carried out in ambient conditions, temperature: 25 °C and relative humidity: 37%.

The rheology of PMMA and of the nanocomposites was studied with a parallel plate rotational rheometer (Ar-G2; TA Instruments, USA), at a temperature of 245 °C.

3. Results and discussion

3.1. Materials characterization

The results of XPS surface analysis of GOIL show the characteristic binding energies of F1s from the tetrafluoroborate anion and N1s from the imidazolium cation, while GO only presents C1s and O1s peaks, as previously described [29], although in the present case a lower IL proportion has been used to obtain the modified graphene oxide nanofiller GOIL (Figure 1).

X-ray diffraction patterns Figure 2 show the displacement of the maximum diffraction peak for GO to a lower angle (higher interlayer distance) when it is modified by IL.

GOIL diffraction pattern also shows the peaks at 22° and at 5°, which are also present in the IL.

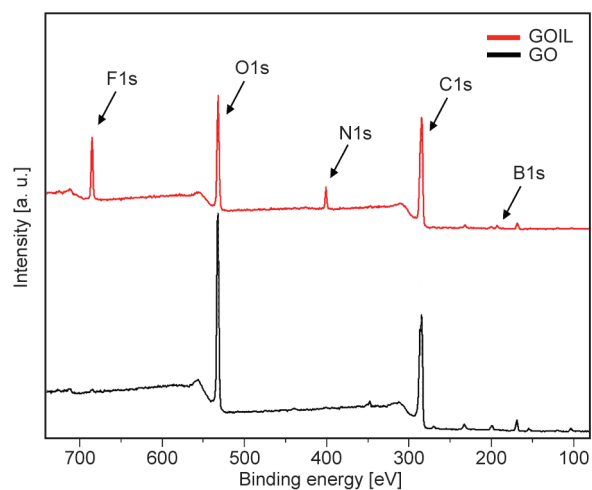


Figure 1. XPS surface analysis spectra for GO and GOIL.

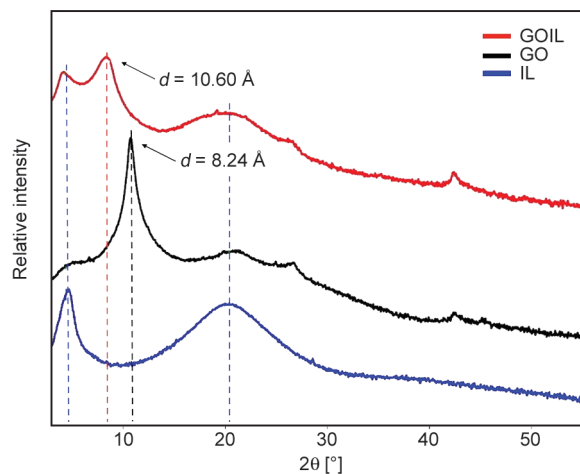


Figure 2. XRD diffractograms of GO; IL; and GOIL.

XPS and XRD results confirm the presence of the IL both at the outer surface and at the GO interlayer distance.

TEM micrographs of PMMA+GO and PMMA+GOIL (Figure 3) show the presence of GO or GOIL platelets inside the PMMA matrix. The presence of folded multilayers inside both nanocomposites could be a result of processing conditions.

The SEM micrograph (Figure 4) of the cryofracture surface of PMMA+GOIL shows the characteristic fragile fracture morphology. The presence of the IL phase was confirmed by the EDX spectrum of the selected area (Figure 4), which shows the presence of fluorine from the tetrafluoroborate anion.

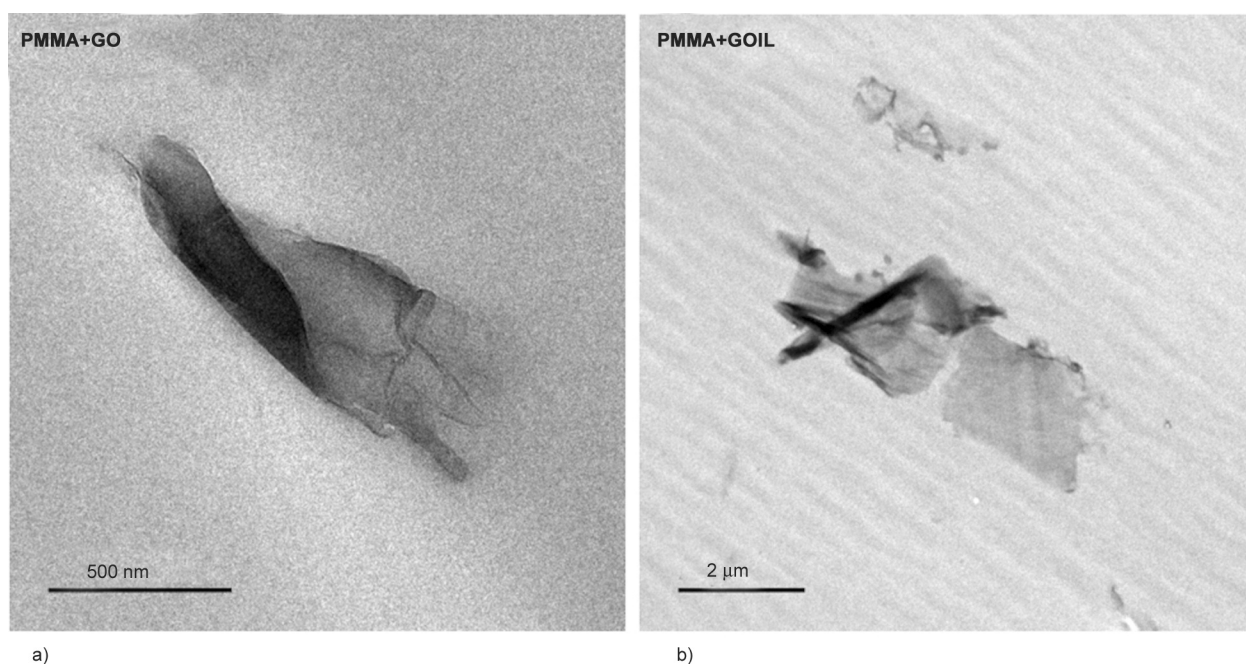


Figure 3. TEM micrographs of a) PMMA+GO and b) PMMA+GOIL.

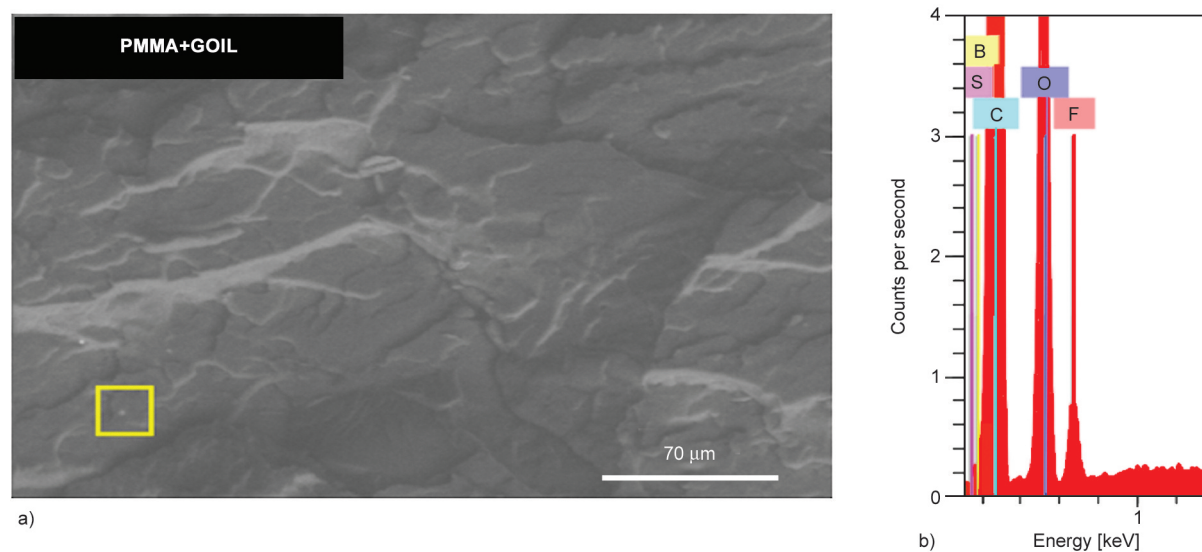


Figure 4. a) SEM micrograph of the cryofracture surface of PMMA+GOIL and b) EDX spectrum of the selected region.

Table 1 shows that glass transition temperatures (T_g), as determined by DSC, are similar for all materials, thus indicating no significant changes in chain mobility in the bulk materials induced by the nanofiller additives. The highest degradation temperature (T_d) (determined by TGA) is observed for PMMA+GOIL nanocomposite, as a result of the higher thermal stability of IL and GOIL with respect to PMMA [29].

Table 2 shows the values of the storage modulus onset (E'_{onset}), loss modulus maximum (E''_{peak}), and loss tangent ($\tan \delta$) maximum ($\tan \delta_{\text{peak}}$), and glass transition temperature values at the onset of storage modulus ($T_g(E'_{\text{onset}})$), at the maximum peak of loss modulus ($T_g(E''_{\text{peak}})$) and at the maximum peak of loss tangent ($T_g(\tan \delta_{\text{peak}})$). As observed in **Table 2**, DMA results are very similar for all materials. Glass transition temperatures and $\tan \delta$ values are the same for PMMA and both nanocomposites. Thus, GO and GOIL additives induce no significant changes in the viscoelastic behavior of injection molded PMMA, at least in the proportion added in the present work. This is also in agreement with the results previously obtained for similar nanocomposite extruded materials [29].

Figure 5 shows the D, G and 2D regions of the Raman spectra of the nanofillers and the nanocomposites.

Table 3 reports the position, intensity, the full width half maximum (FWHM) band width, and areas of each fitted peak.

A decrease in the intensity and FWHM of the D'' band has been related [31] to a crystallinity increase. According to this, as these values are higher for GOIL than for GO, (**Table 3**), the modification with ionic liquid produces a more amorphous hybrid nanofiller.

Table 1. Glass transition (T_g) and degradation (T_d) temperatures.

Material	T_g^* [°C]	T_d^{**} [°C]
PMMA	108.5±0.7	379.9±0.5
PMMA+GO	110.6±2.6	382.1±0.8
PMMA+GOIL	108.3±0.1	385.4±1.3

*Glass transition temperature

**Degradation temperature at 50% weight loss

Table 2. DMA results.

Material	E'_{onset} [MPa]	$T_g(E'_{\text{onset}})$ [°C]	E''_{peak} [MPa]	$T_g(E''_{\text{peak}})$ [°C]	$\tan \delta_{\text{peak}}$ [-]	$T_g(\tan \delta_{\text{peak}})$ [°C]
PMMA	3141.0±89.1	117.9±0.1	258.0±1.6	118.0±0.1	1.5±0.1	133.5±0.1
PMMA+GO	3066.0±45.2	118.7±0.6	260.2±0.1	119.1±0.6	1.5±0.1	134.1±0.6
PMMA+GOIL	3244.5±91.2	117.8±0.4	270.7±1.1	118.1±0.4	1.5±0.1	133.5±0.7

The position of the 2D band is shifted from 2711 cm^{-1} for GO, to 2705 cm^{-1} for GOIL. This decrease is in agreement with a lower content of sp^2 carbon [30]. In the same way, the slight increase in the I_D/I_G ratio (**Table 4**), from 0.92 for GO to 1.06 for GOIL shows a higher proportion of defects and the sp^3 bonds due to the presence of the IL [32, 33]. Crystallite size (L_A) [34] indicates a decrease in crystallinity or in sp^2 carbon [30, 35] and is also lower for GOIL than for GO (**Table 4**), in agreement with the reduction of sp^2 carbon.

The nanocomposites show the lowest crystallite size (**Table 4**) due to the degradation of the nanofillers after the extrusion and injection processing steps.

The effect of injection flow and nanophase orientation is also seen in surface roughness values. Surface topography and average roughness show a significant difference between the exterior and core section surfaces.

Table 5 and **Figure 6** show, respectively, average roughness values and surface topography profiles of PMMA and the nanocomposite materials, both on the exterior surface, which has been in contact with the mold wall [36, 37] and on the core section. The cutting operation to obtain core sections yields very similar R_a values for all materials (**Table 5**).

As expected, roughness values are higher on the exterior surface than on the core section, but this difference is much higher for the nanocomposites than for neat PMMA, which shows similar surface topography and roughness values on both surfaces. The addition of GO increases surface roughness of the exterior surface by a factor of 3.8. In the presence of the IL, in PMMA+GOIL, the roughness increases by a factor of 3.3 with respect to PMMA at the exterior surface. The very high exterior surface roughness of the nanocomposites could increase friction coefficients and wear rates.

3.2. Reciprocating sliding wear tests

In order to study the effect of the nanofiller additives, flow injection and surface topography on the tribological performance of PMMA, reciprocating sliding

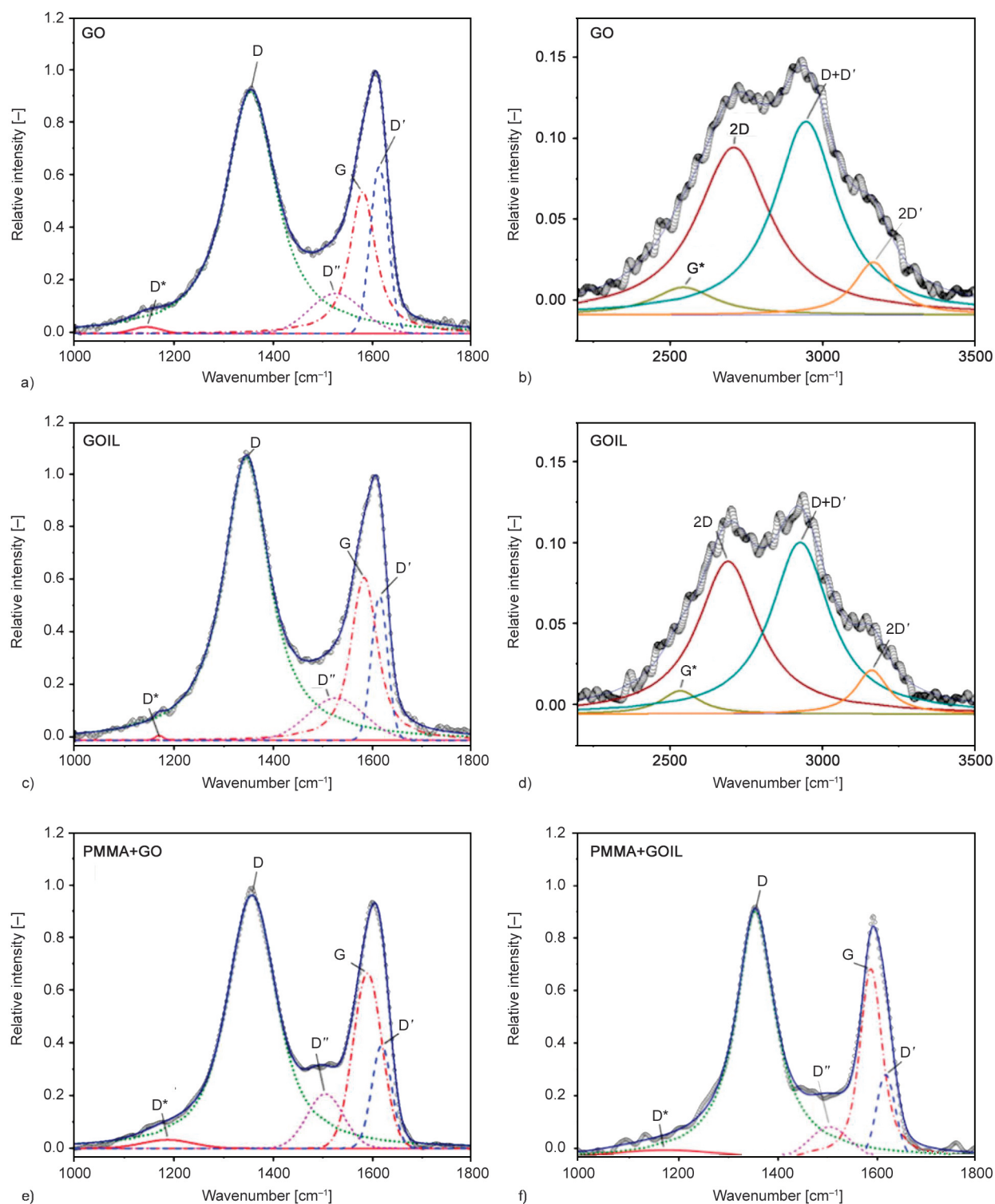


Figure 5. Raman spectra and deconvolution of D, G and 2D bands ($R^2 > 0.99$). a) GO bands D, G; b) GO band 2D; c) GOIL bands D, G; d) GOIL band 2D; e) PMMA+GO band D, G and f) PMMA+GOIL band 2G.

wear tests were performed on both the exterior and the longitudinal core section surfaces, as shown in [Figure 7](#).

[Figure 8](#) shows the characteristic coefficient of friction versus distance curve which are obtained for PMMA and nanocomposites under reciprocating sliding.

Initial or break-in friction coefficient (μ_0) values of approximately 0.10 and final or steady-state friction (μ_f) of 0.60 are obtained. All materials show transition distance values (d) lower than 100 m. Low initial friction coefficients are only maintained without transition to higher values during the whole sliding

Table 3. Raman results.

Nanophase	GO				
Band	D*	D	D''	G	D'
Wavenumber [cm ⁻¹]	1144.2	1354.6	1526.2	1580.1	1613.5
FWHM* [cm ⁻¹]	68.7	122.5	123.9	62.3	42.6
Area [%]	0.7	61.3	7.9	18.7	11.3
Relative intensity [-]	0.025	0.922	0.153	0.540	0.636

Nanophase	PMMA+GO				
Band	D*	D	D''	G	D'
Wavenumber [cm ⁻¹]	1187.0	1356.7	1504.4	1589.5	1618.0
FWHM* [cm ⁻¹]	120.5	118.7	86.5	68.5	47.0
Area [%]	1.7	62.3	7.9	20.1	8.1
Relative intensity [-]	0.032	0.962	0.207	0.664	0.390

*Full width at half maximum

Nanophase	GOIL				
Band	D*	D	D''	G	D'
Wavenumber [cm ⁻¹]	1169.1	1345.4	1526.7	1583.0	1613.9
FWHM* [cm ⁻¹]	20.1	111.2	134.6	63.7	38.3
Area [%]	0.1	62.9	8.6	20.1	8.3
Relative intensity [-]	0.017	1.077	0.161	0.619	0.549

Nanophase	PMMA+GOIL				
Band	D*	D	D''	G	D'
Wavenumber [cm ⁻¹]	1170.0	1355.6	1503.4	1588.0	1617.1
FWHM* [cm ⁻¹]	262.2	93.9	93.0	53.1	44.6
Area [%]	3.7	60.0	5.4	23.9	7.0
Relative intensity [-]	0.030	0.937	0.116	0.716	0.314

Table 4. Raman bands intensity ratios and sp² crystallite size (L_A) values.

Material	I_D/I	I_{2D}/I	L_A [nm]
GO	0.92±0.02	0.14±0.01	20.9
GOIL	1.06±0.04	0.14±0.01	18.1
PMMA+GO	1.08±0.04	–	17.8
PMMA+GOIL	1.10±0.08	–	17.5

Table 5. Surface roughness

Material	Roughness, R_a [μm]	
	Exterior	Core section
PMMA	0.18±0.01	0.15±0.01
PMMA+GO	0.69±0.05	0.17±0.01
PMMA+GOIL	0.60±0.04	0.15±0.01

test for the low roughness core section surface of PMMA+GO nanocomposite.

Figure 9 shows surface topography images of the wear tracks on all materials as a function of sliding direction, either parallel or perpendicular to the injection flow.

Wear volumes were determined from the product of cross-section worn areas [$A1-(A2+A3)$] [37] (where $A1$ is the area below the surface and $(A2+A3)$ are the areas of plastically deformed material accumulated on the edges of the wear track), along the length of the wear track (4 mm), without considering both wear track ends.

On the external surface, PMMA shows similar wear rates for both sliding directions, of the order of 10^{-3} mm³. In contrast, in PMMA+GO, the addition of GO reduces wear volume on the external surface in one order of magnitude, up to 10^{-4} mm³ (with

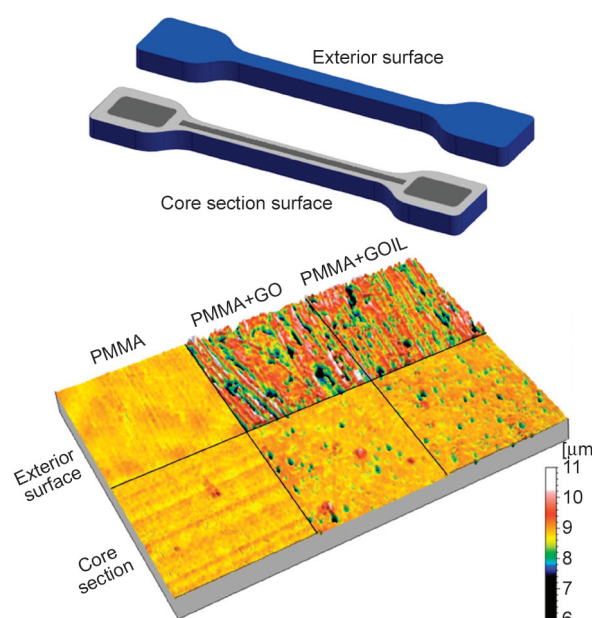


Figure 6. Scheme showing exterior and core section surfaces of injected parts and surface topography for PMMA, PMMA+GO and PMMA+GOIL on exterior and core section surfaces.

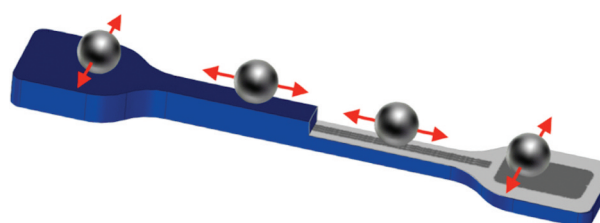


Figure 7. Scheme showing AISI 316L ball reciprocating sliding directions on PMMA and nanocomposites.

standard deviations lower than 10%). Moreover, PMMA+GO shows negligible wear volume on the core section surface, under both sliding directions, in agreement with the extremely mild surface damage shown in Figure 9. For PMMA+GOIL, surface damage is also minimized, but only under sliding

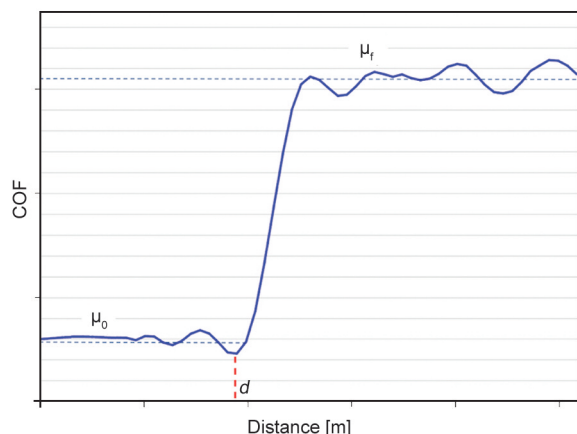


Figure 8. Representative coefficient of friction (COF) vs sliding distance record, under reciprocating sliding, showing transition distance from running-in (μ_0) and steady-state (μ_f).

parallel to the injection flow, in agreement with the longer transition distance of friction coefficients. Under sliding perpendicular to the flow, the wear volume of PMMA+GOIL is of the same order of magnitude as that of PMMA.

Wear scars on the different materials after reciprocating sliding tests were also studied by SEM microscopy.

Figure 10 shows SEM micrographs of the wear scars on core section surfaces. PMMA presents the same surface damage after sliding parallel and perpendicular to flow. Plastic deformation produces smooth

grooves with an accumulation of wear debris particle powder on the edges and at the ends of the scar.

Figure 10 shows very mild surface damage on PMMA+GO for both sliding directions. Wear debris is only observed in a very small amount compared to PMMA.

Figure 10 also shows the influence of sliding direction on PMMA+GOIL. Whilst in the parallel direction, the surface damage is very mild, similar to that observed for PMMA+GO. The wear damage in the perpendicular direction is more severe but shows a stick-slip effect, and some wear debris along the edges of the groove.

SEM micrographs in Figure 11 show the very mild abrasion wear parallel marks on PMMA+GO cross-section surface after reciprocating sliding in the direction parallel to flow.

A Raman study was carried out for a selected region inside the wear path (Figure 11). Raman mapping enables rich GO regions to be identified inside the PMMA matrix, as confirmed by their respective Raman spectra. GO-containing particles (in red), are randomly oriented inside the PMMA matrix (in blue). In order to study the distribution of the nanophases inside the colorless PMMA matrix, different cross-sections of the injected parts were obtained. Figure 12 (top) shows the results of an image composition of digital photographs along the longitudinal cross-sections of PMMA+GO, and PMMA+GOIL. Figure 12

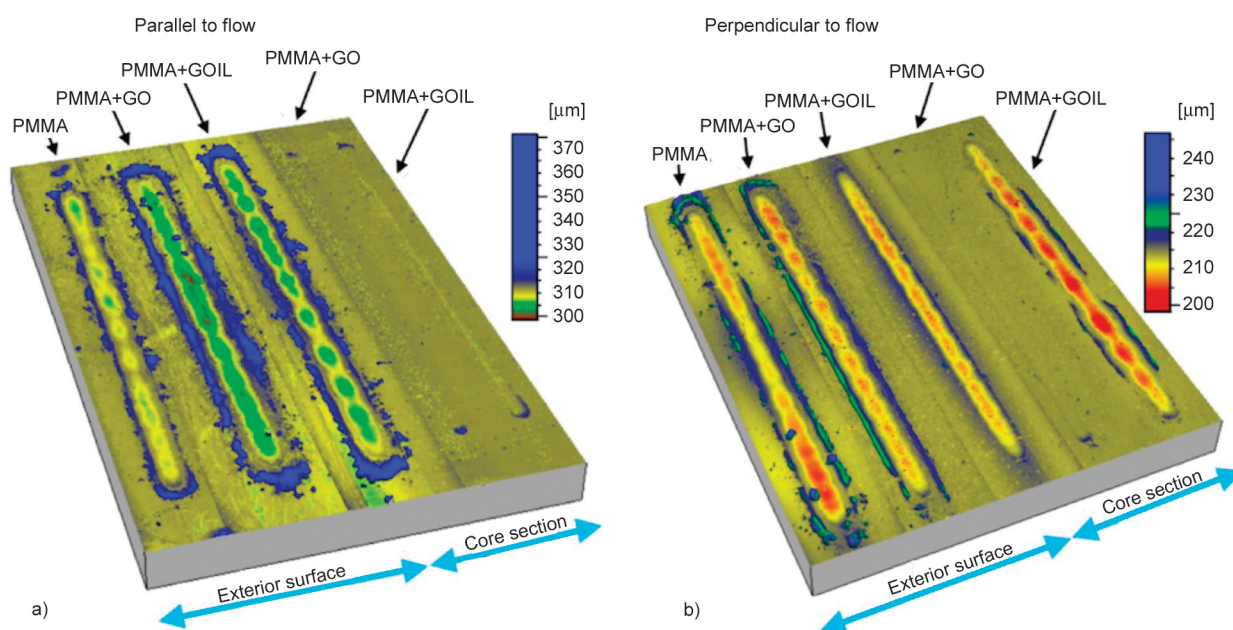


Figure 9. Profilometer surface topography of wear tracks after reciprocating sliding in the directions a) parallel to flow and b) perpendicular to flow.

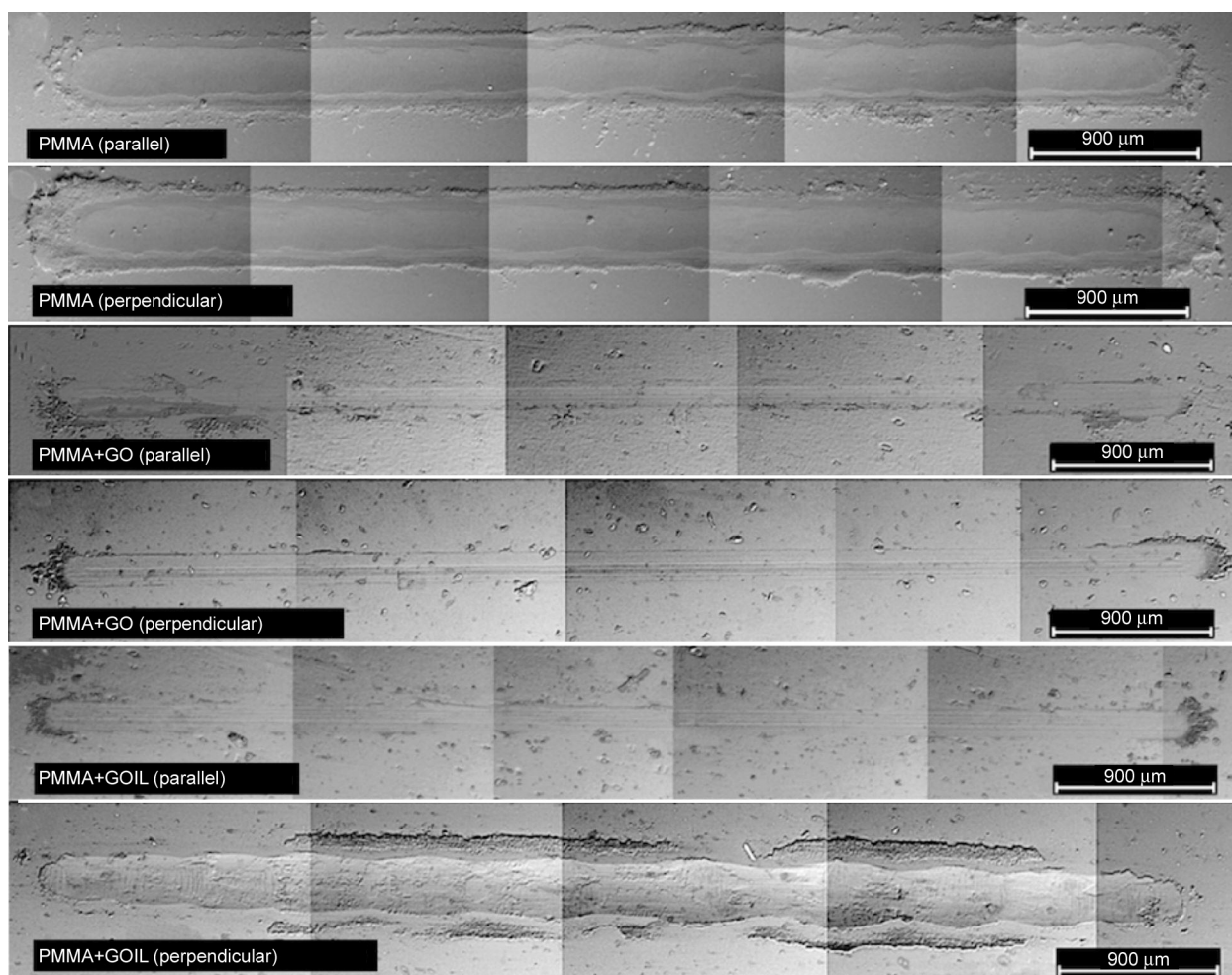


Figure 10. SEM micrographs of wear tracks under sliding parallel and perpendicular to injection flow for PMMA, PMMA+GO and PMMA+GOIL.

also shows a front view of the apparent GO distribution inside PMMA+GO, and a composition of photographs of cross-sections perpendicular to the injection flow in the Gate region (closer to the mold feeding gate) and parallel to the injection flow in the End region.

Apparently, an expansion of the region occupied by the nanophase takes place inside the central channel. According to Dericiler *et al.* [38], the maximum velocity in injection flow samples of PA66 with graphene nanoplatelets is reached inside the narrower central channel. Results showed a variation in the orientation of graphene nanoplatelets along the length of the injected part.

As the weight percentage of the nanophases is the same along the injected part (as determined according to the ASTM D1603 standard), the optical observations in Figures 13 and 14 could be due to a different orientation and distribution of GO or GOIL along the injected parts geometry. Previous studies

on the orientation of carbon nanophases, in particular carbon nanotubes in molded polyvinylfluoride [39], have shown that the nanotubes are oriented parallel to the injection flow close to the mold wall but adopted a disordered orientation in the central core region. A Raman microscopy study was carried out in order to confirm the evolution of the orientation, at least of micron-size agglomerates, inside the injected parts section.

Figure 13 shows optical micrographs and Raman spectra of PMMA matrix and GO nanophase. Figure 14 shows the corresponding Raman study for PMMA+GOIL.

In both cases (Figures 13 and 14), it can be observed that the orientation of GO and GOIL additives is parallel to injection flow inside the regions closer to both exterior surfaces (top and bottom magnifications), and changes to a higher angle, including perpendicular orientation, with respect to the injection flow direction, inside the center region (central

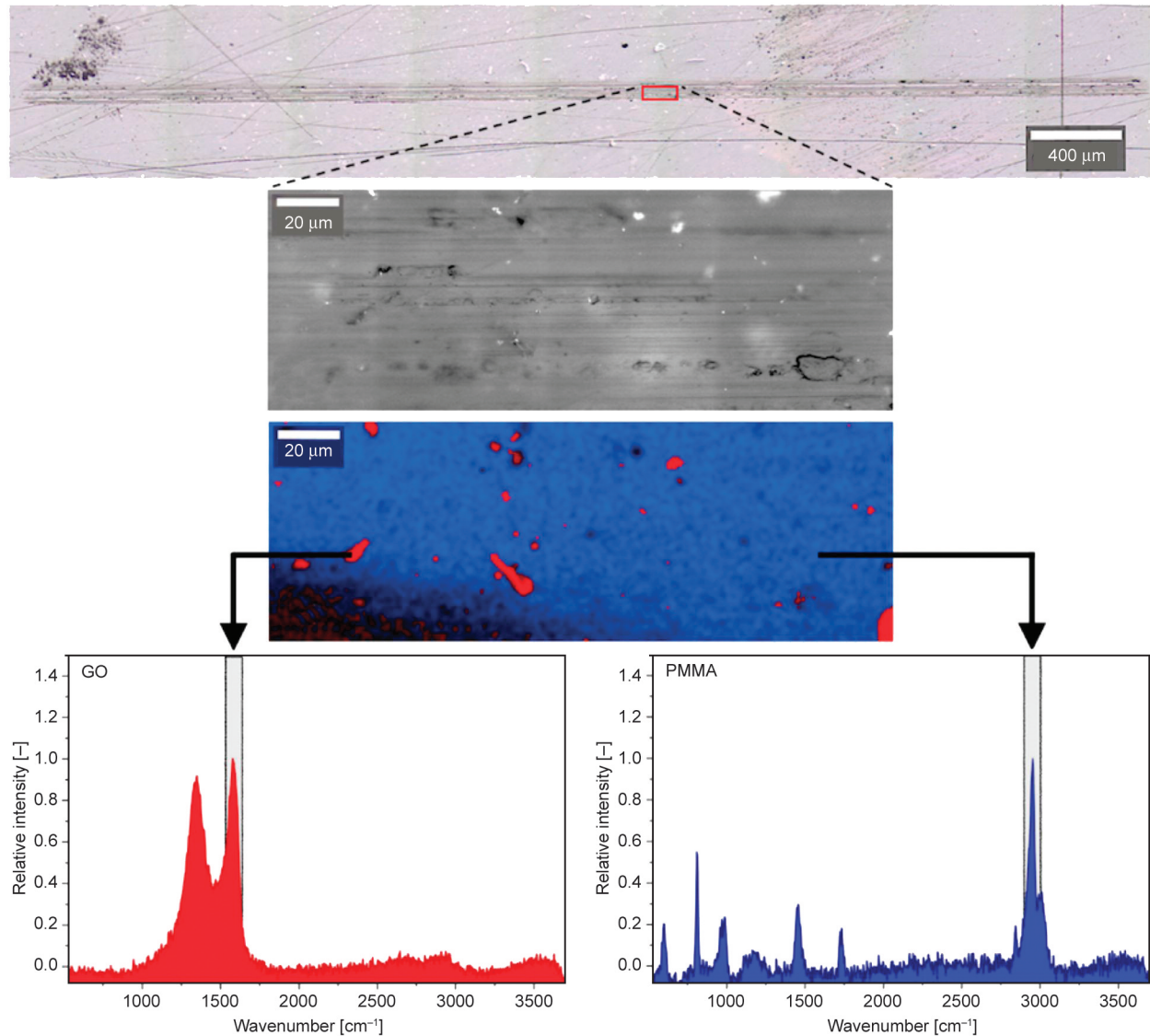


Figure 11. Raman micrograph of the wear scar after sliding parallel to the flow on PMMA+GO core section surface. Magnification of the selected area and Raman map and spectra of PMMA matrix (in blue) and GO nanofiller (in red). Highlighted in grey are the Raman bands used to obtain the Raman map.

magnification image) across the thickness of the injected part.

In all cases, the Raman spectra are in agreement with PMMA matrix (shown in blue) and GO or GOIL nanofillers (shown in red), respectively.

3.3. Abrasive wear tests under multiple scratching

Multiple scratch tests were performed in order to study the abrasion resistance of the new nanocomposites and their ability for viscoelastic recovery. The results of the oscillatory tests described in the previous section have shown the influence of sliding direction with respect to the injection flow, with higher resistance to surface damage under sliding in

the parallel direction. Previous results on the resistance of nanocomposites to abrasion under multiple scratching have also shown a similar effect [40].

With these precedents, the multiple scratch tests for the new nanocomposites were performed on the core section surfaces of the injected parts (see Figure 6), in the direction parallel to flow.

Figure 15 shows the Raman microscopy study of scratch grooves [41] on PMMA+GO. The magnification in Figure 15 shows the presence of very scarce surface defects and microcracks. Finally, GO particles (in red, in Figure 15) show a non-parallel alignment with respect to the injection flow or to the indenter pass at the core section level. These results show that the original orientation of the additives through the

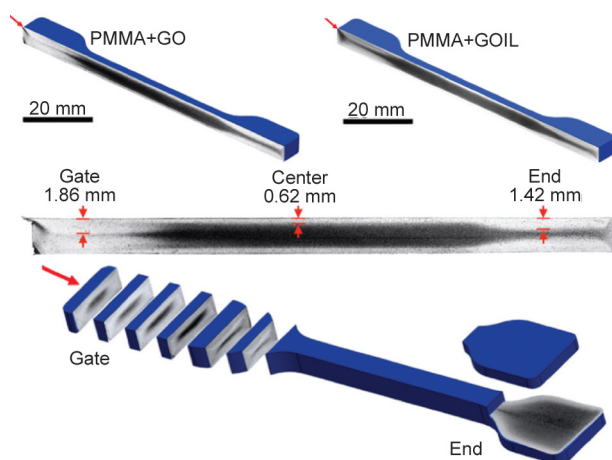


Figure 12. From top to bottom: longitudinal cross-section of PMMA+GO and PMMA+GOIL; front view of the longitudinal cross-section showing thickness of more transparent regions, and perpendicular cross-sections along the Gate region, and parallel core section along the End region. The arrows show the injection flow direction.

thickness of PMMA composites (Figure 13) is not altered under multiple scratching conditions.

Table 6 shows the results of instantaneous penetration (Pd), residual depth (Rd), and viscoelastic recovery

percentage (calculated as $[(Pd - Rd)/Pd] \cdot 100$) for each material. The best performance is found for the material containing graphene oxide modified by ionic liquid. Thus, although instantaneous penetration is higher for PMMA+GOIL than for PMMA+GO, PMMA+GOIL presents a higher viscoelastic recovery. This gives a final permanent damage (Rd) for PMMA+GOIL 21% lower than that for PMMA+GO. This behavior is attributed to the presence of the IL fluid phase and is in agreement with previous results [37]. The fluid ionic liquid phase increases polymer chain displacement and plastic deformation under load but also eases the viscoelastic recovery of the material.

The reinforcing effect of the addition of GO reduces plastic deformation and material loss under all sliding configurations and sliding directions studied here.

The results of multiscratch tests have shown that the mechanism in the case of the hybrid GOIL nanofiller is not the same. Although plastic deformation under load is higher than that of PMMA, the final surface damage is lower. This could be explained by an

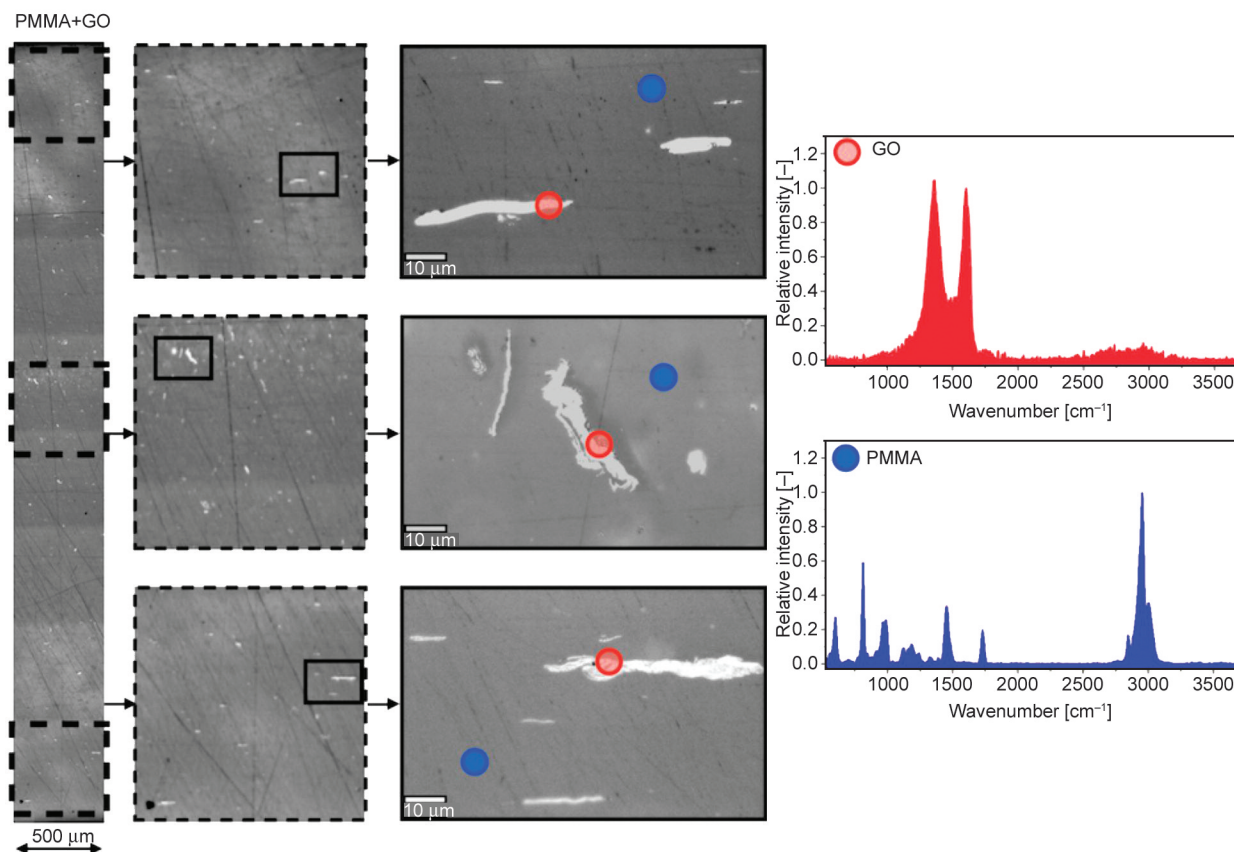


Figure 13. Optical microscopy (100×) images through the thickness of an injected part of PMMA+GO and Raman spectra of the matrix (in blue) and nanofiller (in red).

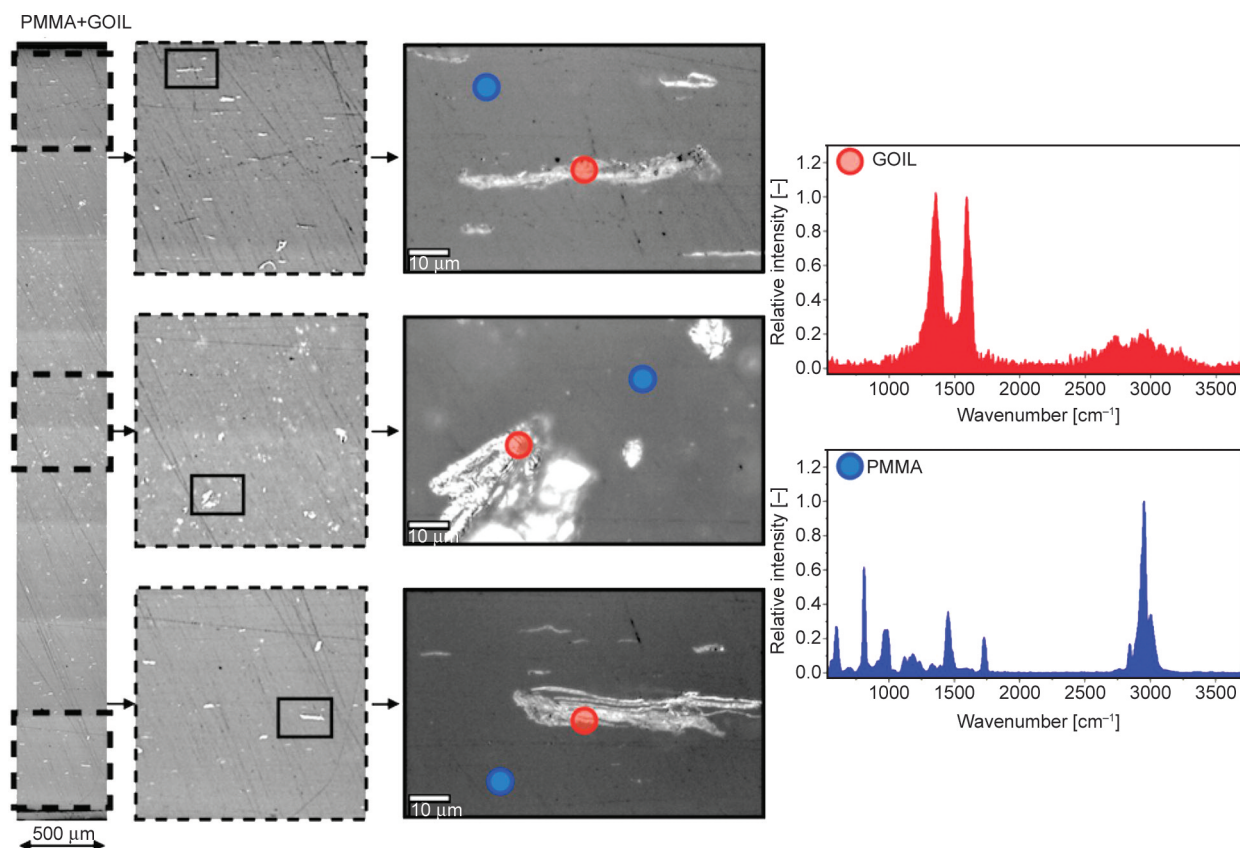


Figure 14. Optical microscopy (100×) images through the thickness of an injected part of PMMA+GOIL and Raman spectra of the matrix (in blue) and nanofiller (in red).

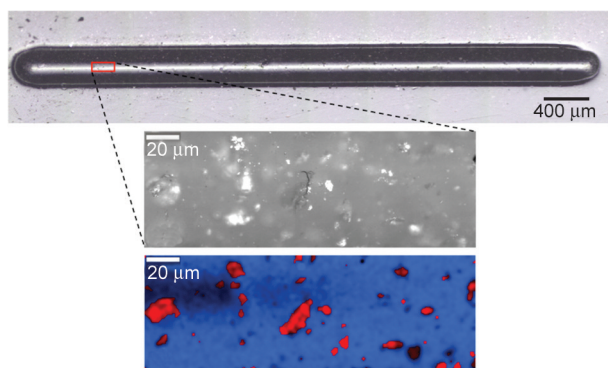


Figure 15. Optical microscopy image of wear scar on the core section surface of PMMA+GO after scratch test, magnification of the selected area and Raman map showing graphene oxide (red) in the PMMA matrix (blue).

Table 6. Abrasive wear resistance under multiple scratching on the core section surface (after 15 successive scratches on the same groove, parallel to flow).

Material	Pd [μm]	Rd [μm]	Recovery [%]
PMMA	68.6±2.7	24.5±0.9	64.3±2.4
PMMA+GO	49.8±2.5	19.2±1.3	61.5±2.6
PMMA+GOIL	75.5±5.5	15.2±1.2	79.7±2.4

internal effect of GOIL that induces localized mobility of PMMA chains under applied load. This mobility is mainly favored in the direction parallel to injection flow, as pointed out by the reciprocating sliding tests (section 3.2).

3.4. Rheological behavior

The rheological behavior of the materials in the softened state was studied in order to establish the influence of the additives on the resistance to flow of PMMA.

Complex viscosity values for PMMA+GO are very similar to those of PMMA (Figure 16), up to the highest angular frequency values, where PMMA+GO presents a sharp transition to higher viscosity values. PMMA+GOIL presents the lowest complex viscosity values (Figure 16) in the whole range of angular frequency. This confirms the ability of GOIL to improve the relative displacements of the polymer chains.

As complex viscosity is a measure of resistance to flow, the results shown in Figure 16, indicate that the ionic liquid phase could act as a processing aid, and

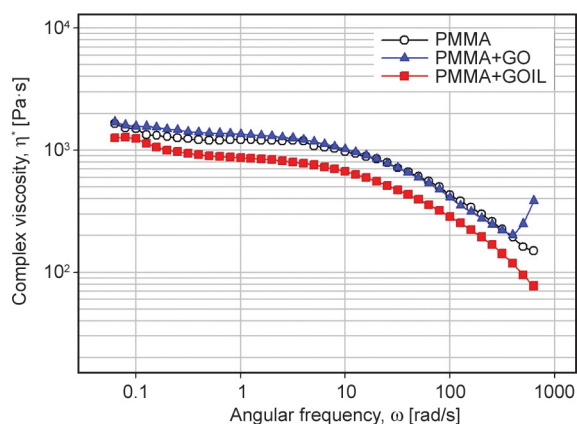


Figure 16. Variation of complex viscosity with angular frequency at 245 °C.

enhance viscoelastic recovery, as we have seen in multiple scratch tests.

4. Conclusions

Extrusion+injection molding melt processing has been used to obtain new PMMA nanocomposites with graphene oxide (GO) or graphene oxide modified by a room-temperature ionic liquid (GOIL), without the use of organic solvents.

Raman characterization of the new nanocomposites shows that modification with IL increases the defects and sp^3 bonds and reduces crystallinity in GO. The crystallite size of the nanophases is reduced when added to the PMMA matrix as a result of degradation induced by the extrusion+injection processing stages. Raman microscopy shows the heterogeneous orientation of the additives inside the polymer matrix, from predominantly parallel to the injection flow at both exterior surfaces, close to the injection mold walls, to a higher angle, including perpendicular orientation, inside the core section furthest from the mold walls.

The wear resistance of the new nanocomposites has been studied under reciprocating sliding both on the exterior and on the core section surfaces of the injected parts.

On the exterior surface, the tribological performance of PMMA+GO and PMMA+GOIL is similar to that of PMMA. This is attributed to the high surface roughness of the surface of the nanocomposite with respect to that of unmodified PMMA.

On the core section surface, with low surface roughness values, similar for all materials, PMMA+GO shows outstanding tribological performance with non-measurable wear under reciprocating sliding

both parallel and perpendicular to the injection flow due to the reinforcing effect of graphene oxide.

For PMMA+GO, negligible surface damage is only observed under sliding parallel to the flow, when the enhanced chain displacement ability of the IL fluid phase can be more effective.

In abrasion tests under multiple scratching on the core surface, in the direction parallel to flow, the nanocomposites reduce permanent surface damage of PMMA. In agreement with the reinforcing effect of GO, the highest resistance to instantaneous damage is reached for PMMA+GO, although the maximum viscoelastic recovery is observed for PMMA+GOIL. This is also attributed to the higher chain mobility induced by the presence of the fluid ionic liquid phase, which enhances instantaneous deformation under load but also viscoelastic recovery after the load is removed.

The ionic liquid modified graphene oxide additive could also act as a processing aid due to its ability to lower the complex viscosity of PMMA in the softened state.

The results presented herein highlight the different antiwear mechanism induced by each nanofiller and the relevance of processing parameters on the tribological behavior of the different regions of nanocomposite injected parts.

Acknowledgements

This research was funded by Spanish Ministerio de Ciencia e Innovación, Agencia Estatal de Investigación (AEI), and the European Union FEDER Program (Grants # MAT2017-85130-P and PID2021-122169NB-I00), and by the Fundación Seneca, Agencia de Ciencia y Tecnología de la Región de Murcia ('Ayuda a las Unidades y Grupos de Excelencia Científica de la Región de Murcia'; Grant # 19877/GERM/15).

References

- [1] Unal H., Mimaroglu A.: Friction and wear behaviour of unfilled engineering thermoplastics. *Materials and Design*, **24**, 183–187 (2003).
[https://doi.org/10.1016/S0261-3069\(03\)00018-9](https://doi.org/10.1016/S0261-3069(03)00018-9)
- [2] Brostow W., Lobland H. E. H., Hnatchuk N., Perez J. M.: Improvement of scratch and wear resistance of polymers by fillers including nanofillers. *Nanomaterials*, **7**, 66 (2017).
<https://doi.org/10.3390/nano7030066>
- [3] Sun J., Du S.: Application of graphene derivatives and their nanocomposites in tribology and lubrication: A review. *RSC Advances*, **9**, 40642–40661 (2019).
<https://doi.org/10.1039/C9RA05679C>

- [4] Chung D. D. L.: A review of multifunctional polymer-matrix structural composites. *Composites Part B: Engineering*, **160**, 644–660 (2019).
<https://doi.org/10.1016/j.compositesb.2018.12.117>
- [5] Friedrich K.: Polymer composites for tribological applications. *Advanced Industrial Engineering Polymer Research*, **1**, 3–39 (2018).
<https://doi.org/10.1016/j.aiepr.2018.05.001>
- [6] Trikkaliotis D. G., Christoforidis A. K., Mitropoulos A. C., Kyzas G. Z.: Graphene oxide synthesis, properties and characterization techniques: A comprehensive review. *ChemEngineering*, **5**, 64 (2021).
<https://doi.org/10.3390/chemengineering5030064>
- [7] Szeluga U., Kumanek B., Trzebicka B.: Synergy in hybrid polymer/nanocarbon composites. A review. *Composites Part A: Applied Science and Manufacturing*, **73**, 204–231 (2015).
<https://doi.org/10.1016/j.compositesa.2015.02.021>
- [8] Stankovich S., Dikin D. A., Dommett G. H. B., Kohlaas K. M., Zimney E. J., Stach E. A., Piner R. D., Nguyen S. T., Ruoff R. S.: Graphene-based composite materials. *Nature*, **442**, 282–286 (2006).
<https://doi.org/10.1038/nature04969>
- [9] Potts J. R., Dreyer D. R., Bielawski C. W., Ruoff R. S.: Graphene-based polymer nanocomposites. *Polymer*, **52**, 5–25 (2011).
<https://doi.org/10.1016/j.polymer.2010.11.042>
- [10] Kumar A., Sharma K., Dixit A. R.: A review of the mechanical and thermal properties of graphene and its hybrid polymer nanocomposites for structural applications. *Journal of Materials Science*, **54**, 5992–6026 (2019).
<https://doi.org/10.1007/s10853-018-03244-3>
- [11] Vallés C., Kinloch I. A., Young R. J., Wilson N. R., Rourke J. P.: Graphene oxide and base-washed graphene oxide as reinforcements in PMMA nanocomposites. *Composite Science and Technology*, **88**, 158–164 (2013).
<https://doi.org/10.1016/j.compscitech.2013.08.030>
- [12] Kausar A.: Poly(methyl methacrylate) nanocomposite reinforced with graphene, graphene oxide, and graphite: A review. *Polymer-Plastics Technology and Materials*, **58**, 821–842 (2019).
<https://doi.org/10.1080/25740881.2018.1563112>
- [13] Mirabedini A., Ang M., Nikzad M., Fox B., Lau K-T., Hameed N.: Evolving strategies for producing multi-scale graphene-enhanced fiber-reinforced polymer composites for smart structural applications. *Advanced Science*, **7**, 1903501 (2020).
<https://doi.org/10.1002/advs.201903501>
- [14] Song J., Zhang J., Lin C.: Influence of graphene oxide on the tribological and electrical properties of PMMA composites. *Journal of Nanomaterials*, **2013**, 846102 (2013).
<https://doi.org/10.1155/2013/846102>
- [15] Livi S., Duchet-Rumeau J., Gérard J-F., Pham T. N.: Polymers and ionic liquids: A successful wedding. *Macromolecular Chemistry and Physics*, **216**, 359–368 (2015).
<https://doi.org/10.1002/macp.201400425>
- [16] Scott M. P., Brazel C. S., Benton M. G., Mays J. W., Holbrey D., Rogers R. D.: Application of ionic liquids as plasticizers for poly(methyl methacrylate). *Chemical Communications*, **13**, 1370–1371 (2002).
<https://doi.org/10.1039/B204316P>
- [17] Scott M. P., Rahman M., Brazel C. S.: Application of ionic liquids as low-volatility plasticizers for PMMA. *European Polymer Journal*, **39**, 1947–1953 (2003).
[https://doi.org/10.1016/S0014-3057\(03\)00129-0](https://doi.org/10.1016/S0014-3057(03)00129-0)
- [18] Zhao L., Li Y., Cao X., You J., Dong W.: Multifunctional role of an ionic liquid in melt-blended poly(methyl methacrylate)/ multi-walled carbon nanotube nanocomposites. *Nanotechnology*, **23**, 255702 (2012).
<https://doi.org/10.1088/0957-4484/23/25/255702>
- [19] Zornio C. F., Livi S., Rumeau J. D., Gerard J-F.: Ionic liquid-nanostructured poly(methyl methacrylate). *Nanomaterials*, **9**, 1376 (2019).
<https://doi.org/10.3390/nano9101376>
- [20] Avilés M-D., Pamies R., Sanes J., Bermúdez M-D.: Graphene-ionic liquid thin film nanolubricant. *Nanomaterials*, **10**, 535 (2020).
<https://doi.org/10.3390/nano10030535>
- [21] Khare V., Pham M-Q, Kumari N., Yoon H-S., Kim C-S., Park J-L., Ahn S-H.: Graphene-ionic liquid based hybrid nanomaterials as novel lubricant for low friction and wear. *ACS Applied Materials and Interfaces*, **5**, 4063–4075 (2013).
<https://doi.org/10.1021/am302761c>
- [22] Avilés M-D., Saurín N., Sanes J., Carrión F-J., Bermúdez M-D.: Ionanocarbon lubricants. The combination of ionic liquids and carbon nanophases in tribology. *Lubricants*, **5**, 14 (2017).
<https://doi.org/10.3390/lubricants5020014>
- [23] Tunckol M., Durand J., Serp P.: Carbon nanomaterial-ionic liquid hybrids. *Carbon*, **50**, 4303–4334 (2012).
<https://doi.org/10.1016/j.carbon.2012.05.017>
- [24] Aldroubi S., Brun N., Malham I. B., Mehdi A.: When graphene meets ionic liquids: A good match for the design of functional materials. *Nanoscale*, **13**, 2750–2779 (2021).
<https://doi.org/10.1039/D0NR06871C>
- [25] Zhao F., Zhang L., Li G., Guo Y., Qi H., Zhang G.: Significantly enhancing tribological performance of epoxy by filling with ionic liquid functionalized graphene oxide. *Carbon*, **136**, 309–319 (2018).
<https://doi.org/10.1016/j.carbon.2018.05.002>
- [26] Sanes J., Avilés M. D., Saurín N., Espinosa T., Carrión F-J., Bermúdez M-D.: Synergy between graphene and ionic liquid lubricant additives. *Tribology International*, **116**, 371–382 (2017).
<https://doi.org/10.1016/j.triboint.2017.07.030>

- [27] Espejo C., Carrión F. J., Bermúdez M. D.: Scratch resistance of new polystyrene nanocomposites with ionic liquid-modified multi-walled carbon nanotubes. *Tribology Letters*, **52**, 271–285 (2013).
<https://doi.org/10.1007/s11249-013-0212-0>
- [28] Bermúdez M. D., Carrión F. J., Espejo C., Martínez-López E., Sanes J.: Abrasive wear under multiscratching of polystyrene + single-walled carbon nanotube nanocomposites. Effect of sliding direction and modification by ionic liquid. *Applied Surface Science*, **257**, 9073–9081 (2011).
<https://doi.org/10.1016/j.apsusc.2011.05.103>
- [29] Sanes J., Ojados G., Pamies R., Bermúdez M. D.: PMMA nanocomposites with graphene oxide hybrid nanofillers. *Express Polymer Letters*, **13**, 910–922 (2019).
<https://doi.org/10.3144/expresspolymlett.2019.79>
- [30] López-Díaz D., Holgado M. L., García-Fierro J. L., Velázquez M. : Evolution of the Raman spectrum with the chemical composition of graphene oxide. *The Journal of Physical Chemistry C*, **121**, 20489–20497 (2017).
<https://doi.org/10.1021/acs.jpcc.7b06236>
- [31] Claramunt S., Varea A., López-Díaz D., Velázquez M. M., Cirera A.: The importance of interbands on the interpretation of the Raman spectrum of graphene oxide. *The Journal of Physical Chemistry C*, **119**, 10123–10129 (2015).
<https://doi.org/10.1021/acs.jpcc.5b01590>
- [32] Lee A. Y., Yang K., Anh N. D., Park C., Lee S. M., Lee T. G., Jeong M. S.: Raman study of D* band in graphene oxide and its correlation with reduction. *Applied Surface Science*, **536**, 147990 (2021).
<https://doi.org/10.1016/j.apsusc.2020.147990>
- [33] Thomas K. J., Sheeba M., Nampoori V. P. N., Vallabhan C. P. G., Radhakrishnan P.: Raman spectra of polymethyl methacrylate optical fibres excited by a 532 nm diode pumped solid state laser. *Journal of Optics A: Pure and Applied Optics*, **10**, 055303 (2008).
<https://doi.org/10.1088/1464-4258/10/5/055303>
- [34] Cançado L. G., Takai K., Enoki T., Endo M., Kim Y. A., Mizusaki H.: General equation for the determination of the crystallite size L_a of nanographite by Raman spectroscopy. *Applied Physics Letters*, **88**, 163106 (2006).
<https://doi.org/10.1063/1.2196057>
- [35] Krishnamoorthy K., Veerapandian M., Yun Q., Kim S.-J.: The chemical and structural analysis of graphene oxide with different degrees of oxidation. *Carbon*, **53**, 38–49 (2013).
<https://doi.org/10.1016/j.carbon.2012.10.013>
- [36] Martínez-Mateo I., Carrión-Vilches F. J., Sanes J., Bermúdez M. D.: Surface damage of mold steel and its influence on surface roughness of injection molded plastic parts. *Wear*, **271**, 2512–2516 (2011).
<https://doi.org/10.1016/j.wear.2010.11.054>
- [37] Carrión-Vilches F. J., González-Vivas A., Martínez-Mateo I. J., Bermúdez M. D.: Study of the abrasion resistance under scratching of polybutylenetereftalateglass fiber composites. *Tribology International*, **192**, 365–378 (2015).
<https://doi.org/10.1016/j.triboint.2015.07.004>
- [38] Dericiler K., Sadeghi H. M., Yagci Y. E., Sas H. S., Okan B. S.: Experimental and numerical investigation of flow and alignment behavior of waste tire-derived graphene nanoplatelets in PA66 matrix during melt-mixing and injection. *Polymers*, **13**, 949 (2021).
<https://doi.org/10.3390/polym13060949>
- [39] Fan B., Lu X., Dang Z., Deng Y., Zhou X., He D., Bai J.: Improved dispersion of carbon nanotubes in poly(vinylidene fluoride) composites by hybrids with core-shell structure. *Journal of Applied Polymer Science*, **135**, 45693 (2018).
<https://doi.org/10.1002/app.45693>
- [40] Bermúdez M. D., Carrión F. J., Espejo C., Martínez-López E., Sanes J.: Abrasive wear under multiscratching of polystyrene + single-walled carbon nanotube nanocomposites. Effect of sliding direction and modification by ionic liquid. *Applied Surface Science*, **257**, 9073–9081 (2011).
<https://doi.org/10.1016/j.apsusc.2011.05.103>
- [41] Brostow W., Chonkaew W., Rapoport L., Soifer Y., Verdyan A., Soifer Y.: Grooves in scratch testing. *Materials Research Society*, **22**, 2483–2487 (2007).
<https://doi.org/10.1557/JMR.2007.0307>

Research article

Wide-temperature-range and anti-aging self-healing polyurethane enabled by dual cooperative cross-linking strategy

Yu Zhang¹, Jian Zheng¹, Wanli Ma², Xiao Zhang^{3,4*}, Yongqiang Du⁵, Ke Li⁶, Yahao Liu⁷, Guibo Yu¹, Yunfei Jia¹

¹Shijiazhuang Campus, Army Engineering University, 050003 Shijiazhuang, China

²Academy of People's Armed Police, 100012 Beijing, China

³Engineering University of PAP, 710086 Xi'an, China

⁴State Key Lab for Strength and Vibration of Mechanical Structures, Department of Engineering Mechanics, Xi'an Jiaotong University, 710049 Xi'an, China

⁵Dalian Naval Academy, 116013 Dalian, China

⁶Unit 92941 of the people's Liberation Army, 125003 Huludao, China

⁷College of Naval Architecture and Ocean Engineering, Naval University of Engineering, 430033 Wuhan, China

Received 1 July 2022; accepted in revised form 26 September 2022

Abstract. The development of skin-compatible polyurethane materials with excellent wide-temperature range and anti-aging self-healing properties is considered crucial for modern applications. However, few polyurethane materials can achieve these characteristics simultaneously because of the chemical bond activity. Here, we report a wide-temperature range and anti-aging self-healing polyurethane material with superior mechanical features. At $-40\text{ }^{\circ}\text{C}$, the polyurethane exhibits a self-healing efficiency of 72.6%, with a tensile strength of $\sim 7.4\text{ MPa}$ and elongation at break of $\sim 1424.5\%$. At $60\text{ }^{\circ}\text{C}$, its self-healing efficiency reached 93.6%, with an elongation at break of 1922.2% without significant reduction of the tensile strength. Notably, its low-temperature self-healing efficiency was 79.3 and 72.6%, respectively, at -20 and $-40\text{ }^{\circ}\text{C}$, and the samples showed some degree of self-healing, even at -60 and $-80\text{ }^{\circ}\text{C}$. Meanwhile, the polyurethane showed excellent anti-aging performance, and its self-healing properties were sufficiently high after aging at $60\text{ }^{\circ}\text{C}$ for 7 days. The designed polyurethane is expected to offer a promising platform for fabricating materials for electronic skin applications, wearable electronic devices, flexible displays, and soft robotics.

Keywords: polyurethane, self-healing, mechanical properties, wide temperature range, anti-aging

1. Introduction

Electronic skin (e-skin), a novel technology that can monitor many kinds of signals and exhibits high sensitivity and wide detection range [1–4], has significant potential in wearable electronic devices, flexible displays, and soft robotics [5–13]. Elastic polyurethane substrates are often used to endow e-skins with excellent mechanical elasticity; however, during the application, polyurethane is inevitably subjected to

accidental damage, such as scratches and penetrations, and therefore highly susceptible to tearing [14, 15]. Inspired by the rapid and efficient self-healing ability of human skin after injury, researchers have attempted to incorporate self-healing functionality into e-skin [7, 16].

In recent decades, significant progress has been achieved in the field of self-healing materials, and two types of such materials have been developed

*Corresponding author, e-mail: zxleo@foxmail.com

© BME-PT

based on extrinsic or intrinsic healing mechanisms [17, 18]. Extrinsic self-healing materials generally rely on a healing agent in implanted microcapsules [19–21]. As the amount of the implanted healing agent is fixed, it can only provide limited repairs, and the preparation process is relatively complicated [22]. In contrast, intrinsic self-healing materials are realized by the reversible exchange reaction of dynamic bonds, such as metal coordination bonds [23–27], hydrogen bonds [28–30], disulfide bonds [31–35], D-A reactions [36, 37], imine bonds [38], and boron-ester bonds [39, 40]. Theoretically, intrinsic self-healing materials can be repaired countless times and have more stable self-healing properties than extrinsic self-healing materials; therefore, intrinsic self-healing has received more attention. Through the introduction of self-healing technology, some self-healing polyurethanes with excellent mechanical properties have been successfully synthesized [41–45]. Wu *et al.* [43] successfully prepared an elastomer with excellent tensile strength, high toughness, high self-healing efficiency, and good puncture resistance by introducing an asymmetric alicyclic structure adjacent to an aromatic disulfide into polyurethane. The tensile strength and toughness of this elastomer were as high as 46.4 MPa and 109.1 MJ/m³, respectively, and it also had a self-healing efficiency of 90.3%. Liu *et al.* [44] developed a nanofiber-reinforced self-healing polymer matrix that mainly mimics the structure and function of human skin. Significantly, its tensile strength and toughness were improved by 836 and 1000%, respectively, compared with those of the pure matrix, while its healing efficiency was largely preserved. Wei *et al.* [45] successfully developed a novel self-healing elastomer enhanced by dynamic supramolecular nanosheets with switchable interfacial interactions. The elastomer has a high self-healing efficiency (91.2%). In addition, supramolecular nanosheets, as layered nanofillers, possess strong interfacial interactions and endow elastomers with outstanding mechanical properties, water insensitivity, and gas barrier properties.

However, these polyurethane materials can only accomplish self-healing at room temperature or high temperatures. At low temperatures, where the molecular chain movement is significantly hindered, the self-healing efficiency of polyurethane decreases abruptly [46]. At present, despite the constantly

increasing number of studies on low-temperature self-healing materials, the contradiction between the strength of the material and its low-temperature self-healing performance persists. Most materials with excellent low-temperature self-healing properties are extremely soft hydrogels, which have extremely low tensile strength, despite their excellent molecular chain mobility. In contrast, high-strength polymer materials have poor low-temperature self-healing properties owing to their high cross-linking density. Li *et al.* [47] synthesized a polydimethylsiloxane polymer chain network cross-linked by coordination compounds, which showed an elongation at break of ~1825% and tensile strength of ~0.23 MPa at 25 °C. However, owing to its high cross-link density and strong Fe-pyridine coordination bonds, its repair efficiency reached only ~68% after self-healing at –20 °C for 72 h. Wang *et al.* [48] prepared a multifunctional ionic hydrogel with a repair efficiency of up to 68.6% at –80 °C with a repair time of only 30 min and an ultra-long elongation at break of >7000%. These features were attributed to the extremely soft hydrogel structure that facilitated the exchange reactions of dynamic bonds (*e.g.*, ionic bonds); however, the material strength was extremely low (~0.02 MPa). Therefore, the design of polyurethane with excellent self-healing and mechanical properties over a wide temperature range is paramount. However, another aspect of the durability of polyurethane, the anti-aging performance, has seldom been studied. In fact, anti-aging is as important as other durability factors because the polyurethane matrix may need to resist ultraviolet rays, humidity, and other environmental factors during its lifecycle. In this study, dual-dynamic-bond cross-linking and copolymerization strategies were synergistically introduced into a polyurethane polymer to prepare an anti-aging material with superior self-healing and mechanical performance over a wide temperature range. The method included the copolymerization of hydroxyl-terminated polyethylene glycol-tetrahydrofuran co-polyether (HTPE) with hydroxyl-terminated polybutadiene (HTPB), followed by the addition of aliphatic disulfides (HEDS) to form ligands; finally, zinc chloride (ZnCl₂) was added to cross-link with the ligands and form polyurethane. The mechanical, self-healing, and anti-aging properties of the synthesized polyurethane were analyzed considering various aspects.

2. Materials and methods

2.1. Materials

HTPB (hydroxyl value = $0.75 \text{ mmol} \cdot \text{g}^{-1}$, functionality (f) = 2, 99% purity), 1,4-butanediol (BDO, 99% purity), ZnCl_2 , and N,N -dimethylformamide (DMF, $\geq 99.8\%$ purity) were purchased from Jining Huakai Resin Co., Ltd. (Jining, China). HTPE (hydroxyl value = $0.68 \text{ mmol} \cdot \text{g}^{-1}$, $f = 2$, 99.5% purity) was purchased from Luoyang Liming Chemical Research and Design Institute Co., Ltd. (Luoyang, China), whose relative molecular weights ($M_w = 3217 \text{ g} \cdot \text{mol}^{-1}$, $M_n = 2925 \text{ g} \cdot \text{mol}^{-1}$, $D = 1.10$) were determined by gel permeation chromatography (GPC, PL-GPC50) (Yuzhong Industrial Co., Ltd., Shanghai, China) (Figure 1). Dibutyl phthalate (DBP, 99.5% purity) was provided by the Tianjin Damao Chemical Reagent Factory (Tianjin, China). Triphenylbismuth (TPB), HEDS (90% purity), isophorone diisocyanate (IPDI, 99% purity), and tetrahydrofuran (THF) were obtained from Shanghai McLean Biochemical Technology Co., Ltd. (Shanghai, China).

2.2. Synthesis of HEPU-Zn polyurethane

First, 2.4 g of HTPB was added to a 100 ml three-necked flask and dried overnight at 60°C in a vacuum environment. Then, 1.8 mg of TPB (catalyst), 0.39 g of DBP (plasticizer), and 0.49 g of IPDI (curing agent) were thoroughly mixed, added to the flask, and stirred at 60°C under nitrogen protection for 2 h. Thereafter, 0.6 g of HTPE was mixed well with 1 ml of DMF, and the mixture was added to the flask to conduct the copolymerization reaction for 1 h. Next, 0.27 g of HEDS (chain extender) was gradually added to the mixture, followed by stirring for 2 h to obtain the ligand. Finally, 58.6 mg of ZnCl_2 was fully dissolved in 2 ml of THF and added to the mixture, reacted at 25°C for 12 h, poured into a polytetrafluoroethylene mold, and dried in a vacuum

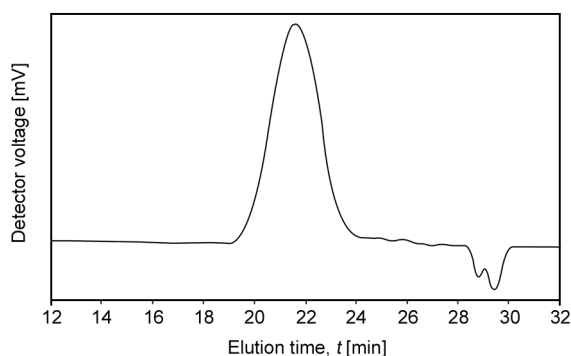


Figure 1. GPC chromatogram of HTPE.

Table 1. Formula and name of samples (mass ratio).

Sample	HTPB	HTPE	IPDI	HEDS	BDO	ZnCl_2
PU	3.0	0.0	0.50	0.00	0.101	0.0000
EPU	2.4	0.6	0.49	0.00	0.099	0.0000
HEPU	2.4	0.6	0.49	0.17	0.000	0.0000
HEPU-Zn	2.4	0.6	0.49	0.17	0.000	0.0586

oven at 60°C for 24 h to evaporate the solvent and obtain the sample (labeled as HEPU-Zn). In addition, three control groups were fabricated, namely, the PU (only HTPB was cross-linked with IPDI, and BDO was used instead of HEDS as the chain extender), the EPU (without HEDS and ZnCl_2 , and BDO was used instead of HEDS as the chain extender) and the HEPU (without ZnCl_2) groups. In our experiments, the R-value (ratio of the isocyanate group to hydroxyl group) of each group was 1. The mass ratios of the formulations for all samples were shown in Table 1.

2.3. Characterization

The structure of the coordination bonds was characterized using a Horiba Labram Raman spectrometer (Horiba Company, Paris, France) equipped with an Ar laser source (excitation wavelength = 633 nm, scanning range = $200\text{--}800 \text{ cm}^{-1}$). The absorption spectra in the wavelength range of $400\text{--}4000 \text{ cm}^{-1}$ were analyzed via Fourier transform infrared spectroscopy (FTIR) using an infrared spectrometer (NICOLET iS10) (Bruker Corporation, Germany) with a resolution of 4 cm^{-1} . The proton nuclear magnetic resonance (^1H NMR) spectrum was collected using a BRUKER AVANCE 400 instrument (NMR), with a supply of $\text{DMSO-}d_6$ as the solvent. Dynamic characteristic analysis was conducted on a dynamic mechanical analyzer (DMA, Q800) (TA Instruments Corporation, USA). Frequency scanning tests were performed on both the original and repaired samples, while temperature scanning and stress-relaxation experiments were performed on the original samples. For the frequency scanning tests, the frequency sweep range was $0.1\text{--}100 \text{ Hz}$, and the temperature was set to 60, 25, -20 , or -40°C . For the temperature scanning tests, the temperature sweep range was $-90\text{--}60^\circ\text{C}$; the heating rate was $3^\circ\text{C} \cdot \text{min}^{-1}$, and the test frequency was 1 Hz. In the stress-relaxation experiments, the temperature was set to 60, 25, -20 , -40 , -60 , or -80°C , and the strain was set to 50%. The relaxation time (τ) of the polyurethane network was defined as the time required for the stress-relaxation

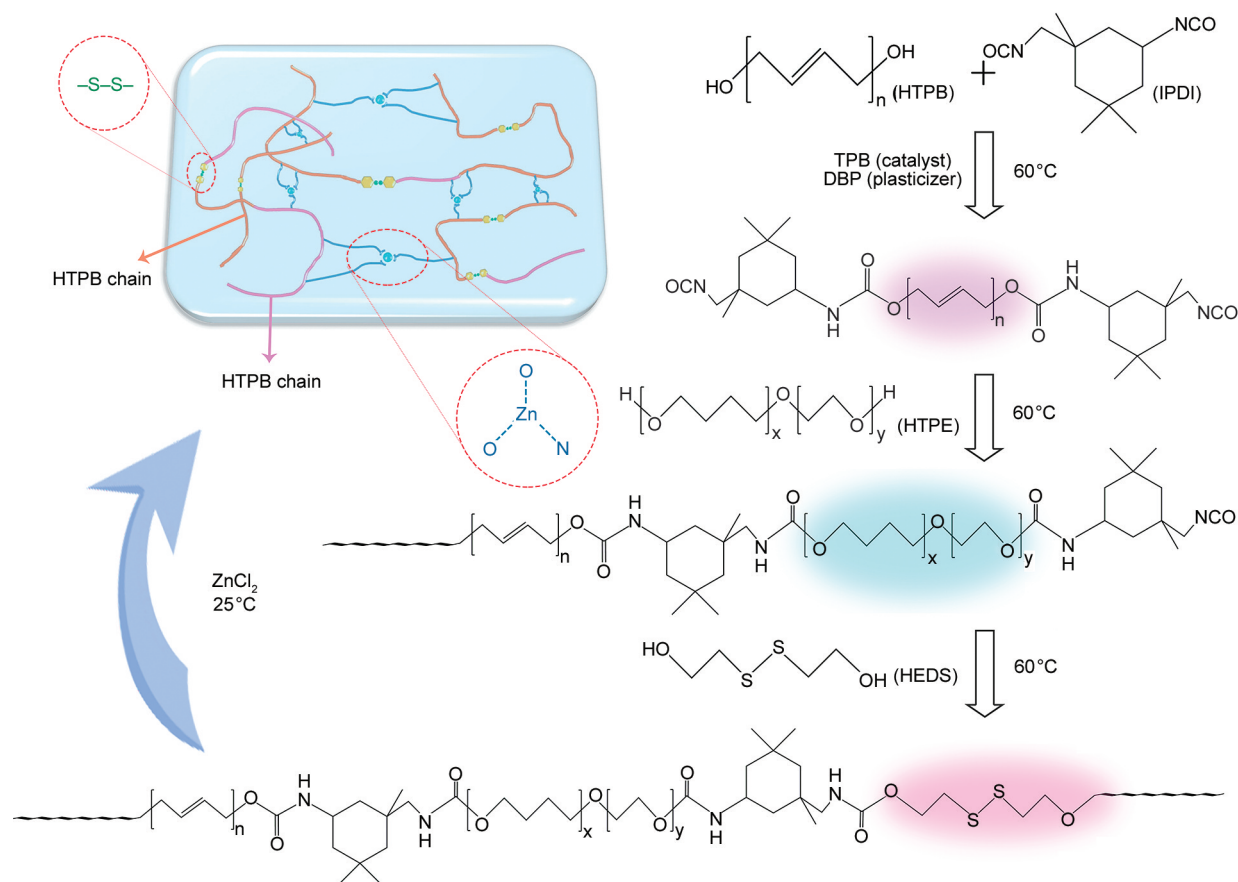


Figure 2. Synthesis of HEPU-Zn polyurethane.

modulus to reach 37% of its original value and was plotted on the curve. In accordance with the GB/T528-92 standard, the tensile tests at -40 , -20 , 25 , and 60 °C were performed at a speed of $100 \text{ mm} \cdot \text{min}^{-1}$ on an Instron 5982 material testing machine (Instron Corporation, USA), and the results were averaged with at least three measured data. Optical microscope images of the healing process of the samples were obtained using an AOSVI polarizing microscope (CM2000-3M100) (AOSVI Optical Instrument Co., Ltd., Shenzhen, China). For the self-healing experiments, the samples were cut into two pieces, contacted without an external force at each set temperature (60 , 25 , -20 , or -40 °C), and left to repair at this temperature for 12 h. Subsequently, they were tested on an Instron 5982 material testing machine. The tensile experiments were performed at each temperature at a speed of $100 \text{ mm} \cdot \text{min}^{-1}$, and the tensile strength (σ_b) and elongation at break (ϵ_b) values were recorded.

The self-healing efficiency based on either the strength or elongation at break (η_σ and η_ϵ , respectively) was defined according to Equations (1) and (2), respectively. The accelerated aging experiments were performed in a constant-temperature blast box, which simulated the daily sun and wind through heating and airflow. During the anti-aging experiments, the mechanical and self-healing properties of the samples were evaluated. Two sets of samples were placed in a constant-temperature blast box (60 °C) and aged for 7 d. After the aging treatment was completed, the samples were cooled to 25 °C, and then one group of samples was subjected to tensile testing using an Instron 5982 material testing machine, while the other group of samples was first cut in half and then repaired at 25 °C for 12 h after contact. Finally, the self-healing performance after aging was evaluated according to Equations (1) and (2):

$$\text{Healing efficiency, } \eta_\epsilon [\%] = \frac{\epsilon_b \text{ of healing sample}}{\epsilon_b \text{ of original sample}} \cdot 100\% \quad (1)$$

$$\text{Healing efficiency, } \eta_\sigma [\%] = \frac{\sigma_b \text{ of healing sample}}{\sigma_b \text{ of original sample}} \cdot 100\% \quad (2)$$

3. Results and discussion

3.1. Material design and structural characterization

The main purpose of this study was to develop a wide-temperature range and anti-aging self-healing polyurethane material with superior mechanical performance. To achieve this objective, dynamic bond cross-linking and copolymerization strategies were simultaneously applied to the polyurethane network (Figure 2). Initially, HTPB and IPDI were used as raw materials to synthesize long chains terminated with isocyanate groups. After the chains were copolymerized with HTPE, HEDS was added to form HEPU ligands. Finally, HEPU ligands were cross-linked with Zn^{2+} to obtain polyurethane (HEPU-Zn). The introduction of HTPE into HTPB effectively reduced the cross-linking density, which benefited the molecular chain mobility of polyurethane [49]. In addition, HEDS provided disulfide bonds and introduced self-healing properties to polyurethane. Concurrently, the dynamic disulfide bonds effectively eliminated free radicals, endowing polyurethane with anti-aging capabilities [50–54]. Moreover, the $ZnCl_2$ formed Zn-coordination bonds with the ligands, where the zinc ions have an alternating configuration, where transformation between the tetrahedral and octahedral structure is possible. This endowed the zinc coordination bonds with high dynamic exchange characteristics and provided excellent self-repairing properties for polyurethane, especially at low temperatures [55].

Figure 3a shows the Raman spectra of HEPU-Zn, where the characteristic peaks at 245 and 319 cm^{-1} correspond to the stretching vibrations of Zn–N and Zn–O coordination bonds, respectively, indicating the presence of Zn-ligand bonds. The characteristic peak at $\sim 626\text{ cm}^{-1}$ is due to the tensile vibration of the S–S covalent bond [56, 57], suggesting the successful introduction of disulfide bonds into HEPU-Zn. Figure 3b shows the FTIR spectra of EPU, HEPU, and HEPU-Zn. Compared with the HEPU spectrum, new absorption peaks at 1526 and 520 cm^{-1} were observed for HEPU-Zn, which are attributed to the stretching vibrations of Zn–N and Zn–O, respectively [55]; this further indicates the existence of Zn-ligand bonds. In addition, the spectrum of EPU had a prominent absorption peak at 2257 cm^{-1} , which was due to the excess of –NCO groups. However, HEPU and HEPU-Zn showed no characteristic –NCO peak, which indicates that –NCO was completely

consumed, and the disulfide bonds were successfully introduced. From the above characterization results, it is concluded that the HEPU-Zn polyurethane samples containing Zn-coordination bonds and disulfide bonds were successfully synthesized.

As shown in Figure 3c, the chemical structures of HEDS, HTPE and HEPU were characterized by proton nuclear magnetic resonance. HEDS: δ 2.19 (s, 1H), 3.92 (s, 2H) and 2.91 (s, 3H) ppm; HTPE: δ 1.62 (s, 1H), 3.41 (s, 2H) and 3.64 (s, 3H) ppm. The chemical shift at 7.28 ppm for three samples was due to the deuterated solvent $CDCl_3$. HEPU contains the unique chemical shifts of HEDS and HTPE, and it does not show the chemical shift of protons in the hydroxyl groups belonging to HEDS at 2.19 ppm. These indicate that HEDS and HTPE have been successfully introduced into HEPU, which provides a necessary condition for the next preparation of HEPU-Zn.

3.2. Dynamic characteristic analysis

The superior self-repairing properties of the prepared HEPU-Zn polyurethane suggested that it might also have good dynamic properties. To verify this, rigorous temperature and frequency scanning tests were comparatively conducted between HEPU-Zn and the control group (PU) (Figures 4–6). In the temperature scanning curves (Figure 4), negligible differences were observed in the glass transition temperatures (T_g) of PU and HEPU-Zn (approximately -64 to $-82^\circ C$ for HEPU-Zn and -66 to $-83^\circ C$ for PU). However, the loss factor ($\tan \delta = G''/G'$) of HEPU-Zn showed a gradual increase when the temperature rose above $-40^\circ C$, indicating the better molecular chain fluidity of HEPU-Zn than that of PU. Figure 5 shows the frequency scanning curves of PU and HEPU-Zn. Generally, higher G''/G' ratios indicate better flexibility of the molecular chain of polyurethane [58]. From Figures 5, and 6, the G''/G' ratio in both HEPU-Zn and PU decreased with decreasing temperature in general trend, implying that the fluidity of the polyurethane molecular chain was impaired at lower temperatures. In addition, the G''/G' ratio of HEPU-Zn was higher than that of PU in general trend at -40 , -20 , 25 , and $60^\circ C$, thereby indicating the overall higher molecular chain mobility of HEPU-Zn, which was consistent with our previous conclusion. This behavior was theoretically attributed to the simultaneous introduction of the HTPE long chains and dual dynamic bonds in the

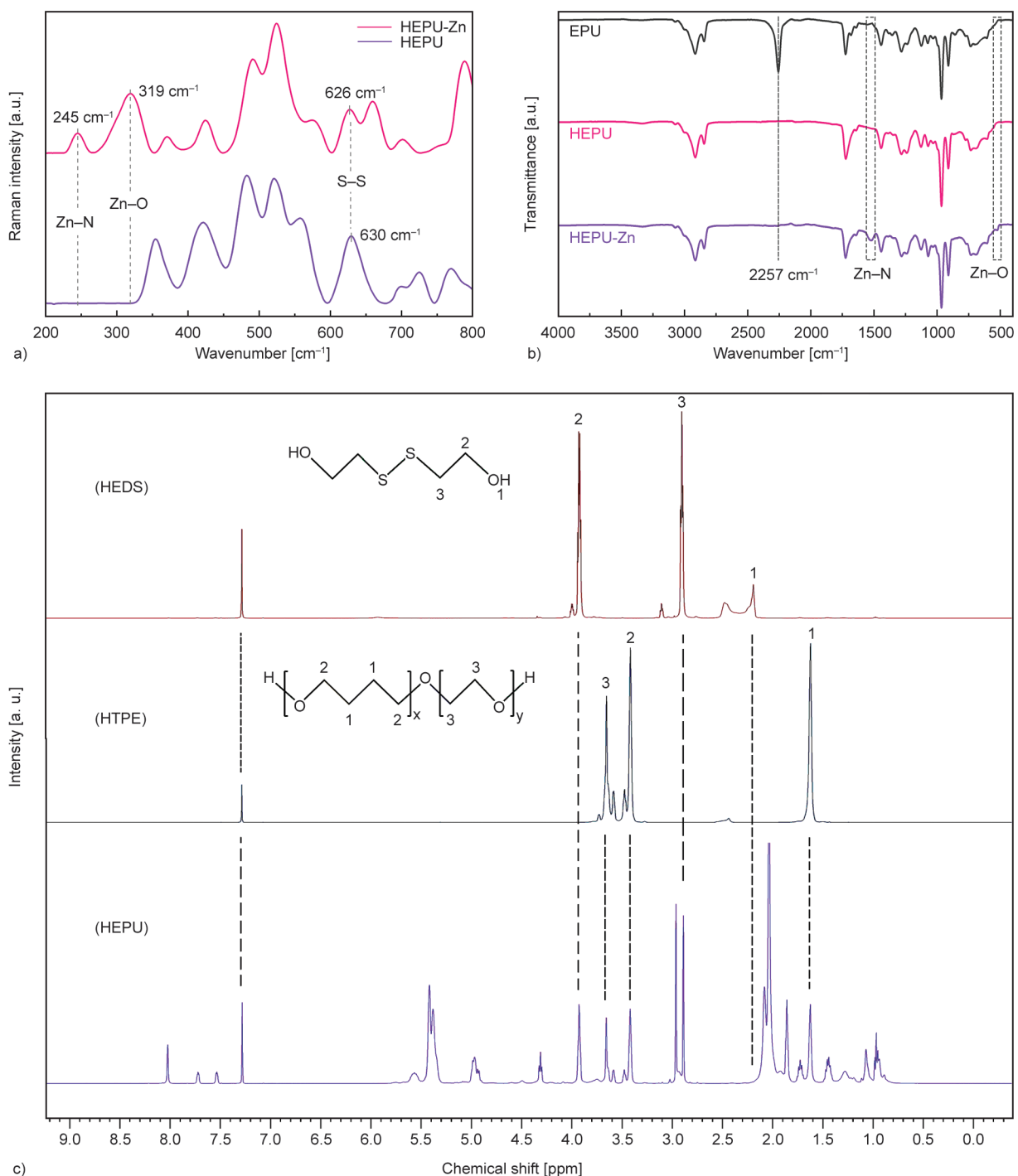


Figure 3. a) Raman spectra of HEPU and HEPU-Zn. b) FTIR spectra of EPU, HEPU, and HEPU-Zn. c) ¹H NMR spectra of HEDS, HTPE, and HEPU.

HEPU-Zn structure. On the one hand, the copolymerization with HTPE increases the length of the molecular chain and reduces its cross-linking density; on the other hand, the dynamic exchange reactions between dual dynamic bonds enhance energy dissipation and promote the flow of the molecular chain.

3.3. Mechanical performances

Table 2 shows the tensile mechanical properties of the HEPU-Zn, HEPU, and PU samples at -40, -20, 25, and 60 °C. PU exhibited the highest tensile strength and lowest elongation at break, which can be attributed to its poor molecular chain mobility and irreversible cross-linked network. At all tested

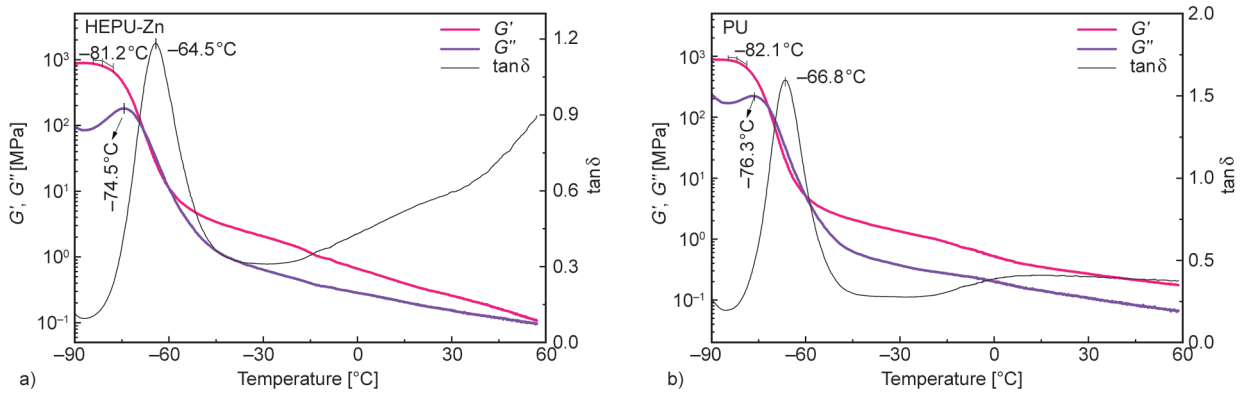


Figure 4. Temperature scanning curves of a) HEPU-Zn and b) PU from -90 to 60 °C.

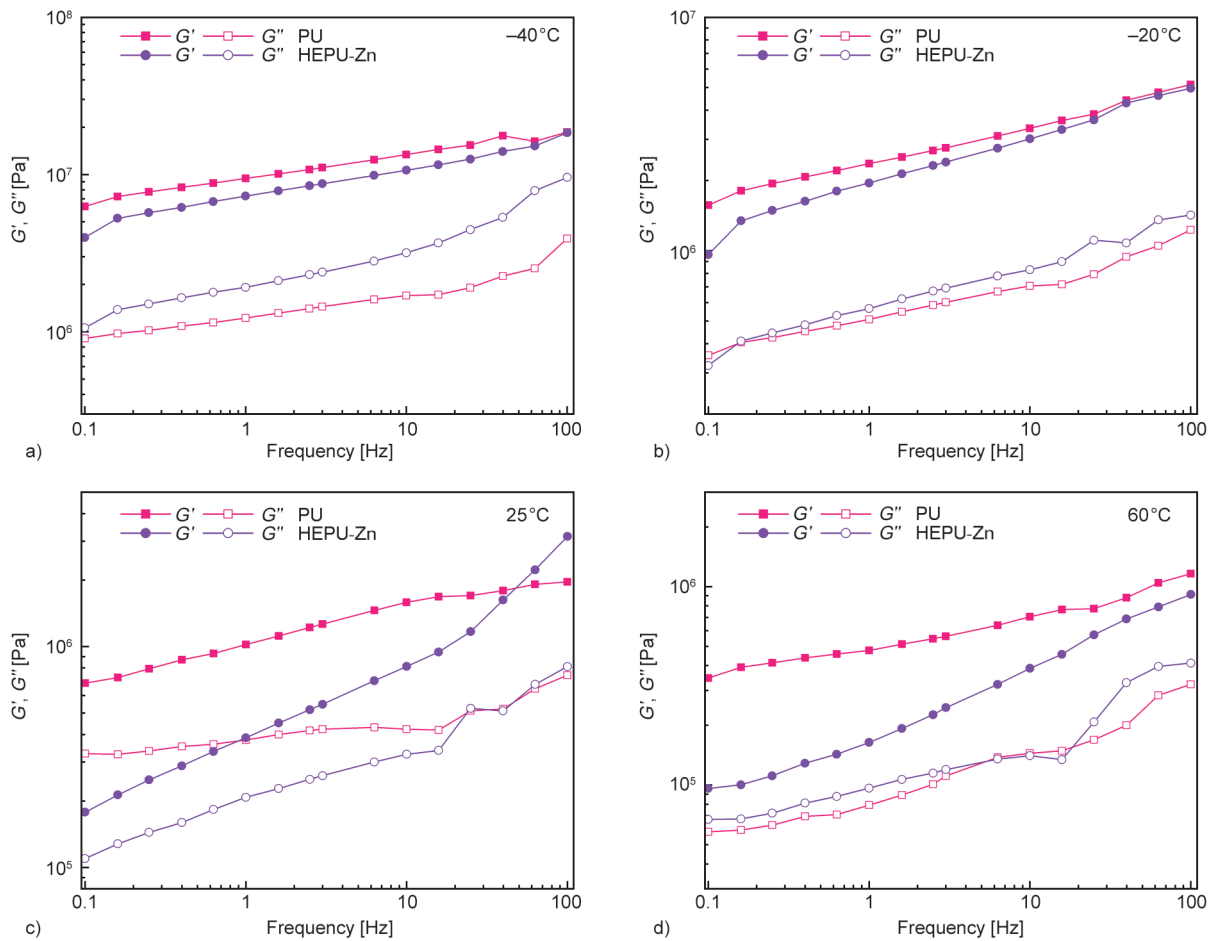


Figure 5. Frequency scanning curves of PU and HEPU-Zn at a) -40 °C, b) -20 °C, c) 25 °C, and d) 60 °C.

temperatures, the HEPU samples showed an evidently improved ϵ_b compared with that of PU, but its σ_b was significantly impaired. This was theoretically attributed to the significantly improved molecular chain fluidity that provided by both the copolymerization with HTPe and the dynamic exchange reactions of disulfide bonds. In parallel, owing to the decrease in the cross-linking density, the σ_b of HEPU decreased. However, compared with those of HEPU, the ϵ_b and σ_b of HEPU-Zn were significantly higher,

and the σ_b was even close to that of PU. This was attributed to the fact that the Zn-coordination bonds formed by Zn^{2+} and the ligands increased the cross-linking density of the polyurethane network, thereby increasing its strength. Furthermore, the alternating configuration of zinc ions that can change from tetrahedral to octahedral endowed the zinc coordination bonds with high dynamic exchange characteristics, thereby further increasing the molecular chain fluidity of polyurethane. Specifically, the ϵ_b of HEPU-Zn

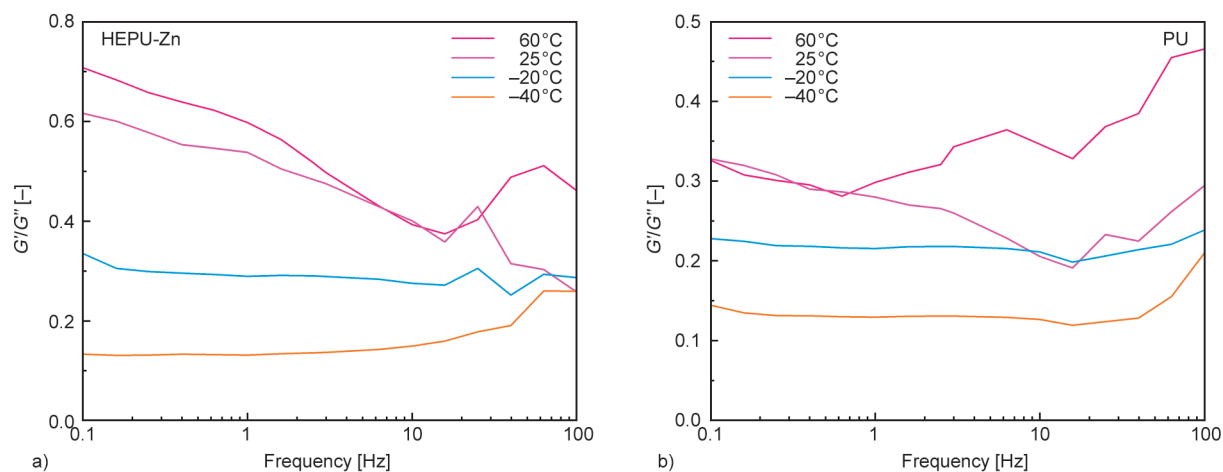


Figure 6. The curve of G''/G' ratio of a) HEPU-Zn and b) PU samples at different temperatures.

Table 2. Elongation at break [%] and tensile strength [MPa] of polyurethane samples at -40 , -20 , 25 , and 60 °C.

Sample	-40 °C		-20 °C		25 °C		60 °C	
	ε_b [%]	σ_b [MPa]	ε_b [%]	σ_b [MPa]	ε_b [%]	σ_b [MPa]	ε_b [%]	σ_b [MPa]
PU	302.9	9.37	466.7	6.29	656.2	0.50	324.6	0.23
HEPU	622.0	5.13	883.4	3.30	1401.2	0.27	1053.8	0.17
HEPU-Zn	1424.5	7.40	1618.9	4.40	2723.6	0.40	1922.2	0.19

at -40 , -20 , 25 , and 60 °C was ~ 1424.5 , 1618.9 , 2723.6 , and 1922.2% , respectively (all values $>1400\%$), while its σ_b was 7.4 , 4.4 , 0.4 , and 0.19 MPa, respectively. Therefore, it was inferred that the combined introduction of copolymerization and dual-dynamic bond cross-linking strategies into polyurethane effectively enhanced its mechanical properties over a wide temperature range.

3.4. Wide-temperature-range self-healing performance

Figure 7a shows the self-healing properties of HEPU-Zn, HEPU, and PU at 60 °C. The self-healing efficiency of PU was extremely low, even at 60 °C, primarily attributed to its irreversible cross-linked network. Although its healing performance was improved after copolymerization and the introduction of disulfide bonds, the healing efficiency was only $\sim 65\%$. When Zn^{2+} species were further introduced, its self-healing efficiency was significantly increased, with η_ε and η_σ reaching 93.6 and 89.5% , respectively. This was attributed to the synergistic effect of the disulfide and Zn-coordination bonds that both enhanced the self-healing ability of polyurethane. According to the images demonstrating the self-healing performance (Figure 7b–7d), the self-healing efficiency of HEPU-Zn at all four temperatures remained considerably high; particularly, its η_σ

and η_ε values at -40 °C were ~ 87.8 and $\sim 72.6\%$, respectively. These results suggest its excellent self-healing efficiency over a wide temperature range that could be attributed to the following factors: first, the low cross-linking density and segmentation effect of the disulfide bonds endowed polyurethane with high molecular chain mobility; second, the cross-linked network formed by the disulfide and Zn-ligand bonds provides good dynamic mechanical properties, enhancing the self-healing ability of polyurethane over a wide temperature range. Finally, the dynamic exchange reactions of the Zn-ligand bonds facilitate the reduction of the energy barrier of the polymer chain slip, thereby endowing the polyurethane network with good self-healing properties, even at low temperatures.

Figure 8 shows the frequency scanning curves of the original and healed HEPU-Zn polyurethanes. The self-healing performance of polyurethane can be further characterized by comparing the frequency scanning curves before and after repair [59, 60]. According to Figure 8, the G' and G'' of the repaired HEPU-Zn samples were lower than those of the original samples, which is theoretically ascribed to the incomplete healing of the crack. In addition, as the healing degree of the crack increased with increasing temperature, the gap between the G' and G'' values of the healed and original specimens gradually

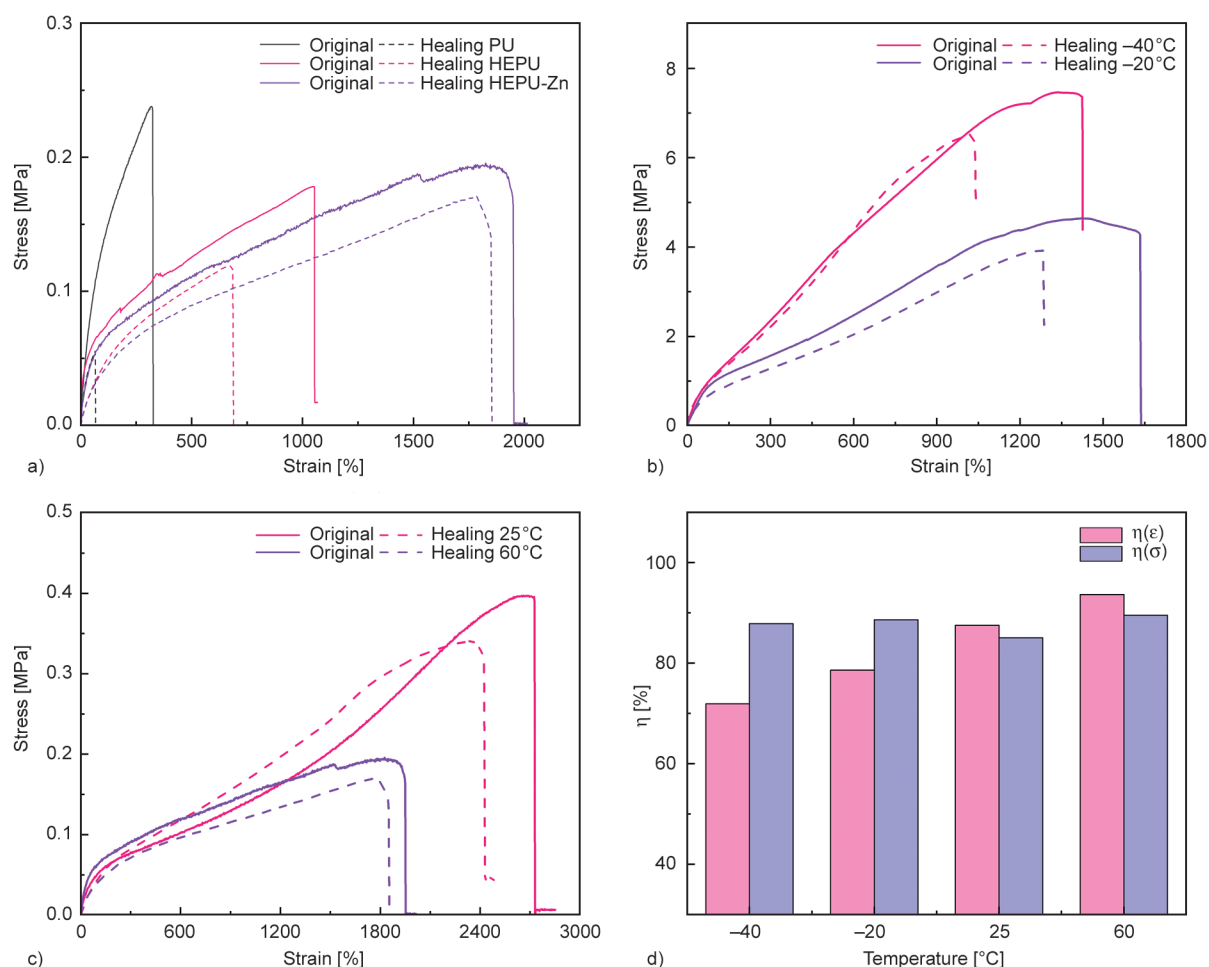


Figure 7. a) Self-healing performance of PU, HEPU, and HEPU-Zn at 60°C. b, c) Self-healing performances of HEPU-Zn at -40, -20, 25, and 60°C. d) Self-healing efficiency (η) of HEPU-Zn at different temperatures.

decreased as the temperature increased. Notably, the frequency scanning curves of the original and healed samples were very similar at 60°C, indicating that the healing efficiency was close to 100%. This is because HEPU-Zn has excellent molecular chain mobility at 60°C, and the dynamic reversibility of disulfide bonds and Zn-urethane coordination bonds are also extremely high currently, which greatly promotes HEPU-Zn self-healing process. This is consistent with the results in Figure 6, further validating the excellent self-healing properties conferred by the dual cooperative cross-linking strategy. Figure 9a illustrates the healing mechanism of the HEPU-Zn polyurethane. When the HEPU-Zn polyurethane is damaged, there will be many reversible active groups on the fractured surface, which is the key to realize self-healing. When the fracture surfaces contact each other, with the help of the rapid migration of molecular chains, the active groups contact each other to form new coordination bonds and disulfide bonds and finally realize self-healing. The corresponding

microscopy images (Figure 9b) verify that the healed cracks at 60 and 25°C were almost indistinguishable, and the healing degree decreased with decreasing temperature. The polyurethane evidently achieved a relatively high degree of healing above -40°C, which proves our previous conclusions. Significantly, the polyurethane showed partial healing capabilities, even at ultra-low temperatures (-60 and -80°C). To visualize the self-healing ability at -60 and -80°C, manual tensile experiments of HEPU-Zn polyurethane were carried out, and the results are shown in Figure 9c. After healing at -60 and -80°C, the polyurethane was relatively intact, highlighting its excellent molecular chain fluidity and self-repairing ability at low temperatures, which is of great application value.

Subsequently, stress-relaxation experiments were carried out at a constant temperature and deformation rate, and the recombination ability of the polyurethane network was evaluated to reflect its healing ability. A shorter τ value implies a higher reorganization

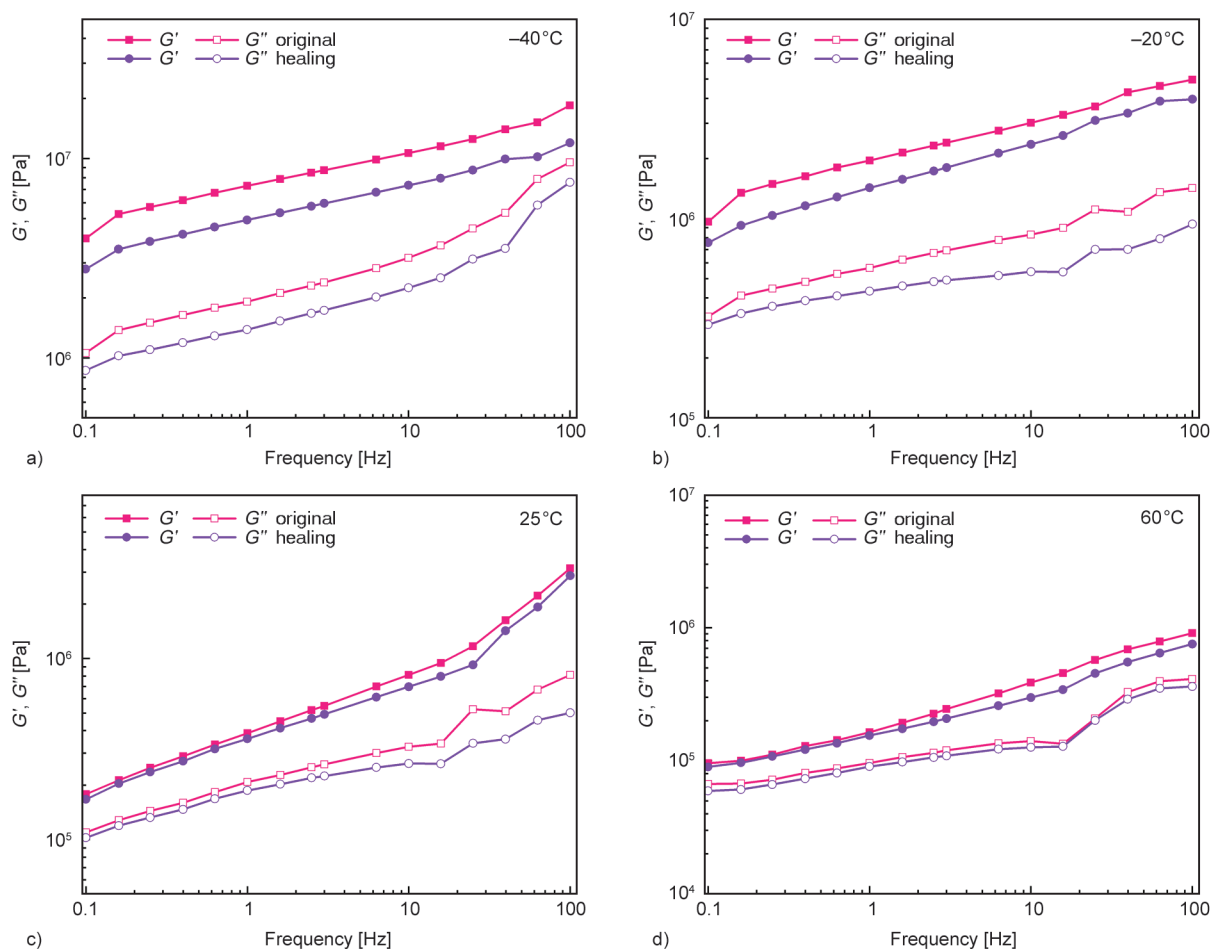


Figure 8. DMA frequency sweep curves of the original and repaired HEPU-Zn polyurethanes at a) -40°C , b) -20°C , c) 25°C , and d) 60°C .

ability of the polyurethane network, which is conducive to self-healing [55, 61]. Figure 10a shows the stress-relaxation curves of HEPU-Zn polyurethane at 60, 25, -20 , -40 , -60 , and -80°C , and the stress relaxation experimental results of PU at 60, 25, and -20°C are shown in Figure 10b. The τ value of HEPU-Zn is named τ_1 and that of PU is τ_2 . The τ_2 values of PU at 60 and 25°C are 15.89 and 44.32 min, respectively, while the internal stress at -20°C can only decrease to $\sim 63\%$ of its initial value. Note that τ_1 was extremely small, with values of only 0.89 and 1.79 min at 60 and 25°C , respectively, which indicates that HEPU-Zn has excellent dynamic properties at 60 and 25°C . When the temperature decreased to -20 and -40°C , τ_1 increased to 7.02 and 22.46 min, respectively. This is because the molecular chain movement is hindered at low temperatures, the recombination ability of the polyurethane network is weakened, thus τ value increased as the temperature decreased. While compared with PU, HEPU-Zn still had strong molecular chain fluidity at

this time. When the temperature decreased from -40 to -60°C , τ_1 increased from 22.46 to 45.65 min, and the corresponding self-healing ability decreased significantly, but it was still close to the molecular chain mobility of PU at 25°C . When the temperature decreased to -80°C , although the internal stress of the polyurethane could not even reach up to 37% of the original stress, it could decrease to $\sim 62\%$ within 60 min. This demonstrated that at -80°C , the polyurethane still had a certain healing ability, which was consistent with the results obtained from optical microscopy. These results further illustrated that the synergistic cross-linking strategy of copolymerization and dual dynamic bonds endowed polyurethane with excellent wide-temperature-range self-healing performance.

3.5. Anti-aging properties

In addition to the self-healing ability, an excellent anti-aging performance is paramount for the long-term use of polyurethane. Figure 11a depicts the

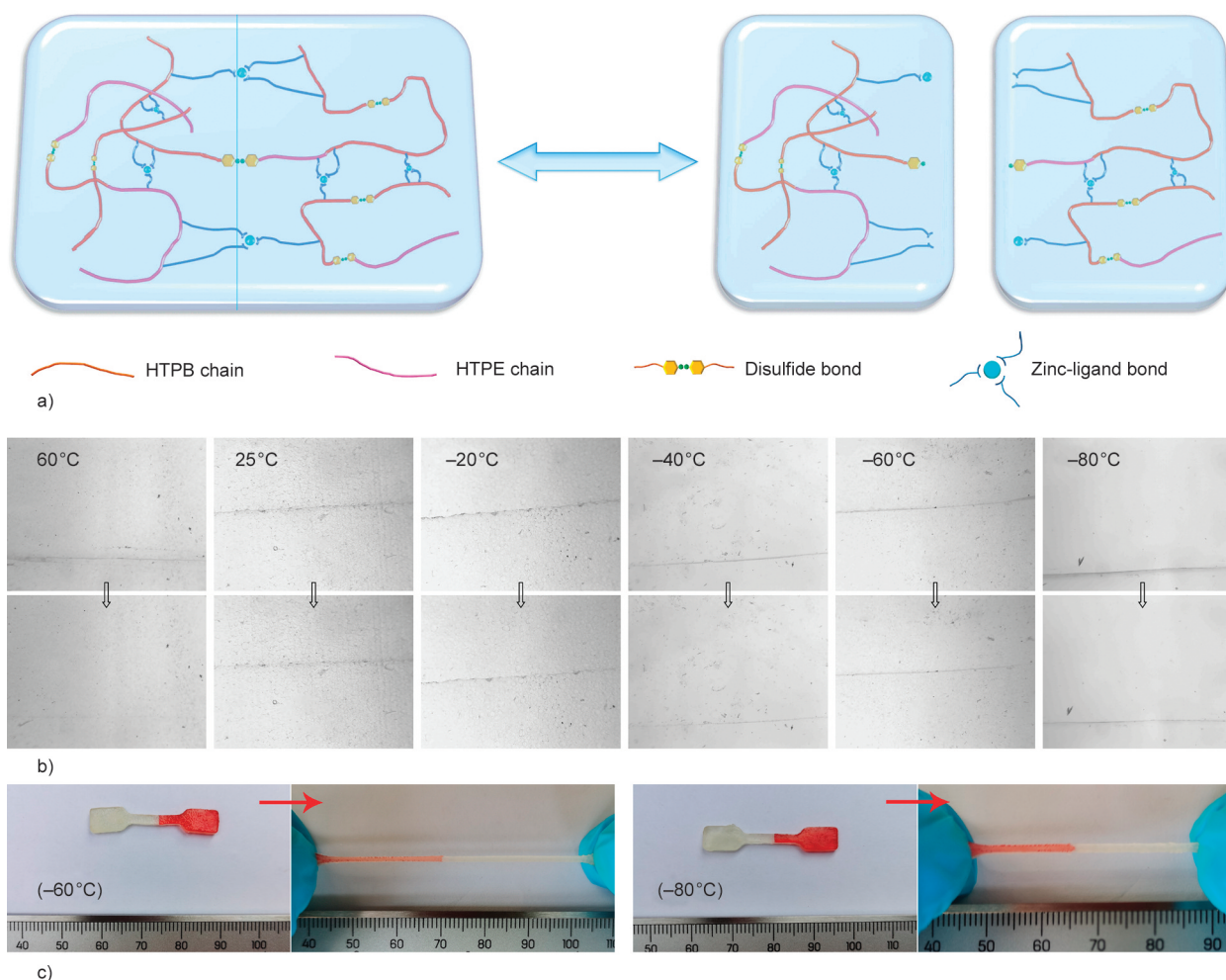


Figure 9. a) Self-healing mechanism of HEPU-Zn. b) Repair of HEPU-Zn occurring under optical microscopy observation. c) Photographs of manual tensile testing of HEPU-Zn samples repaired at -60 and -80 °C.

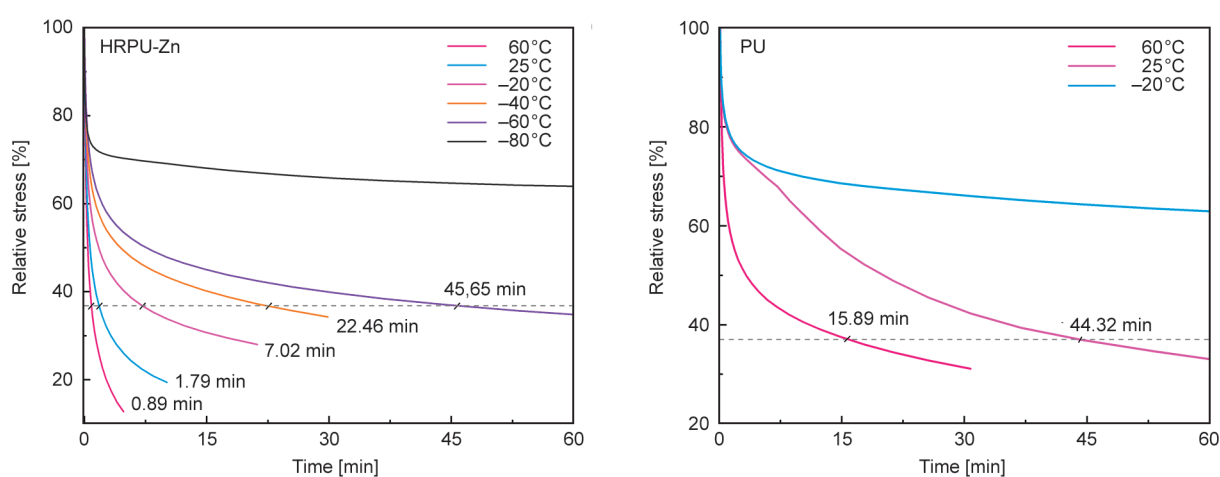


Figure 10. Stress-relaxation curves of a) HEPU-Zn and b) PU at different temperatures.

stress-strain curves of PU aged for 7 d at 60 °C under airflow. Both the tensile strength and elongation at break of the aged PU decreased significantly. This is because of the degrading influence of external factors such as heat and oxygen; the groups containing active hydrogen in polyurethane molecules are easily

attacked by oxidizing components to form macromolecular free radicals, resulting in a series of free-radical chain reactions that promote aging. In contrast, no significant degradation of the tensile strength and elongation at break of the aged HEPU-Zn polyurethane samples was observed (Figure 11b); the

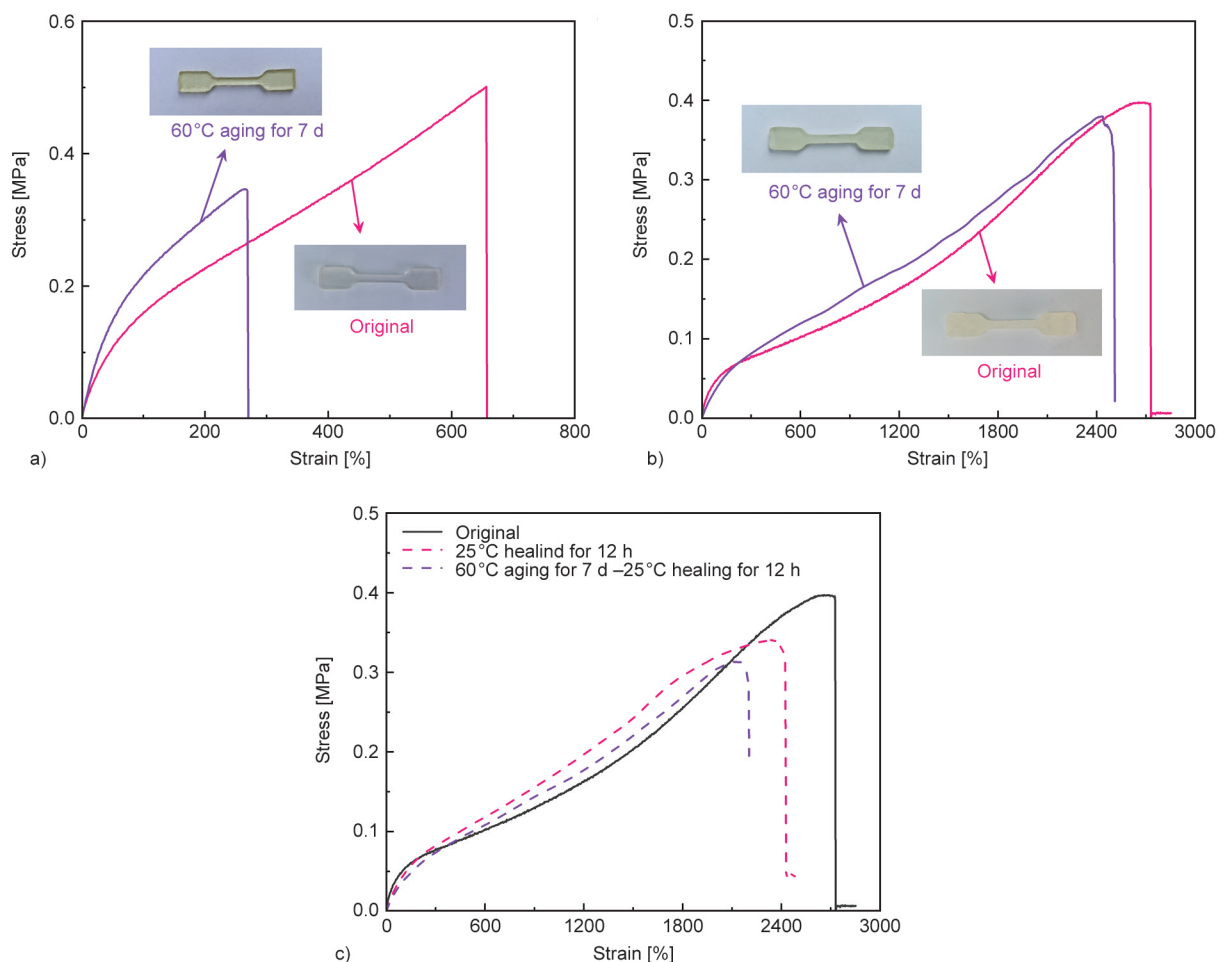


Figure 11. Stress–strain curves of a) PU and b) HEPU-Zn aged for 7 d under air flow at 60 °C. c) Stress–strain curves of HEPU-Zn samples aged at 60 °C for 7 d, cut in half, and healed at 25 °C for 12 h after contact.

tensile strength was ~ 0.37 MPa, which was 92.5% of the original value, while the elongation at break was $\sim 2437.2\%$, which was 89.4% of the original value. This superior anti-aging performance is attributed to the anti-aging property of disulfide bonds, which effectively prevented free-radical generation in the polyurethane network [54, 62–64]. These results show that HEPU-Zn polyurethane has relatively stable mechanical properties. To further study the stability of the self-healing properties of HEPU-Zn, after accelerated aging for 7 d, HEPU-Zn samples were cooled to 25 °C, cut in half and contacted, and then healed at 25 °C for 12 h. Their tensile mechanical properties were then measured, as shown in Figure 11c. The η_e and η_σ of the aged HEPU-Zn samples reached 79.9 and 77.5%, respectively. Compared with the original sample (87.9%/85.0%), the healing ability decreased to some extent, but remained at a high level, which further proves the excellent anti-aging characteristics of disulfide bonds. As for the slight decrease in self-healing efficiency,

this may be due to the molecular chain fluidity. The active groups on the fracture surface directly form new bonds with the adjacent groups, thus reducing the number of new bonds that can be formed between the two fracture surfaces, which shows the decline of tensile strength, elongation, and self-repairing efficiency in a macroscopic view. The above results show that HEPU-Zn polyurethane can maintain relatively high mechanical and self-healing performance, even after accelerated aging for 7 d. This will enable this material to be used in practical operating environments for a sufficiently long time.

4. Conclusions

In this study, dual-dynamic-bond cross-linking and copolymerization strategies were synergistically applied to polyurethane materials to provide wide-temperature-range and anti-aging self-healing performance. The final obtained polyurethane had a self-healing efficiency of $\sim 93.6\%$ and an elongation at break of $\sim 1922\%$ at 60 °C, and its tensile strength

was like that of the PU control group. At -40°C , it had a tensile strength of ~ 7.4 MPa and an elongation at break of $\sim 1425\%$, along with a high self-healing efficiency. Significantly, the low-temperature self-healing efficiencies of the polyurethane were 79.3 and 72.6% at -20 and -40°C , respectively, and intact samples were achieved after healing, even at -60 and -80°C . Furthermore, when the polyurethane was aged at 60°C for 7 d, its mechanical and self-healing properties were still relatively high. The findings presented here highlight the feasibility of polyurethane as a potential material for applications in wearable electronics, flexible displays, and soft robotics.

Acknowledgements

This work was supported by the National Defense Pre-Research Projects (Grant No. LJ20212A031130), NSFC (Grant No. 11732012), and NSSFC (Grant No.2020SKJJC108).

References

- [1] Jin M. L., Park S., Lee Y., Lee J. H., Chung J., Kim J. S., Kim J.-S., Kim S. Y., Jee E., Kim D. W., Chung J. W., Lee S. G., Choi D., Jung H. T., Kim D. H.: An ultrasensitive, visco-poroelastic artificial mechanotransducer skin inspired by Piezo2 protein in mammalian merkel cells. *Advanced Materials*, **29**, 1605973 (2017).
<https://doi.org/10.1002/adma.201605973>
- [2] Liu R., Lai Y., Li S., Wu F., Shao J., Liu D., Dong X., Wang J., Wang Z. L.: Ultrathin, transparent, and robust self-healing electronic skins for tactile and non-contact sensing. *Nano Energy*, **95**, 107056 (2022).
<https://doi.org/10.1016/j.nanoen.2022.107056>
- [3] Han T.-Y., Lin C.-H., Lin Y.-S., Yeh C.-M., Chen Y.-A., Li H.-Y., Xiao Y.-T., Chang J.-W., Su A.-C., Jeng U.-S., Chou H.-H.: Autonomously self-healing and ultrafast highly-stretching recoverable polymer through trans-octahedral metal-ligand coordination for skin-inspired tactile sensing. *Chemical Engineering Journal*, **438**, 135592 (2022).
<https://doi.org/10.1016/j.cej.2022.135592>
- [4] Amoli V., Kim J. S., Kim S. Y., Koo J., Chung Y. S., Choi H., Kim D. H.: Ionic tactile sensors for emerging human-interactive technologies: A review of recent progress. *Advanced Functional Materials*, **30**, 1904532 (2019).
<https://doi.org/10.1002/adfm.201904532>
- [5] Zhou K., Zhao Y., Sun X., Yuan Z., Zheng G., Dai K., Mi L., Pan C., Liu C., Shen C.: Ultra-stretchable triboelectric nanogenerator as high-sensitive and self-powered electronic skins for energy harvesting and tactile sensing. *Nano Energy*, **70**, 104546 (2020).
<https://doi.org/10.1016/j.nanoen.2020.104546>
- [6] Rich S. I., Wood R. J., Majidi C.: Untethered soft robotics. *Nature Electronics*, **1**, 102–112 (2018).
<https://doi.org/10.1038/s41928-018-0024-1>
- [7] Kang J., Tok J. B.-H., Bao Z.: Self-healing soft electronics. *Nature Electronics*, **2**, 144–150 (2019).
<https://doi.org/10.1038/s41928-019-0235-0>
- [8] Li G.-Y., Li J., Li Z.-J., Zhang Y.-P., Zhang X., Wang Z.-J., Han W.-P., Sun B., Long Y.-Z., Zhang H.-D.: Hierarchical PVDF-HFP/ZnO composite nanofiber-based highly sensitive piezoelectric sensor for wireless workout monitoring. *Advanced Composites and Hybrid Materials*, **5**, 766–775 (2021).
<https://doi.org/10.1007/s42114-021-00331-z>
- [9] Huang X., Qin Q., Wang X., Xiang H., Zheng J., Lu Y., Lv C., Wu K., Yan L., Wang N., Xia C., Wang Z. L.: Piezoelectric nanogenerator for highly sensitive and synchronous multi-stimuli sensing. *ACS Nano*, **15**, 19783–19792 (2021).
<https://doi.org/10.1021/acsnano.1c07236>
- [10] Lu L., Jiang C., Hu G., Liu J., Yang B.: Flexible non-contact sensing for human-machine interaction. *Advanced Materials*, **33**, 2100218 (2021).
<https://doi.org/10.1002/adma.202100218>
- [11] Pu X., An S., Tang Q., Guo H., Hu C.: Wearable triboelectric sensors for biomedical monitoring and human-machine interface. *iScience*, **24**, 102027 (2021).
<https://doi.org/10.1016/j.isci.2020.102027>
- [12] Chen J., Han K., Luo J., Xu L., Tang W., Wang Z. L.: Soft robots with self-powered configurational sensing. *Nano Energy*, **77**, 105171 (2020).
<https://doi.org/10.1016/j.nanoen.2020.105171>
- [13] Ounkaew A., Kasemsiri P., Srichiangsa N., Jetsrisuparb K., Knijnenburg J. T. N., Okhawilai M., Hiziroglu S., Theerakulpisut S.: Multifunctional gluten/guar gum copolymer with self-adhesion, self-healing, and remolding properties as smart strain sensor and self-powered device. *Express Polymer Letters*, **16**, 607–623 (2022).
<https://doi.org/10.3144/expresspolymlett.2022.45>
- [14] Du R., Xu Z., Zhu C., Jiang Y., Yan H., Wu H.-C., Vardoulis O., Cai Y., Zhu X., Bao Z., Zhang Q., Jia X.: A highly stretchable and self-healing supramolecular elastomer based on sliding crosslinks and hydrogen bonds. *Advanced Functional Materials*, **30**, 1907139 (2019).
<https://doi.org/10.1002/adfm.201907139>
- [15] Zhang Y., Zheng J., Zhang X., Du Y., Li K., Liu Y., Yu G., Jia Y., Song S.: Dual dynamic bonds self-healing polyurethane with superior mechanical properties over a wide temperature range. *European Polymer Journal*, **163**, 110934 (2022).
<https://doi.org/10.1016/j.eurpolymj.2021.110934>
- [16] Huynh T.-P., Sonar P., Haick H.: Advanced materials for use in soft self-healing devices. *Advanced Materials*, **29**, 1604973 (2017).
<https://doi.org/10.1002/adma.201604973>

- [17] Cao J., Lu C., Zhuang J., Liu M., Zhang X., Yu Y., Tao Q.: Multiple hydrogen bonding enables the self-healing of sensors for human-machine interactions. *Angewandte Chemie-International Edition*, **56**, 8795–8800 (2017). <https://doi.org/10.1002/anie.201704217>
- [18] Ying W. B., Liu H., Gao P., Kong Z., Hu H., Wang K., Shen A., Jin Z., Zheng L., Guo H., Zhang R., Zhu J.: An anti-stress relaxation, anti-fatigue, mildew proof and self-healing poly(thiourethane-urethane) for durably stretchable electronics. *Chemical Engineering Journal*, **420**, 127691 (2021). <https://doi.org/10.1016/j.cej.2020.127691>
- [19] Romero-Sabat G., Gago-Benedí E., Rovira J. J. R., González-Gálvez D., Mateo A., Medel S., Chivite A. T.: Development of a highly efficient extrinsic and autonomous self-healing polymeric system at low and ultra-low temperatures for high-performance applications. *Composites Part A: Applied Science and Manufacturing*, **145**, 106335 (2021). <https://doi.org/10.1016/j.compositesa.2021.106335>
- [20] Liu Y., Zheng J., Zhang X., Du Y., Li K., Yu G., Jia Y., Zhang Y.: Mussel-inspired and aromatic disulfide-mediated polyurea-urethane with rapid self-healing performance and water-resistance. *Journal of Colloid and Interface Science*, **593**, 105–115 (2021). <https://doi.org/10.1016/j.jcis.2021.03.003>
- [21] Zhang M. Q.: Polymer self-heals in seconds. *Express Polymer Letters*, **9**, 84 (2015). <https://doi.org/10.3144/expresspolymlett.2015.9>
- [22] Ambekar R. S., Kandasubramanian B.: Advancements in nanofibers for wound dressing: A review. *European Polymer Journal*, **117**, 304–336 (2019). <https://doi.org/10.1016/j.eurpolymj.2019.05.020>
- [23] Das M., Pal S., Naskar K.: Exploring various metal-ligand and coordination bond formation in elastomers: Mechanical performance and self-healing behavior. *Express Polymer Letters*, **14**, 860–880 (2020). <https://doi.org/10.3144/expresspolymlett.2020.71>
- [24] Lai J-C., Jia X-Y., Wang D-P., Deng Y-B., Zheng P., Li C-H., Zuo J-L., Bao Z.: Thermodynamically stable whilst kinetically labile coordination bonds lead to strong and tough self-healing polymers. *Nature Communications*, **10**, 1164–1172 (2019). <https://doi.org/10.1038/s41467-019-09130-z>
- [25] Li C-H., Zuo J-L.: Self-healing polymers based on coordination bonds. *Advanced Materials*, **32**, 1903762 (2020). <https://doi.org/10.1002/adma.201903762>
- [26] Zhang L., Liu Z., Wu X., Guan Q., Chen S., Sun L., Guo Y., Wang S., Song J., Jeffries E. M., He C., Qing F-L., Bao X., You Z.: A highly efficient self-healing elastomer with unprecedented mechanical properties. *Advanced Materials*, **31**, 1901402 (2019). <https://doi.org/10.1002/adma.201901402>
- [27] Li M. X., Rong M. Z., Zhang M. Q.: Enhancement of mechanochemical self-blocking and self-healing of early minor damages in polymers through hyperbranched architecture. *Express Polymer Letters*, **15**, 781–790 (2021). <https://doi.org/10.3144/expresspolymlett.2021.62>
- [28] Burattini S., Greenland B. W., Merino D. H., Weng W., Seppala J., Colquhoun H. M., Hayes W., Mackay M. E., Hamley I. W., Rowan S. J.: A Healable supramolecular polymer blend based on aromatic π - π stacking and hydrogen-bonding interactions. *Journal of the American Chemical Society*, **132**, 12051–12058 (2010). <https://doi.org/10.1021/ja104446r>
- [29] Wu X., Wang J., Huang J., Yang S.: Robust, stretchable, and self-healable supramolecular elastomers synergistically cross-linked by hydrogen bonds and coordination bonds. *ACS Applied Materials & Interfaces*, **11**, 7387–7396 (2019). <https://doi.org/10.1021/acsami.8b20303>
- [30] Yan X., Liu Z., Zhang Q., Lopez J., Wang H., Wu H-C., Niu S., Yan H., Wang S., Lei T., Li J., Qi D., Huang P., Huang J., Zhang Y., Wang Y., Li G., Tok J. B-H., Chen X., Bao Z.: Quadruple H-bonding cross-linked supramolecular polymeric materials as substrates for stretchable, antitearing, and self-healable thin film electrodes. *Journal of the American Chemical Society*, **140**, 5280–5289 (2018). <https://doi.org/10.1021/jacs.8b01682>
- [31] Rekondo A., Martin R., de Luzuriaga A. L., Cabañero G., Grande H. J., Odriozola I.: Catalyst-free room-temperature self-healing elastomers based on aromatic disulfide metathesis. *Materials Horizons*, **1**, 237–240 (2014). <https://doi.org/10.1039/C3MH00061C>
- [32] Yang Y., Lu X., Wang W.: A tough polyurethane elastomer with self-healing ability. *Materials & Design*, **127**, 30–36 (2017). <https://doi.org/10.1016/j.matdes.2017.04.015>
- [33] Wan T., Chen D.: Synthesis and properties of self-healing waterborne polyurethanes containing disulfide bonds in the main chain. *Journal of Materials Science*, **52**, 197–207 (2016). <https://doi.org/10.1007/s10853-016-0321-x>
- [34] Liu M., Zhong J., Li Z., Rong J., Yang K., Zhou J., Shen L., Gao F., Huang X., He H.: A high stiffness and self-healable polyurethane based on disulfide bonds and hydrogen bonding. *European Polymer Journal*, **124**, 109475 (2020). <https://doi.org/10.1016/j.eurpolymj.2020.109475>
- [35] Aguirresarobe R. H., Martin L., Fernandez-Berridi M. J., Irusta L.: Autonomic healable waterborne organic-inorganic polyurethane hybrids based on aromatic disulfide moieties. *Express Polymer Letters*, **11**, 266–277 (2017). <https://doi.org/10.3144/expresspolymlett.2017.27>

- [36] Lin C., Sheng D., Liu X., Xu S., Ji F., Dong L., Zhou Y., Yang Y.: Effect of different sizes of graphene on Diels-Alder self-healing polyurethane. *Polymer*, **182**, 121822 (2019).
<https://doi.org/10.1016/j.polymer.2019.121822>
- [37] Yang S., Du X., Deng S., Qiu J., Du Z., Cheng X., Wang H.: Recyclable and self-healing polyurethane composites based on Diels-Alder reaction for efficient solar-to-thermal energy storage. *Chemical Engineering Journal*, **398**, 125654 (2020).
<https://doi.org/10.1016/j.cej.2020.125654>
- [38] Yang Z., Li H., Zhang L., Lai X., Zeng X.: Highly stretchable, transparent and room-temperature self-healable polydimethylsiloxane elastomer for bending sensor. *Journal of Colloid and Interface Science*, **570**, 1–10 (2020).
<https://doi.org/10.1016/j.jcis.2020.02.107>
- [39] Chen Y., Tang Z., Zhang X., Liu Y., Wu S., Guo B.: Covalently cross-linked elastomers with self-healing and malleable abilities enabled by boronic ester bonds. *ACS Applied Materials & Interfaces*, **10**, 24224–24231 (2018).
<https://doi.org/10.1021/acsami.8b09863>
- [40] Cromwell O. R., Chung J., Guan Z.: Malleable and self-healing covalent polymer networks through tunable dynamic boronic ester bonds. *Journal of the American Chemical Society*, **137**, 6492–6495 (2015).
<https://doi.org/10.1021/jacs.5b03551>
- [41] Hussain I., Ma X., Luo Y., Luo Z.: Fabrication and characterization of glycogen-based elastic, self-healable, and conductive hydrogels as a wearable strain-sensor for flexible e-skin. *Polymer*, **210**, 122961 (2020).
<https://doi.org/10.1016/j.polymer.2020.122961>
- [42] Wu H., Jin B., Wang H., Wu W., Cao Z., Wu J., Huang G.: A degradable and self-healable vitrimer based on non-isocyanate polyurethane. *Frontiers in Chemistry*, **8**, 585569 (2020).
<https://doi.org/10.3389/fchem.2020.585569>
- [43] Wu H-T., Jin B-Q., Wang H., Wu W-Q., Cao Z-X., Yuan Z-Y., Huang Y., Li W-H., Huang G-S., Liao L-S., Wu J-R.: A robust self-healing polyurethane elastomer enabled by tuning the molecular mobility and phase morphology through disulfide bonds. *Chinese Journal of Polymer Science*, **39**, 1299–1309 (2021).
<https://doi.org/10.1007/s10118-021-2607-y>
- [44] Liu J., Zhang L., Wang N., Zhao H., Li C.: Nanofiber-reinforced transparent, tough, and self-healing substrate for an electronic skin with damage detection and program-controlled autonomic repair. *Nano Energy*, **96**, 107108 (2022).
<https://doi.org/10.1016/j.nanoen.2022.107108>
- [45] Wei H., Yang Y., Huang X., Zhu Y., Wang H., Huang G., Wu J.: Transparent, robust, water-resistant and high-barrier self-healing elastomers reinforced with dynamic supramolecular nanosheets with switchable interfacial connections. *Journal of Materials Chemistry A*, **8**, 9013–9020 (2020).
<https://doi.org/10.1039/D0TA01352H>
- [46] Sun F., Xu J., Liu T., Li F., Poo Y., Zhang Y., Xiong R., Huang C., Fu J.: An autonomously ultrafast self-healing, highly colourless, tear-resistant and compliant elastomer tailored for transparent electromagnetic interference shielding films integrated in flexible and optical electronics. *Materials Horizons*, **8**, 3356–3367 (2021).
<https://doi.org/10.1039/D1MH01199E>
- [47] Li C-H., Wang C., Keplinger C., Zuo J-L., Jin L., Sun Y., Zheng P., Cao Y., Lissel F., Linder C., You X-Z., Bao Z.: A highly stretchable autonomous self-healing elastomer. *Nature Chemistry*, **8**, 618–624 (2016).
<https://doi.org/10.1038/nchem.2492>
- [48] Wang C., Liu Y., Qu X., Shi B., Zheng Q., Lin X., Chao S., Wang C., Zhou J., Sun Y., Mao G., Li Z.: Ultra-stretchable and fast self-healing ionic hydrogel in cryogenic environments for artificial nerve fiber. *Advanced Materials*, **34**, 2105416 (2022).
<https://doi.org/10.1002/adma.202105416>
- [49] Zhang Y., Zheng J., Zhang X., Du Y., Li K., Yu G., Jia Y., Liu Y.: Effect of chemical copolymerization and mixed chain extenders on mechanical properties of HTPB polyurethane. *IOP Conference Series: Materials Science and Engineering*, **1167**, 012012 (2021).
<https://doi.org/10.1088/1757-899X/1167/1/012012>
- [50] Li T., Xie Z., Xu J., Weng Y., Guo B-H.: Design of a self-healing cross-linked polyurea with dynamic cross-links based on disulfide bonds and hydrogen bonding. *European Polymer Journal*, **107**, 249–257 (2018).
<https://doi.org/10.1016/j.eurpolymj.2018.08.005>
- [51] Grande A. M., Bijleveld J. C., Garcia S. J., Zwaag S.: A combined fracture mechanical – rheological study to separate the contributions of hydrogen bonds and disulfide linkages to the healing of poly(urea-urethane) networks. *Polymer*, **96**, 26–34 (2016).
<https://doi.org/10.1016/j.polymer.2016.05.004>
- [52] Xie H., Sheng D., Zhou Y., Xu S., Wu H., Tian X., Sun Y., Liu X., Yang Y.: Thermally healable polyurethane with tailored mechanical performance using dynamic crosslinking motifs. *New Journal of Chemistry*, **44**, 13584–13590 (2020).
<https://doi.org/10.1039/D0NJ02671A>
- [53] Xiao L., Shi J., Wu K., Lu M.: Self-healing supramolecular waterborne polyurethane based on host-guest interactions and multiple hydrogen bonds. *Reactive and Functional Polymers*, **148**, 104482 (2020).
<https://doi.org/10.1016/j.reactfunctpolym.2020.104482>
- [54] Li F., Xu Z., Hu H., Kong Z., Chen C., Tian Y., Zhang W., Ying W. B., Zhang R., Zhu J.: A polyurethane integrating self-healing, anti-aging and controlled degradation for durable and eco-friendly E-skin. *Chemical Engineering Journal*, **410**, 128363 (2021).
<https://doi.org/10.1016/j.cej.2020.128363>
- [55] Wu X., Luo R., Li Z., Wang J., Yang S.: Readily self-healing polymers at subzero temperature enabled by dual cooperative crosslink strategy for smart paint. *Chemical Engineering Journal*, **398**, 125593 (2020).
<https://doi.org/10.1016/j.cej.2020.125593>

- [56] Zhang W., Wang M., Zhou J., Sheng Y., Xu M., Jiang X., Ma Y., Lu X.: Preparation of room-temperature self-healing elastomers with high strength based on multiple dynamic bonds. *European Polymer Journal*, **156**, 110614 (2021).
<https://doi.org/10.1016/j.eurpolymj.2021.110614>
- [57] Xu J., Chen W., Wang C., Zheng M., Ding C., Jiang W., Tan L., Fu J.: Extremely stretchable, self-healable elastomers with tunable mechanical properties: Synthesis and applications. *Chemistry of Materials*, **30**, 6026–6039 (2018).
<https://doi.org/10.1021/acs.chemmater.8b02320>
- [58] Matxain J. M., Asua J. M., Ruiperez F.: Design of new disulfide-based organic compounds for the improvement of self-healing materials. *Physical Chemistry Chemical Physics*, **18**, 1758–1770 (2016).
<https://doi.org/10.1039/C5CP06660C>
- [59] Cui Y., Song S., Tang Y., Chen Y., Yang H., Yang B., Huang J.: Decoupling the roles of the catechol content from those of glass transition temperature and dynamic mechanical modulus in determining self-healing and anti-corrosion of mussel-inspired polymers. *Polymer*, **185**, 121928 (2019).
<https://doi.org/10.1016/j.polymer.2019.121928>
- [60] Gupta A., Simmons W., Schueneman G. T., Hylton D., Mintz E. A.: Rheological and thermo-mechanical properties of poly(lactic acid)/lignin-coated cellulose nanocrystal composites. *ACS Sustainable Chemistry & Engineering*, **5**, 1711–1720 (2017).
<https://doi.org/10.1021/acssuschemeng.6b02458>
- [61] Zhang Y., Chen J., Zhang G., Xv J., Xv J., Hu Y., Guo H., Guo F., Fu J., Jiang W.: Mechanically robust, highly adhesive and autonomously low-temperature self-healing elastomer fabricated based on dynamic metal – ligand interactions tailored for functional energetic composites. *Chemical Engineering Journal*, **425**, 130665 (2021).
<https://doi.org/10.1016/j.cej.2021.130665>
- [62] Marykutty C. V., Mathew G., Mathew E. J., Thomas S.: Studies on novel binary accelerator system in sulfur vulcanization of natural rubber. *Journal of Applied Polymer Science*, **90**, 3173–3182 (2003).
<https://doi.org/10.1002/app.13023>
- [63] Alam M. N., Mandal S. K., Debnath S. C.: Bis(N-benzyl piperazino) thiuram disulfide and dibenzothiazyl disulfide as synergistic safe accelerators in the vulcanization of natural rubber. *Journal of Applied Polymer Science*, **126**, 1830–1836 (2012).
<https://doi.org/10.1002/app.36874>
- [64] Das A., Naskar N., Basu D. K.: Thiophosphoryl disulfides as crosslinking agents for chloroprene rubber. *Journal of Applied Polymer Science*, **91**, 1913–1919 (2004).
<https://doi.org/10.1002/app.13300>

Research article

The effect of functionalized hydroxyapatite on the crystallization process, morphology and thermomechanical properties of polyoxymethylene composites

Klaudia Król-Morkisz¹, Monika Kuźnia², Zbigniew Olejniczak³, Małgorzata Lekka⁴,
Kinga Pielichowska^{1*}

¹AGH University of Science and Technology, Faculty of Materials Science and Ceramics, Department of Biomaterials and Composites, al. Mickiewicza 30, 30-059 Kraków, Poland

²AGH University of Science and Technology, Faculty of Metals Engineering and Industrial Computer Science, Department of Heat Engineering and Environment Protection, Al. Mickiewicza 30, 30-059 Kraków, Poland

³Institute of Nuclear Physics Polish Academy of Sciences, ul. Radzikowskiego, 152, 31-342, Kraków, Poland

⁴Department of Biophysical Microstructures, Institute of Nuclear Physics, Polish Academy of Sciences, PL-31342 Kraków, Poland

Received 7 April 2022; accepted in revised form 28 September 2022

Abstract. In this work, hydroxyapatite (HAp) was functionalized by using poly(ethylene glycol) (PEG) with different average molar mass and diisocyanates as linkers and then incorporated into the polyoxymethylene (POM) matrix by means of melt processing methods. The effectiveness of the functionalization process and the chemical structure of the obtained hybrid systems were analyzed using thermogravimetric analysis (TG), elemental analysis, and nuclear magnetic resonance (NMR) methods. In the next stage of research, the calculation of the POM crystallization kinetic parameters in the presence of the hybrid filler were calculated. Microscopic and dynamic mechanical analysis (DMA) tests, as well as ¹³C and ³¹P and nuclear magnetic resonance (NMR) analyses were done to show the effect of the HAp-g-PEG hybrid filler on the crystallization kinetics and crystallinity of the POM composites. Transmission electron microscopy (TEM) confirmed the uniform distribution of the HAp-g-PEG hybrid additives. Differential scanning calorimetry (DSC) tests did not show any significant effect on the key processing parameters, *i.e.* melting point and supercooling, which allowed the processing parameters to be maintained for all samples. The study of crystallization kinetics showed a three-dimensional process of POM crystals' growth in the form of spherulites. The addition of HAp-g-PEG to POM significantly accelerated the crystallization process.

Keywords: polyoxymethylene, functionalization, poly(ethylene glycol), hydroxyapatite, crystallization kinetics

1. Introduction

Polyacetals are the group of plastics obtained by the polymerization of aldehydes. The most popular polyacetal is polyoxymethylene (POM), which is obtained from formaldehyde (homopolymer) or trioxane (copolymer) [1, 2]. POM is also called polyacetal or acetal resin and is a semicrystalline thermoplastic polymer. POM may be in the form of a homopolymer having the general formula $-(CH_2-O)_n-$ or a copolymer

of the formula $-(CH_2-O)_n-(CH_2-CH_2-O)_m-$. In practice, a copolymer is used much more frequently. Among other polymeric materials, these materials are distinguished by better performance properties, including high mechanical strength, stiffness, hardness, resistance to abrasive wear, low water absorption, good chemical resistance, and ease of processing [3]. Polyoxymethylene owes these features to the high degree of ordering of the polymer chains, which

*Corresponding author, e-mail: kingapie@agh.edu.pl

© BME-PT

is possible because of their simple, regular, and linear structure. POM is a linear semicrystalline polymer with a high degree of crystallinity ranging from 50 to 80% for polymers prepared and used on an industrial scale. The conditions that prevail during POM crystallization strongly affect the amount and morphology of the crystalline phase formed. POM chains crystallize in the hexagonal (9/5) system, creating a stable α phase, and in the orthorhombic (2/1) system leading to a metastable β phase. A POM elementary cell crystallizing in a hexagonal system has dimensions $a = b = 4.45 \text{ \AA}$, $c = 17.3 \text{ \AA}$, and contains nine monomer units derived from one polymer chain. POM crystallizes in hexagonal form from the melt or from dilute solutions. The orthorhombic form of POM is characterized by the structure of an elementary cell consisting of two polymer chains, with two mers from each chain in the elementary cell with dimensions $a = 4.77 \text{ \AA}$, $b = 7.65 \text{ \AA}$, $c = 17.80 \text{ \AA}$. Orthorhombic POM can be obtained by polymerization from a liquid basic solution of formaldehyde. However, the orthorhombic form of POM is metastable and transforms into a stable hexagonal form at 69°C [4]. In POM, the orthorhombic phase is the high-density crystalline with the high compactness of 2/1 helices along the c axis, while the less dense hexagonal phase which is less stable at a lower temperature (below ca. 70°C) and which is the most stable phase at higher temperatures. In some cases, due to kinetic reasons, thermodynamically permitted processes may be hindered, and it can lead to the formation of less thermodynamically stable products. For instance, orthorhombic POM formation was found during polymerization at a temperature below 70°C . Below 70°C orthogonal form is the most stable and formed faster than the less stable hexagonal form. On the other hand, during POM crystallization from the melt, mainly the formation of the hexagonal phase was found since crystallites are formed rapidly during cooling at temperature higher than 70°C . For the transition of orthorhombic to hexagonal form, a slight expansion along the b axis and a contraction along the a axis of the orthorhombic phase is necessary. According to these changes and distortion, the inverse hexagonal to orthorhombic forms transformation is theoretically possible by cooling the POM to a temperature below 70°C ; however, it has not been observed in practice. This effect was attributed to the hindering of necessary structural changes or extremely slow transformation at low temperatures and

pressure [5]. Therefore, each thermal treatment, including processing, causes the POM used to be only in the hexagonal form [6].

POM chains form crystals with two morphological forms during crystallization. The first is extended chain crystal (ECC), the second is folded chain crystal (FCC). POM chains, under appropriate conditions, can also form shish-kebab structures, where FCC crystallize around a core made of a single ECC. ECCs are less stable, formed and melt at around 140°C , unlike FCCs that melt at around 156°C [7, 8]. The cationic polymerization of 1,3,5-trioxane promotes the formation of crystallites in the form of whiskers. ECC POM crystallites can also be obtained by the electrospinning method. In the case of POM crystallization from solution and melt, the folded POM chains form lamellar structures composed of a single layer with a thickness of approximately 100 \AA [9]. The crystallization behaviour of POM in the presence of different nanoparticles has recently been investigated [10]. Hence, Zeng *et al.* [11] investigated the effect of silver nanoparticles on non-isothermal crystallization behavior of POM using Jeziorny, Jeziorny-modified Avrami, Ozawa, Liu, and Mo, Ziabicki, and Kissinger models. They revealed that small amounts of Ag nanoparticles incorporated into the POM matrix act as nucleating agents and could enhance the crystallization rate of POM and increase the number of growing POM spherulites with simultaneous reduction of POM spherulites size. The incorporation of higher content of Ag nanoparticles leads to their aggregation and hindrance of POM crystallization. Slouf *et al.* [12] studied POM composites with talc micropowder (POM/mTalc), chalk nanopowder (POM/nChalk), and titanate nanotubes (POM/TiNT). They revealed that the crystallization half-times change in the following order: POM/nChalk < POM/mTalc < POM/TiNT ~ POM and mTalc and nChalk are strong nucleating agents. POM with graphene nanoplatelets (GNP) was investigated by de Souza Santos *et al.* [13]. It has been found that incorporating GNP hinders the polymer crystallization process, changes the degree of crystallinity, and increases the crystallization temperature. The authors suggested that GNP acts as a nucleating agent for POM. Another approach was presented by Jiao *et al.* [14] investigated the crystallization behavior of POM in the presence of a small amount of ionic liquid – tributyl(octyl)phosphonium bis(trifluoromethanesulfonyl)imide (TBOP-TFSI) – as a

nucleating agent. The differential scanning calorimetry (DSC) results and microscopic observations in polarized light showed that the incorporation of TBOP-TFSI induces crystal nucleation and formation of fine crystal grains of POM, which leads to significant improvement in the impact strength of POM blends.

In this work, hydroxyapatite (HAp) was functionalized with poly(ethylene glycol) (PEG) using diisocyanates as linkers. For this purpose, several different diisocyanates were used, including those for medical use, as well as PEGs with selected different average molar masses. From the obtained systems, those with the highest content of incorporated organic phase were selected based on thermogravimetric analysis (TG). The next stage of the research included analysis of POM crystallization kinetics in the presence of the hybrid filler, microscopic and dynamic mechanical analysis (DMA) tests, as well as ^{13}C NMR and ^{35}P NMR investigations to show the effect of the HAp-g-PEG hybrid filler on the crystallization kinetics and crystallinity of POM composites.

2. Experimental part

2.1. Materials

A commercially available polyoxymethylene copolymer (POM_C, Ultraform[®], BASF) with a melt flow index (MFI) of 2,6 g/10 min was used as the matrix of polyacetal composites. Stoichiometric HAp ($\text{Ca}_{10}(\text{PO}_4)_6\text{OH}_2$) in the form of a nanopowder with a spherical nanoparticle shape and size 99% <100 nm, was the product of nGimat Co. (USA).

1,6-hexamethylene diisocyanate (HDI), 4,4'-diphenylmethane diisocyanate (MDI), methylene bis-(4-cyclohexanemethylene diisocyanate) (HMDI) and 3-isocyanatomethyl-3,5 isocyanate, and 5-trimethylcyclohexyl (isophorone diisocyanate (iPDI)) were Sigma Aldrich products. PEG (Sigma Aldrich) with selected three different mass average molar masses – 600, 2000, and 6000 g/mol, was used to modify HAp. The catalyst, dibutyltin dilaurate (DBTL), was also manufactured by Sigma Aldrich. Dehydrated *N,N*-dimethylformamide (DMF), and ethyl alcohol were products of Avantor. Before the grafting process, HAp was dried at 110 °C for 2 h, and PEG was dried at 90 °C under a vacuum also for 2 h. PEG with the selected molar mass was grafted onto the HAp surface using one of the selected diisocyanates as a linker.

2.2. HAp functionalization and POM composites preparation

The process of grafting PEG chains on the HAp surface was carried out in two stages. Table 1 shows the amounts of reagents used in the grafting process. The molar ratio of HAp:diisocyanate:PEG reagents was 1:2:1.

In the first step, 9 g of HAp was gradually dispersed by sonication in a three-necked flask under a nitrogen atmosphere in 90 ml of DMF over a period of 1 h, without exceeding the suspension temperature of 30 °C. 9 µl of catalyst was then added to the obtained HAp suspension in DMF. Simultaneously, a 1:2 weight ratio of the diisocyanate in a DMF solution was prepared, which was then added dropwise to the HAp slurry. After the dropwise addition of the diisocyanate solution, over a period of about 30 minutes, the system was heated with a heating mantle and stirred with a magnetic stirrer under a nitrogen atmosphere to a temperature of 80 °C where the diisocyanate-HAp coupling reaction was carried out for 2 hours. After this time, the system was cooled to room temperature, and then the solution of PEG in DMF was added dropwise in a mass ratio of 1:1. After the PEG solution was dosed, the system was reheated to 60 °C, whereby PEG grafting reaction to isocyanate groups was performed for another 1.5 hours, and then the reaction mixture was cooled down to the room temperature. After completion of the reaction, the mixture was centrifuged using a laboratory centrifuge for 20 minutes at a speed of 4000 rpm. After centrifugation, the precipitate was washed three more times with dry ethanol. After washing and centrifuging, the material obtained was transferred to a Petri dish and dried, first for 24 h at room temperature and then for 24 h at 40 °C. After this time, the dried material was ground in a mortar and then stored in a desiccator.

Table 1. Amounts of reagents used in the PEG grafting on the HAp surface.

Nr.	HAp	Mass [g]	Diisocyanate	Mass [g]	PEG	Mass [g]
1	HAp	9.00	HDI	6.00	600	10.75
2					2000	35.83
3					6000	107.50
4			MDI	8.93	600	10.75
5			HMDI	9.36		10.75
6			iPDI	7.93		10.75

Polyacetal composites (POM/HAp-g-PEG) were obtained by means of two-stage melt processing – extrusion and injection moulding. After TG analysis of the obtained HAp-g-PEG powders, the percentage content of the inorganic phase was determined as a solid residue at a temperature of 600 °C. On this basis, the concentration of HAp was calculated in each of the HAp-g-PEG systems. In the next step, the blends obtained were subjected to an extrusion process to disperse HAp-g-PEG in the polymer – composites with HAp-g-PEG content 0.5; 1.0; 2.5; 5.0, and 10.0% were obtained. The extrusion process was carried out with a laboratory twin-screw co-rotating extruder (HAAKE™ MiniLab Micro Compounder) at a temperature of 210 °C, with the rotation speed of the screws 50 rpm. The injection process was carried out using a Zamak WT12 injection moulding machine. The injection process parameters were as follows: mould temperature – 90 °C, plasticization temperature – 210 °C, plasticization time – 3 minutes, injection pressure – 10 bar.

2.3. Testing methods

Thermogravimetric analysis (TGA) was performed using a Netzsch STA 449 Jupiter® thermal analyzer. Samples of ca. 10 mg were placed in open alumina crucibles. Measurements were carried out at a heating rate of 10 K/min, from 40 to 600 °C, under a nitrogen atmosphere (flow 30 ml/min). Elemental analysis of elements: carbon, oxygen, and hydrogen in HAp-g-PEG samples was performed with the LECO CHN628 elemental analyzer according to ASTM D 5373 standard. The test samples were burned in pure oxygen at a temperature of 950 °C to completely burn the organic part. The content of C and H in the flue gas was determined successively – based on the analysis of the infrared absorption spectra, while N – based on the measurement of thermoconductivity. NMR measurements (¹H MAS-NMR, ³¹P MAS-NMR, and ¹³C MAS-NMR) were carried out in the solid-state for HAp-g-PEG powders and POM_C/HAp-g-PEG composites. High-resolution Magic Angle Spinning (MAS-NMR) spectra in the solid state were measured on a Tecmag APOLLO spectrometer, working with a Magnex superconducting magnet with a field of 7.05 T and a diameter of 89 mm. A Bruker HP-WB MAS probe was used to spin the sample. The sample was placed in a zirconium rotor with a diameter of 4 mm, equipped with a KEL-F turbine. The free precession signal was

recorded after a single excitation pulse with a length of 3 μs, corresponding to the magnetization rotation by 90°. ³¹P MAS-NMR spectra were measured at a resonance frequency of 121.26 MHz, spinning the sample at 4 kHz. The spectrum resulted from averaging 128 measurements made with a repetition time of 10 s. The ppm scale was determined using a liquid sample of 85% H₃PO₄ solution. ¹³C MAS-NMR spectra were measured at a resonance frequency of 75.33 MHz, while the sample was spinning at 8 kHz. The spectrum resulted from averaging 400 measurements made with a repetition time of 20 s. The ppm scale was determined using a liquid TMS (tetramethyl-silane) sample (Si(CH₃)₄). ¹H MAS-NMR spectra were measured at a resonance frequency of 299.56 MHz by spinning the sample at 8 kHz. The spectrum resulted from averaging 1000 measurements made with a repetition time of 1 s. The ppm scale was determined using a liquid TMS (tetramethyl-silane) sample (Si(CH₃)₄). FTIR spectra were recorded with the Vertex 70v spectrometer (Bruker) at room temperature, in the air atmosphere, with a resolution of 2 cm⁻¹, in the range of 4000–500 cm⁻¹. For HAp-g-PEG samples, measurement was performed using potassium bromide (KBr) pellets. For POM/HAp-g-PEG composites, measurements were carried out using the attenuated total reflectance (ATR) technique with the HATR PIKE attachment on a diamond crystal. The surface morphology of POM composites was investigated using a scanning electron microscope (SEM) (Nova NanoSEM 200, FEI) at an accelerating voltage of 1 kV, after previously sputtering the samples with carbon. A microscope equipped with an EDAX X-ray spectrometer (EDX) was used to analyse chemical elements on the surface of the tested samples. A TEM microscope (LEO 912AB, Carl Zeiss, Germany) was used to assess the degree of dispersion of HAp-g-PEG in the polymer matrix. Prior to observation, the samples were cut with an MTX ultramicrotome (RMC Products, Tucson, USA).

The DSC 1 differential scanning calorimeter (Mettler Toledo) was used for the DSC measurements. Measurements were made at a heating and cooling rate of 10 K/min in a nitrogen atmosphere (flow 30 ml/min). The samples weighing ca. 5 mg were placed in closed and pierced aluminum pans. The reference sample was an empty aluminum pan. An intracooler was used for cooling. For composite samples (POM/HAp-g-PEG), the measurement was carried out in a

dynamic mode, in which the sample was heated (25–200 °C), then cooled (200–25 °C), and reheated to 200 °C. On the basis of the obtained DSC curves, the enthalpy of melting (ΔH_m) of POM was determined, and then the degree of crystallinity of POM in POM/HAp-g-PEG composites was determined using the Equation (1):

$$X_c = \frac{\Delta H_m}{(1-w)\Delta H_m^0} \cdot 100\% \quad (1)$$

where X_c – degree of crystallinity of the POM, ΔH_m – heat of fusion of the sample, w – weight fraction of the additive (HAp-g-PEG) in the composite, ΔH_m^0 – heat of fusion of 100% crystalline polymer ($X_c = 100\%$), for POM $\Delta H_m^0 = 326.3$ J/g. For the purpose of calculating the crystallization kinetics, isothermal measurements were also carried out, during which samples weighing about 5 mg were heated to a temperature of 180 °C, kept for 5 minutes until the polymer completely melted, and then rapidly cooled at a rate of 80 K/min to the crystallization temperature of POM.

Measurements using the dynamic mechanical analysis method were carried out using a DMA 850 Discovery (TA Instruments, USA) operating in the bending

mode with the specimen fixed at one end (single cantilever). The measurements were carried out in a nitrogen atmosphere, in the temperature range of –90 to 150 °C, by heating the samples at a rate of 3 °C/min, deforming them at a frequency of 10 Hz with an amplitude of 10 μ m. The dimensions of the samples for measurement are 20×4.75×4.05 mm. The atomic force microscope (AFM, XE120 Park Systems) was used to image the surface of the composites. Measurements were carried out in the contact mode, in the air atmosphere. A probe with a scanning blade (MLCT-C) by Bruker, made of non-conductive V-shaped silicon nitride, was used for the measurements. The measurement probe (MLCT-C) was characterized by the following parameters: resonant frequency 4–10 kHz. As a result of the measurements, images with dimensions of 90×90 μ m, were obtained.

3. Results and discussion

Hybrid HAp-g-PEG systems were analyzed in the first stage of the investigation to assess the amount of organic phase in the systems – Figure 1.

For systems containing HDI as a coupling agent in their structure, a much higher proportion of the

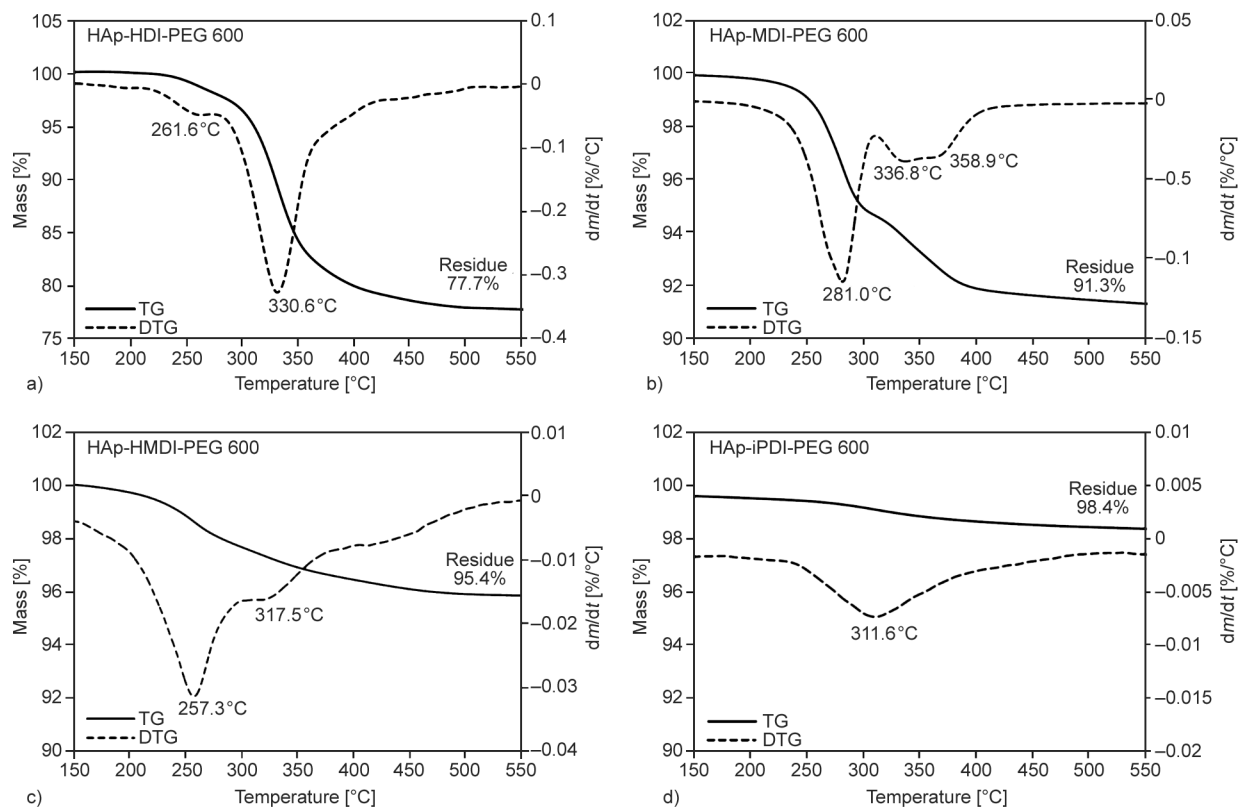


Figure 1. TG and derivative thermogravimetry (DTG) curves of hybrid HAp-g-PEG systems a) HAp-HDI-PEG 600, b) HAp-MDI-PEG 600, c) HAp-HMDI-PEG 600, d) HAp-iPDI-PEG 600.

organic phase ($21.2\pm 3.6\%$) than the other diisocyanates was observed. The degradation process of the organic part of HAp-g-PEG systems was carried out in three stages, which is confirmed by the presence of three peaks in the DTG curves. The onset of decomposition was around $210\text{ }^\circ\text{C}$. The first decomposition peak was observed at $250\text{--}280\text{ }^\circ\text{C}$, the second peak at $310\text{--}340\text{ }^\circ\text{C}$, and the third at $350\text{--}400\text{ }^\circ\text{C}$. The grafting reaction was unsuccessful for the system containing iPDI as the coupling agent. In the sample analyzed $>98\%$ of the inorganic phase (HAp) was present. For systems containing MDI and HMDI diisocyanates, the content of the incorporated organic phase did not exceed 10% of the sample weight.

The highest efficiency of the grafting reaction was obtained for HDI. The process of degradation of the organic part of the hybrid HAp-g-PEG system was similar to the degradation of polyurethanes obtained with polyethers as a soft segment, where the thermal decomposition of polyurethane (PU) hard segments (derived from the isocyanates used) at temperatures of $200\text{ to }300\text{ }^\circ\text{C}$ occurs as a result of the degradation of urethane bonds. The urethane bond can be degraded by dissociation to isocyanate and alcohol (re-formation of --NCO and --OH groups), or to primary amines (R--NH_2) and olefins ($\text{CH}_2=\text{C--R}'$) to form carbon dioxide (CO_2) and by eliminating CO_2 from the urethane bond to give secondary amines ($\text{R--NH--R}'$). After this stage, there was a further degradation of the material at temperatures of $355\text{--}385\text{ }^\circ\text{C}$, related to the degradation of soft segments derived from polyols. At this stage, the processes such as chain depolymerization, random chain breaking, and cross-linking take place. With further heating ($>550\text{ }^\circ\text{C}$), complete decomposition of PU occurs with the formation of simple hydrocarbons and other residues [15, 16]. At temperatures up to $100\text{ }^\circ\text{C}$, HAp shows a slight weight loss (about 2%) [17] due to the release of absorbed water from the material; therefore, the solid residue at $550\text{ }^\circ\text{C}$ is almost entirely composed of HAp.

The organic phase content in the HAp-g-PEG hybrid systems was also examined by means of elemental analysis of nitrogen, carbon, and hydrogen. The measurement results are presented in Table 2.

A much larger weight fraction of the examined elements was observed in the samples obtained with HDI. Among the elements examined, each of the samples contained the highest percentage by weight of C. In the sample obtained from iPDI, the presence

Table 2. Elemental analysis results for HAp-g-PEG systems.

Sample	Elements [wt%]			
	N	C	H	Summa
HAp-HDI-PEG 600	2.10	13.72	1.97	17.78
HAp-HDI-PEG 2000	1.55	15.06	2.67	19.28
HAp-HDI-PEG 6000	1.62	10.89	1.86	14.37
HAp-MDI-PEG 600	0.38	7.31	0.50	8.18
HAp-HMDI-PEG 600	0.02	3.31	0.12	3.45
HAp-iPDI-PEG 600	0.00	1.62	0.00	1.62

of the elements N and H was not observed. The elemental analysis confirmed the presence of an organic phase in the HAp-g-PEG systems. The analysis results of the analysis coincide with the relationships obtained by the TG method, which indicates the highest efficiency of the syntheses performed with the use of HDI as a coupling agent and the lack of iPDI reactivity in a given system. The elemental analysis for the HAp-iPDI-PEG 600 sample indicates that the hydrogen comes only from the organic phase of the test compounds. The method does not detect hydrogen in HAp particles, whose weight ratio is 0.2%. The difference in the percentage of elements in the measurement compared to the TG analysis results from the lack of detection of a significant amount of oxygen atoms that make up the organic phase of the tested compounds.

In the next research stage of the research, NMR measurements of HAp-g-PEG powders were performed. The ^{31}P NMR spectra of all tested powders, the ^{13}C NMR spectra and ^1H NMR spectra for the powders with the highest organic phase content are presented in Figure 2.

For the ^{31}P NMR spectra of all powders tested, a single peak was visible, the maximum of which was 2.64 ppm, and its half-width was 2.07 ± 0.02 ppm. This peak corresponds to the PO_4^{3-} phosphate groups present in the crystalline HAp; however, a slight chemical shift is observed in relation to the unmodified HAp for which the maximum from the PO_4^{3-} groups is 2.8 ppm [18]. The width of the peaks does not change much, while the intensity of the peaks obtained changes, which decreases in proportion to the increasing amount of the organic phase in HAp-g-PEG systems. These results are consistent with previous data from the TG analysis and elemental analysis of elements, in which the greatest share of this phase is present in systems containing HDI. In all the powders analyzed, the phosphorus environment is similar, which is related to the presence of

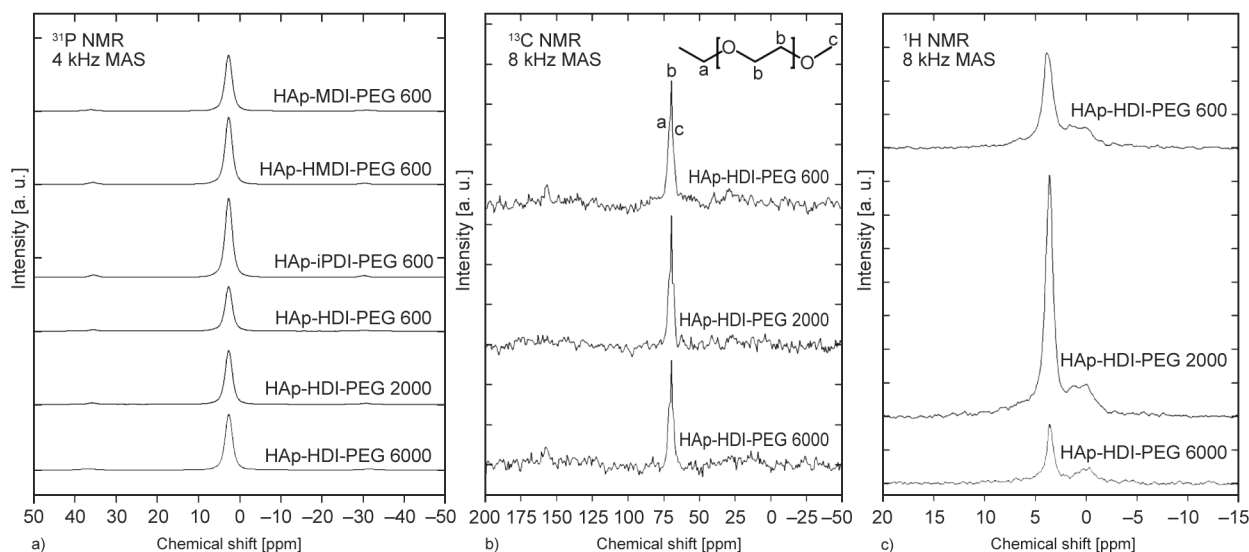


Figure 2. a) ^{31}P NMR, b) ^{13}C NMR, and c) ^1H NMR spectra of hybrid HAp-g-PEG systems.

the organic phase in the tested systems, which may affect the chemical shift compared to pure HAp. The lack of change in the half-width of the phosphate ions also proves that their crystal structure in HAp is preserved.

In the ^{13}C NMR spectra, there is a single asymmetric peak with a maximum at 69.7 ppm. The half-width is 3.56, 3.30, and 2.97 ppm, respectively, and decreases with increasing molar mass of PEG in the tested powders. This peak is from the PEG backbone $(-\text{CH}_2-\text{CH}_2-\text{O})_n-$ and consists of three adjacent C-derived peaks in the PEG chains. Furthermore, the spectra show weak peaks with a maximum of about 156.3 ppm due to the presence of carbon atoms in the urethane bond $(-\text{NH}(\text{C}=\text{O})\text{O}-)$ [19, 20]. NMR analysis confirmed the chemical structure of the compounds tested, in which both organic and inorganic parts are present. The obtained results agree with the TG analysis carried out earlier, confirming the different content of HAp in the tested systems. The dominant peak is visible in the ^1H NMR spectra, the maximum of which is 3.6 ppm (3.8 ppm for HAp-g-PEG 600) which corresponds to the H atoms in the PEG backbone $(-\text{CH}_2-\text{CH}_2-\text{O}-)$, confirming thus the presence of this compound in the tested samples [21]. In addition, a much weaker double peak around 1.6–1.1 ppm is visible, corresponding to the hydrogen atoms in the chains derived from HDI $(\dots-\text{CH}_2-\text{CH}_2-\text{CH}_2-\dots)$, the position of which shifts towards lower numbers as the molecular weight of poly(ethylene glycol) increases. The peak of hydrogen atoms near the urethane bond $(\text{NH}-\text{CO}-\text{O})$ should be visible around 3.0 ppm but is overlapped

by the PEG peak [22]. Furthermore, around 5.5 ppm, weak peaks appear from hydrogen atoms derived from HAp, being components of hydroxyl groups and H_2O molecules associated in the structure of HAp [23].

Because of the highest efficiency of the syntheses performed with the use of HDI as a coupling agent, the next part of this work focused mainly on the systems obtained with the use of this diisocyanate. Studies were carried out for HAp-g-PEG X systems, where grafting was performed with HDI, and X was the average molecular weight of the PEG ($X=600$, 2000 or 6000).

TEM micrographs (Figure 3) show the distribution of the selected HAp-g-PEG systems in the POM_C matrix containing 1.0 and 5.0% of the additive. Hybrid HAp-g-PEG systems are visible in the form of interconnected HAp molecules embedded in the organic phase of the hybrid system made of HDI and PEG. Both HDI and PEG used for HAp-g-PEG preparation possess two functional groups, while on the surface of HAp nanoparticles there are more hydroxyl groups able to react with HDI. That probably leads to the formation of interconnections between HAp nanoparticles and agglomerates of HAp nanoparticles. The distribution of HAp-g-PEG agglomerates in the POM_C matrix is relatively uniform, even for composites containing 5.0% additive. It is contrary to the unmodified HAp in POM, which in the POM_C matrix was visible in the form of individual nanospheres or physically connected agglomerates containing up to several linked HAp nanoparticles [24, 25].

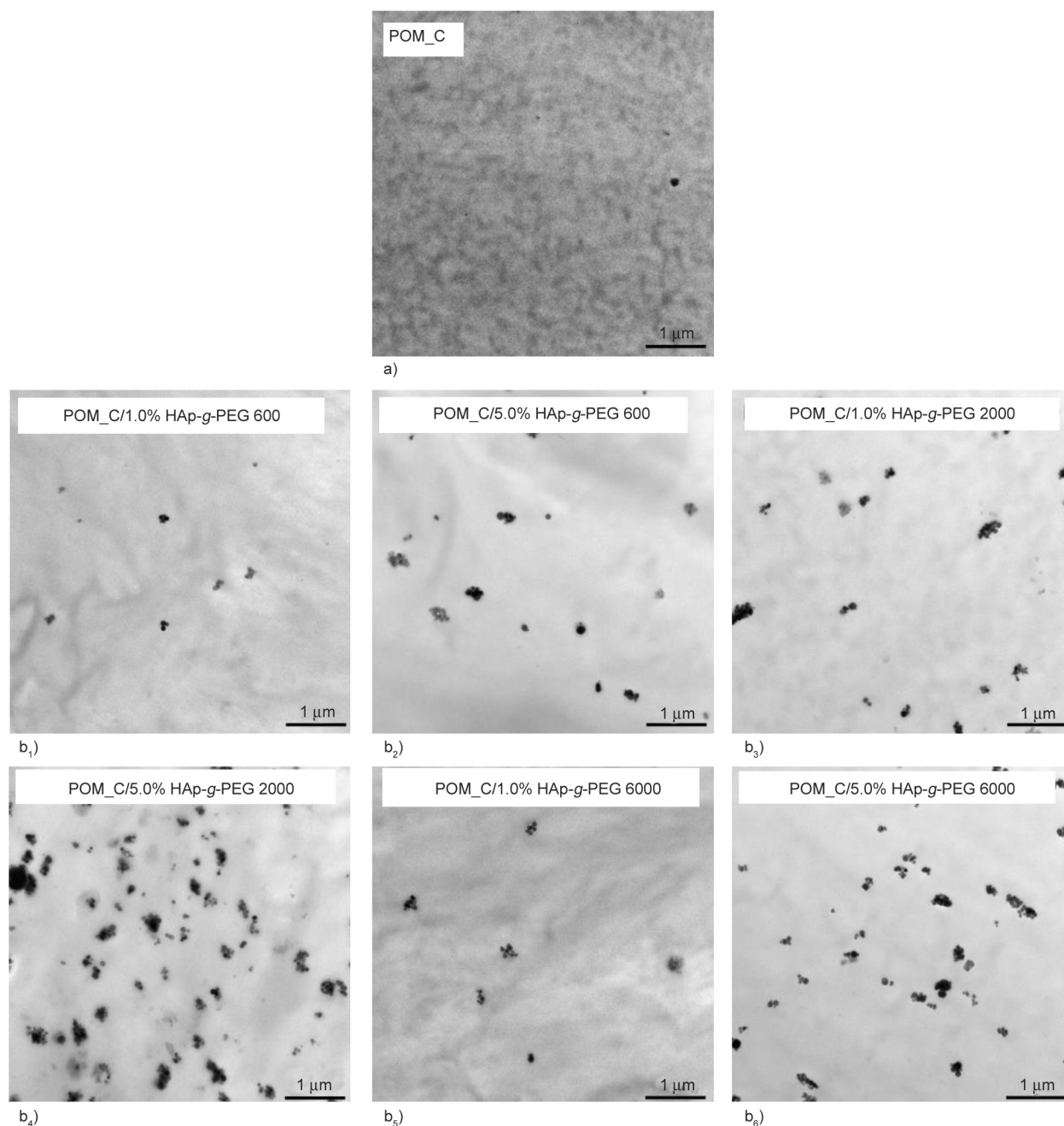


Figure 3. TEM micrographs of POM_C (a) and its composites with 1.0 and 5.0% load of HAp-g-PEG 600, HAp-g-PEG 2000, and HAp-g-PEG 6000 (b), (b₁) POM_C/1.0% HAp-g-PEG 600, (b₂) POM_C/5.0% HAp-g-PEG 600, (b₃) POM_C/1.0% HAp-g-PEG 2000, (b₄) POM_C/5.0% HAp-g-PEG 2000, (b₅) POM_C/1.0% HAp-g-PEG 6000, (b₆) POM_C/5.0% HAp-g-PEG 6000.).

In the first stage, all the obtained POM/HAp-g-PEG composites were subjected to DSC analysis to determine the effect of the applied additive on the melting point, as it is one of the most important processing parameters. The measurement results are presented in Figure 4 and Table 3.

The addition of HAp-g-PEG insignificantly influenced the shape of the DSC curves, the melting point, and the degree of POM crystallinity in the composites. For samples containing a large amount of

HAp-g-PEG ($\geq 5\%$), the supercooling value was reduced even by 3 °C. In the second heating, the differences in melting point compared to unmodified POM did not exceed 1.6 °C. The degree of crystallinity calculated from the second melting increased by up to 5% , compared to the first heating. For the second heating, no major changes in the degree of POM crystallinity were observed (approximately 1–2% increase). The slight influence of the addition of HAp-g-PEG on the melting point of the

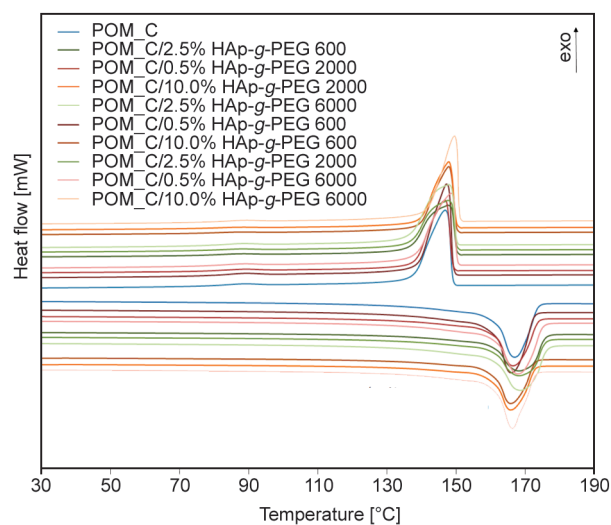


Figure 4. DSC curves (crystallization and melting, 2nd heating run) of POM_C and POM composites with HAp-g-PEG 600, with HAp-g-PEG 2000, and HAp-g-PEG 6000. Data for POM_C was taken from Ref. [26].

tested composites is important information because of the lack of necessity to change the processing conditions of the tested materials. No peak was observed in any of the DSC curves obtained, corresponding to the melting process of PEG, which are 17–22, 50–53, and 58–63 °C for PEG 600, 2000, and 6000, respectively [28]. The lack of peaks may suggest the chemical bonding of PEG in an inorganic-organic compound with HAp, which limits the mobility of the chains, and therefore they do not undergo the process of crystallization.

Contrary to the previously tested POM_C/HAp [25], no double peak in the 1st heating profile was observed, suggesting that the addition of HAp-g-PEG does not significantly affect the thickness variation of POM lamellae formed during the crystallization process. In contrast to unmodified HAp, where HAp nanopowder additionally induced the nucleation effect of POM crystals, no significant improvement in the degree of POM crystallinity was observed as a result of the presence of HAp-g-PEG. This may be due to too many HAp-g-PEG agglomerates linked by organic chains.

The presence of a double melting peak is probably related to the melting of the poorly formed POM_C crystals. Additionally, the presence of HAp-g-PEG may interfere with the POM_C crystallization process, especially with a high amount of additive. As a result, the intensity of the recrystallization phenomenon of imperfect POM_C crystals increases,

which precedes further melting of better-formed POM_C crystals. A similar phenomenon was observed by Pielichowska *et al.* [29] for polyurethanes of MDI-PEG-BDO structure modified with nanographite. In the next stage, the samples were subjected to spectroscopic examination. The FTIR-ATR spectra and their second derivative are shown in Figure 5. In the analyzed spectra, there is a group of two bands: 2981 and 2923 cm^{-1} , which were not included in the figures, corresponding to the symmetrical stretching vibrations (ν) of the CH_2 groups. The band visible at about 1475 cm^{-1} is related to the bending vibrations (δ) of the CH_2 groups. The band at about 1393 cm^{-1} was created as a result of the wagging vibrations of the CH_2 groups, while the average size band at about 1236 cm^{-1} is the effect of the torsional vibrations of the CH_2 groups. The two strong bands at 1093 and 895 cm^{-1} and the weaker band at 1139 cm^{-1} are the results of asymmetric stretching vibrations, and the band at 929 cm^{-1} is caused by symmetric stretching vibrations of the C–O–C bonds. Moreover, at 630 cm^{-1} a peak appears that is related to the bending vibrations of C–O–C bonds [31]. For samples containing at least 2.5% HAp-g-PEG addition, two bands (607 and 578 cm^{-1}) are visible, resulting from asymmetric bending vibrations of PO_4^{3-} phosphate ions derived from HAp.

As is known, POM most often crystallizes in the hexagonal system, in which the polymer chains exist in a 9/5 helical conformation. Only under specific conditions do POM chains in the 2/1 spiral form crystallize in the orthorhombic system to form metastable crystals. In the classic hexagonal arrangement, POM chains crystallize in both an extended and a folded form. Although IR spectroscopy is one of the few methods that can distinguish the bands from each type of crystal produced, it is relatively difficult to separate the peaks from each of them. According to data presented in the literature [32], only two bands are characteristic of one type of POM crystals. These are the band at 1136 cm^{-1} , coming only from the vibrations of the FCC crystals, and the band at 891 cm^{-1} , which is the result of vibrations of the ECC crystals. The remaining bands (1236, 1089, 933, 630 cm^{-1}) result from the superposition of vibrations of both the ECC and FCC crystals. No changes in the values and the number of peaks in POM/HAp-g-PEG composites indicate that, similarly to unmodified POM, crystals in the form of ECC and FCC are also present in these materials.

Table 3. Temperature and heat of fusion or crystallization of POM_C and composites.
POM_C/HAp-g-PEG 600, POM_C/HAp-g-PEG 2000 and POM_C/HAp-g-PEG 6000*

Sample	T_{onset} [°C]	T_{max} [°C]	T_{endset} [°C]	Heat of melting POM_C/HAp-g-PEG [J/g]	Degree of crystallinity [%]
HAp-g-PEG 600					
Melting					
POM_C_0%	160	167	174	171	52.4
POM_C_0,5%	160	166	173	173	53.2
POM_C_1%	160	168	175	167	51.6
POM_C_2,5%	160	169	176	172	54.1
POM_C_5%	160	167	174	160	51.7
POM_C_10%	160	165	174	157	53.0
Crystallization					
POM_C_0%	149	147	137	168	
POM_C_0,5%	149	147	139	171	
POM_C_1%	149	147	137	168	
POM_C_2,5%	150	147	136	170	
POM_C_5%	150	148	139	161	
POM_C_10%	151	149	139	155	
HAp-g-PEG 2000					
Melting					
POM_C_0%	160	167	174	171	52.4
POM_C_0,5%	160	166	174	167	51.5
POM_C_1%	160	167	174	170	52.6
POM_C_2,5%	160	168	176	170	53.5
POM_C_5%	160	166	174	165	53.4
POM_C_10%	160	166	173	159	54.0
Crystallization					
POM_C_0%	149	147	137	168	
POM_C_0,5%	149	147	138	172	
POM_C_1%	150	147	138	170	
POM_C_2,5%	150	148	137	169	
POM_C_5%	150	148	139	164	
POM_C_10%	150	148	140	155	
HAp-g-PEG 6000					
Melting					
POM_C_0%	160	167	174	171	52.4
POM_C_0,5%	160	168	175	169	52.0
POM_C_1%	160	166	172	172	53.2
POM_C_2,5%	160	169	176	169	53.1
POM_C_5%	160	168	176	160	51.7
POM_C_10%	160	167	173	153	52.2
Crystallization					
POM_C_0%	149	147	137	168	
POM_C_0,5%	150	149	138	168	
POM_C_1%	151	149	141	172	
POM_C_2,5%	150	148	136	168	
POM_C_5%	150	148	137	159	
POM_C_10%	151	150	142	156	

*Data for POM_C, POM_C_1% and POM_C_5% were taken from Ref. [27].

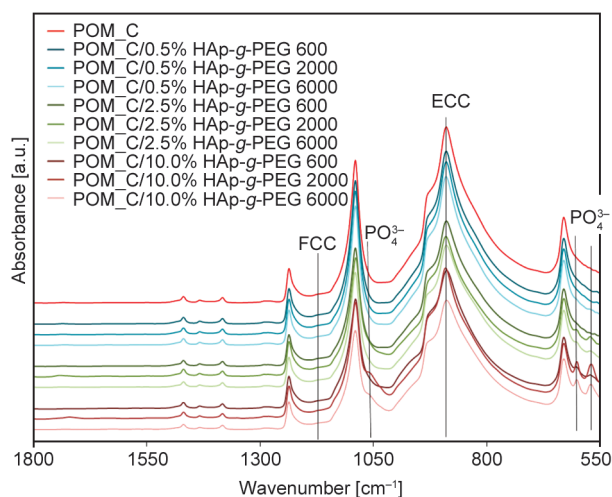


Figure 5. FTIR-ATR spectra of unmodified POM_C and composite spectra POM_C with HAp-g-PEG 600, HAp-g-PEG 2000, and HAp-g-PEG 6000. Data for POM_C were taken from Ref. [30]

In the next stage of the research, the analysis by ^{31}P NMR and ^{13}C NMR methods was carried out for POM_C and its composites with 1.0 and 5.0% HAp-g-PEG 600, HAp-g-PEG 2000 and HAp-g-PEG 6000. Due to the lack of phosphorus atoms in the samples of the unmodified POM, the ^{31}P NMR

analysis was not performed for the pristine polymer. The results of both measurements are presented in Figure 6.

On the ^{31}P NMR spectra for each of the composites tested, a symmetric peak with a constant position of 2.52 ppm and a half-width of 2.10 ± 0.06 ppm was visible, which differed in intensity for various contents of HAp in the tested samples. In the ^{13}C NMR spectra, an asymmetric peak is visible, the maximum of which is 88.31 ppm, which is characteristic of the carbon atoms in the main chain of the polyacetal $[-\text{CH}_2-\text{O}]_n-$ forming the crystalline phase [33]. Additionally, the broadening of each of the peaks at the bottom left is visible with an additional shoulder that corresponds to the POM carbon atoms in the amorphous phase [34]. The half-width of the observed peak is 5.5 ± 0.2 ppm, and there is a slight effect of the addition of HAp-g-PEG on the half-width of the analysed peak. Moreover, for the sample containing 5.0% HAp-g-PEG 2000, the spectrum shows a second peak with a maximum of 69.6 ppm, corresponding to the carbon atoms environment due to the addition of HAp-g-PEG 2000.

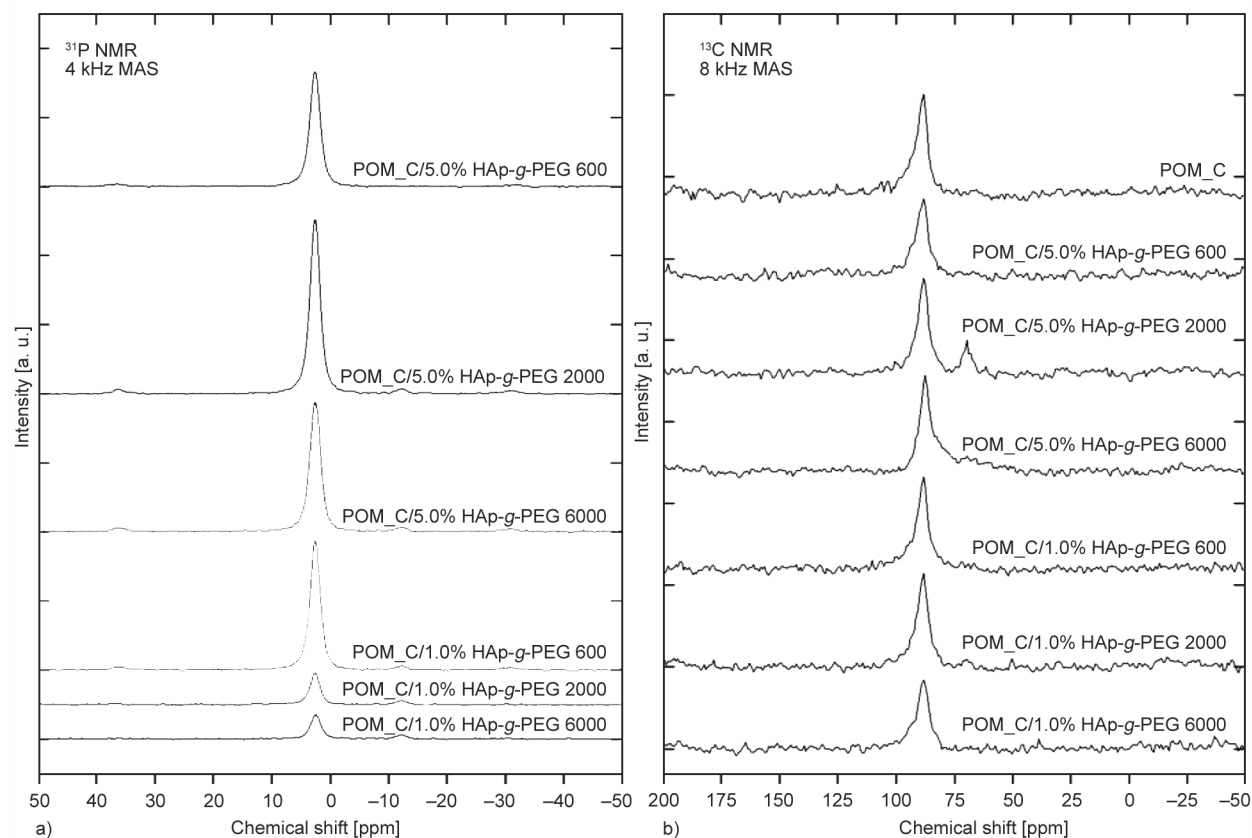


Figure 6. ^{31}P NMR (a) and ^{13}C NMR (b) spectra for POM_C and POM_C composites with 1.0 and 5.0% HAp-g-PEG 600, HAp-g-PEG 2000, and HAp-g-PEG 6000.

NMR tests confirmed the presence of various amounts of HAp in the tested samples. A clear chemical shift for PO_4^{3-} ions compared to unmodified HAp may indicate the presence of an inoculated organic phase. Moreover, NMR analysis revealed the semicrystalline nature of POM_C. However, the addition of HAp-g-PEG did not change the structure of the POM_C chains, as it was confirmed by the XRD analysis performed earlier [26].

For POM_C samples and their composites containing 1.0 and 5.0% of HAp-g-PEG 600, HAp-g-PEG 2000, and HAp-g-PEG 6000, measurements were carried out using a DSC to analyze the kinetics of crystallization. After crystallization of the samples under isothermal conditions at four selected temperatures, the obtained DSC curves were subjected to integration to determine the relative degree of crystallinity, or (X_t), according to Equation (2):

$$X_t = \frac{\int_0^t \frac{dH}{dt} dt}{\int_0^\infty \frac{dH}{dt} dt} \quad (2)$$

where X_t – relative crystallinity, dH/dt – heat flux of accompanying the transformation.

The curves of the dependence of the degree of relative crystallinity X_t on the crystallization time t obtained in this way for selected samples are presented in Figure 7.

As can be seen from the analyzed curves, the higher the temperature of the crystallization, the longer its time. The characteristic sigmoidal shape of the obtained curves, for which a rapid increase in the rate of crystallization takes place in the first stage, is related to the occurrence of the so-called primary crystallization, which precedes secondary crystallization taking

place much more slowly. After the primary crystallization is completed, secondary crystallization begins, which includes the further process of organizing the amorphous areas remaining in the polymer [35]. The kinetics of primary crystallization of a number of polymers, including POM, under isothermal conditions can be described using the Avrami Equation (3):

$$X_t = 1 - \exp(-kt^n) \quad (3)$$

where X_t – the relative degree of crystallinity achieved by the polymer that crystallizes over time t , k – Avrami constant, the isothermal crystallization rate constant depending on the nucleation frequency and spherulite growth rate, n – Avrami exponent, depending on the nucleation mechanism and shape of growing crystallites [36].

The doubly logarithmic form of the Avrami equation is used to determine the parameters n and k (Equation (4)):

$$\log[-\ln(1 - X_t)] = \log k + n \log t \quad (4)$$

From the dependency graph $\log[-\ln(1 - X_t)]$ vs. $\log t$ – for selected samples shown in Figure 8, the Avrami exponent n and the constant k were determined from the straight line equation.

By knowing the value of the Avrami constant (k), the half-time of crystallization was determined using Equation (5):

$$t_{1/2} = \left(\frac{\ln 2}{5}\right)^{\frac{1}{n}} \quad (5)$$

where $t_{1/2}$ – half-time crystallization, that is the time taken to reach the relative degree of crystallinity of 50% and the rate of crystallization as reciprocal of the half time (G) based on the Equation (6):

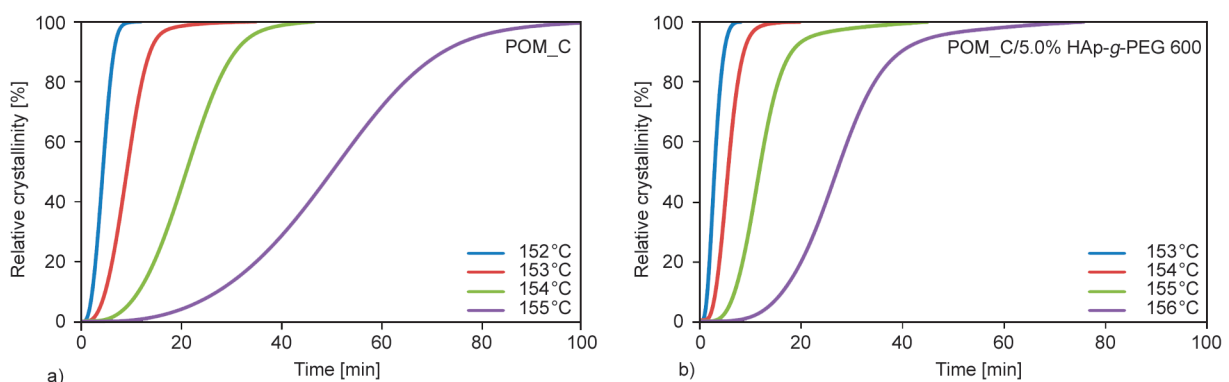


Figure 7. Relative crystallinity (X_t) vs. time (t) for isothermal crystallization process of a) POM_C and b) POM_C composites with 5.0% HAp-g-PEG 600.

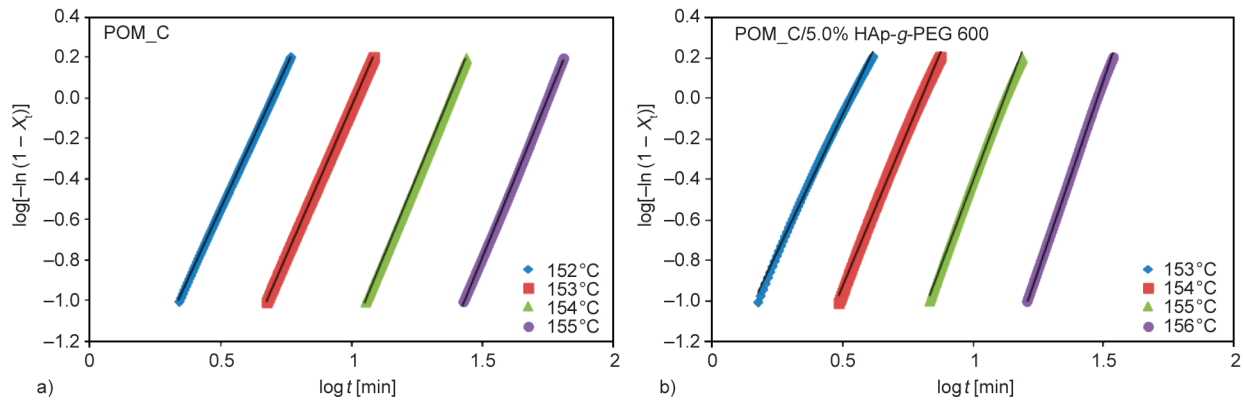


Figure 8. $\log[-\ln(1 - X_i)]$ vs. $\log t$ for isothermal crystallization process of a) POM_C and b) POM_C composites with 5.0% HAp-g-PEG 600.

$$G = \frac{1}{t_{1/2}} \quad (6)$$

The time required to reach the maximum crystallization rate (t_{\max}) can be calculated from Equation (7):

$$t_{\max} = \left(\frac{n-1}{nk} \right)^{\frac{1}{n}} \quad (7)$$

The values of the parameters determined n , k , $t_{1/2}$, G , t_{\max} including isothermal crystallization temperatures (T_K) and the R^2 coefficient, are summarized in Table 4.

For POM_C composites containing 1.0% additive HAp-g-PEG 600, HAp-g-PEG 2000, and HAp-g-PEG 6000 at 153 °C, compared to unmodified POM_C, there was a significant acceleration of crystallization (t_{\max}) by 46, 52, and 62%, respectively. For all composites containing 5.0% HAp-g-PEG, crystallization at 153 °C was accelerated by 67.6±0.7%. This indicates accelerated crystallization as a result of the presence of HAp-g-PEG, which may constitute nuclei for POM, thus supporting the heterogeneous nucleation process of this polymer [37]. With a small proportion of HAp-g-PEG addition (1.0%), the greater the average molar mass of PEG in the HAp-g-PEG, the more enhanced the crystallization acceleration effect, while with a higher amount of additive (5.0%), all additives work in a similar manner. The value of the Avrami exponent for unmodified POM_C ranges from 2.80 (at 152 °C) to 3.16 (at 155 °C), indicating the formation – under given conditions – of three-dimensional POM crystal structures in the form of spherulites [38]. Data from the literature show that for the value of the Avrami exponent $n = 3$, there is a two-dimensional growth of crystallites formed as a result of thermal nucleation

and a three-dimensional growth of spherulites formed through thermal nucleation [38]. For most of the POM/HAp-g-PEG composites, the Avrami exponent (n) slightly decreased by 0.1 to approx. 0.5, with the greatest reduction of n occurring mainly in the composites containing 5.0% of HAp-g-PEG.

The reduction of the n value of the tested composites may indicate that the presence of HAp-g-PEG, especially in a larger amount, may hinder the formation of three-dimensional spherulites during POM crystallization. Polymer chains can crystallize in a two-dimensional form, in the form of lamellas arranged in flat disks [39]. The value of the constant k decreases with the increasing crystallization temperature for both pure POM_C and its composites. This is because the difference between the temperature at which crystallization is carried out and the temperature corresponding to the highest crystallization rate increases. In composite materials, the k value is significantly greater than the k value for pure POM_C at the corresponding crystallization temperatures. At the same time, the increase in k value is much greater for composites containing 5.0% HAp-g-PEG. Analogous dependencies exist for the parameter G , which is the reciprocal of the half-time of crystallization. A similar relationship was noticed by Xu [40] when studying POM with attapulgite, which was used as a nucleating agent. The addition of attapulgite reduced the size of POM spherulites, significantly accelerated the rate of crystallization, and improved impact toughness, but did not affect the hexagonal form of the crystallizing POM, similarly to the HAp-g-PEG additives used in our study.

Figure 9 shows the rate of crystallization (G) described as the reciprocal of the half-time, which determines the crystallization rate vs. isothermal

Table 4. Values of the kinetic parameters of the crystallization process obtained from the Avrami equation for POM_C and composites with 1.0 and 5.0% HAp-g-PEG 600, HAp-g-PEG 2000, HAp-g-PEG 6000.

Sample	T_K [°C]	n	k [min ⁻¹]	R^2	t_{max} [min]	$t_{1/2}$ [min]	G [min ⁻¹]
POM_C	152	2.80	$1.16 \cdot 10^{-2}$	1.0000	4.20	4.31	0.2320
	153	2.94	$1.04 \cdot 10^{-3}$	1.0000	8.96	9.11	0.1098
	154	3.13	$5.12 \cdot 10^{-5}$	0.9999	20.84	20.97	0.0477
	155	3.16	$3.00 \cdot 10^{-6}$	0.9995	49.71	49.93	0.0200
POM_C/1.0% HAp-g-PEG 600	153	2.69	$9.22 \cdot 10^{-3}$	0.9997	4.80	4.98	0.2006
	154	2.90	$8.25 \cdot 10^{-4}$	0.9996	9.98	10.17	0.0983
	155	3.05	$4.85 \cdot 10^{-5}$	0.9993	23.20	23.44	0.0427
	156	3.25	$1.32 \cdot 10^{-6}$	0.9999	57.75	57.78	0.0173
POM_C/5.0% HAp-g-PEG 600	153	2.72	$3.64 \cdot 10^{-2}$	0.9976	2.86	2.96	0.3380
	154	3.11	$3.21 \cdot 10^{-3}$	0.9985	5.58	5.62	0.1781
	155	3.40	$1.55 \cdot 10^{-4}$	0.9987	11.88	11.82	0.0846
	156	3.71	$3.38 \cdot 10^{-6}$	0.9997	27.52	27.14	0.0368
POM_C/1.0% HAp-g-PEG 2000	153	2.60	$1.62 \cdot 10^{-2}$	0.9988	4.05	4.23	0.2262
	154	2.58	$2.99 \cdot 10^{-3}$	0.9994	7.85	8.23	0.1214
	155	2.71	$2.09 \cdot 10^{-4}$	0.9992	19.28	19.97	0.0501
	156	2.58	$2.59 \cdot 10^{-5}$	0.9964	49.81	52.28	0.0191
POM_C/5.0% HAp-g-PEG 2000	153	2.41	$4.65 \cdot 10^{-2}$	0.9992	2.86	3.07	0.3256
	154	2.69	$4.05 \cdot 10^{-3}$	0.9991	6.51	6.75	0.1481
	155	2.78	$3.19 \cdot 10^{-4}$	0.9998	15.44	15.89	0.0629
	156	2.85	$1.18 \cdot 10^{-5}$	0.9998	46.17	47.26	0.0212
POM_C/1.0% HAp-g-PEG 6000	153	2.71	$2.27 \cdot 10^{-2}$	0.9988	3.41	3.53	0.2833
	154	3.08	$1.64 \cdot 10^{-3}$	0.9993	7.07	7.13	0.1403
	155	3.27	$9.08 \cdot 10^{-5}$	0.9996	15.35	15.34	0.0652
	156	3.49	$2.42 \cdot 10^{-6}$	0.9998	36.88	36.57	0.0273
POM_C/5.0% HAp-g-PEG 6000	153	2.48	$3.97 \cdot 10^{-2}$	0.9989	2.98	3.17	0.3153
	154	2.69	$5.39 \cdot 10^{-3}$	0.9987	5.87	6.09	0.1642
	155	2.85	$4.29 \cdot 10^{-4}$	0.9978	13.07	13.37	0.0748
	156	3.01	$2.12 \cdot 10^{-5}$	0.9984	31.14	31.53	0.0317

crystallization temperature of POM_C and POM_C composites with 1.0 and 5.0% HAp-g-PEG 600, HAp-g-PEG 2000, and HAp-g-PEG 6000.

The presented dependencies confirm the increase in the rate of POM_C crystallization with the increase in the concentration of HAp-g-PEG addition. Based on Hoffman-Week diagrams, the equilibrium melting point T_m^0 for pure POM_C was 189 °C, and it decreases with increasing content of HAp-g-PEG as it was presented in Table 5. A larger decrease in T_m^0 was also observed with an increase in the average molar mass of PEG in the additive used. The drop in the equilibrium melting point indicates the formation of less developed and more defective POM_C crystals in the presence of HAp-g-PEG, the presence of which most likely disturbed the polymer crystallization process as a result of an increased share of heterogeneous POM_C nucleation in composites. The increased proportion of additional nucleation seeds

in the polymer can result in the formation of smaller, more defective POM_C crystals, in this case, three-dimensional spherulites. A similar phenomenon was observed by Wu and Chen [41] when investigating PCL/MWCNT composites, where, also with the increase in the amount of additive, the temperature T_m^0 was decreased, and consequently, the microstructure of the composites changed by forming much smaller and less perfect PCL spherulites. Another explanation for the reduction of the equilibrium temperature T_m^0 is a significant reduction in the duration of crystallization as a result of heterogeneous POM_C nucleation on the surfaces of HAp-g-PEG particles, which reduces the time for the formation of polymer crystallites [42].

Depression of equilibrium melting point was described in the literature for many polymeric systems, especially for blends, but also for (nano)composites, and it is connected to the interactions between

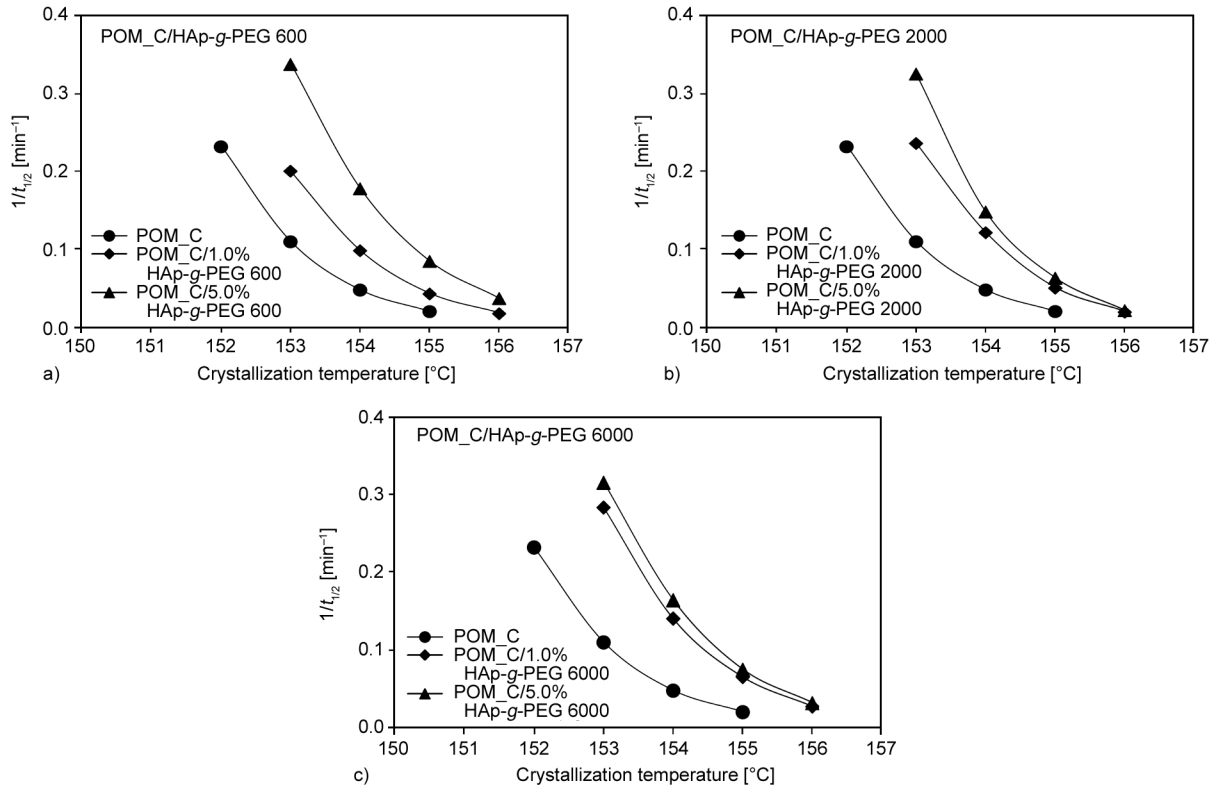


Figure 9. Plots of the reciprocal of the half-time (G) vs isothermal crystallization temperature (T_K) for POM_C and POM_C composites with 1.0 and 5.0% HAp-g-PEG 600 (a), HAp-g-PEG 2000 (b) and HAp-g-PEG 6000 (c).

components of the system and their miscibility [43] Depression of equilibrium melting point was analysed by Lee *et al.* [44] as a measure of interactions between PLA and MWCNTs.

The effective activation energy (E) was determined on the basis of Hoffman-Lauritzen theory using Equation (8):

$$E = a \cdot \frac{d(\ln G)}{dT^{-1}} = U \frac{T_K^2}{(T_K - T_\infty)^2} + K_g R \frac{(T_m^0)^2 - T_K^2 - T_m^0 T_K}{(T_m^0 - T_K) T_K} \quad (8)$$

where E depends on the parameters U^* and K_g , which represent the energy barriers of mass transport and nucleation, respectively. In the assumed model, the linear growth rate of the polymer crystals (G) depends on the temperature, according to the Equation (9):

$$G = G_0 \exp\left[\frac{-U^*}{R(T_K - T_\infty)}\right] \exp\left[\frac{-K_g}{T_K \cdot \Delta T \cdot f}\right] \quad (9)$$

where G_0 – it is a pre-exponential factor, U^* – the activation energy necessary to initiate crystallization (for polymers, U^* has a constant value of 6.3 kJ/mol), R – universal gas constant, $\Delta T = T_m^0 - T_K$ and this is supercooling, $f = 2T_K/(T_m^0 + T_K)$ – correction factor,

T_∞ – temperature of crystallization decay ($T_\infty = T_g - 30$ K, where T_g – polymer glass transition temperature).

The kinetic parameter K_g denotes the energy barrier for the nucleation of crystals of a critical size. K_g is strongly dependent on the degree of supercooling and can be calculated by Equation (10):

$$K_g = \frac{nb\sigma\sigma_e T_m^0}{\Delta h_f^0 k_B} \quad (10)$$

where b – thickness of the crystallite growth surface ($b = 4.46 \cdot 10^{-10}$ m), σ – is the lateral surface free energy ($\sigma = 0.0147$ J/m²), σ_e – is the fold surface free energy, Δh_f^0 – is the heat of fusion per unit volume of crystal ($\Delta h_f^0 = 3.55 \cdot 10^8$ Jm⁻³), k_B – Boltzman's constant, n takes a value depending on the crystallization regime in a given system, for I and III regimes $n = 4$, for II regime $n = 2$ [45].

Taking the logarithm of Equation (9), the Equation (11) was obtained:

$$\log G + \left[\frac{-U^*}{R(T_K - T_\infty)}\right] = \log G_0 - \frac{-K_g}{T_K \cdot \Delta T \cdot f} \quad (11)$$

which can also be used to determine the parameter K_g . This parameter is determined from the linear relationship $\log G + U^*/[(R(T_K - T_\infty))] vs. 1/(T_K \cdot \Delta T \cdot f)$.

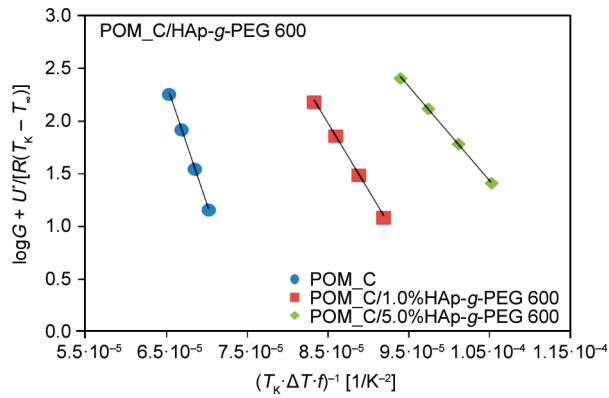


Figure 10. $\log G + U^*/[R(T_K - T_\infty)]$ vs. $1/(T_K \cdot \Delta T \cdot f)$ for POM_C and POM_C composites with 1.0 and 5.0% HAp-g-PEG 600.

This relationship for POM_C/HAp-g-PEG 600 is shown in Figure 10. The K_g values were read as the slope of the regression line fitted to the measuring points.

In Figure 10, a decrease in the degree of slope of the straight lines is visible with an increase in the content of the HAp-g-PEG additive. This, in turn, corresponds to a significant reduction of the energy barrier of crystal nucleation (K_g) in POM_C/HAp-g-PEG composites. Knowing the value of K_g and transforming the relationship in Equation (9), the amount of free energy was determined from the fold surface free energy of crystallites (σ_e). To determine the value of σ_e , the presence of the III crystallization regime was assumed in the materials tested, therefore the value of the parameter $n = 4$ was assumed. The determined K_g and σ_e values are summarized in Table 5.

Both values decreased with an increase in the HAp-g-PEG content and with an increase in the average molar mass of PEG in the addition of HAp-g-PEG. The process of forming polymer crystals on the surface of alien inclusions (in this case, HAp-g-PEG) requires less energy input than for the production of a sufficiently large homogeneous nucleus from the

polymer chain, from which the crystal could be formed. Consequently, as the content of HAp-g-PEG increases, the material’s surface, on which nucleation and formation of polymer crystals can occur, increases [46].

The last calculated parameter was the thickness of the lamella formed during crystallization L [nm], which was determined from the Gibbs-Thomson Equation (12) at 153 °C – Table 5.

$$T_m = T_m^0 \left(1 - \frac{2\sigma_e}{\Delta h_0 L} \right) \quad (12)$$

where T_m – the melting point of POM after isothermal crystallization at 153 °C, T_m^0 – equilibrium melting point, Δh_0 – thermodynamic enthalpy of change per unit volume of the crystalline phase, σ_e – is the fold surface free energy of the lamellae, related to the crystallization process.

For pure POM_C, the average thickness of the formed lamellae was about 10.2 nm. The addition of HAp-g-PEG influenced the average value of the thickness of the lamellas by reducing it. The largest decrease was recorded for the POM_C/5.0% HAp-g-PEG 600 sample. The thickness of the lamellae depended on the equilibrium value of the melting point and the fold surface free energy of the lamellae formed, and it decreased as both values decreased. In the next stage of the investigation, selected samples based on POM_C were melted and then placed at a temperature of 153 °C in order to carry out slow crystallization. The surface of the tested samples was observed using the SEM and AFM microscopic techniques to verify the resulting POM_C crystal structures. The results of the observations are presented in Figure 11.

The observations show that POM_C, both in its pure form and as a matrix for composites, crystallized in the form of spherulites, which, in contact with each other, filled the entire surface of the sample. This

Table 5. K_g , T_m^0 , σ_e and L determined for POM_C and POM_C composites with 1.0 and 5.0% HAp-g-PEG 600, HAp-g-PEG 2000 and HAp-g-PEG 6000.

Sample	$K_g \cdot 10^5$ [K ²]	T_m^0 [K]	σ_e [J/m ²]	L at 153 °C [nm]
POM_C	2.24	463	0.0866	10.2
POM_C/1.0% HAp-g-PEG 600	1.28	455	0.0503	9.3
POM_C/5.0% HAp-g-PEG 600	0.88	452	0.0350	8.6
POM_C/1.0% HAp-g-PEG 2000	1.27	455	0.0495	9.3
POM_C/5.0% HAp-g-PEG 2000	1.14	453	0.0451	9.9
POM_C/1.0% HAp-g-PEG 6000	1.05	453	0.0415	9.1
POM_C/5.0% HAp-g-PEG 6000	0.84	451	0.0334	9.5

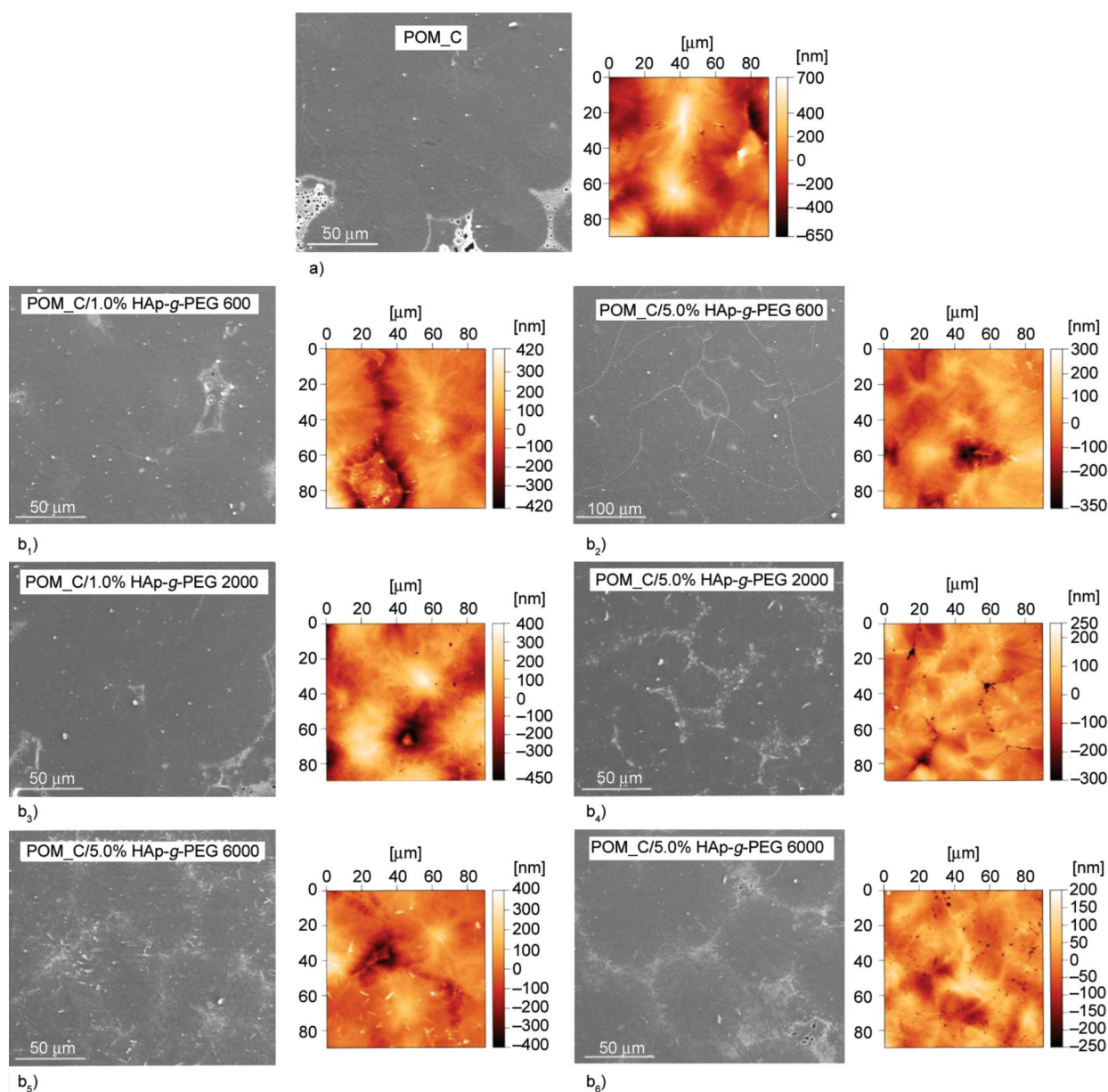


Figure 11. SEM and AFM images of a) POM_C surfaces and b) POM_C composites with 1.0 and 5.0% HAp-g-PEG, b₁) POM_C/1.0% HAp-g-PEG 600, b₂) POM_C/5.0% HAp-g-PEG 600, b₃) POM_C/1.0% HAp-g-PEG 2000, b₄) POM_C/1.0% HAp-g-PEG 2000, b₅) POM_C/1.0% HAp-g-PEG 6000, b₆) POM_C/1.0% HAp-g-PEG 6000.

result is consistent with the results of kinetic calculations, where the value of the Avrami exponent indicated just such a crystalline form of POM_C. With the 1.0% HAp-g-PEG addition, the size and shape of the spherulites are similar to those of the unmodified POM_C. On the other hand, for an increased amount of additive (5.0%), the spherulites are reduced and distorted; it is much more difficult to distinguish the boundaries between them. The increased amount of HAp-g-PEG addition may hinder the formation of POM_C three-dimensional crystal structures, which was also confirmed in the crystallization kinetics studies, where the Avrami exponent decreased with an increase in the HAp-g-PEG content.

Then, DMA tests were carried out for POM_C and selected composite samples in order to determine the glass transition temperature. The results of the DMA tests are presented in Figure 12 and Table 6.

For unmodified POM_C and all composite samples, the course of the mechanical loss coefficient ($\tan\delta$) in the function of temperature shows three peaks corresponding to the three relaxations occurring in POM. For unmodified POM_C, the temperature values corresponding to relaxation effects are -60.6°C (γ), -3.3°C (β), and 115.7°C (α), and are similar to the values reported in the literature [47]. Some differences in these temperatures may result, among others, from the oscillation frequency values that were

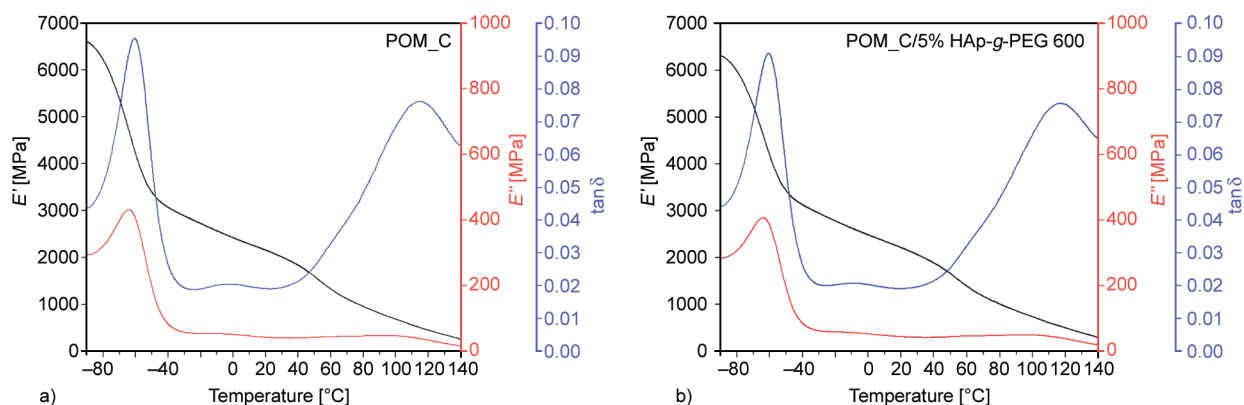


Figure 12. Dependence of the storage modulus E' , loss modulus E'' and $\tan \delta$ vs. temperature for POM_C (a) and POM_C composites with and 5.0% HAp-g-PEG 600 (b).

Table 6. Relaxation temperatures of POM_C and POM_C composites with 1.0 and 5.0% HAp-g-PEG 600, HAp-g-PEG 2000 and HAp-g-PEG 6000.

Sample	γ [°C]	β [°C]	α [°C]
POM_C	-60	-3	116
POM_C/1.0% HAp-g-PEG 600	-61	-5	117
POM_C/5.0% HAp-g-PEG 600	-61	-9	117
POM_C/1.0% HAp-g-PEG 2000	-60	-7	116
POM_C/5.0% HAp-g-PEG 2000	-60	-6	118
POM_C/1.0% HAp-g-PEG 6000	-61	-6	116
POM_C/5.0% HAp-g-PEG 6000	-61	-3	118

used during the DMA measurements [48]. The first relaxation, γ , is generally considered as the POM glass transition temperature, related to local movements of the POM segments forming amorphous areas [49].

Based on the obtained thermomechanical results, it has been found that the addition of HAp-g-PEG did not have a significant effect on the glass transition temperature (T_g for the γ transformation) of POM_C. A slightly greater effect was observed for the remaining POM_C relaxations, where the addition of the hybrid filler caused a slight decrease of the β relaxation temperature in the crystalline phase by a maximum of 5.4 °C and a slight increase in the α relaxation temperature – also in the amorphous phase, increasing its value by a maximum of 2.3 °C. The addition of HAp-g-PEG decreased the value of the mechanical loss coefficient ($\tan \delta$), which indicates a weaker ability to dampen vibrations in the tested composites compared to the unmodified POM_C. Moreover, the storage modulus (E'), representing the values of energy storage and return during successive deformation cycles, decreased with increasing temperature for all analyzed samples. This effect is

associated with an increase in the mobility of the polymer chain segments with increasing temperature [50]. At -90 °C, for POM_C, the storage modulus reaches a maximum value of 6593 MPa. With increasing temperature, there is a sharp decrease in the E' value, down to 3392 MPa (at -50 °C), associated with the transition of the polymer from the glassy state, where the polymer is hard and brittle, to the elastic state. With an increase in temperature, a further, less rapid decrease of the storage modulus E' to 1730 MPa (at 45 °C) was recorded, followed by another decrease in E' due to the relaxation of the crystalline phase. This transformation (called T_{cc}) takes place in some semicrystalline polymers and is associated with the appearance of limited movements of the polymer chain segments within the folded crystals. It is accompanied by a decrease in the value of the E' , which occurs before the polymer melting process [51]. Samples containing the addition of HAp-g-PEG have a slightly lower storage modulus than pure POM_C, which indicates a slight decrease in the stiffness of the tested composites, but the shape of the E' curves remains similar to pure POM_C. The last parameter measured in DMA is the loss modulus (E''), which reaches its maximum at the glass transition temperature of the polymer [52]. For pure POM_C, the maximum value of E'' is 432 MPa (at -64.3 °C). The maximum temperature E'' is lower than the maximum temperature read from the maximum $\tan \delta$, which is also a characteristic phenomenon in DMA measurements for polymers. For composite materials, the maximum value of the loss modulus reflecting the amount of energy dissipated by the material during deformation was lower than for pure POM_C. The E'' value for POM_C/5.0% HAp-g-PEG 2000 decreased the most

by as much as 15%. As it can be seen for this sample, the highest relaxation/glass transition temperatures have been found that suggest the stiffest material with the lowest ability for vibration damping. In summary, POM_C and its composites were characterized by viscoelastic properties, as evidenced by the presence of the $E' \neq 0$ component and the $E'' \neq 0$ component. All of the tested materials were characterized by the presence of three relaxations occurring during material heating related to the relaxation of both the crystalline and amorphous phases. The addition of HAp-g-PEG did not significantly affect the T_g temperature value, which, according to the literature data for POM_C, ranges from -65 to -60 °C [53].

4. Conclusions

In the presented work, the influence of the chemical composition of the hybrid inorganic-organic HAp-based additive (HAp-g-PEG) on selected properties of POM composites was investigated. Among all the diisocyanates tested (HDI, MDI, HMDI, and IPDI), HDI turned out to be the most reactive. It was observed that the average molecular weight of PEG had a much smaller influence on the course of the grafting process, although the best results were obtained for the shortest chains (PEG 600) due to the highest concentration of their hydroxyl groups. On the basis of the obtained results, for further research, the HAp-HDI-PEG 600, HAp-HDI-PEG 2000, and HAp-HDI-PEG 6000 hybrid systems were selected, which were introduced into the polyoxymethylene matrix, both POM_C and POM_H, in an amount from 0.5 to 10.0 wt% based on the content of pure HAp. TEM confirmed the uniform distribution of HAp-g-PEG hybrid additives, even with a large amount of additive. DSC tests did not show any significant effect on the key processing parameters, *i.e.*, melting point and supercooling, which allows the processing parameters to be maintained for all samples.

FTIR-ATR analysis confirmed the complexity of the crystal forms formed in POM_C crystallization from the melt. This study did not show any changes in the POM crystallization method under the influence of the additives used.

The study of the crystallization kinetics showed a three-dimensional process of POM crystals' growth in the form of spherulites. The addition of HAp-g-PEG in POM_C significantly accelerated the

crystallization process. The results of the microstructure analysis of POM_C and its composites using SEM and AFM methods confirmed the three-dimensional crystallization of POM_C chains in the form of spherulites. DMA method allowed for the determination of the POM_C glass transition temperature in the tested composites. Noteworthy, no significant influence of each of the additives used, regardless of its type and amount, on the glass transition temperature was observed.

Acknowledgements

The authors are grateful to the Polish National Science Centre for financial support under the Contract No. UMO-2016/21/B/ST8/00449. This work was also supported from the subsidy of the Ministry of Education and Science for the AGH University of Science and Technology in Kraków (Project No 16.16.160.557).

References

- [1] Masamoto J., Iwaisako T., Chohnno M., Kawamura M., Ohtake J., Matsuzaki K.: Development of a new advanced process for manufacturing polyacetal resins. Part I. Development of a new process for manufacturing highly concentrated aqueous formaldehyde solution by methylal oxidation. *Journal of Applied Polymer Science*, **50**, 1299–1305 (1993).
<https://doi.org/10.1002/app.1993.070500801>
- [2] Lüftl S., Visakh P. M., Chandran S.: *Polyoxymethylene handbook: Structure, properties, applications and their nanocomposites*. Wiley, Hoboken (2014).
- [3] Pielichowska K.: Polyacetal. in 'Handbook of thermoplastics' (eds.: Olabisi O., Adewale K.) CRC Press, Boca Raton (2015).
- [4] Tashiro K.: Crystal structure and crystallization behavior of pom and its microscopically-viewed relation with the physical and thermal properties on the basis of X-ray scattering, vibrational spectroscopy and lattice dynamical theory. in 'Polyoxymethylene handbook: Structure, properties, applications and their nanocomposites' (eds.: Lüftl S., Visakh P. M., Chandran S.) Wiley, Hoboken, 193–226 (2014).
<https://doi.org/10.1002/9781118914458.ch7>
- [5] Raimo M.: Impact of thermal properties on crystalline structure, polymorphism and morphology of polymer matrices in composites. *Materials*, **14**, 2136 (2021).
<https://doi.org/10.3390/ma14092136>
- [6] Raimo M.: Structure and morphology of polyoxymethylene. in 'Polyoxymethylene handbook: Structure, properties, applications and their nanocomposites' (eds.: Lüftl S., Visakh P. M., Chandran S.) Wiley, Hoboken, 163–191 (2014).
<https://doi.org/10.1002/9781118914458.ch6>

- [7] Hama H., Tashiro K.: Structural changes in non-isothermal crystallization process of melt-cooled polyoxymethylene[II] evolution of lamellar stacking structure derived from SAXS and WAXS data analysis. *Polymer*, **44**, 2159–2168 (2003).
[https://doi.org/10.1016/S0032-3861\(03\)00093-4](https://doi.org/10.1016/S0032-3861(03)00093-4)
- [8] Hama H., Tashiro K.: Structural changes in non-isothermal crystallization process of melt-cooled polyoxymethylene. [I] Detection of infrared bands characteristic of folded and extended chain crystal morphologies and extraction of a lamellar stacking model. *Polymer*, **44**, 3107–3116 (2003).
[https://doi.org/10.1016/S0032-3861\(03\)00207-6](https://doi.org/10.1016/S0032-3861(03)00207-6)
- [9] Tashiro K.: Recognition of high sensitivity of vibrational spectroscopy in study of higher-order structure of polymers. *J-Stage*, **58**, 253–261 (2002).
<https://doi.org/10.2115/fiber.58.253>
- [10] Pielichowska K.: Polyoxymethylene processing. in ‘Polyoxymethylene handbook: Structure, properties, applications and their nanocomposites’ (eds.: Lüfl S., Visakh P. M., Chandran S.) Wiley, Hoboken, 107–151 (2014).
<https://doi.org/10.1002/9781118914458.ch4>
- [11] Zeng Y., Liu Y., Wang L., Huang H., Zhang X., Liu Y., Min M., Li Y.: Effect of silver nanoparticles on the microstructure, non-isothermal crystallization behavior and antibacterial activity of polyoxymethylene. *Polymers* **12**, 424 (2020).
<https://doi.org/10.3390/polym12020424>
- [12] Slouf M., Krejčíková S., Vacková T., Kratochvíl J., Novák L.: *In situ* observation of nucleated polymer crystallization in polyoxymethylene sandwich composites. *Frontiers in Materials*, **2**, 23 (2015).
<https://doi.org/10.3389/fmats.2015.00023>
- [13] de Souza Santos C. L., Dias M. L., da Silva M. H. P.: Polyoxymethylene/graphene nanocomposites: Thermal, crystallization, melting and rheological behavior. *Journal of Composite Materials*, **55**, 1485–1498 (2020).
<https://doi.org/10.1177/0021998320972179>
- [14] Jiao Q., Chen Q., Wang L., Chen H., Li Y.: Investigation on the crystallization behaviors of polyoxymethylene with a small amount of ionic liquid. *Nanomaterials*, **9**, 206 (2019).
<https://doi.org/10.3390/nano9020206>
- [15] Navarro-Baena I., Arrieta M. P., Mujica-García A., Sessini V., Lopez D., Kenny J. M., Peponi L.: Thermal degradation effects on polyurethanes and their nanocomposites. in ‘Reactions and mechanisms in thermal analysis of advanced materials’ (eds.: Tiwari A., Raj B.) Wiley, Hoboken, 165–189 (2015).
- [16] Chattopadhyay D. K., Webster D. C.: Thermal stability and flame retardancy of polyurethanes. *Progress in Polymer Science*, **34**, 1068–1133 (2009).
<https://doi.org/10.1016/j.progpolymsci.2009.06.002>
- [17] Lee S. C., Choi H. W., Lee H. J., Kim K. J., Chang J. H., Kim S. Y., Choi J., Oh K.-S., Jeong Y.-K.: *In-situ* synthesis of reactive hydroxyapatite nano-crystals for a novel approach of surface grafting polymerization. *Journal of Materials Chemistry*, **17**, 174–180 (2007).
<https://doi.org/10.1039/B611401F>
- [18] Edwin N., Saranya S., Wilson P.: Strontium incorporated hydroxyapatite/hydrothermally reduced graphene oxide nanocomposite as a cytocompatible material. *Ceramics International*, **45**, 5475–5485 (2019).
<https://doi.org/10.1016/j.ceramint.2018.12.002>
- [19] Malakooti S., Rostami S., Churu H. G., Luo H., Clark J., Casarez F., Rettenmaier O., Daryadel S., Minary-Jolandan M., Sotiriou-Leventis C., Leventis N., Lu H.: Scalable, hydrophobic and highly-stretchable poly(isocyanurate-urethane) aerogels. *RSC Advances*, **8**, 21214–21223 (2018).
<https://doi.org/10.1039/C8RA03085E>
- [20] Mahou R., Wandrey C.: Versatile route to synthesize heterobifunctional poly(ethylene glycol) of variable functionality for subsequent PEGylation. *Polymers*, **4**, 561–589 (2012).
<https://doi.org/10.3390/polym4010561>
- [21] Dust J. M., Fang Z. H., Harris J. M.: Proton NMR characterization of poly(ethylene glycols) and derivatives. *Macromolecules*, **23**, 3742–3746 (1990).
<https://doi.org/10.1021/ma00218a0105>
- [22] Fu H., Gao H., Wu G., Wang Y., Fan Y., Ma J.: Preparation and tunable temperature sensitivity of biodegradable polyurethane nanoassemblies from diisocyanate and poly(ethylene glycol). *Soft Matter*, **7**, 3546–3552 (2011).
<https://doi.org/10.1039/C0SM01350A>
- [23] Kolmas J., Kołodziejcki W.: Inverse $^{31}\text{P} \rightarrow ^1\text{H}$ NMR cross-polarization in hydrated nanocrystalline calcium hydroxyapatite. *Chemical Physics Letters*, **554**, 128–132 (2012).
<https://doi.org/10.1016/j.cplett.2012.10.025>
- [24] Pielichowska K.: The influence of molecular weight on the properties of polyacetal/hydroxyapatite nanocomposites. Part 1. Microstructural analysis and phase transition studies. *Journal of Polymer Research*, **19**, 9775 (2012).
<https://doi.org/10.1007/s10965-011-9775-3>
- [25] Pielichowska K., Szczygielska A., Spasówka E.: Preparation and characterization of polyoxymethylene-copolymer/hydroxyapatite nanocomposites for long-term bone implants. *Polymers for Advanced Technologies*, **23**, 1141–1150 (2012).
<https://doi.org/10.1002/pat.2012>
- [26] Król-Morkisz K., Karaś E., Majka T. M., Pielichowski K., Pielichowska K.: Thermal stabilization of polyoxymethylene by PEG-functionalized hydroxyapatite: Examining the effects of reduced formaldehyde release and enhanced bioactivity. *Advances in Polymer Technology*, **2019**, 9728637 (2019).
<https://doi.org/10.1155/2019/9728637>

- [27] Król-Morkisz K., Pielichowska K.: Thermal decomposition of polymer nanocomposites with functionalized nanoparticles. in 'Polymer composites with functionalized nanoparticles' (eds.: Pielichowski K., Majka T. M.) Elsevier, Amsterdam 405–435 (2019).
<https://doi.org/10.1016/B978-0-12-814064-2.00013-5>
- [28] Pielichowski K., Flejtuch K.: Differential scanning calorimetry studies on poly(ethylene glycol) with different molecular weights for thermal energy storage materials. *Polymers for Advanced Technologies*, **13**, 690–696 (2002).
<https://doi.org/10.1002/pat.276>
- [29] Pielichowska K., Bieda J., Szatkowski P.: Polyurethane/graphite nano-platelet composites for thermal energy storage. *Renewable Energy*, **91**, 456–465 (2016).
<https://doi.org/10.1016/j.renene.2016.01.076>
- [30] Król-Morkisz K., Karaś E., Majka T. M., Pielichowski K., Pielichowska K.: Thermal stabilization of polyoxymethylene by PEG-functionalized hydroxyapatite: Examining the effects of reduced formaldehyde release and enhanced bioactivity. *Advances in Polymer Technology*, **2019**, 9728637 (2019).
<https://doi.org/10.1155/2019/9728637>
- [31] Rahman M. S., Shaislamov U., Yang J-K., Kim J-K., Yu Y. H., Choi S., Lee H-J.: Effects of electron beam irradiation on tribological and physico-chemical properties of polyoxymethylene copolymer (POM-C). *Nuclear Instruments and Methods in Physics Research Section B: Beam Interactions with Materials and Atoms*, **387**, 54–62 (2016).
<https://doi.org/10.1016/j.nimb.2016.10.001>
- [32] Li Y., Zhou T., Chen Z., Hui J., Li L., Zhang A.: Non-isothermal crystallization process of polyoxymethylene studied by two-dimensional correlation infrared spectroscopy. *Polymer*, **52**, 2059–2069 (2011).
<https://doi.org/10.1016/j.polymer.2011.03.007>
- [33] Kurosu H., Komoto T., Ando I.: ¹³C NMR chemical shift and crystal structure of polyoxymethylene in the solid state. *Journal of Molecular Structure*, **176**, 279–283 (1988).
[https://doi.org/10.1016/0022-2860\(88\)80247-3](https://doi.org/10.1016/0022-2860(88)80247-3)
- [34] Matsumoto A., Egawa Y., Matsumoto T., Horii F.: Miscibility of polyoxymethylene blends as revealed by high-resolution solid-state ¹³C-NMR spectroscopy. *Polymers for Advanced Technologies*, **8**, 250–256 (1997).
[https://doi.org/10.1002/\(SICI\)1099-1581\(199704\)8:4<250::AID-PAT636>3.0.CO;2-9](https://doi.org/10.1002/(SICI)1099-1581(199704)8:4<250::AID-PAT636>3.0.CO;2-9)
- [35] Gupta S., Yuan X., Chung T. C. M., Cakmak M., Weiss R. A.: Isothermal and non-isothermal crystallization kinetics of hydroxyl-functionalized polypropylene. *Polymer*, **55**, 924–935 (2014).
<https://doi.org/10.1016/j.polymer.2013.12.063>
- [36] Avrami M.: Kinetics of phase change. I General theory. *The Journal of Chemical Physics*, **7**, 1103–1112 (1939).
<https://doi.org/10.1063/1.1750380>
- [37] Xu W-B., He P-S.: Crystallization characteristics of polyoxymethylene with attapulgite as nucleating agent. *Polymer Engineering and Science*, **41**, 1903–1912 (2001).
<https://doi.org/10.1002/pen.10887>
- [38] Mandelkern L.: *Crystallization of polymers: Kinetics and mechanisms*. Cambridge University Press, Cambridge (2004).
- [39] Gedde U. W., Hedenqvist M. S.: *Fundamental polymer science*. Springer, Cham (2019).
- [40] Xu W., He P.: Isothermal crystallization behavior of polyoxymethylene with and without nucleating agents. *Journal of Applied Polymer Science*, **80**, 304–310 (2001).
[https://doi.org/10.1002/1097-4628\(20010411\)80:2<304::AID-APP1100>3.0.CO;2-N](https://doi.org/10.1002/1097-4628(20010411)80:2<304::AID-APP1100>3.0.CO;2-N)
- [41] Wu T-M., Chen E-C.: Crystallization behavior of poly(ε-caprolactone)/multiwalled carbon nanotube composites. *Journal of Polymer Science Part B: Polymer Physics*, **44**, 598–606 (2006).
<https://doi.org/10.1002/polb.20722>
- [42] Pracella M., Chionna D., Anguillesi I., Kulinski Z., Piorkowska E.: Functionalization, compatibilization and properties of polypropylene composites with hemp fibres. *Composites Science and Technology*, **66**, 2218–2230 (2006).
<https://doi.org/10.1016/j.compscitech.2005.12.006>
- [43] Plans J., MacKnight W. J., Karasz F. E.: Equilibrium melting point depression for blends of isotactic polystyrene with poly(2,6-dimethylphenylene oxide). *Macromolecules*, **17**, 810–814 (1984).
<https://doi.org/10.1021/ma00134a048>
- [44] Lee J. H., Park S. H., Kim S. H., Ito H.: Replication and surface properties of micro injection molded PLA/MWCNT nanocomposites. *Polymer Testing*, **83**, 106321 (2020).
<https://doi.org/10.1016/j.polymertesting.2019.106321>
- [45] Hoffman J. D.: Regime III crystallization in melt-crystallized polymers: The variable cluster model of chain folding. *Polymer*, **24**, 3–26 (1983).
[https://doi.org/10.1016/0032-3861\(83\)90074-5](https://doi.org/10.1016/0032-3861(83)90074-5)
- [46] Li J., Fang Z., Zhu Y., Tong L., Gu A., Liu F.: Isothermal crystallization kinetics and melting behavior of multiwalled carbon nanotubes/polyamide-6 composites. *Journal of Applied Polymer Science*, **105**, 3531–3542 (2007).
<https://doi.org/10.1002/app.24606>
- [47] Psarras G. C., Siengchin S., Karahaliou P. K., Georga S. N., Krontiras C. A., Karger-Kocsis J.: Dielectric relaxation phenomena and dynamics in polyoxymethylene/polyurethane/alumina hybrid nanocomposites. *Polymer International*, **60**, 1715–1721 (2011).
<https://doi.org/10.1002/pi.3136>

- [48] Keating M. Y., Sauer B. B., Flexman E. A.: Dynamic mechanical characterization of relaxations in poly(oxy-methylene), miscible blends, and oriented filaments. *Journal of Macromolecular Science Part B*, **36**, 717–732 (1997).
<https://doi.org/10.1080/00222349708212398>
- [49] Karahaliou P. K., Kerasidou A. P., Georga S. N., Psarras G. C., Krontiras C. A., Karger-Kocsis J.: Dielectric relaxations in polyoxymethylene and in related nanocomposites: Identification and molecular dynamics. *Polymer*, **55**, 6819–6826 (2014).
<https://doi.org/10.1016/j.polymer.2014.10.056>
- [50] Yang W., Wang X-L., Yan X., Guo Z.: Toughened polyoxymethylene by polyolefin elastomer and glycidyl methacrylate grafted high-density polyethylene. *Polymer Engineering & Science*, **57**, 1119–1126 (2017).
<https://doi.org/10.1002/pen.24489>
- [51] van Krevelen D. W., te Nijenhuis K.: Properties of polymers: Their correlation with chemical structure; Their numerical estimation and prediction from additive group contributions. Elsevier, Amsterdam (2009).
- [52] Matsuoka S.: Thermodynamic theory of viscoelasticity. *Journal of Thermal Analysis*, **46**, 985–1010 (1996).
<https://doi.org/10.1007/BF01983616>
- [53] Archodoulaki V-M., Lüftl S.: Thermal properties and flammability of polyoxymethylene. in ‘Polyoxymethylene handbook: Structure, properties, applications and their nanocomposites’ (eds.: Lüftl S., Visakh P. M., Chandran S.) Wiley, Hoboken, 257–275 (2014).
<https://doi.org/10.1002/9781118914458.ch10>

Research article

Effect of waste zinc oxide particles on properties of natural rubber vulcanizates

Dusadee Tumnantong^{1,2}, Pattarapan Prasassarakich^{1,2,3}, Sirilux Poompradub^{1,2,3*}

¹Department of Chemical Technology, Faculty of Science, Chulalongkorn University, 10330 Bangkok, Thailand

²Center of Excellence in Green Materials for Industrial Application, Faculty of Science, Chulalongkorn University, 10330 Bangkok, Thailand

³Center of Excellence on Petrochemical and Materials Technology, Chulalongkorn University, 10330 Bangkok, Thailand

Received 21 July 2022; accepted in revised form 30 September 2022

Abstract. Natural rubber (NR) vulcanizates with waste zinc oxide (ZnO) particles were prepared through a sulfur vulcanization process. This research aimed to investigate the effect of different ZnO sources as an activator: commercial ZnO (ZO), waste ZnO obtained from a ceramic industry (WZO), and calcinated WZO (C-WZO) on the properties of NR vulcanizates. The ZnO particles were characterized using X-ray fluorescence spectrometer, X-ray diffractometer, and transmission electron microscopy. It was found that the calcination at 800 °C for 6 h could reduce the sulfur components in WZO; consequently, the particle size and appearance were changed. For rubber vulcanizates, the composition of ZnO in the activator had an effect on the crosslink density of the obtained vulcanizates, resulting in changes to the mechanical tensile, thermal, and dynamic mechanical properties. The crosslink density, tensile strength, and tear strength of the rubber vulcanizate filled with C-WZO (NR/C-WZO (II), 0.18 mmol/cm³, 21.3 MPa, 68.4 N/mm, respectively) was acceptable for rubber products compared with those of the vulcanizate filled with ZO (NR/ZO, 0.19 mmol/cm³, 26.4 MPa, 71.6 N/mm, respectively). Accordingly, C-WZO could be used as an effective activator in rubber vulcanization.

Keywords: rubber, zinc oxide, vulcanization, mechanical properties, thermal properties

1. Introduction

Natural rubber (NR) is widely used as a polymeric material in various applications such as tires, medical devices, footwear, sports accessories, rubberized coil forms, road rubberization, and so on, because of its unique elasticity and mechanical properties [1, 2]. For practical applications, the raw rubber materials are generally mixed with chemicals and subjected to vulcanization via sulfur or peroxide crosslinking [3]. The long-chain molecules of rubber become chemically joined (cross-linked) to form three-dimensional structures at various points along the chain, which then provide enhanced mechanical properties [4]. In the case of peroxide vulcanization, the mechanical properties of rubber vulcanizates are inferior compared to

sulfur vulcanization [5]. The vulcanization of NR with sulfur, originally discovered by Goodyear in 1839, forms sulfur linkages (mono-, di-, and polysulfide bridges) between the polymer chains [6]. Rubber vulcanization in a sulfur system generally uses an accelerator, activator, and co-activator to improve the vulcanization rate and cross-linking efficiency. In the rubber industry, zinc oxide (ZnO) is the most efficient activator for sulfur vulcanization and can reduce the vulcanization time of rubber compounds and enhance the properties of vulcanizates. Therefore, ZnO plays an important role in the transformation of rubber vulcanization [7, 8].

There has not been much research on the effect of ZnO on rubber vulcanization in terms of synthesis,

*Corresponding author, e-mail: sirilux.p@chula.ac.th

© BME-PT

properties, and compounding applications. Recently, short prism-like ZnO particles synthesized by a hydrothermal method were compounded with NR latex at different contents to prepare vulcanized NR films that exhibited high mechanical properties [9]. Similarly, the octylamine-capped ZnO nanoparticles with a 5 nm diameter were used in vulcanization to give a high curing efficiency and enhanced mechanical performances of the NR because this structure could improve the ZnO dispersion in the rubber matrix [10]. Active ZnO (3 parts per hundred of rubber [phr]) and nano ZnO (1.5 phr) presented excellent properties for rubber compounds filled with carbon black, which allowed for reduced ZnO usage in forming an elastomeric rubber [11]. For rubber film preparation, ZnO modified with calcium carbonate (CaCO_3) at a 9:1 (w/w) ratio effectively activated the NR crosslinking and improved the anti-microbial properties of the rubber products [12]. For styrene-butadiene rubber (SBR) vulcanizates, ZnO nanoparticles (rod-like particles) [13] and rod-like ZnO with different crystal facets [14] were found to give a better vulcanization activity and a good performance with a high crosslink density and a large reduction in the polysulfide crosslinking. In addition, the nanosized ZnO cooperated with ionic liquids [15], while the ZnO nanoparticles prepared by a sol-gel process [16] could reduce the vulcanization time, increase the degree of rubber crosslinking, and improve the tensile properties of the SBR and polyisoprene vulcanizates, respectively. In contrast, ZnO coated on a nano- CaCO_3 surface [17], and ZnO dispersed in CaCO_3 [18], effectively activated the vulcanization of tire tread compound and ethylene, propylene, and diene monomer elastomer, respectively. For SBR/polybutadiene rubber blends, polyethylene glycol-coated ZnO nanoparticles with a rod-like structure (3 phr) helped to increase the tensile strength of the vulcanizates [19]. These results indicated the importance of investigating the source of ZnO particles in the sulfur vulcanization of rubber.

The ceramic industry has many waste materials during the process [20, 21], so the reuse of ceramic waste has been widely studied in many applications. In ceramic manufacturing, ZnO as glaze coating [22] can ensure crystallization [23], improve the glaze surface properties of floor tiles [24], reduce the coefficient of thermal expansion [25], affect the melting point of the glaze [26], etc. would be one type of ceramic waste. From these mentioned superior properties, the

ZnO from ceramic waste is an attractive chemical to substitute for the ZnO as an activator in the vulcanization process. The present work focused on the vulcanization of NR compounds using three different types of ZnO particles as activators, *i.e.*, commercial ZnO (ZO), waste ZnO (WZO) obtained from a ceramic glaze industry, and calcined WZO (C-WZO). To obtain the C-WZO, the WZO was first treated via calcination at 800 °C for 6 h. The physical, thermal, and dynamic mechanical properties of NR vulcanized with the different ZnO types were elucidated.

2. Experimental

2.1. Materials

The NR (STR 5L or Standard Thai Rubber 5L) and curing reagents for rubber compounds: ZO, stearic acid, *n*-cyclohexyl-2-benzothiazole sulfenamide (CBS), and sulfur, were supplied from the Rubber Research Institute of Thailand. The WZO was obtained from a ceramic glaze industry (Siam Frit Co., Ltd., Samutsakhon, Thailand) and then calcined at 800 °C for 6 h to obtain the C-WZO.

2.2. Preparation of NR vulcanizates

The formulations of the rubber compounds are listed in Table 1. The common rubber compound formula I was filled with 5 phr of ZnO powder and 2.5 phr of sulfur. For the adjusted rubber compound formula II, the actual sulfur content obtained from the ZnO sample and added sulfur was adjusted to be a total of 5 phr. All ingredients were mixed in a two-roll mill at room temperature for 9 min to form NR compounds. Measurement of Mooney viscosity (ML 1+4 at 100 °C) was carried out using Premier™ MV Mooney Viscometer (Alpha Technologies, USA) according to ISO 289-1: 2015. The cure characteristics were determined using a moving die rheometer (MDR, TechPro MD+, USA) at 155 °C following ASTM D5289-19. Optimum cure time (t_{c90}), scorch time (t_{s2}), minimum torque (M_L), maximum torque (M_H) and torque difference ($M_H - M_L$) are presented in Table 1. The sample sheets with dimensions of 150×150×2 mm were prepared at 155 °C and 150 kg/m² for 10 min using a compression mold (Scientific LabTech Engineering Co., Ltd., Thailand).

The NR vulcanized samples with ZO, WZO, and C-WZO were denoted as NR/ZO, NR/WZO, and NR/C-WZO, respectively.

Table 1. Formulation of NR compounds in parts per hundred of rubber [phr] and vulcanization parameters.

Sample code	NR/ZO	NR/WZO (I)	NR/WZO (II)	NR/C-WZO (I)	NR/C-WZO (II)
Chemicals					
NR	100.00	100.00	100.00	100.00	100.00
ZO	5.00	0.00	0.00	0.00	0.00
WZO	0.00	5.00	5.58 ^a	0.00	0.00
C-WZO	0.00	0.00	0.00	5.00	5.14 ^a
Stearic acid	2.00	2.00	2.00	2.00	2.00
CBS	0.60	0.60	0.60	0.60	0.60
Sulfur	2.50	2.50	1.92 ^b	2.50	2.36 ^b
Cure characteristics					
ML (1+4) at 100 °C	27.0	31.0	30.8	29.5	28.9
t_{c90} [min]	8.72	7.76	7.95	8.53	8.65
t_{s2} [min]	5.34	5.79	5.73	5.67	5.55
M_L [dN·m]	0.43	0.43	0.54	0.43	0.53
M_H [dN·m]	5.62	4.70	4.99	5.12	5.43
$M_H - M_L$ [dN·m]	5.19	4.27	4.45	4.69	4.90

^athe adjusted WZO or C-WZO and^bthe adjusted sulfur to make the actual sulfur (2.5 phr)

2.3. Characterization of ZnO

Thermogravimetric analysis (TGA) of the ZO, WZO, and C-WZO was performed using a thermal analysis instrument (Perkin-Elmer Pyris Diamond, USA). The sample (10 mg) was placed on a platinum pan and heated from room temperature to 1000 °C at a constant heating rate of 10 °C/min under nitrogen (N₂) at a flow rate of 50 ml/min. The TGA result was used to find the suitable temperature for WZO calcination.

The X-ray diffraction (XRD) analysis of the different types of ZnO was performed on a Bruker D8 Advance X-ray diffractometer (USA) with CuK_α radiation ($\lambda = 1.54 \text{ \AA}$). The X-ray source was operated at 40 kV and 40 mA with a scanning rate of 5–80°, changing at 0.1°/s. The elemental composition was evaluated using wavelength dispersive X-ray fluorescence spectrometry (WDXRF, JEOL Bruker S8 TIGER, USA).

The N₂ adsorption-desorption isotherms of different ZnO samples were measured using a Micromeritics ASAP-2020 surface area and porosity analyzer (USA). The sample (0.15 g) was degassed at 120 °C for 2 h under an N₂ atmosphere to remove the adsorbed moisture. The specific surface area of the samples was evaluated using the Brunauer–Emmett–Teller (BET) method. Theoretical particle size can be determined from the adsorption data and calculated according to Equation (1) [27]:

$$D = \frac{6}{S_{sp} \cdot \rho_a} \quad (1)$$

where D is the theoretical particle diameter [μm], S_{sp} is the specific surface area per unit mass, and ρ_a is the theoretical density of the solid material.

The morphology of ZnO particles was examined using scanning electron microscopy (SEM, JSM-6480LV, Japan) at an acceleration voltage of 15 kV. The samples were first sputter-coated with gold. The morphology of ZnO particles was also obtained using transmission electron microscopy (TEM, JEOL JEM-1400, Japan) operated at an acceleration voltage of 80 kV. A small amount of the sample was dispersed in ethanol solution and the suspension was put on a copper grid.

2.4. Characterization of the NR vulcanizates

The swelling measurement of the NR vulcanizates was determined according to ASTM D471. The sample (10×10×2 mm) was immersed in toluene for 7 d at room temperature. The swelling ratio (Q) of the NR vulcanized samples was then calculated according to Equation (2):

$$Q = \frac{W_2 - W_1}{W_1} \quad (2)$$

where W_1 and W_2 are the weight of the vulcanizates before and after toluene immersion [g], respectively.

The volume fraction (V_r) and crosslink density (η_c) of vulcanizates were determined following Equations (3) and (4), respectively, [28, 29]:

$$V_r = \left[1 + \frac{W_2 - W_1}{W_1} \cdot \frac{\rho_r}{\rho_s} \right]^{-1} \quad (3)$$

$$\eta_c = \frac{-[\ln(1 - V_r) + V_r + \chi \cdot V_r^2]}{V_s [V_r^{1/3} - \frac{V_r}{2}]} \quad (4)$$

where ρ_r is the density of the vulcanizates, ρ_s is the density of toluene (0.862 g/cm³), V_s is the molar volume of toluene (106.4 cm³/mol), and χ is the NR-toluene interaction parameter (Flory-Huggins value, 0.39) [30].

The mechanical properties of the NR vulcanizates were evaluated using a universal testing machine (Instron 3366, USA) at a 500 mm/min cross-head speed according to ASTM D412. All samples were cut into a dumbbell-type shape. The hardness (Shore A) was measured using the Shore A hardness tester (BAREISS: model Digi test II, USA) according to ASTM D2240. Tear properties and compression set were measured using a universal testing machine (Hounsfield model UTM1T, USA) according to ASTM D624 (die C) and ASTM C165, respectively.

Initial decomposition temperature (T_{id}) and maximum decomposition temperatures (T_{max}) of the NR vulcanizates were measured using thermal analysis (Perkin-Elmer Pyris Diamond, USA). Each sample (10 mg) was placed on a platinum pan and heated from room temperature to 800 °C at a constant heating rate of 10 °C/min under N₂ gas at a flow rate of 50 mL/min.

The glass transition temperature (T_g) of the samples was measured using a dynamic mechanical analyzer (DMA, GABO MODEL: EPLEXOR QC 100, Germany). The temperature was run in the range of –100 to 100 °C at an oscillation frequency of 5 Hz and a heating rate of 2 °C/min. The storage modulus (E') and the loss tangent ($\tan \delta$) curves were observed.

3. Results and discussion

3.1. Characterization of ZnO particles

The elemental compositions of ZO, WZO, and C-WZO are presented in Table 2. The commercial ZO had no sulfur components, while the sulfur content in WZO (10.4 wt%) was almost four-fold higher than that in C-WZO (2.7 wt%), indicating that calcining at 800 °C reduced the sulfur components in WZO. Accordingly, the zinc content of the ZnO particles was decreased in the order: ZO (80.3 wt%) > C-WZO (74.9 wt%) > WZO (59.5 wt%). Moreover, these results were supported by the XRD analysis (Figure 1). For the commercial ZO, the characteristic peaks of ZnO were observed without impurity phases. The WZO diffraction peaks consisted of both zinc sulfide (ZnS) and ZnO peaks, according to powder diffraction standards of the Joint Committee on Powder Diffraction Standards (JCPDS) with cards number 36–1450 and 36–1451 [31], respectively. After the calcination of WZO, the XRD patterns presented both ZnS and ZnO peaks, but the intensity of ZnS peaks in C-WZO was lower than that in WZO. The sulfur components (ZnS) of WZO were converted to ZnO during calcination, but the conversion was not complete as it still contained some ZnS.

The TGA thermograms of ZO, WZO, and C-WZO are shown in Figure 2. For the ZO curve, the ZnO weight was 100%, with no significant change. However, the

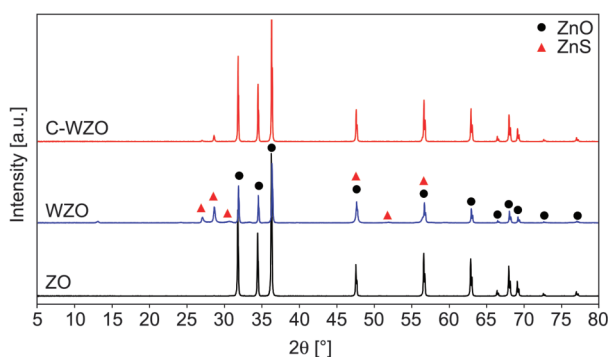


Figure 1. Representative XRD patterns of ZO, WZO, and C-WZO

Table 2. Elemental composition, specific surface area, and particle size of ZO, WZO, and C-WZO.

Sample	Element ^a [wt%]			ZnO ^a [wt%]	Multipoint BET ^b [m ² /g]	Total pore volume ^b [cm ³ /g]	Average pore diameter ^b [Å]	Average particle size ^b [nm]
	Zn	S	O					
ZO	80.3	0.0	19.7	100.0	5.33	0.0062	46.6	201
WZO	59.5	10.4	30.0	74.0	3.50	0.0040	45.3	306
C-WZO	74.9	2.7	22.4	93.3	1.93	0.0007	15.0	554

^aXRF

^bSurface area and porosity analyzer

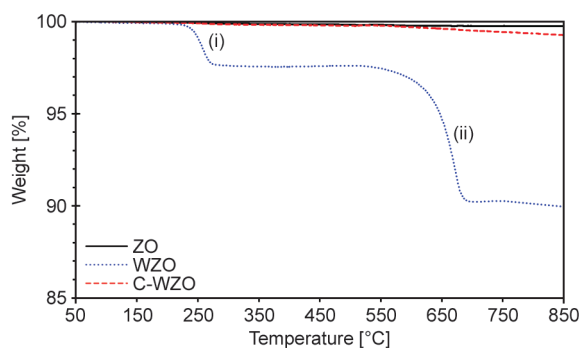
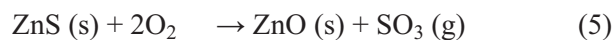


Figure 2. Representative TGA thermograms of ZO, WZO, and C-WZO.

WZO curve presented a two-step degradation with a weight loss of about 2% at 250 °C and a further 7% at 650 °C due to the decomposition of ZnS. It was clearly observed that the C-WZO weight was slightly changed, with a residual weight of 99.5% due to the small loss of light compounds. In accordance with the XRF and XRD analyses, the conversion of ZnS to ZnO proceeded by the oxidation of ZnS to ZnO, and so increasing the ZnO content in C-WZO, as shown in Equations (5) and (6):



The BET specific surface area and particle size of ZO, WZO, and C-WZO are presented in Table 2. The surface area of WZO (3.50 m²/g) was less than that of ZO (5.33 m²/g) because of contamination during the ceramic processing. For C-WZO, the surface area was decreased to 1.93 m²/g as a result of temperature-induced coalescence during calcination [32]. As mentioned above, the particle size can be calculated from the adsorption data of the surface area and porosity analyzer. The ZO, WZO, and C-WZO had an average particle size of 201, 306, and 554 nm, respectively. These particle size results were in accordance with the SEM and TEM micrographs (Figure 3). The ZO particles (Figure 3a) exhibited a small size with an average size of 200 nm, while the WZO particles (Figure 3b) were slightly larger than the ZO particles. However, C-WZO particles (Figure 3c) were much larger and agglomerated particles compared to the other ZnO samples, which was due to thermal sintering.

3.2. Characterization of NR vulcanizates

The swelling ratio and crosslink density of NR vulcanizates filled with different types of ZnO powder

and formula are presented in Table 3. For the formulation of NR compounds, the common rubber compound formula I with WZO or C-WZO and sulfur of 5 and 2.5 phr, respectively, would have the less actual ZnO and higher sulfur than 5 and 2.5 phr, respectively, due to the ZnS amount. For the adjusted rubber compound formula II, the increased WZO or C-WZO (5.58 or 5.14 phr) and decreased sulfur in NR/WZO or NR/C-WZO (1.92 or 2.36 phr) could adjust to the actual sulfur of 2.5 phr in vulcanization system.

The swelling properties related to the crosslink density and the crosslinking of the vulcanized rubber were used to explain the effect of ZnO particles on the vulcanization process. The crosslink density of NR/ZO (0.19 mmol/cm³) was higher than that of NR/C-WZO and NR/WZO due to the high ZnO purity of the ZO sample. Comparing the formula of NR vulcanizates with ZnO powder at 5 phr and sulfur at 2.5 phr, the crosslink density of NR/WZO (I) (0.11 mmol/cm³) was lower than that of NR/C-WZO (I) (0.15 mmol/cm³) due to the lower ZnO content of the NR/WZO sample. WZO and C-WZO had a ZnO content of 74.0 wt% and 93.3%, respectively, corresponding to the crosslink density of their respective vulcanizates. Subsequently, when the actual sulfur content obtained from the WZO or C-WZO and added sulfur was adjusted to be a total of 2.5 phr, the crosslink density of NR/WZO (II) (0.13 mmol/cm³) was also lower than that of NR/C-WZO (II) (0.18 mmol/cm³). These results implied that the sulfur content obtained from the ZnO sample (as ZnS) did not participate in the sulfur vulcanization process. Moreover, the crosslink density of NR/C-WZO (II) and NR/WZO (II) was higher than that of NR/C-WZO (I) and NR/WZO (I), respectively, indicating that the ZnO amount affected the crosslinking of rubber vulcanizates.

The proposed sulfur vulcanization process of the vulcanized rubber filled with different ZnO samples is shown in Figure 4 and is explained as follows. (i) The ZnO component releases zinc ions (Zn²⁺) that activate sulfur to form the chemical crosslinking of the rubber matrix in the vulcanization process. (ii) Elemental zinc and sulfur in the ZnS were in a non-active structure and did not participate in the rubber sulfur vulcanization. (iii) Sulfur in the S₈ form was suitable to initiate the sulfur crosslinks between rubber chains to create mono-, di- or polysulfide crosslinks. Therefore, the ZnO content of the

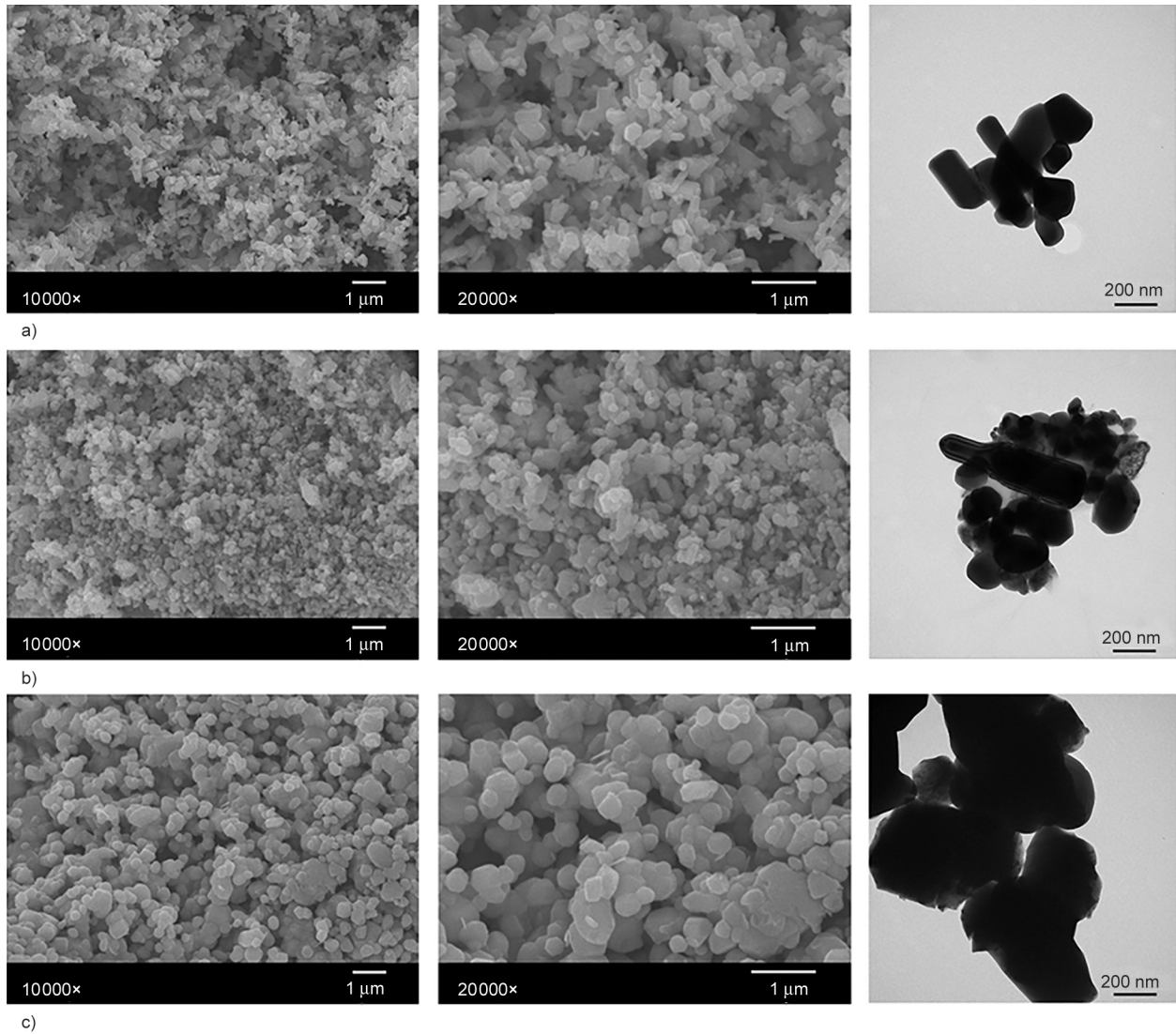


Figure 3. Representative SEM and TEM images of (a) ZO, (b) WZO, and (c) C-WZO.

Table 3. Swelling ratio and crosslink density of NR vulcanizates.

Sample	Swelling ratio [-]	Crosslink density [mmol/cm ³]
NR/ZO	3.31	0.19
NR/WZO (I)	4.52	0.11
NR/WZO (II)	4.05	0.13
NR/C-WZO (I)	3.70	0.15
NR/C-WZO (II)	3.42	0.18

ZO, WZO, and C-WZO particles was a major factor in the NR sulfur vulcanization in this research.

3.3. Physical and thermal properties of the NR vulcanizates

The mechanical properties of the NR vulcanizates are presented in Table 4. The tensile strength of NR/ZO (26.4 MPa) was higher than that of NR/C-WZO and NR/WZO. Comparing the formula of NR

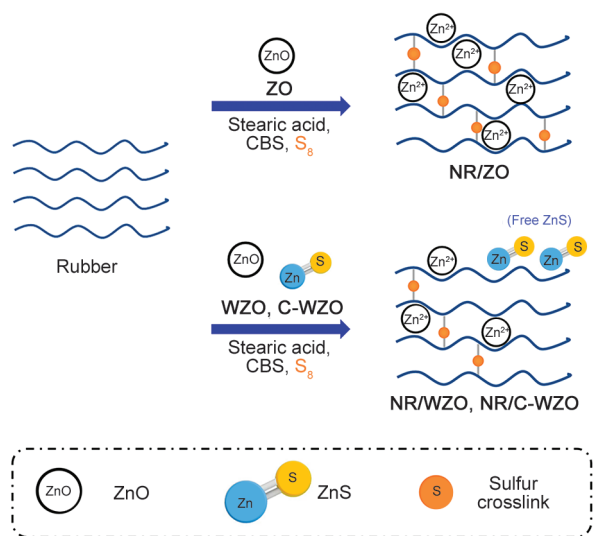


Figure 4. Proposed sulfur vulcanization process of NR vulcanizates.

Table 4. Mechanical properties of NR vulcanizates.

Samples	Tensile strength [MPa]	Elongation at break [%]	100% Modulus [MPa]	300% Modulus [MPa]	Hardness [Shore A]	Tear strength [N/mm]	Compression set [%]
NR/ZO	26.4±1.80	684±16	0.93±0.01	2.49±0.06	40.3±0.3	71.6±3.3	28.1±2.1
NR/WZO (I)	17.1±0.93	693±08	0.76±0.01	1.72±0.03	33.9±0.2	54.2±1.0	25.1±1.0
NR/WZO (II)	16.8±1.18	678±15	0.77±0.02	1.75±0.03	34.8±0.2	63.1±1.5	25.1±1.6
NR/C-WZO (I)	22.0±1.40	677±10	0.89±0.01	2.18±0.06	38.4±0.3	57.1±2.4	24.4±1.2
NR/C-WZO (II)	21.3±2.15	642±20	0.96±0.02	2.45±0.05	39.3±0.2	68.4±1.5	25.1±2.8

Data are shown as the mean±one standard deviation.

vulcanizates with ZnO powder at 5 phr and sulfur at 2.5 phr, the tensile strength of NR/C-WZO (I) (22.0 MPa) was higher than that of NR/WZO (I) (17.1 MPa). When the actual sulfur content obtained from the ZnO sample and added sulfur was adjusted to be a total of 5 phr, the tensile strength of NR/C-WZO (II) (21.3 MPa) was also higher than that of NR/WZO (II) (16.8 MPa). It can be noted that the tensile strength of the NR vulcanizates increased with an increasing crosslink density. In addition, the tensile strength of NR/C-WZO (I) and NR/WZO (I) was about the same (no difference) as those for NR/C-WZO (II) and NR/WZO (II), respectively, while the crosslink density of NR/C-WZO (II) and NR/WZO (II) was higher than that of NR/C-WZO (I) and NR/WZO (I), respectively. This might reflect that some sulfur in the vulcanization system affected the tensile strength of elastomers. Although, the elongation at break of the NR vulcanizates did not show a clear trend, it was quite high in the range of 642–693% due to the elastomeric matrix.

The modulus at 300% strain, hardness, and tear strength of NR/ZO (2.49 MPa, 40.3, 71.6 N/mm) were higher than those of NR/WZO and NR/C-WZO. For the rubber vulcanizates filled with 5 phr ZnO powder and 2.5 phr sulfur, the modulus at 300% strain, hardness, and tear strength of NR/C-WZO (I) (2.18 MPa, 38.4, 57.1 N/mm) were higher than those of NR/WZO (I) (1.72 MPa, 33.9, 54.2 N/mm). For the rubber vulcanizates with an actual sulfur content of 2.5 phr, the modulus at 300% strain, hardness and tear strength of NR/C-WZO (II) (2.45 MPa, 39.3, 68.4 N/mm) were higher than those of NR/WZO (II) (1.75 MPa, 34.8, 63.1 N/mm). In addition, the modulus at 300% strain and hardness of NR/WZO (I) and NR/C-WZO (I) were lower than those of NR/WZO (II) and NR/C-WZO (II), respectively. The modulus at 300% strain and hardness decreased with

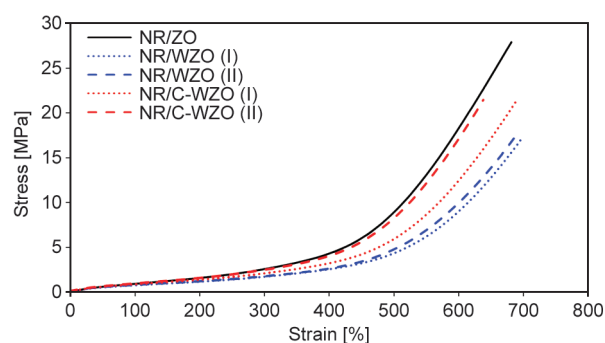


Figure 5. Representative stress–strain curves from the tensile tests of NR vulcanizates.

a decreasing crosslink density due to the restriction on the mobility of rubber chains [33]. Moreover, the compression set of NR/ZO (28.1%) was also higher than that of NR/WZO and NR/C-WZO (24.4–25.1%). Figure 5 shows the stress–strain curves of NR vulcanizates. The rubber vulcanizates had an elastomer behavior with a positive slope and the curve of NR/C-WZO (II) was similar to that of NR/ZO. These results indicated that the C-WZO had a good potential for use as an activator in rubbers with high tensile strength and tear strength (21.3 MPa, 68.4 N/mm) that could be increased by the presence of silica /or carbon black reinforcement in commercial rubber products.

From the thermogravimetric analysis (TGA) and derivative thermogravimetry (DTG) analysis (Figure 6 and Table 5), the NR vulcanizates formed with different types of ZnO all showed a one-step thermal degradation with smooth weight loss. The T_{id} and T_{max} values were in the range of 346.3–348.8 and 375.8–378.4 °C, respectively, corresponding to the decomposition of the NR matrix. Thus, the different types of ZnO (ZO, WZO, and C-WZO) did not influence the thermal stability of the vulcanizates (NR/ZO, NR/C-WZO, and NR/WZO), which retained the same high thermal stability.

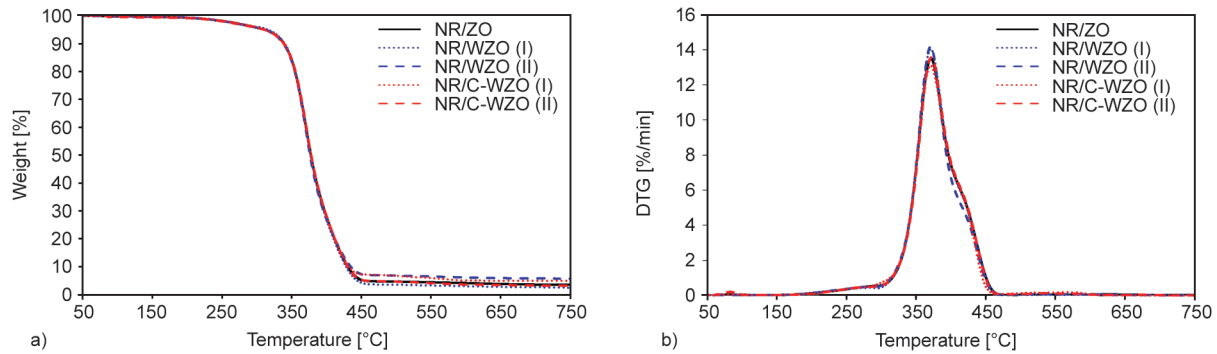


Figure 6. Representative (a) TGA and (b) DTG curves of NR vulcanizates.

Table 5. Thermal and dynamic mechanical properties of NR vulcanizates.

Sample	T_{id} [°C]	T_{max} [°C]	T_g [°C]	E'_{max} [MPa]	$E'_{20^\circ C}$ [MPa]	$\tan \delta$ at the peak [-]
NR/ZO	347.6	377.8	-44.8	2412	1.87	2.41
NR/WZO (I)	348.1	377.7	-45.3	2093	1.67	2.33
NR/WZO (II)	347.5	375.8	-47.4	2295	1.58	2.46
NR/C-WZO (I)	346.3	376.6	-45.0	2417	1.73	2.28
NR/C-WZO (II)	348.8	378.4	-44.4	2409	1.89	2.41

3.4. Dynamic mechanical properties of the NR vulcanizates

The elastic modulus of a polymeric material and its mechanical damping or energy dissipation characteristics as a function of the temperature and frequency can be evaluated by DMA. The storage modulus (E') of the NR vulcanizates is shown in Figure 7 and Table 5. At a low temperature, the E'_{max} value of NR/WZO (2093–2295 MPa) was lower than those of NR/ZO and NR/C-WZO (2409–2417 MPa) due to the presence of ZnS. In addition, the E' values of the vulcanized rubber were decreased around the transition region being a state after the onset of a noticeable reduction in the storage modulus, because the mobility of the polymer chains increased with increasing temperature. Above the glass transition temperature

(T_g), the $E'_{20^\circ C}$ values of NR/ZO and NR/C-WZO (1.73–1.89 MPa) were slightly higher than NR/WZO (1.58–1.67 MPa). Therefore, C-WZO could be used as an activator in rubber vulcanization.

The loss tangent ($\tan \delta$) of the NR vulcanizates was calculated from the ratio of the dynamic loss modulus (E'') to the storage modulus (E') and is shown in Figure 7 and Table 5. The height of the $\tan \delta$ curve showed the damping property of the material. The $\tan \delta$ values of NR vulcanizates were in the range of 2.28–2.46 and were not significantly different. Moreover, the T_g of vulcanized rubber could be determined from the highest value of the $\tan \delta$ peak. The T_g values of NR/ZO and NR/C-WZO (-44.4 to -45.0 °C) were slightly higher than NR/WZO (-45.3 to -47.4 °C). Thus, the tensile and dynamic mechanical

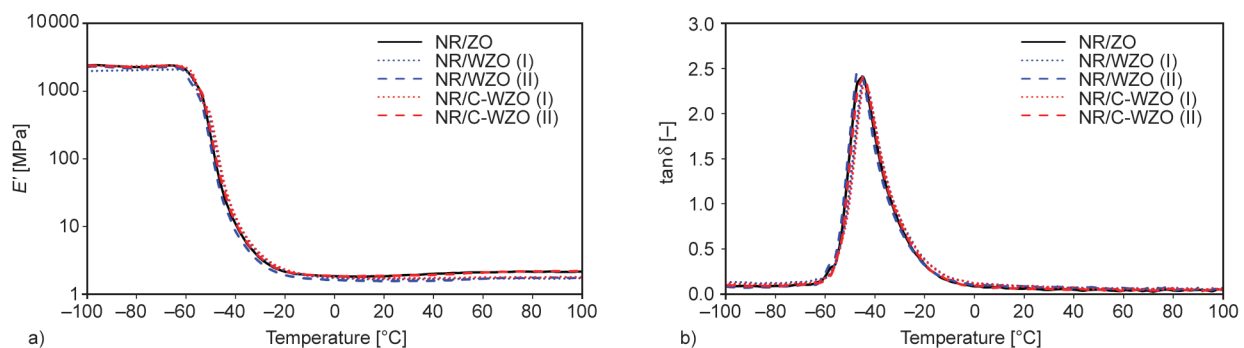


Figure 7. Representative (a) storage modulus (E') and (b) loss tangent ($\tan \delta$) of NR vulcanizates.

properties of NR vulcanizates showed the same trend, with C-WZO being an efficient activator in rubber vulcanization.

4. Conclusions

The WZO particles obtained from ceramic processing could be treated via calcination to remove the sulfur components (ZnS). The particle size of WZO and C-WZO was about 1.5 and 2.75-fold larger than the ZO particles, respectively. For NR vulcanizates, the NR/C-WZO had similar physical and dynamic mechanical properties to NR/ZO. As a result of the enhanced crosslink density, the tensile strength, modulus at 300% strain, hardness, tear strength, and storage modulus of NR/C-WZO were superior to NR/WZO. For thermal properties, the rubber vulcanizates with different ZnO particles retained the same high thermal stability. Therefore, C-WZO had the potential to be used as a substance in the sulfur vulcanization process.

Acknowledgements

The authors gratefully acknowledge the support from the Ratchadapisek Somphot Fund for Postdoctoral Fellowship, Chulalongkorn University, and the Center of Excellence in Green Materials for Industrial Application, Chulalongkorn University. The authors also thank Siam Frit Co., Ltd., Samutsakhon, Thailand for raw material support, and Dr. Robert Butcher for editing the article and suggestions.

References

- [1] Ikeda Y., Kato A., Kohjiya S., Nakajima Y.: Rubber science. Springer, Singapore (2018).
- [2] Thomas S., Chan C. H., Pothen L., Joy J., Maria H.: Natural rubber materials: Volume 2: Composites and nanocomposites. Royal Society of Chemistry, Cambridge (2013).
<https://doi.org/10.1039/9781849737654>
- [3] Kruželák J., Sýkora R., Hudec I.: Sulphur and peroxide vulcanisation of rubber compounds – Overview. Chemical Papers, **70**, 1533–1555 (2016).
<https://doi.org/10.1515/chempap-2016-0093>
- [4] Schaefer R. J.: Mechanical properties of rubber. in ‘Harris’ shock and vibration handbook’ (eds.: Piersol A., Paez T.) McGraw-Hill, Woodland Hills, 1–18 (2010).
- [5] Kruželák J., Hložeková K., Kvasničáková A., Tomanová K., Hudec I.: Application of sulfur and peroxide curing systems for cross-linking of rubber composites filled with calcium lignosulfonate. Polymers, **14**, 1921 (2022).
<https://doi.org/10.3390/polym14091921>
- [6] Rodgers B.: Rubber compounding: Chemistry and applications. CRC press, New York (2015).
- [7] Maciejewska M., Sowińska A., Kucharska J.: Organic zinc salts as pro-ecological activators for sulfur vulcanization of styrene–butadiene rubber. Polymers, **11**, 1723 (2019).
<https://doi.org/10.3390/polym11101723>
- [8] Mostoni S., Milana P., Di Credico B., D’Arienzo M., Scotti R.: Zinc-based curing activators: New trends for reducing zinc content in rubber vulcanization process. Catalysts, **9**, 664 (2019).
<https://doi.org/10.3390/catal9080664>
- [9] Junlapong K., Suwanboon S., Khaokong C.: Effects of zinc oxide particle shape on properties of a prevulcanized latex. Iranian Polymer Journal, **28**, 325–335 (2019).
<https://doi.org/10.1007/s13726-019-00702-w>
- [10] Qin X., Xu H., Zhang G., Wang J., Wang Z., Zhao Y., Wang Z., Tan T., Bockstaller M. R., Zhang L., Matyjaszewski K.: Enhancing the performance of rubber with nano ZnO as activators. ACS Applied Materials and Interfaces, **12**, 48007–48015 (2020).
<https://doi.org/10.1021/acsami.0c15114>
- [11] Sreethu T. K., Naskar K.: Zinc oxide with various surface characteristics and its role on mechanical properties, cure-characteristics, and morphological analysis of natural rubber/carbon black composites. Journal of Polymer Research, **28**, 183 (2021).
<https://doi.org/10.1007/s10965-021-02536-8>
- [12] Krainoi A., Poomputsa K., Kalkornsurapranee E., Johns J., Songtipya L., Nip R., Nakaramontri Y.: Disinfectant natural rubber films filled with modified zinc oxide nanoparticles: Synergetic effect of mechanical and antibacterial properties. Express Polymer Letters, **15**, 1081–1100 (2021).
<https://doi.org/10.3144/expresspolymlett.2021.87>
- [13] Bieliński D. M., Klajn K., Gozdek T., Kruszyński R., Świątkowski M.: Influence of n-ZnO morphology on sulfur crosslinking and properties of styrene-butadiene rubber vulcanizates. Polymers, **13**, 1040 (2021).
<https://doi.org/10.3390/polym13071040>
- [14] Cui J., Zhang L., Wu W., Cheng Z., Sun Y., Jiang H., Li C.: Zinc oxide with dominant (1 0 0) facets boosts vulcanization activity. European Polymer Journal, **113**, 148–154 (2019).
<https://doi.org/10.1016/j.eurpolymj.2019.01.032>
- [15] Maciejewska M., Zaborski M.: Thermal analysis and mechanical methods applied to studying properties of SBR compounds containing ionic liquids. Polymer Testing, **61**, 349–363 (2017).
<https://doi.org/10.1016/j.polymertesting.2017.05.041>
- [16] Abd-Ali N. K.: The effect of cure activator zinc oxide nanoparticles on the mechanical behavior of polyisoprene rubber. Journal of Engineering Science and Technology, **15**, 2051–2061 (2020).
- [17] Thaptong P., Boonbumrung A., Jittham P., Sae-oui P.: Potential use of a novel composite zinc oxide as eco-friendly activator in tire tread compound. Journal of Polymer Research, **26**, 226 (2019).
<https://doi.org/10.1007/s10965-019-1895-1>

- [18] Gujel A. A., Bandeira M., Menti C., Perondi D., Guégan R., Roesch-Ely M., Giovanela M., Crespo J. S.: Evaluation of vulcanization nanoactivators with low zinc content: Characterization of zinc oxides, cure, physico-mechanical properties, Zn²⁺ release in water and cytotoxic effect of EPDM compositions. *Polymer Engineering and Science*, **58**, 1800–1809 (2018).
<https://doi.org/10.1002/pen.24781>
- [19] Maiti M., Basak G. C., Srivastava V. K., Jasra R. V.: Influence of synthesized nano-ZnO on cure and physico-mechanical properties of SBR/BR blends. *International Journal of Industrial Chemistry*, **8**, 273–283 (2017).
<https://doi.org/10.1007/s40090-016-0107-7>
- [20] Samadi M., Huseien G. F., Mohammadhosseini H., Lee H. S., Lim N. H. A. S., Tahir M. M., Alyousef R.: Waste ceramic as low cost and eco-friendly materials in the production of sustainable mortars. *Journal of Cleaner Production*, **266**, 121825 (2020).
<https://doi.org/10.1016/j.jclepro.2020.121825>
- [21] Skorulska A., Piszko P., Rybak Z., Szymonowicz M., Dobrzyński M.: Review on polymer, ceramic and composite materials for CAD/CAM indirect restorations in dentistry – Application, mechanical characteristics and comparison. *Materials*, **14**, 1592 (2021).
<https://doi.org/10.3390/ma14071592>
- [22] Burluson M.: *The ceramic glaze handbook: Materials, techniques, formulas*. Lark Books, New York (2003).
- [23] Rudkovskaya N. V., Mikhailenko N. Y.: Decorative zinc-containing crystalline glazes for ornamental ceramics (A review). *Glass and Ceramics*, **58**, 387–390 (2001).
<https://doi.org/10.1023/A:1014958309094>
- [24] Yekta B. E., Alizadeh P., Rezazadeh L.: Floor tile glass-ceramic glaze for improvement of glaze surface properties. *Journal of the European Ceramic Society*, **26**, 3809–3812 (2006).
<https://doi.org/10.1016/j.jeurceramsoc.2005.12.016>
- [25] Da Silva R. C., Pianaro S. A., Tebcherani S. M.: Preparation and characterization of glazes from combinations of different industrial wastes. *Ceramics International*, **38**, 2725–2731 (2012).
<https://doi.org/10.1016/j.ceramint.2011.11.041>
- [26] Moezzi A., McDonagh A. M., Cortie M. B.: Zinc oxide particles: Synthesis, properties and applications. *Chemical Engineering Journal*, **185–186**, 1–22 (2012).
<https://doi.org/10.1016/j.cej.2012.01.076>
- [27] Doostmohammadi A., Monshi A., Salehi R., Fathi M. H., Karbasi S., Pieles U., Daniels A. U.: Preparation, chemistry and physical properties of bone-derived hydroxyapatite particles having a negative zeta potential. *Materials Chemistry and Physics*, **132**, 446–452 (2012).
<https://doi.org/10.1016/j.matchemphys.2011.11.051>
- [28] Chongcharoenchaikul T., Miyaji K., Junkong P., Poompradub S., Ikeda Y.: Synergistic effect of cuttlebone particles and non-rubber components on reinforcing ability of natural rubber and synthetic isoprene rubber composites. *Journal of Applied Polymer Science*, **139**, 52375 (2022).
<https://doi.org/10.1002/app.52375>
- [29] Chongcharoenchaikul T., Miyaji K., Junkong P., Poompradub S., Ikeda Y.: Effects of organic components in cuttlebone on the morphological and mechanical properties of peroxide cross-linked cuttlebone/natural rubber composites. *RSC Advances*, **12**, 13557–13565 (2022).
<https://doi.org/10.1039/D2RA01885C>
- [30] Ikeda Y., Higashitani N., Hijikata K., Kokubo Y., Morita Y., Shibayama M., Osaka N., Suzuki T., Endo H., Kohjiya S.: Vulcanization: New focus on a traditional technology by small-angle neutron scattering. *Macromolecules*, **42**, 2741–2748 (2009).
<https://doi.org/10.1021/ma802730z>
- [31] Li H., Zhao K., Tian S., Zeng D., Pang A., Wang X., Xie C.: Origin of the efficient catalytic thermal decomposition of ammonium perchlorate over (2–1–10) facets of ZnO nanosheets: Surface lattice oxygen. *RSC Advances*, **7**, 40262–40269 (2017).
<https://doi.org/10.1039/C7RA07906K>
- [32] Dengo N., De Fazio A. F., Weiss M., Marschall R., Dolcet P., Fanetti M., Gross S.: Thermal evolution of ZnS nanostructures: Effect of oxidation phenomena on structural features and photocatalytic performances. *Inorganic Chemistry*, **57**, 13104–13114 (2018).
<https://doi.org/10.1021/acs.inorgchem.8b01101>
- [33] Zhao F., Bi W., Zhao S.: Influence of crosslink density on mechanical properties of natural rubber vulcanizates. *Journal of Macromolecular Science Part B*, **50**, 1460–1469 (2011).
<https://doi.org/10.1080/00222348.2010.507453>

Research article

Long-chain branched poly(butylene succinate-co-terephthalate) copolyesters: Impact of (reactive) synthesis strategies on melt strength properties

Mohamed Yousfi^{1,2*}, Cédric Samuel¹, Tarek Dadouche², Rosica Mincheva³,
Marie-France Lacrampe²

¹IMT Nord Europe, Institut Mines-Télécom, Univ. Lille, Centre for Materials and Processes, F-59000 Lille, France

²Univ Lyon, CNRS, UMR 5223, Ingénierie des Matériaux Polymères, Université Claude Bernard Lyon 1, INSA Lyon, Université Jean Monnet, F-69621 Villeurbanne, France

³Laboratory of Polymeric and Composite Materials (LPCM), University of Mons, Place du Parc, 23, B-7000 Mons, Belgium

Received 21 July 2022; accepted in revised form 3 October 2022

Abstract. Highly biobased poly(butylene succinate-co-terephthalate) (PBST) with processing temperatures close to those of commodity polymers (160–180 °C) and long-chain branched architectures (LCB) are synthesized by different strategies. Their rheological properties are investigated, in particular their melt strength properties. A two-step synthesis route is first proposed based on linear LCBs produced by polycondensation followed by reactive extrusion with an epoxy-based multifunctional agent Joncryl[®] at concentrations up to 2 wt%. A one-step synthesis strategy is also developed using glycerol as a branching agent, introduced at a low concentration (0.5 wt%) directly during the PBST polycondensation process. The molecular weights, LCB structures, and thermal properties are determined by triple detection size exclusion chromatography and differential scanning calorimetry. For PBSTs synthesized in two steps, gelation takes place simultaneously with the branching reactions. However, a concentration of Joncryl[®] close to 2 wt% is required to improve the melt strength properties, with strain hardening effects under elongation conditions. Interestingly, PBSTs synthesized by *in-situ* addition of glycerol show remarkable melt strength and a high melt stabilization process. Dynamic rheology investigations allow attributing these effects to statistical/homogeneous gel-free LCB architectures obtained during reactive extrusion without any additional post-processing. The effectiveness of approaches to easily improve the melt strength of highly biobased aliphatic-aromatic copolyesters (theoretical biobased content up to 85%) and to eliminate extrusion defects/instabilities in PBSTs is thus demonstrated, allowing the possibility of expanding the industrial application domains of these polymers in packaging and sustainable applications.

Keywords: biodegradable polymers, rheology, long chain branching, polymer synthesis, molecular engineering

1. Introduction

Driven by international legislation, end-of-life consideration and treatment of plastic wastes have become major issues for the plastics industry and the academic community. Indeed, the production of plastics is continuously increasing for more than 50 years to reach 368 million tons in 2020 [1]. But, despite many efforts around the world, a large proportion of

plastic waste is not recycled, causing significant economic and environmental damage. One possible approach to solving these issues is to replace current petroleum-based thermoplastic polymers with renewable bio-based polymers that are more sustainable. Their ability to compost and/or biodegradability under certain conditions makes them very attractive, in particular for succinic acid (co)polyesters.

*Corresponding author, e-mail: mohamed.yousfi@insa-lyon.fr

© BME-PT

However, their processability by conventional technologies of the plastics/textile industry remains rather limited. Indeed, their macromolecular architectures need to be modified by introducing chain extension and/or branching to adapt their rheological properties in the molten state, thus limiting the loss of molecular weight caused by thermal/hydrolytic degradation and widening their processing window by extrusion/injection technologies.

Among succinic acid-based aliphatic (co)polyesters such as poly(butylene succinate) (PBS, Bionolle[®], Showa Denko) and poly(butylene succinate-co-adipate) (PBSA, BioPBS[™], Mitsubishi), aliphatic-aromatic versions such as poly(butylene succinate-co-terephthalate) (PBST) represent one of the most promising sustainable polymers due to their renewable/biodegradable nature (high biobased content up to 85%) together with high melting temperatures (150–180 °C) close to those of commodity polyolefins (high-density polyethylene, polypropylene) and polyamides (e.g. polyamide 12), high rate of crystallization, excellent shape memory [2] and superior mechanical properties [3, 4].

PBST copolyesters have subsequently received significant attention in the last few years and have been extensively investigated in relation to various research topics including PBST synthesis [5], crystallinity [4], biodegradability [6], gas barrier [7], and mechanical properties [8]. Currently, the main industrial application of PBST is the manufacturing of fibers and yarns used in the textile industry [9].

However, the production of PBST-based items by classical industrial processes such as film blowing, thermoforming, extrusion blow molding, or extrusion foaming processes is hindered by its inadequate rheological behavior. Actually, the rheological and melt strength properties of polymers with linear macromolecular structures are known to induce dramatic processing instabilities, in particular under elongational flows during the above-mentioned processes [10]. On the contrary, polymers with long chain branched (LCB) architectures usually display high viscosities, elasticities, and melt strengths that improve the stability/quality of extruded items and favor recyclability, as the melt rheological properties can be maintained close to those of the original virgin material. Candal *et al.* [11] found that the formation of long-chain branches by reactive extrusion is an efficient way to recycle opaque polyethylene terephthalate (PET) into a new material with enhanced

mechanical and rheological performances that are comparable to those of typical virgin PET.

Actually, compared to classical reptation–tube theories of linear polymers, additional relaxation processes are observed for LCB architectures [12] and these architectures particularly require more time to fully relax due to topological constraints at the anchoring points [13–15]. Therefore, under a fast elongational flow, additional stresses are induced that generate strain hardening phenomena of high interest for extrusion processing [15–17]. LCB architectures with high melt strengths could be directly produced during the polymerization process, as depicted in the case of low-density polyethylene produced by free-radical polymerization [18, 19]. The use of specific agents coupled with reactive extrusion processes also represents a widespread method to induce chain extension, crosslink, and to graft reactions leading to LCB architectures [20–23]. It could be noticed that blending and nucleation (with filler or nucleation agent) could also represent alternative approaches to improve the melt strength of thermoplastic polymers [24–28].

In the case of biobased polyesters obtained by polycondensation or ring-opening polymerization and displaying *quasi*-linear architectures, numerous reactive agents are effective in producing LCB architectures with high melt strength for the development of advanced grades [29–33]. The most common way to synthesize LCB co-polyesters is to introduce multifunctional ($f \geq 3$) monomers or oligomers as long chain branching agents, such as multifunctional acids, alcohols, peroxides, isocyanates, and epoxides, in high-temperature polycondensation reaction. Al-Itry *et al.* [34] have used multifunctional epoxy-based agents as chain extenders to adapt the rheological behavior of poly(lactic acid) (PLA) in shear and elongational conditions for the extrusion-blowing process. Li *et al.* [35] have utilized acrylic-based additives to produce LCB-PLA by UV-induced reaction for extrusion foaming processes. Wei and McDonald [31] used peroxide-based agents as crosslinking agents to improve the melt processability of poly(3-hydroxybutyrate). Interestingly, some authors recently considered the case of PBST. Sun *et al.* [36] used epoxy-based agents for the preparation of LCB-PBST. The existence of LCB architectures greatly improved the rheological properties of PBST in shear conditions, but an obvious decrease in ductility is observed. Recently, Lu *et al.* [37] utilized pentaerythritol as a

branching agent for PBST during esterification – polycondensation at 230–250 °C in the presence of a specific catalyst. According to the authors, higher branching efficiencies were attested compared to epoxy-based agents. A slight modification of PBST crystallization parameters is attested for LCB-PBST compared to linear PBST. However, the rheological behavior in elongational conditions of such LCB-PBST has not been documented elsewhere, and, in this context, the efficiency of various reactive agents cannot be clearly concluded.

In the present work, the rheological properties of highly-biobased LCB-PBST in elongational conditions are mainly targeted to fulfill the requirements of industrial elongational processes, in particular, extrusion processing into films. Two different approaches are proposed to synthesize LCB-PBST with melting/processing temperatures close to 160–180 °C (close to those of commodity thermoplastic polymers such as poly(propylene) and Nylon 11).

A classical two-step approach is first proposed based on linear LCBs produced by polycondensation then processes by reactive extrusion with an epoxy-based multifunctional agent Joncryl® at concentrations up to 2 wt%. A one-step approach is also investigated, using glycerol introduced at 0.5 wt% directly during the PBST synthesis by polycondensation. Macromolecular structures and thermal properties of LCB-PBST are evaluated by size-exclusion chromatography (SEC) and differential scanning calorimetry (DSC). Their transient elongational viscosities as a function of the stretching time are then investigated using a rheometer equipped with Sentmanat extensional apparatus. Their linear viscoelastic properties in shear conditions are finally analyzed to depict correlations with macromolecular structures and synthesis strategies.

2. Experimental section

2.1. Materials

Succinic acid (SA, purity 99%, Kosher), 1,4-butanediol (BDO, purity 99%, Kosher), titanium tetra-isopropoxide (TTiPO, purity 98%, Aldrich, USA), and terephthalic acid (TPA, purity 98%, BP Chemicals, UK) were all used as received. Glycerol was purchased from Fisher Scientific, USA. Epoxy-based styrene-acrylic oligomers were kindly supplied by BASF, Germany (Joncryl ADR®-4300F, T_g 56 °C, the epoxy equivalent weight 445 g/mol, molar mass M_w 5500 g/mol, and functionality number (f) is 5)

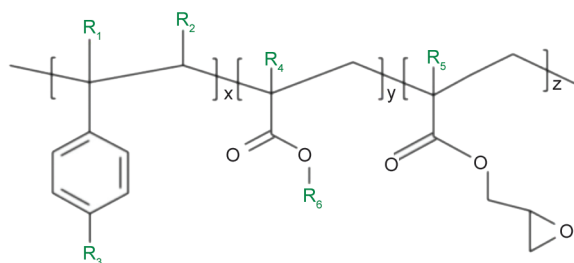


Figure 1. The general structure of epoxy-based styrene-acrylic Joncryl® oligomers (R_1 - R_2 - R_3 - R_4 are H, CH_3 , a higher alkyl group, or combinations of them) (R_5 is an alkyl group) (x , y are each between 1 and 20) (z is between 1 and 12) [38].

[38]. The general structure of these oligomers designed for chain extension/branching reactions of polyesters, polyamides, and polycarbonates is depicted in Figure 1. The food and drug administration (FDA) compliance was delivered by the European Union for its use in food packaging [39].

2.2. One-step synthesis of LCB-PBST by polycondensation

An Autoclave® reactor (Autoclave France, France) specially designed for polycondensation reactions was used. It was equipped with a condenser, a mechanical stirrer, and a vacuum line. The temperature inside the reactor, the pressure, and the torque was monitored during the synthesis. The reactor was fed with TPA and SA powders (molar ratio of TPA to SA equal to 60:40) and a desired amount of BDO was added under stirring. Thereafter, 0.01 mmol of TTiPO used as catalyst was introduced under protective nitrogen flux. The reactor was gradually heated to 210 °C and esterification reactions proceeded at a stirring speed of 80 rpm for 2 hours to produce PBST oligomers. Afterward, glycerol was introduced at a concentration of 0.5 wt% (relative to PBST), and polycondensation reactions were carried out at reduced pressure. For this purpose, the reactor temperature was gradually increased to 250 °C, and the polycondensation reaction was terminated once the stirring torque reached a constant/maximal value. As-prepared PBSTs were dissolved in chloroform and then precipitated in methanol for purification followed by drying in a vacuum oven. The use of glycerol bearing three hydroxyl groups (–OH) is expected to react with PBST carboxyl end groups (–COOH) during polycondensation to form a branching point according to Figure 2.

It should be noted here that long chain branching or crosslinked molecular structures could be obtained according to the glycerol content in the medium [40].

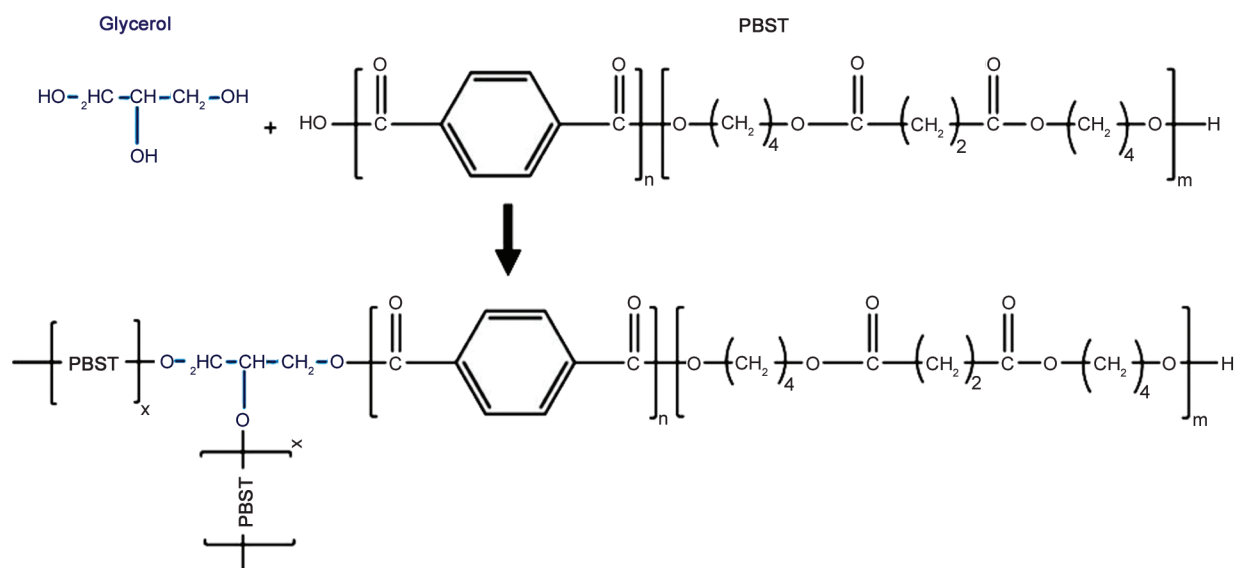


Figure 2. Schematic proposed mechanism for the production of LCB-PBST using glycerol during PBST polycondensation.

In this study, to avoid a possible formation of gels or crosslinked structures, glycerol content was limited to 0.5 wt%. Beyond this concentration, gelification or crosslinking shall occur.

2.3. Two-step synthesis of LCB-PBST by polycondensation – reactive extrusion

The classical two-step synthesis of LCB-PBST involves (i) the production of *quasi*-linear PBST by polycondensation and (ii) reactive extrusion using Joncryl[®]. The first part is similar to the above procedure, except for the absence of glycerol during polycondensation reactions to yield *quasi*-linear PBST. The second part is performed using a twin-screw μ -extruder (MiniLabII, Thermoscientific, Germany). PBST solids were dried overnight under vacuum at 60 °C and were dry-blended with Joncryl[®] flakes at concentrations up to 2 wt% just before extrusion. The extrusion temperature is set to 180 °C with a screw speed of 100 rpm for a mixing time of 5 min. The expected mechanisms yielding LCB-PBST by reactive extrusion with Joncryl[®] are depicted in Figure 3. Finally, all materials were molded into rectangular bars, discs, or cylinders for rheology testing using a Dolouets thermocompression molding machine at 180 °C for 10 min under 80–110 bar. The following Table 1 gathers all PBST materials used in this study with their nomenclature.

2.4. Characterizations

2.4.1. Molecular weight analysis by size-exclusion chromatography (SEC)

Size exclusion chromatography (SEC) was performed on as-prepared materials to determine their molecular weights (M_n , M_w), polydispersity index, and macromolecular architectures. The SEC system is composed of a chromatographic pump (LC-20AD, Shimadzu, Japan), a chromatographic injector (Perkin Elmer Series 200, Germany), one precolumn (PLgel 20 μ m Guard 50 \times 7.5 mm, Agilent, Germany) and three columns (PLgel 5 μ m Mixed-C, 300 \times 7.5 mm, polystyrene/divinylbenzene stationary phase, Agilent, Germany). The SEC was coupled with a multiangle light scattering detector (WTRE-OS-01, 3 angles, Wyatt, Germany), a refractometer (RID 10A, Shimadzu, Japan), a UV detector (SPD-20A, Shimadzu, Japan), and a viscosimeter (WVISC-04, Wyatt, Germany). As-prepared PBSTs were dissolved in chloroform at a concentration of 1 mg/ml for 48 h. Solutions were filtrated over polytetrafluoroethylene filters (0.25 μ m) to prevent the passage of the gels contained in some LCB-PBSTs into the columns and eluted in the SEC system with chloroform at a flow rate of 1 ml/min. The differential index of refraction dn/dc was measured by a refractometer (Wyatt Optilab T-rex, $\lambda = 658$ nm), and a value of 0.08 ml/g was used for data processing.

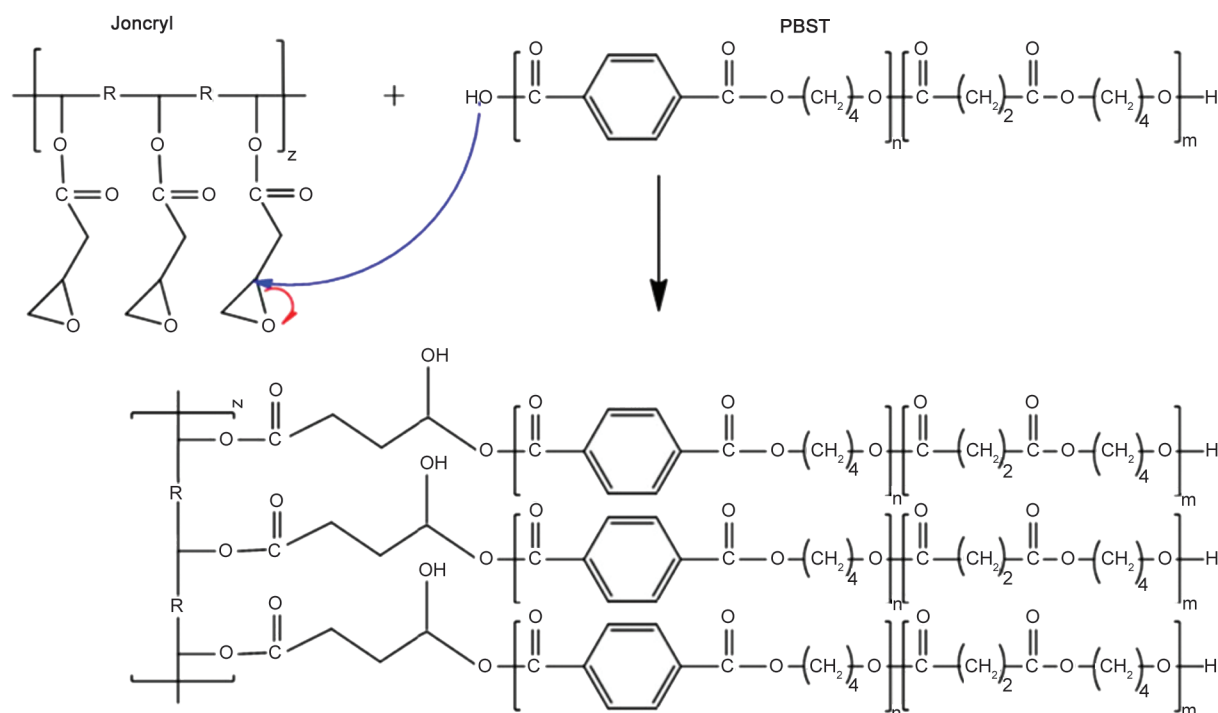


Figure 3. Schematic proposed mechanism for the production of LCB-PBST using epoxy-based styrene-acrylic Joncryl[®] oligomers.

Table 1. Nomenclature and description of as-prepared PBST.

Nomenclature	Description
L-PBST	Linear PBST synthesized by polycondensation
LCB1-PBST-G	LCB-PBST synthesized by polycondensation using glycerol
LCB2-PBST-J1	LCB-PBST synthesized from L-PBST and reactive extrusion with 1 wt% Joncryl [®]
LCB2-PBST-J2	LCB-PBST synthesized from L-PBST and reactive extrusion with 2 wt% Joncryl [®]

2.4.2. Gel determination

It is well-documented in the literature that high contents of a high multifunctional chain extender agent can lead to gelification or even crosslinking. The latter can impact the end-product mechanical performances, like the elongation at break [41]. The linear and LCB-PBST samples were analyzed by the solvent extraction technique [41]. Each sample was dissolved in chloroform without stirring and filtered after 4 days using a 0.2 μm filter. Then, the percentage of gel was determined by weighing residues of insoluble compounds after extraction of the solvent at the end of the drying step in an oven at 50 °C for 48 hours.

2.4.3. Thermal properties by DSC

The thermal properties of the as-prepared materials were determined using a DSC (Mettler Toledo, Switzerland) calibrated with the indium reference (melting point of 156.6 °C). Experiments were carried out under a nitrogen atmosphere with heat – cool

– heat cycles at 10 °C/min between –60 to 200 °C. Crystallization temperatures (T_c) were determined during the cooling scan using the exothermic phenomena and melting temperatures (T_m) were determined during the second heating scan using the endothermic phenomena. On the other hand, the glass transition temperature T_g was calculated from the middle point of the step change in heat flow.

2.4.4. Dynamic rheological measurements

Rheological tests in shear conditions were carried out under a nitrogen atmosphere using a stress-controlled dynamic rheometer (Haake MarsIII, Thermo Scientific, Germany). The samples were systematically dried under a vacuum at 60 °C for 24 h before measurement. A parallel-plate geometry (diameter 35 mm) was chosen. Frequency sweeps between 100–0.1 rad/s were performed at 180 °C using a constant strain of 10%. Strain sweeps at a constant angular frequency of 100 rad/s were performed to ensure working into the linear viscoelastic domain for each material.

2.4.5. Elongational rheology measurements

Transient extensional viscosities of as-prepared PBST as a function of the stretching time at various strain rates were evaluated using the previous dynamic rheometer equipped with an SER (Sentmanat Extensional Rheometer, Thermo Scientific, Germany) tool. The working principle is based on two drums attached to the rheometer motor, drums rotating in the opposite direction at the same speed. A pure uniaxial stretching is consequently applied to the test sample. The theoretical details behind the measurement of the transient extensional viscosity are reported in detail by Yousfi *et al.* [28]. Tests were here carried out at 180 °C and, after rheometer calibration and temperature calibration, the sample was fixed between the two drums. A temperature stabilization period of 120 s was set followed by a pre-stretching step at 300 Pa for 10 s to compensate for sample creep at high temperature. Then, the sample was stretched at a given strain rate (between 0.1–1 s⁻¹). Using the motor torque developed during stretching, the transient extensional viscosity was evaluated. It could be noticed that the SER experimental procedure was optimized on reference low-density polyethylene samples using a video analysis system, in particular, to validate the homogeneity of the applied strain and the true strain rate value.

3. Results and discussions

3.1. Molecular characterization and thermal analysis of as-prepared LCB-PBST

Macromolecular parameters and architectures of as-prepared PBSTs were analyzed by SEC equipped with multiple detection techniques. Therefore, the presence of LCB could be also qualitatively approached to some extent using viscosimetric data. The elution profiles of as-prepared PBST can be found in Figure 4a and 4b with molecular weight distribution profiles and viscosimetric profiles (Figure 4c and 4d). Macromolecular parameters are tabulated in Table 2. The elution profile of L-PBST exhibits a unimodal elution peak, and data processing yields $M_n - M_w$ values close to 20 000–27 000 g/mol for L-PBST. The polydispersity index (\mathcal{D}) of 1.35 is in good accordance with a polycondensation synthesis route [42, 43]. Similar molecular weights (M_w of 28 000 g/mol) and a rather narrow molar mass distribution (\mathcal{D} of 1.35) were obtained by Ren *et al.* [42] in the case of linear PBSTs produced through traditional polycondensation reaction. Nevertheless, the viscosimetric

profile displays a power-law dependence with a power-law index (Mark-Houwink-Sakurada parameter α_{MHS}) close to 0.7–0.73, in agreement with literature data on linear poly(butylene succinate) using the same solvent [44–46]. Garin *et al.* [44] found $[\eta] = 39.9 \cdot 10^{-5} \cdot M_n^{-0.71}$ at 30 °C in chloroform with molecular weights measured by SEC with a triple detection system. These elements confirm the linear architecture of L-PBST as expected with a classical polycondensation synthesis route [47]. Concerning LCB1-PBST-G synthesized by one-step polycondensation using glycerol, the unimodal elution peak is clearly broader and shifted to low elution times. Compared to L-PBST, higher molecular weights and broader molecular weight distributions are obtained with a 1.5-fold increase for M_w and a polydispersity index up to 1.98. The viscosimetric profile also displays a power-law dependence but the power-law index is reduced down to 0.59, indicating the effective presence of LCB in significant amounts [41]. It is useful to mention that gel-free branched PBSTs were obtained when glycerol was used as an LCB agent. Indeed, no insoluble residues were found after solvent removal, and thus no gel was detected.

It can be concluded that a homogenous macromolecular architecture with a statistical distribution of LCB (according to Figure 2) was obtained for LCB1-PBST-G due to the use of glycerol as an LCB branching agent during polycondensation [47]. LCB2-PBST-J1 and LCB2-PBST-J2 synthesized from L-PBST coupled to reactive extrusion with Joncryl[®] were marked by a complex population of molecular weights and the appearance of a minor population displaying ultra-high molecular weights. From viscosimetric profiles, a significant deviation from the power-law dependence was attested for molecular weights higher than approx. 60 000 g/mol, and a dramatic reduction of the power-law index was observed for molecular weights higher than approx. 100 000 g/mol. In this respect, it could be suspected that (i) the principal population corresponds to initial and unreacted L-PBST with linear architectures, and (ii) the minor population corresponds to the formation of LCB-PBST with a high LCB density [48]. A preferential reactivity between Joncryl[®] and low-molecular components of L-PBST fits with these observations. Based on molecular weight distribution profiles, the amount of LCB-PBST lies close to 10–20% by weight, depending on Joncryl[®] concentration. The molecular weights of LCB-PBST seem to lie in the

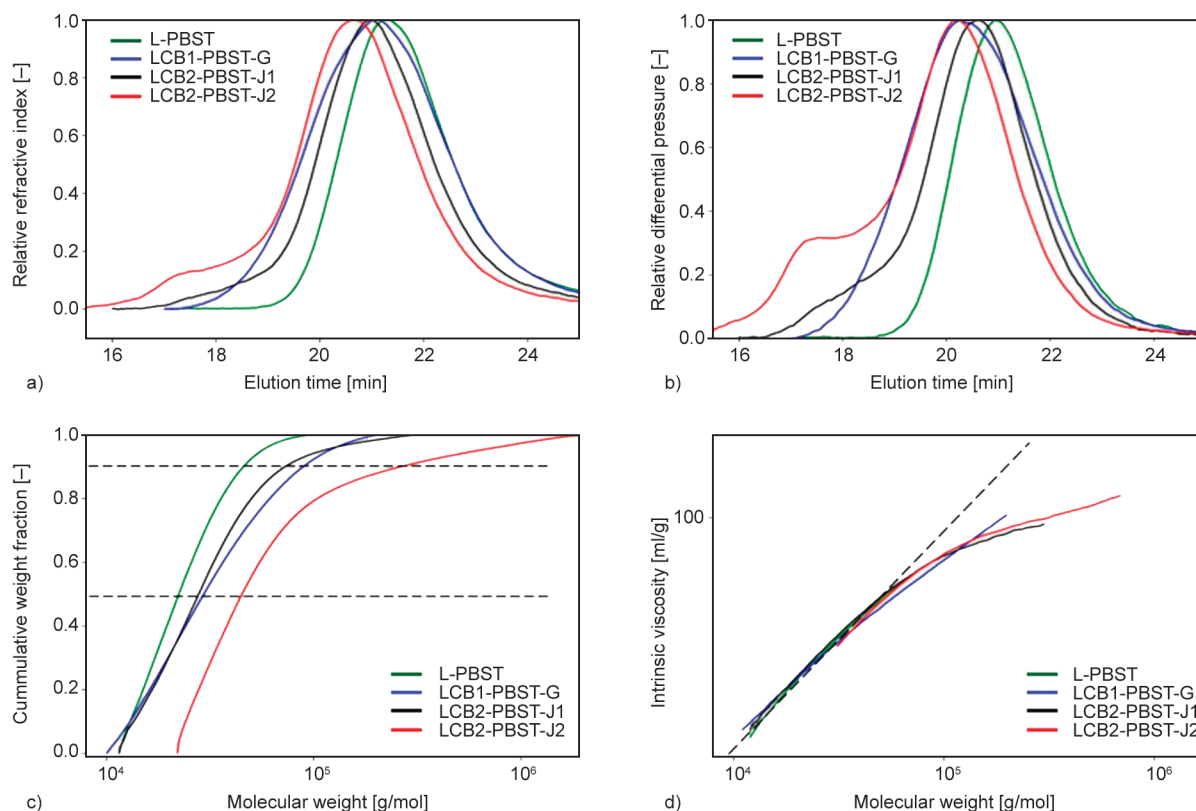


Figure 4. Molecular weight analysis by SEC of as-produced PBST (green L-PBST, blue LCB1-PBST-G, black LCB2-PBST-J1, and red LCB2-PBST-J2). (a, b) Elution profiles (*i.e.*, relative refractive index and relative differential pressure as a function of elution time), (c) molecular weight distribution profiles (*i.e.*, cumulative weight fraction as a function of molecular weight), and (d) viscosimetric profiles (*i.e.*, intrinsic viscosity as a function of molecular weight).

range 60 000–200 000 g/mol in accordance with the reaction scheme displayed in Figure 3 between L-PBST and Joncryl[®] with an epoxy functionality of 5. Moreover, we note the occurrence of partial gelification of PBST for high Joncryl[®] concentrations due to side reactions. The gel content was 35 ± 1.2 wt% for LCB2-PBST-J2 and 15 ± 0.9 wt% for LCB2-PBST-J1, as proven by solvent extraction. It has been reported in several literatures reports that the addition of Joncryl beyond 0.6 wt% could change the structure of LCB-polymers toward the sol–gel transition point [48]. Thus, a high Joncryl content can lead to excessive branching and even crosslinking, which was responsible for the formation of gel

[47]. The two-step approach by reactive extrusion with Joncryl[®] clearly yields heterogenous macromolecular architectures comprising initial linear L-PBST and LCB-PBST with a high LCB density. In conclusion, LCB-PBST was efficiently produced by the two proposed synthesis approaches, but different macromolecular architectures were clearly achieved for LCB1-PBST-G and LCB2-PBST-J1/2.

As mentioned earlier, glycerol has three reactive hydroxyl groups (two primary hydroxyl groups and one secondary hydroxyl group). Thus, glycerol could be considered as a tri-functional additive in polycondensation reactions leading to branching points on the PBST backbone (in accordance with higher molecular

Table 2. Macromolecular parameters of as-produced PBST (number average molecular weight M_n , weight average molecular weight M_w , polydispersity index $D = M_w/M_n$, and Mark-Houwink-Sakurada parameter α_{MHS} , n.d. not determined).

Sample	M_n [g/mol]	M_w [g/mol]	D [-]	α_{MHS} [-]	Gel content [wt%]
L-PBST	20 000	27 000	1.35	0.70–0.73	0
LCB1-PBST-G	22 000	43 000	1.98	0.59	0
LCB2-PBST-J1	23 000	32 000	1.38	n.d.	15.0 ± 0.9
LCB2-PBST-J2	41 000	145 000	3.50	n.d.	35.0 ± 1.2

weights and architectures detected by SEC). Glycerol seems to have a comparable efficiency with tris(hydroxymethyl)ethane for polyester branching. It can be noticed that Nifant'ev *et al.* [48] found similar results when using glycerol as a long chain branching agent (LCB) of poly(butylene adipate terephthalate) (PBAT). However, the M_w of PBAT copolymers obtained in the presence of trimethyl 1,3,5-benzenetricarboxylate (tri-ester-based LCB) was lower in comparison with the M_w of the PBAT synthesized with the use of glycerol. According to the authors, this was due to the lower reactivity of aromatic esters in polycondensation compared to aliphatic $-\text{CH}_2\text{OH}$ functional groups present in glycerol.

Typical DSC thermograms are displayed in Figure 5 for L-PBST and LCB1-PBST-G that clearly attest for semi-crystalline thermoplastic materials. Thermal parameters are tabulated in Table 3. Concerning L-PBST, a glass transition temperature of -16.5°C was recorded with a crystallization temperature of 130.9°C . Two distinct shoulder melting peaks located at 156.2 and 165.5°C were observed which could be ascribed to the recrystallization and remelting mechanism [43, 49]. Indeed, Jie *et al.* [50] provided direct evidence to support this mechanism through the study by modulated differential scanning calorimetry. In this study, the obtained DSC values were in accordance with bibliographic data concerning various linear PBSTs [51–53]. It can be interestingly noticed that the thermal properties of L-PBST can be tuned and get closer to those of commodity polyolefins according to the molar ratio (X_{mol}) of TPA to SA during synthesis (*i.e.* the content of butylene terephthalate (BT) comonomer in the composition). When X_{mol} is equal to 35:65, L-PBST displays thermal parameters (glass transition temperature T_g , melting temperature T_m , crystallization temperature T_c) close to those of

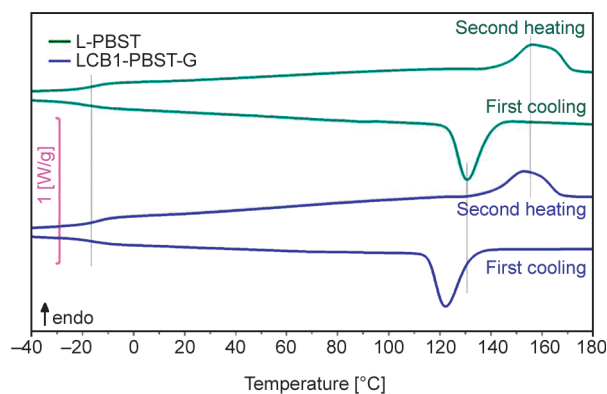


Figure 5. DSC traces (first cooling scan and second heating scan at $10^\circ\text{C}/\text{min}$) were obtained for L-PBST and LCB1-PBST-G.

low-density poly(ethylene). And *vice versa*, when X_{mol} is around 66:34, L-PBST possesses thermal characteristics close to those of isotactic poly(propylene) as seen in Table 3 [53, 54].

The crystallinity of L-PBST still remains challenging to address because the melting enthalpy of fully-crystalline PBST is largely unknown, but crystallization/melting enthalpy seems to be close to various semi-crystalline aliphatic(-aromatic) polyesters such as poly(butylene succinate) and poly(butylenes terephthalate) [55–57].

From DSC data, it was found that the crystallization temperature (T_c) increased first and then decreased with the increase in Joncryl content. The crystallization was first favored probably because of enhanced mobility of chains, but excessive branching (2 wt% of joncryl) led to less regularity of macromolecular chains and consequently retarded crystallization. Similar trends were observed by Lu *et al.* [37] in the case of PBST modified by pentaerythritol (PER) used as a branching agent. In the case of LCB1-PBST-G, the decrease in the crystallization temperature (T_c)

Table 3. Thermal properties of as-produced PBST (glass transition temperature T_g , melting temperature T_m , crystallization temperature T_c and their associated enthalpies).

Sample	T_g^a [°C]	T_m^a [°C]		ΔH_m^a [J/g]	T_c^b [°C]	ΔH_c^a [J/g]
		$T_{m,1}^a$	$T_{m,2}^a$			
L-PBST	-16.5	156.2	165.5	27.8	130.9	27.4
LCB1-PBST-G	-16.1	152.7	160.1	26.5	122.4	25.9
LCB2-PBST-J1	-16.0	158.8	167.4	25.0	133.9	24.2
LCB2-PBST-J2	-14.0	157.9	166.1	24.2	127.5	23.7
iPP ^c	-10.0	–	165.6	117.0	122.7	111.0

^aEvaluated at the second heating scan

^bEvaluated at the first cooling scan

^cData from Purohit *et al.* [60].

could be explained by the increase in intermolecular entanglement induced by branching with glycerol. Such increased molecular entanglement reduces segmental mobility leading to the lower T_c . On the other hand, similar glass transition temperatures close to -16°C are reported for L-PBST, LCB1-PBST-G, and LCB2-PBST-J1, except for a slight increase to -14°C for LCB2-PBST-J2 that could be linked to segmental mobility hindrance for elevated LCB density [58]. The main phenomenon lies in a significant reduction of the melting/crystallization temperatures for LCB1-PBST-G compared to L-PBST. Reduced melting/crystallization temperatures suggest significant modification of the crystal nucleation/growth mechanisms and the production of defective crystals due to LCB [58, 59].

It can be interestingly noticed that this phenomenon confirms the statistical/homogenous architecture for LCB1-PBST-G. In conclusion, semi-crystalline LCB-PBSTs with glass transition temperatures below room temperature were obtained. Thermal properties were close to those of commodity polyolefins, in particular, isotactic poly(propylene) for these highly-biobased LCB-PBSTs, and processing temperatures could be set to $160\text{--}180^\circ\text{C}$ [3]. Moderate modifications of thermal properties were attested for LCB-PBSTs, but correlations to LCB architectures were detected, *i.e.*, statistical/homogenous architectures for LCB1-PBST-G and production of highly-branched architectures for LCB2-PBST-J2.

3.2. Melt-state rheological stability of as-prepared LCB-PBST

The macromolecular structure of polyesters could be evolved at high temperatures, in particular at relevant processing temperatures in the melt state. A reduction of their melt viscosity at elevated residence times is often observed due to macromolecular degradation. Several degradation reactions could be encountered for polyesters, such as (i) hydrolytic/mechanical degradation with random chain scission along polyester chains (ii) and degradation by hydrogen transfer with a localized chain scission close to end-chains, and production of small molecules [61–65]. The use of Joncryl[®] is known to improve the viscosity of polyesters (according to Figure 3) and compensate for viscosity drops due to chain degradation/chain branching recombination reactions [34]. The complex viscosity and the magnitude of degradation reactions were subsequently evaluated by dynamic rheology

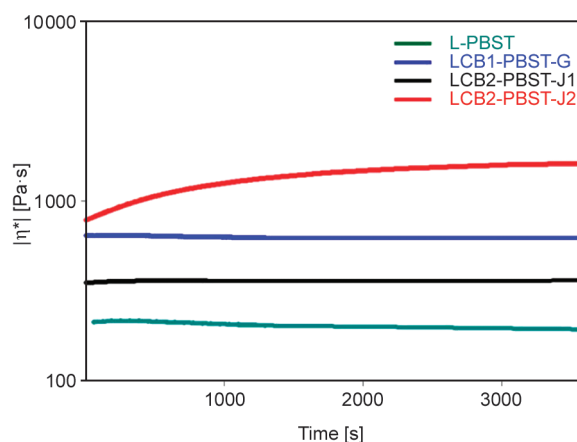


Figure 6. Evolution of the complex viscosity versus time at 180°C for as-prepared PBST.

for as-prepared LCB-PBST. Time sweep tests at 180°C and 10 rad/s in the linear regime were carried out, and the results are presented in Figure 6.

The initial complex viscosity of L-PBST was close to $210\text{ Pa}\cdot\text{s}$, and a slight degradation of L-PBST was observed with a continuous viscosity drop up to $190\text{ Pa}\cdot\text{s}$ in approx. 1 h. A higher complex viscosity was evidenced for LCB1-PBST-G with an initial complex viscosity of $660\text{ Pa}\cdot\text{s}$, and LCB1-PBST-G also slightly degraded with a viscosity drop to $620\text{ Pa}\cdot\text{s}$ in 1 h. The degradation of L-PBST and LCB-PBST-G in the melt state was consequently found quite slow. This slight degradation behavior is probably linked to (i) the low residual water content after appropriate drying and (ii) the low processing temperature of these polyesters. Concerning LCB2-PBST-J1 and LCB2-PBST-J2, their initial complex viscosities were evaluated to 360 and $780\text{ Pa}\cdot\text{s}$ as classical effects encountered with the use of Joncryl[®]. It can be noticed that the complex viscosity of LCB2-PBST-J1 was highly stable over time which corresponds to a perfect balance between chain degradation/recombination reactions. For LCB2-PBST-J2, a high increase in viscosity was observed as a function of time, and a stable value was achieved after a residence time of 1 h at 180°C . Based on these rheological results, *quasi*-stable rheological parameters in shear conditions were concluded for L-PBST, LCB1-PBST-G, and LCB2-PBST-J1. Higher viscosities were also detected for LCB1-PBST-G and LCB2-PBST-J1 in accordance with previous macromolecular analyses (higher M_w , higher polydispersity index, and presence of LCB in significant amounts). LCB2-PBST-J2 displayed an unstable rheological behavior due to intensive chain recombination reactions.

3.3. Shear rheological properties of as-prepared LCB-PBST

L-PBST displayed a constant complex viscosity (η^*) over the entire frequency range with a Newtonian viscosity (or zero-shear viscosity at low frequency) close to 200 Pa·s. in accordance with relatively low molecular weights for L-PBST (Figure 7). A significant increase in Newtonian viscosity was observed for LCB1-PBST-G, and the evolution of the storage modulus (G') (at low frequencies displayed a classical trend with a slope of approx. 2. The rheological behaviors of the two-step chain-extended LCB2-PBST-J1/2 were quite different from PBST produced by the one-step route with glycerol (LCB1-PBST-G). LCB2-PBST-J1 only displayed a moderate increase in Newtonian viscosity, but the evolution of the storage modulus G' at low frequencies displayed a lower slope. Noting that LCB2-PBST-J1 contains 15% of gels but still had a Newtonian viscosity plateau at low frequencies, which suggests that these gels may have crosslink points of low densities and are partially miscible with the linear and branched chains [66]. For LCB2-PBST-J2, the complex viscosity strongly increased at low frequencies. The storage modulus G' also reached a plateau at a low frequency for LCB2-PBST-J2, which is related to a long-time-relaxation mechanism due to the formation of long-chain branches (LCB) during reactive extrusion with Joncryl [27, 67] and to the presence of the high amount of gels (35 wt%) in the structure.

It is useful to mention that a pronounced shear thinning behavior was found at high frequencies for the LCB-PBST samples compared to L-PBST [68]. The pseudoplasticity indices were 0.86, 0.66, and 0.60 for LCB2-PBST-J1, LCB1-PBST-G, and LCB2-PBST-J2, respectively. According to the literature [41], this non-Newtonian behavior is the result of long-chain branching (*i.e.*, the increased molecular entanglement of the branched structure) and a broadening of the molecular weight distribution (demonstrated by SEC measurements). Such behavior has been correlated with better melt processability by film blowing and extrusion foaming by gas injection (the increased elasticity would hinder the cell coalescence and cell wall rupture) [48, 67, 68].

The relaxation spectra $H(\lambda)$ at 180 °C of as-produced PBST were calculated from G' data using the standard nonlinear regularization method proposed by Honerkamp and Weese [69]. Results are shown in Figure 7c. The relaxation peak of L-PBST cannot

be identified in the frequency range studied. The relaxation time of L-PBST was consequently very fast and probably lower than 0.01 s. However, two relaxation peaks were clearly attested for LCB-PBST-G, with a first peak close to 0.15 s and a second close to 1 s. This phenomenon can be interpreted by the presence of two modes of relaxation, with a first relaxation mode corresponding to the relaxation of LCB and a second relaxation mode corresponding to the PBST backbone with restricted mobility [23, 67]. These phenomena clearly attested to the presence of LCB in low amounts along the PBST backbone. LCB2-PBST-J1 displayed a unique relaxation peak close to 0.9 s, and the relaxation peak of LCB2-PBST-J2 cannot be identified in the frequency range studied. The presence of complex LCB architectures without relaxation modes for the PBST backbone was thus suspected for LCB2-PBST-J1/2 [28, 70].

Figure 8 shows the results of the reduced Van-Gurp–Palmen diagram (rVGP) at 180 °C of as-produced PBST. An rVGP diagram is made up with loss angle δ against the reduced modulus G_{red} (complex modulus G^* divided by the plateau modulus G_{N}^0 , evaluated at high frequencies when phase angle δ tends to 0). According to Trinkle *et al.* [71], the shape of the rVGP diagram is unaffected by the molecular weight, but the polydispersity index/LCB architectures have specific signatures [28, 70]. The rVGP diagram is consequently a clear way to assess chain topologies. It is clear that L-PBST displayed a viscous behavior at low G_{red} . The phase angle sharply decreased for G_{red} values above approx. 0.1 as a typical signature of linear thermoplastic polymers with a narrow polydispersity index [71]. The rheological responses of L-PBST (frequency sweeps, relaxation spectra, and rVGP diagram) were consistent with previous conclusions by SEC (moderate molecular weight, narrow polydispersity index, and linear architectures). For LCB1-PBST-G, the phase angle started to decrease for G_{red} values above 0.01 and the phase angle drop was slightly broader than that of L-PBST. This rVGP behavior can be mainly ascribed to the high polydispersity of LCB1-PBST-G. A slight inflection point was noticed for phase angle close to 50° and G_{red} close to 1. No clear similitude with model chain topology was attested but this critical point of low intensity could correspond to comb-like architectures with LCB and PBST backbones displaying similar molecular weights [71]. The LCB density along the PBST backbone is probably quite low. The

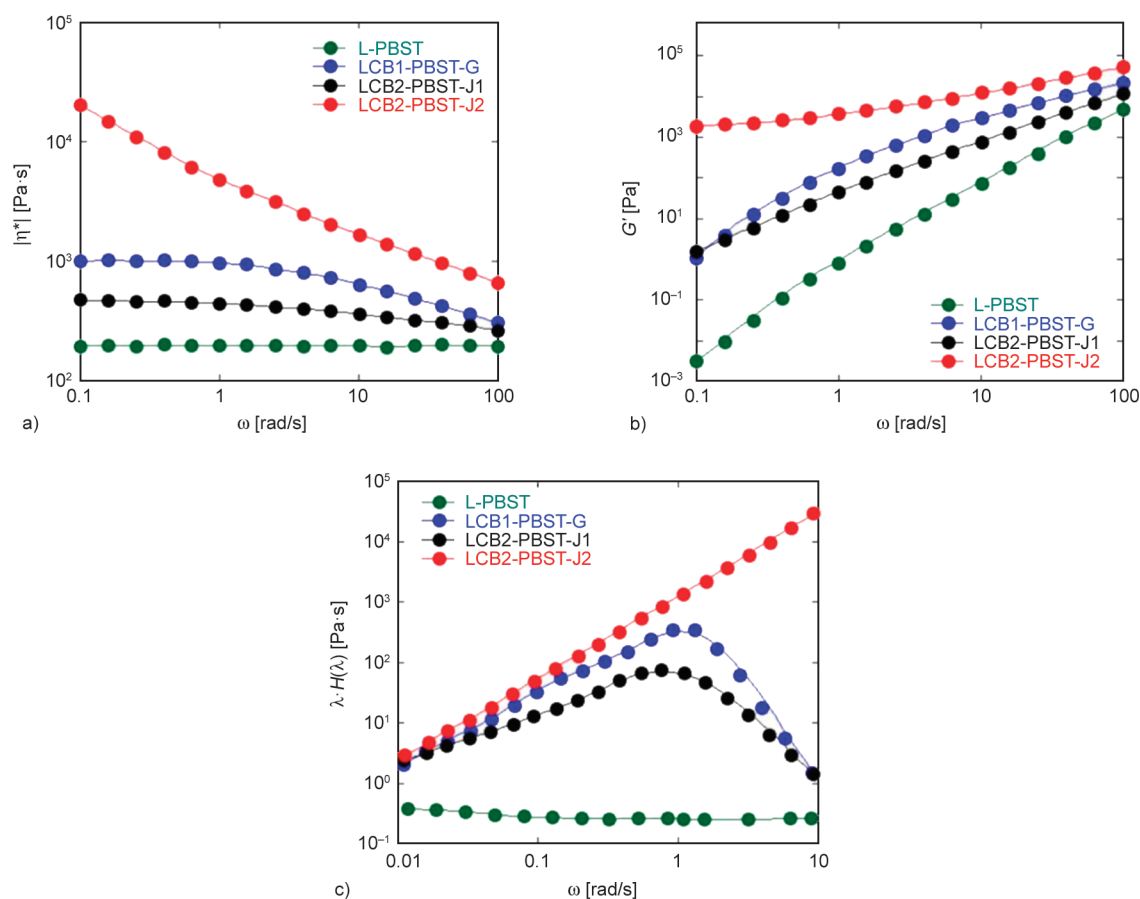


Figure 7. Complex viscosity (a) and storage modulus (b) at 180 °C of as-prepared PBST. Weighted relaxation time spectrum at 180 °C of as-prepared PBST (c).

rheological responses of LCB1-PBST-G consequently fitted with previous conclusions by SEC (high/broad molecular weight, presence of LCB in low amount, statistical/homogeneous distribution of LCB along the PBST backbone, similar molecular weights for LCB/backbone). It could be also noticed that the rVGP diagram was quite similar to that of strain-hardening metallocene polyethylene [72], indicating that the rheological response in elongational conditions of LCB1-PBST-G could be of good interest.

Concerning LCB2-PBST-J1 and LCB2-PBST-J2, the rVGP diagrams were quite different from those of LCB1-PBST-G. LCB1-PBST-J1 displayed a mixed behavior between L-PBST and LCB1-PBST-G. The presence of LCB was suspected in a low amount, along with unreacted L-PBST. No inflection was noticed for LCB1-PBST-J1. LCB2-PBST-J2 displayed phase angles lower than 40–50° for any G_{red} . The phase angle also decreased in the low G_{red} region with maximum observed for G_{red} values close to 0.2. This behavior was in agreement with an elastic

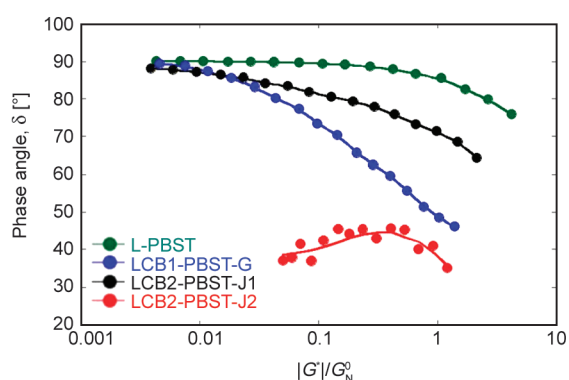


Figure 8. Reduced Van–Gurp–Palmen diagram at 180 °C of as-prepared PBST.

behavior at low frequencies and, according to Trinkle *et al.* [71], this rVGP diagram probably fitted with star-like LCB architectures with high entanglement density. The rheological responses of LCB2-PBST-J1 and LCB2-PBST-J2 could consequently agree with previous conclusions by SEC (residual L-PBST fraction, the appearance of LCB-PBST structures with a high LCB density, partial gelification/cross-linking).

3.4. Elongational rheological behavior of as-prepared LCB-PBST

LCB architectures are known to improve the rheological behavior of polymer melts in elongational flow conditions marked by higher melt strengths (or transient elongational viscosity) and the appearance of a strain hardening phenomenon. Processing defects and instabilities are drastically reduced for polymers displaying LCB architectures, in particular during extrusion processing (extrusion casting/calendarizing, extrusion blowing, co-extrusion, extrusion blow molding, *etc.*) [11]. In this context, the rheological behavior of as-prepared LCB-PBST in elongational conditions was investigated to identify their processability potential by extrusion.

LCB-PBST were uniaxially-stretched in the molten state at 180 °C at different strain rates (between 0.1 and 1 s⁻¹) in order to assess their transient elongational viscosity (η_E) as a function of stretching time (Figure 9). The transient elongational viscosity of L-PBST could not be evaluated due to a poor melt strength inducing an intensive creep before stretching in the melt state. Such behavior is typically observed with thermoplastic polymers displaying moderate molecular weights and linear architectures

[11, 26]. These materials do not exhibit any strain hardening phenomena in elongational flow conditions [11, 26], and as-prepared L-PBST is consequently of poor interest for further processing by extrusion.

Concerning LCB2-PBST-J1, a significant melt strength was obtained with a transient elongational viscosity close to 2000–3000 Pa·s at 0.1 s⁻¹. However, no strain hardening phenomenon was detected at any strain rate. The amount of LCB was, therefore, not sufficient to induce strong modifications of the rheological behavior in elongational flow conditions. However, LCB2-PBST-J2 displayed a high melt strength close to 10 000 Pa·s at a low stretching time for any strain rate with an intense strain hardening. Such behavior indicates that LCB2-PBST-J2 exhibits relaxation times higher than approx. 1 s [73], in accordance with previous rheological behavior in shear conditions. As a consequence, the two-step synthesis route requires Joncryl[®] concentrations close to 2 wt% to produce LCB-PBST with a suitable rheological behavior for further extrusion processing due to adequate LCB architectures (amount/topology). LCB1-PBST-G interestingly displayed a high melt strength close to 8000–10 000 Pa·s at a low stretching time. A strain hardening phenomenon

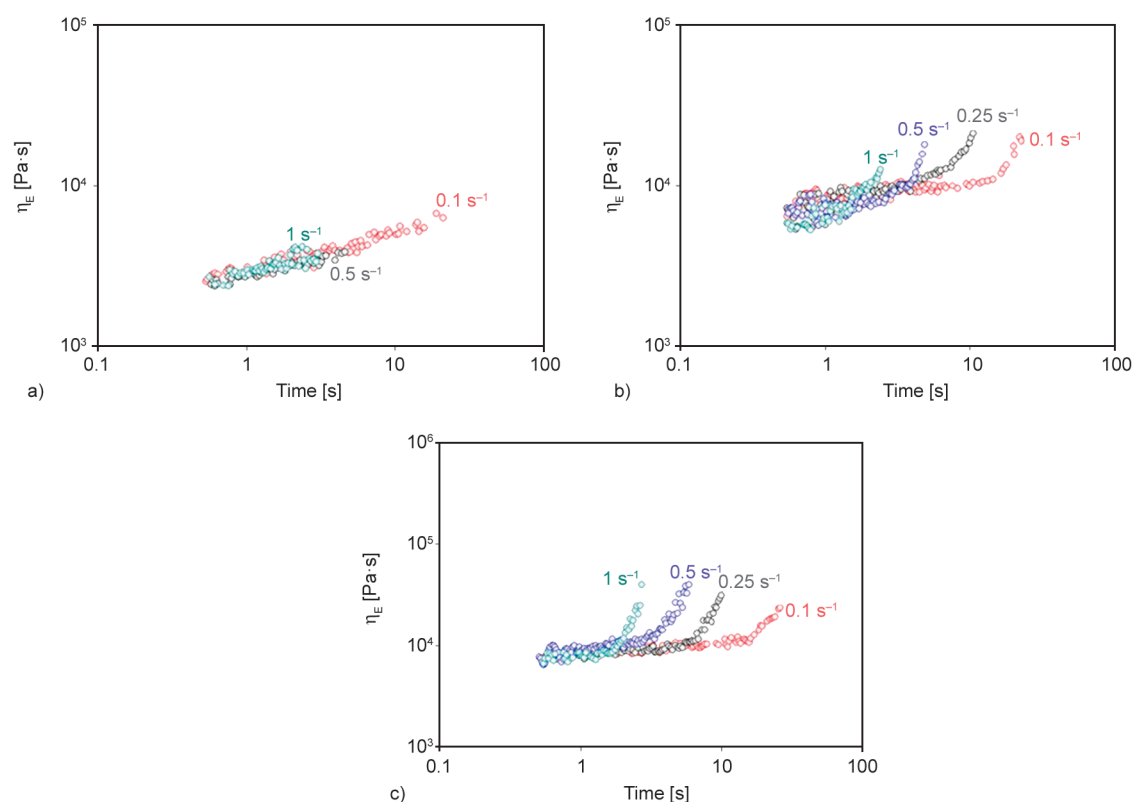


Figure 9. Transient elongational viscosity at 180 °C as a function of stretching time and strain rate for LCB2-PBST-J1 (a), LCB1-PBST-G (b), and LCB2-PBST-J2 (c).

was also observed with a slightly lower intensity than that of LCB2-PBST-J2. These observations were in accordance with the rheological behavior in shear conditions of LCB1-PBST-G, in particular, the detection of relaxation times higher than 1 s. Nevertheless, the pronounced elongational features of LCB1-PBST-G compared to L-PBST could eventually significantly improve stretching ability, stability in thickness, and resistance to melting breakup for processing applications (*e.g.*, extrusion film blowing) where the strain hardening plays an important role [74, 75].

4. Conclusions

Highly-biobased poly(butylene succinate-*co*-terephthalate) (PBST) (potential biobased content close to 85%) with processing temperatures close to those of commodity polymers (160–180 °C) and long-chain branched (LCB) architectures were successfully synthesized by various strategies. The two-step synthesis route starting from linear PBST produced by polycondensation followed by reactive extrusion required a concentration of Joncryl® close to 2 wt% to improve melt strength properties of PBST and induce strain hardening phenomenon effects in elongational conditions.

In this context, it could be concluded that LCB-PBST with an appropriate rheological behavior for further extrusion processing could be directly obtained without any additional post-treatments by reactive extrusion by the one-step synthesis route using glycerol in low concentration (up to 0.5 wt%) during PBST polycondensation. The use of Joncryl® with intense rheological instabilities (*e.g.*, the melt reaction that often continues over time with the unpredictable process and end-product characteristics) in addition to gel formation (problematic recycling capabilities) could be particularly avoided with this approach. The peculiar LCB architecture (high/broad molecular weight, statistical/homogeneous distribution of LCB along the PBST backbone without the formation of gels) probably represents a key element to reaching such rheological behavior due to a significant modification of relaxation dynamics of the PBST backbone.

This work provided an effective approach based on the one-step synthesis method to improve the melt strength of highly-biobased aliphatic-aromatic copolyesters and eliminate extrusion defects/instabilities of PBST using glycerol as a promising long-chain

branching agent. This may expand the industrial implementation of these polymers with modern continuous technology production into high-value packaging applications.

Acknowledgements

The authors gratefully acknowledge Ms. Agnes Crepet from the University Claude Bernard Lyon 1 and Mr. Ahmed Belhadj from INSA Lyon for their experimental support and recommendations regarding the SEC-MALS and gel determination measurements. The authors acknowledge the European Community (FEDER funds) and the International Campus on Safety and Intermodality in Transportation (CISIT, France) as well as the Hauts-de-France Region (France) for the financial contribution of the dynamic rheometer and extrusion machines.

References

- [1] Marinova D., Bogueva D.: Reducing food waste and packaging. in ‘Food in a planetary emergency’ (eds.: Marinova D., Bogueva D.) Springer, Singapore, 57–72 (2022).
https://doi.org/10.1007/978-981-16-7707-6_4
- [2] Shi Y., Zheng C., Zhu G., Ren Y., Liu L-Z., Zhang W., Han L.: A heat initiated 3D shape recovery and biodegradable thermoplastic tolerating a strain of 5. *Reactive and Functional Polymers*, **154**, 104680 (2020).
<https://doi.org/10.1016/j.reactfuncpolym.2020.104680>
- [3] Jacquelin N., Saint-Loup R., Pascault J-P., Rousseau A., Fenouillot F.: Bio-based alternatives in the synthesis of aliphatic–aromatic polyesters dedicated to biodegradable film applications. *Polymer*, **59**, 234–242 (2015).
<https://doi.org/10.1016/j.polymer.2014.12.021>
- [4] Li F., Luo S., Ma C., Yu J., Cao A.: The crystallization and morphology of biodegradable poly(butylene succinate-*co*-terephthalate) copolyesters with high content of BT units. *Journal of Applied Polymer Science*, **118**, 623–630 (2010).
<https://doi.org/10.1002/app.32381>
- [5] Tsai P-H., Wang C-H., Kan L-S., Chen C. W.: Studies on the optimal conditions for synthesizing poly(butylene succinate-*co*-terephthalate) copolyesters with targeted properties. *Asia-Pacific Journal of Chemical Engineering*, **7**, S88-S94 (2012).
<https://doi.org/10.1002/apj.645>
- [6] Honda N., Taniguchi I., Miyamoto M., Kimura Y.: Reaction mechanism of enzymatic degradation of poly(butylene succinate-*co*-terephthalate) (PBST) with a lipase originated from *Pseudomonas cepacia*. *Macromolecular Bioscience*, **3**, 189–197 (2003).
<https://doi.org/10.1002/mabi.200390023>
- [7] Qin P., Wu L., Li B., Li N., Pan X., Dai J.: Superior gas barrier properties of biodegradable PBST vs. PBAT copolyesters: A comparative study. *Polymers*, **13**, 3449 (2021).
<https://doi.org/10.3390/polym13193449>

- [8] Li F., Luo S., Zhang J., Yu J.: Temperature dependences of solid structure and properties of biodegradable poly(butylene succinate-*co*-terephthalate) (PBST) copolyester. *Journal of Thermal Analysis and Calorimetry*, **113**, 915–921 (2013).
<https://doi.org/10.1007/s10973-012-2772-x>
- [9] Zhang J., Wang X., Li F., Yu J.: Mechanical properties and crystal structure transition of biodegradable poly(butylene succinate-*co*-terephthalate) (PBST) fibers. *Fibers and Polymers*, **13**, 1233–1238 (2012).
<https://doi.org/10.1007/s12221-012-1233-2>
- [10] Xu M., Lu J., Zhao J., Wei L., Liu T., Zhao L., Park C. B.: Rheological and foaming behaviors of long-chain branched polyamide 6 with controlled branch length. *Polymer*, **224**, 123730 (2021).
<https://doi.org/10.1016/j.polymer.2021.123730>
- [11] Candal M. V., Safari M., Fernández M., Otaegi I., Múgica A., Zubitur M., Gerrica-Echevarria G., Sebastián V., Irusta S., Loaeza D., Maspoch M. L., Santana O. O., Müller A. J.: Structure and properties of reactively extruded opaque post-consumer recycled PET. *Polymers*, **13**, 3531 (2021).
<https://doi.org/10.3390/polym13203531>
- [12] Seo Y. P., Seo Y.: Effect of molecular structure change on the melt rheological properties of a polyamide (nylon 6). *ACS omega*, **3**, 16549–16555 (2018).
<https://doi.org/10.1021/acsomega.8b02355>
- [13] Larson R. G., Zhou Q., Shanbhag S., Park S. J.: Advances in modeling of polymer melt rheology. *AIChE Journal*, **53**, 542–548 (2007).
<https://doi.org/10.1002/aic.11064>
- [14] Liu J., Yu W., Zhou C.: Polymer chain topological map as determined by linear viscoelasticity. *Journal of Rheology*, **55**, 545–570 (2011).
<https://doi.org/10.1122/1.3569136>
- [15] Narimissa E., Wagner M. H.: Review on tube model based constitutive equations for polydisperse linear and long-chain branched polymer melts. *Journal of Rheology*, **63**, 361–375 (2019).
<https://doi.org/10.1122/1.5064642>
- [16] Al-Itry R., Lamnawar K., Maazouz A.: Biopolymer blends based on poly(lactic acid): Shear and elongation rheology/structure/blowing process relationships. *Polymers*, **7**, 939–962 (2015).
<https://doi.org/10.3390/polym7050939>
- [17] Sugimoto M., Tanaka T., Masubuchi Y., Takimoto J-I., Koyama K.: Effect of chain structure on the melt rheology of modified polypropylene. *Journal of Applied Polymer Science*, **73**, 1493–1500 (1999).
[https://doi.org/10.1002/\(SICI\)1097-4628\(19990822\)73:8<1493::AID-APP18>3.0.CO;2-2](https://doi.org/10.1002/(SICI)1097-4628(19990822)73:8<1493::AID-APP18>3.0.CO;2-2)
- [18] Yan D., Wang W-J., Zhu S.: Effect of long chain branching on rheological properties of metallocene polyethylene. *Polymer*, **40**, 1737–1744 (1999).
[https://doi.org/10.1016/S0032-3861\(98\)00318-8](https://doi.org/10.1016/S0032-3861(98)00318-8)
- [19] Romanini D., Savadori A., Gianotti G.: Long chain branching in low density polyethylene: 2. Rheological behaviour of the polymers. *Polymer*, **21**, 1092–1101 (1980).
[https://doi.org/10.1016/0032-3861\(80\)90045-2](https://doi.org/10.1016/0032-3861(80)90045-2)
- [20] Forsythe J. S., Cheah K., Nisbet D. R., Gupta R. K., Lau A., Donovan A. R., O'Shea M. S., Moad G.: Rheological properties of high melt strength poly(ethylene terephthalate) formed by reactive extrusion. *Journal of Applied Polymer Science*, **100**, 3646–3652 (2006).
<https://doi.org/10.1002/app.23166>
- [21] Cao K., Li Y., Lu Z-Q., Wu S-L., Chen Z-H., Yao Z., Huang Z-M.: Preparation and characterization of high melt strength polypropylene with long chain branched structure by the reactive extrusion process. *Journal of Applied Polymer Science*, **121**, 3384–3392 (2011).
<https://doi.org/10.1002/app.34007>
- [22] Stanic S., Gottlieb G., Koch T., Göpperl L., Schmid K., Knaus S., Archodoulaki V-M.: Influence of different types of peroxides on the long-chain branching of PP *via* reactive extrusion. *Polymers*, **12**, 886 (2020).
<https://doi.org/10.3390/polym12040886>
- [23] Corre Y-M., Duchet J., Reignier J., Maazouz A.: Melt strengthening of poly(lactic acid) through reactive extrusion with epoxy-functionalized chains. *Rheologica Acta*, **50**, 613–629 (2011).
<https://doi.org/10.1007/s00397-011-0538-1>
- [24] Wang L., Jing X., Cheng H., Hu X., Yang L., Huang Y.: Blends of linear and long-chain branched poly(L-lactide)s with high melt strength and fast crystallization rate. *Industrial and Engineering Chemistry Research*, **51**, 10088–10099 (2012).
<https://doi.org/10.1021/ie300526u>
- [25] Zhang H., Bai H., Liu Z., Zhang Q., Fu Q.: Toward high-performance poly(L-lactide) fibers *via* tailoring crystallization with the aid of fibrillar nucleating agent. *ACS Sustainable Chemistry and Engineering*, **4**, 3939–3947 (2016).
<https://doi.org/10.1021/acssuschemeng.6b00784>
- [26] Dadouche T., Yousfi M., Samuel C., Lacrampe M-F., Soulestin J.: (Nano)fibrillar morphology development in biobased poly(butylene succinate-*co*-adipate)/poly(amide-11) blown films. *Polymer Engineering and Science*, **61**, 1324–1337 (2021).
<https://doi.org/10.1002/pen.25645>
- [27] Yousfi M., Dadouche T., Chomat D., Samuel C., Soulestin J., Lacrampe M-F., Krawczak P.: Development of nanofibrillar morphologies in poly(L-lactide)/poly(amide) blends: Role of the matrix elasticity and identification of the critical shear rate for the nodular/fibrillar transition. *RSC Advances*, **8**, 22023–22041 (2018).
<https://doi.org/10.1039/C8RA03339K>

- [28] Yousfi M., Soulestin J., Marcille S., Lacrampe M-F.: *In-situ* nano-fibrillation of poly(butylene succinate-co-adipate) in isosorbide-based polycarbonate matrix. Relationship between rheological parameters and induced morphological and mechanical properties. *Polymer*, **217**, 123445 (2021). <https://doi.org/10.1016/j.polymer.2021.123445>
- [29] Zhang Z., Wan D., Xing H., Zhang Z., Tan H., Wang L., Zheng J., An Y., Tang T.: A new grafting monomer for synthesizing long chain branched polypropylene through melt radical reaction. *Polymer*, **53**, 121–129 (2012). <https://doi.org/10.1016/j.polymer.2011.11.033>
- [30] Wang L., Jing X., Cheng H., Hu X., Yang L., Huang Y.: Rheology and crystallization of long-chain branched poly(L-lactide)s with controlled branch length. *Industrial and Engineering Chemistry Research*, **51**, 10731–10741 (2012). <https://doi.org/10.1021/ie300524j>
- [31] Wei L., McDonald A. G.: Peroxide induced cross-linking by reactive melt processing of two biopolyesters: Poly(3-hydroxybutyrate) and poly(L-lactic acid) to improve their melting processability. *Journal of Applied Polymer Science*, **132**, 41724 (2015). <https://doi.org/10.1002/app.41724>
- [32] Przybysz-Romatowska M., Haponiuk J., Formela K.: Reactive extrusion of biodegradable aliphatic polyesters in the presence of free-radical-initiators: A review. *Polymer Degradation and Stability*, **182**, 109383 (2020). <https://doi.org/10.1016/j.polymdegradstab.2020.109383>
- [33] Reichert C. L., Bugnicourt E., Coltelli M-B., Cinelli P., Lazzeri A., Canesi I., Braca F., Martínez B. M., Alonso R., Agostinis L., Verstichel S., Six L., de Mets S., Gómez E. C., Ißbrücker C., Geerinck R., Nettleton D. F., Campos I., Sauter E., Pieczyk P., Schmid M.: Bio-based packaging: Materials, modifications, industrial applications and sustainability. *Polymers*, **12**, 1558 (2020). <https://doi.org/10.3390/polym12071558>
- [34] Al-Itry R., Lamnawar K., Maazouz A.: Improvement of thermal stability, rheological and mechanical properties of PLA, PBAT and their blends by reactive extrusion with functionalized epoxy. *Polymer Degradation and Stability*, **97**, 1898–1914 (2012). <https://doi.org/10.1016/j.polymdegradstab.2012.06.028>
- [35] Li S., He G., Liao X., Park C. B., Yang Q., Li G.: Introduction of a long-chain branching structure by ultraviolet-induced reactive extrusion to improve cell morphology and processing properties of polylactide foam. *RSC Advances*, **7**, 6266–6277 (2017). <https://doi.org/10.1039/C6RA26457C>
- [36] Sun Y., Wu L., Bu Z., Li B-G., Li N., Dai J.: Synthesis and thermomechanical and rheological properties of biodegradable long-chain branched poly(butylene succinate-co-butylene terephthalate) copolyesters. *Industrial and Engineering Chemistry Research*, **53**, 10380–10386 (2014). <https://doi.org/10.1021/ie501504b>
- [37] Lu J., Wu L., Li B-G.: Long chain branched poly(butylene succinate-co-terephthalate) copolyesters using pentaerythritol as branching agent: Synthesis, thermo-mechanical, and rheological properties. *Journal of Applied Polymer Science*, **134**, 44544 (2017). <https://doi.org/10.1002/app.44544>
- [38] Quiles-Carrillo L., Fenollar O., Balart R., Torres-Giner S., Rallini M., Dominici F., Torre L.: A comparative study on the reactive compatibilization of melt-processed polyamide 1010/polylactide blends by multi-function-alized additives derived from linseed oil and petroleum. *Express Polymer Letters*, **14**, 583–604 (2020). <https://doi.org/10.3144/expresspolymlett.2020.48>
- [39] Cailloux J., Santana O. O., Franco-Urquiza E., Bou J. J., Carrasco F., Gámez-Pérez J., MasPOCH M. L.: Sheets of branched poly(lactic acid) obtained by one step reactive extrusion calendaring process: Melt rheology analysis. *Express Polymer Letters*, **7**, 304–318 (2013). <https://doi.org/10.3144/expresspolymlett.2013.27>
- [40] Celli A., Marchese P., Sullalti S., Berti C., Barbiroli G., Commereuc S., Verney V.: Preparation of new biobased polyesters containing glycerol and their photodurability for outdoor applications. *Green Chemistry*, **14**, 182–187 (2012). <https://doi.org/10.1039/C1GC15973A>
- [41] Härth M., Kaschta J., Schubert D. W.: Shear and elongational flow properties of long-chain branched poly(ethylene terephthalates) and correlations to their molecular structure. *Macromolecules*, **47**, 4471–4478 (2014). <https://doi.org/10.1021/ma5002657>
- [42] Ren L., Wang Y., Ge J., Lu D., Liu Z.: Enzymatic synthesis of high-molecular-weight poly(butylene succinate) and its copolymers. *Macromolecular Chemistry and Physics*, **216**, 636–640 (2015). <https://doi.org/10.1002/macp.201400550>
- [43] Wang J-M., Ding S-J., Wu T-M.: Rheology, crystallization behavior, and mechanical properties of poly(butylene succinate-co-terephthalate)/cellulose nanocrystal composites. *Polymer Testing*, **87**, 106551 (2020). <https://doi.org/10.1016/j.polymertesting.2020.106551>
- [44] Garin M., Tighzert L., Vroman I., Marinkovic S., Estrine B.: The influence of molar mass on rheological and di-lute solution properties of poly(butylene succinate). *Journal of Applied Polymer Science*, **131**, 40887 (2014). <https://doi.org/10.1002/app.40887>
- [45] Härth M., Dörnhöfer A.: Film blowing of linear and long-chain branched poly(ethylene terephthalate). *Poly-mers*, **12**, 1605 (2020). <https://doi.org/10.3390/polym12071605>
- [46] Charlier Q., Girard E., Freyermouth F., Vandesteene M., Jacquelin N., Ladavière C., Rousseau A., Fenouillot F.: Solution viscosity – molar mass relationships for poly(butylene succinate) and discussion on molar mass analysis. *Express Polymer Letters*, **9**, 424–434 (2015). <https://doi.org/10.3144/expresspolymlett.2015.41>

- [47] Härth M., Dörnhöfer A., Kaschta J., Münstedt H., Schubert D. W.: Molecular structure and rheological properties of a poly(ethylene terephthalate) modified by two different chain extenders. *Journal of Applied Polymer Science*, **138**, 50110 (2021).
<https://doi.org/10.1002/app.50110>
- [48] Nifant'ev I. E., Bagrov V. V., Komarov P. D., Ilyin S. O., Ivchenko P. V.: The use of branching agents in the synthesis of PBAT. *Polymers*, **14**, 1720 (2022).
<https://doi.org/10.3390/polym14091720>
- [49] Standau T., Nofar M., Dörr D., Ruckdäschel H., Altstädt V.: A review on multifunctional epoxy-based Joncryl[®] ADR chain extended thermoplastics. *Polymer Reviews*, **62**, 296–350 (2022).
<https://doi.org/10.1080/15583724.2021.1918710>
- [50] Jie Z., Fa-xue L., Jiang-yong Y.: Multiple melting behavior of biodegradable poly(butylene succinate-co-terephthalate) (PBST) copolyester. *Journal of Thermal Analysis and Calorimetry*, **111**, 711–715 (2013).
<https://doi.org/10.1007/s10973-012-2229-2>
- [51] Li F., Xu X., Hao Q., Li Q., Yu J., Cao A.: Effects of comonomer sequential structure on thermal and crystallization behaviors of biodegradable poly(butylene succinate-co-butylene terephthalate)s. *Journal of Polymer Science Part B: Polymer Physics*, **44**, 1635–1644 (2006).
<https://doi.org/10.1002/polb.20797>
- [52] Luo S., Li F., Yu J., Cao A.: Synthesis of poly(butylene succinate-co-butylene terephthalate) (PBST) copolyesters with high molecular weights *via* direct esterification and polycondensation. *Journal of Applied Polymer Science*, **115**, 2203–2211 (2010).
<https://doi.org/10.1002/app.31346>
- [53] Luo S., Li F., Yu J.: The thermal, mechanical and viscoelastic properties of poly(butylene succinate-co-terephthalate) (PBST) copolyesters with high content of BT units. *Journal of Polymer Research*, **18**, 393–400 (2011).
<https://doi.org/10.1007/s10965-010-9429-x>
- [54] Wojtczak M., Dutkiewicz S., Galeski A., Gutowska A.: Classification of aliphatic-butylene terephthalate copolyesters in relation to aliphatic/aromatic ratio. *Polymer*, **113**, 119–134 (2017).
<https://doi.org/10.1016/j.polymer.2017.02.054>
- [55] Zheng C., Zhu G., Shi Y., Liu L.-Z., Ren M., Zhang W., Han L.: Crystallization, structures and properties of biodegradable poly(butylene succinate-co-butylene terephthalate) with a symmetric composition. *Materials Chemistry and Physics*, **260**, 124183 (2021).
<https://doi.org/10.1016/j.matchemphys.2020.124183>
- [56] Ishioka R., Kitakuni E., Ichikawa Y.: Aliphatic polyesters: 'Bionolle'. in 'Biopolymers online' (eds.: Hofrichter M., Steinbüchel A.) Wiley-VCH, Weinheim, Vol 4, 275–297 (2002).
<https://doi.org/10.1002/3527600035.bpo14010>
- [57] Duborper C., Samuel C., Akue-Asseko A. C., Loux C., Lacrampe M.-F., Krawczak P.: Design of biobased poly(butylene succinate) foams by single-screw extrusion: Identification of relevant rheological parameters controlling foam morphologies. *Polymer Engineering and Science*, **58**, 503–512 (2018).
<https://doi.org/10.1002/pen.24733>
- [58] Arayesh H., Ebrahimi N. G., Khaledi B., Esfahani M. K.: Introducing four different branch structures in PET by reactive processing – A rheological investigation. *Journal of Applied Polymer Science*, **137**, 49243 (2020).
<https://doi.org/10.1002/app.49243>
- [59] Han Y.-K., Um J. W., Im S. S., Kim B. C.: Synthesis and characterization of high molecular weight branched PBA. *Journal of Polymer Science Part A: Polymer Chemistry*, **39**, 2143–2150 (2001).
<https://doi.org/10.1002/pola.1190>
- [60] Purohit P. J., Huacuja-Sánchez J. E., Wang D.-Y., Emmerling F., Thünemann A., Heinrich G., Schönhals A.: Structure–property relationships of nanocomposites based on polypropylene and layered double hydroxides. *Macromolecules*, **44**, 4342–4354 (2011).
<https://doi.org/10.1021/ma200323k>
- [61] Henton D. E., Gruber P., Lunt J., Randall J.: Polylactic acid technology. in 'Natural fibers, biopolymers, and biocomposites' (eds.: Mohanty A. K., Misra L., Drzal L. T.) Taylor and Francis, Michigan, 527–577 (2005).
<https://doi.org/10.1201/9780203508206>
- [62] Witzke D. R., Narayan R., Kolstad J. J.: Reversible kinetics and thermodynamics of the homopolymerization of L-lactide with 2-ethylhexanoic acid tin(II) salt. *Macromolecules*, **30**, 7075–7085 (1997).
<https://doi.org/10.1021/ma970631m>
- [63] Gupta M. C., Deshmukh V. G.: Thermal oxidative degradation of poly-lactic acid. Part I: Activation energy of thermal degradation in air. *Colloid and Polymer Science*, **260**, 308–311 (1982).
<https://doi.org/10.1007/BF01447969>
- [64] Sivasamy P., Palaniandavar M., Vijayakumar C., Lederer K.: The role of β -hydrogen in the degradation of polyesters. *Polymer Degradation and Stability*, **38**, 15–21 (1992).
[https://doi.org/10.1016/0141-3910\(92\)90017-Y](https://doi.org/10.1016/0141-3910(92)90017-Y)
- [65] Nguyen Q. T., Japon S., Luciani A., Leterrier Y., Månson J.-A. E.: Molecular characterization and rheological properties of modified poly(ethylene terephthalate) obtained by reactive extrusion. *Polymer Engineering and Science*, **41**, 1299–1309 (2001).
<https://doi.org/10.1002/pen.10830>
- [66] Yang Z., Xin C., Mughal W., Li X., He Y.: High-melt-elasticity poly(ethylene terephthalate) produced by reactive extrusion with a multi-functional epoxide for foaming. *Journal of Applied Polymer Science*, **135**, 45805 (2018).
<https://doi.org/10.1002/app.45805>

- [67] Dhavalikar R., Yamaguchi M., Xanthos M.: Molecular and structural analysis of a triepoxide-modified poly (ethylene terephthalate) from rheological data. *Journal of Polymer Science Part A: Polymer Chemistry*, **41**, 958–969 (2003).
<https://doi.org/10.1002/pola.10641>
- [68] Chen P., Zhao L., Gao X., Xu Z., Liu Z., Hu D.: Engineering of polybutylene succinate with long-chain branching toward high foamability and degradation. *Polymer Degradation and Stability*, **194**, 109745 (2021).
<https://doi.org/10.1016/j.polymdegradstab.2021.109745>
- [69] Honerkamp J., Weese J.: Determination of the relaxation spectrum by a regularization method. *Macromolecules*, **22**, 4372–4377 (1989).
<https://doi.org/10.1021/ma00201a036>
- [70] Maroufkhani M., Ebrahimi N. G.: Melt rheology of linear and long-chain branched polypropylene blends. *Iranian Polymer Journal*, **24**, 715–724 (2015).
<https://doi.org/10.1007/s13726-015-0357-9>
- [71] Trinkle S., Walter P., Friedrich C.: van Gorp-Palmen plot II – Classification of long chain branched polymers by their topology. *Rheologica Acta*, **41**, 103–113 (2002).
<https://doi.org/10.1007/s003970200010>
- [72] Stadler F. J., Kaschta J., Münstedt H.: Thermorheological behavior of various long-chain branched polyethylenes. *Macromolecules*, **41**, 1328–1333 (2008).
<https://doi.org/10.1021/ma702367a>
- [73] Bourg V., Valette R., le Moigne N., Jenny P., Guillard V., Bergeret A.: Shear and extensional rheology of linear and branched polybutylene succinate blends. *Polymers*, **13**, 652 (2021).
<https://doi.org/10.3390/polym13040652>
- [74] Münstedt H., Kurzbeck S., Stange J.: Importance of elongational properties of polymer melts for film blowing and thermoforming. *Polymer Engineering and Science*, **46**, 1190–1195 (2006).
<https://doi.org/10.1002/pen.20588>
- [75] Liu G., Ma H., Lee H., Xu H., Cheng S., Sun H., Chang T., Quirk R. P., Wang S-Q.: Long-chain branched polymers to prolong homogeneous stretching and to resist melt breakup. *Polymer*, **54**, 6608–6616 (2013).
<https://doi.org/10.1016/j.polymer.2013.10.007>

Research article

Tunable mechanical properties of thermoplastic foams produced by additive manufacturing

Abdullah Alduais¹, Sezer Özerinç^{1,2*}

¹Department of Mechanical Engineering, Middle East Technical University, 06800 Ankara, Turkey

²Department of Micro and Nanotechnology, Middle East Technical University, 06800 Ankara, Turkey

Received 24 June 2022; accepted in revised form 4 October 2022

Abstract. Fused deposition modeling (FDM) is a versatile additive manufacturing technique for producing polymeric parts. Incorporating a foaming agent into the filament material enables the FDM-printing of thermoplastic foams, which opens up new possibilities for achieving desired mechanical property combinations. This study explored the process-property design space of FDM-printed polylactic acid (PLA) foams. Tensile and compression specimens were produced at a wide range of printing parameters using a commercial thermoplastic filament containing a foaming agent. Increasing the nozzle temperature and decreasing the filament feed rate increased the extent of foaming. Adjustment of the nozzle temperature, feed rate, and infill ratio controlled porosity over a density range of 0.24 to 1.17 g/cm³. Tuning of the mechanical properties over an order of magnitude was demonstrated, with elastic moduli ranging from 0.24 to 3.7 GPa and tensile strength ranging from 4.2 to 34.5 MPa. The mechanical behavior closely followed the Gibson-Ashby model predictions. Foaming filaments provide a new tool for tuning the mechanical response of FDM-printed parts to achieve unique combinations of mechanical properties that are not attainable through conventional methods.

Keywords: mechanical properties, additive manufacturing, fused deposition modeling, polymer foaming, polylactic acid

1. Introduction

Material extrusion is a low-cost and easy-to-use method for the manufacturing of prototypes as well as complex load-bearing components in small quantities. When the printed material is thermoplastic, the technique is commonly referred to as fused deposition modelling (FDM) or fused filament fabrication (FFF) [1].

The FDM process, schematically described in Figure 1, is based on the thermoplastic material's melting and extrusion through a heated nozzle. The printing head deposits the molten polymer in the desired locations by moving in the XY plane. Upon completing a layer, the build plate moves down incrementally, and the process is repeated [2].

The simplicity of the FDM process makes it a cost-effective and versatile alternative for manufacturing

complex geometries in small quantities. While earlier applications have been primarily focused on prototyping, recent advances in the process and filament material technology have enabled the use of FDM-produced parts for load-bearing and impact-absorbing components [3].

Due to their desirable rheological properties and low cost, polylactic acid (PLA) and acrylonitrile butadiene styrene (ABS) have been the most commonly used filament materials in FDM. On the other hand, there have been several advancements in materials for FDM. Some examples include polymer blends such as PLA/polyhydroxyalkanoate (PHA) for improved ductility, elastomeric filaments for producing compliant and hyperelastic components, and fiber-reinforced filaments for improved strength [4].

*Corresponding author, e-mail: ozerin@metu.edu.tr

© BME-PT

Recent advances in filament fabrication technology have also enabled the production of foaming filaments. The unique nature of the foaming process during printing allows the spatial control of the porosity. The capability of printing polymeric foams and the direct control over their properties adds a new design parameter to the additive manufacturing of polymeric structures for achieving the desired combinations of stiffness, strength, and density [5].

In FDM printing of an in-situ foaming polymer, the chemical foaming agent in the filament forms gas bubbles triggered by the heating in the extrusion process [6–8]. The subsequent solidification of the printed thermoplastic provides a foam with a relatively uniform distribution of pores, analogous to the well-established foam extrusion process [9]. PLA samples produced by injection-molding foaming [10] and FDM-printed samples share similar closed-foam morphologies. Compared to microcellular injection molding [11], FDM printing with in-situ foaming tends to provide a higher number density of pores [6].

As opposed to the conventional manufacturing of polymeric foams, FDM enables the adjustment of the porosity on the fly through changes in the nozzle temperature or filament feed rate. The resulting ability to spatially control the porosity provides a unique opportunity to design mechanical responses that conventional manufacturing cannot achieve. FDM's capability of producing architected cellular structures [12, 13] complements this added feature of variable porosity, which offers a further degree of freedom in generating lightweight and compliant structures.

Thermal insulation and mechanical cushioning applications widely use conventional polymeric foams [14]. The development of superior polymeric foams, especially for functional and structural applications, is an active field of research [15]. The pore morphology and the density of foams are a complicated function of the polymer and precursor chemistry, as well as the dynamics of the cell nucleation, cell growth, and eventual stabilization of the structure through solidification [16, 17]. The mechanical response depends on the solid volume fraction and the general features of the ligament geometry, which has been widely studied through modeling [18] and experimental studies [19–21].

FDM of polymeric foams provides new possibilities for designing and manufacturing optimized structures for various applications. The foaming combined with the existing capability of FDM in producing

cellular structures can give hierarchical architectures at two different scales. Such structures enhance the performance of biomedical scaffolds [7, 22], and PLA's high biocompatibility and biodegradability make this route a readily applicable approach. In addition, the spatially tunable porosity enables the production of parts with variable stiffness, useful for implementing energy-absorbing structures and soft robotics [23].

The studies on the FDM printing of polymeric foams have focused on developing foaming technology and optimizing the synthesis process. A common approach has been to saturate the filament with CO₂, followed by the in-situ foaming during 3D printing, demonstrated for polyethyleneimine (PEI) [24, 25], and PLA [26]. The second approach has been to post-process the non-porous FDM part by applying CO₂ gas-foaming [27, 28]. For the in-situ foaming method, the current understanding regarding the effect of FDM parameters on the mechanical performance of printed parts is quite limited.

Compared to the conventional manufacturing of polymeric foams, the in-situ foaming-based FDM process exhibits additional complications regarding the process parameters. FDM-produced parts' properties strongly depend on the nozzle temperature, raster orientation, build direction, and infill ratio. While the associated process-property relationships have been investigated for common filament materials such as PLA and ABS [4, 29, 30, 31], there has not been a similar investigation for the FDM of foaming filaments.

This work investigates the process-structure-property relationships for a commercially available foaming PLA filament. The study considers the effect of nozzle temperature, infill ratio, feed rate, and printing speed on the foaming characteristics, density, and strength of the produced parts. The results provide insight into the design space offered by the FDM printing of foaming polymers.

2. Experimental details

An Ultimaker 2+ FDM 3D printer (Ultimaker B.V., Utrecht, Netherlands) printed the specimens. The filament was the commercially available LW-PLA (Colorfabb, Belfeld, Netherlands) with a diameter of 2.85 mm and a density of 1.24 g/cm³ [32]. The filament mainly consists of PLA and is designed to foam under certain printing conditions. While the manufacturer does not give detailed information about the filament formulation, a common approach is to saturate

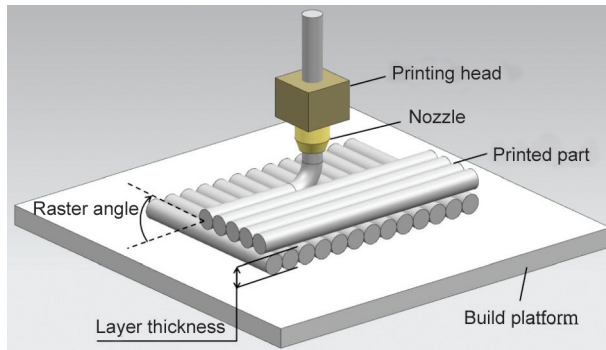


Figure 1. Schematic description of the fused deposition modeling (FDM) technique.

the filament with CO₂ or mix the filament with a chemical foaming agent, which facilitates in-situ foaming during printing [6, 24, 25].

Figure 2 shows a summary of the test specimen geometries employed. The dog bone-shaped specimens were based on the Type 4 geometry of the ASTM D638 Standard Test Method for Tensile Properties [33]. Cylindrical specimens having a diameter and height of 25.4 mm were produced for compression testing according to ASTM D1621 Standard Test Method for Compressive Properties of Rigid Cellular Plastics [34]. The third geometry was a rectangular slab with varying printing parameters over the build direction for Shore A hardness testing, according to ASTM D2240 Standard Test Method for Rubber Property – Durometer Hardness [35].

Figure 1 shows a schematic description of the printing process and indicates some process parameters. Table 1 summarizes the printing parameters that are common to all specimens. The printing trajectory

Table 1. Printing parameters that are common for all tensile and compression specimens.

Parameter	Value
Filament diameter [mm]	2.85
Filament density [g/cm ³]	1.24
Nozzle diameter [mm]	0.4, 0.6*
Nozzle temperature [°C]	215–260*
Bed temperature [°C]	60
Layer thickness [mm]	0.2–0.7 for the parametric study, 0.45 elsewhere*
Infill pattern	±45°, except for the infill ratio study with grid pattern
Infill ratio [%]	25–100 for the parametric study, 100% elsewhere*
Inwall layers	3, except the infill ratio study that used 2
Top and bottom layers	Same as other layers

*See Table 2 for further details on these parameters.

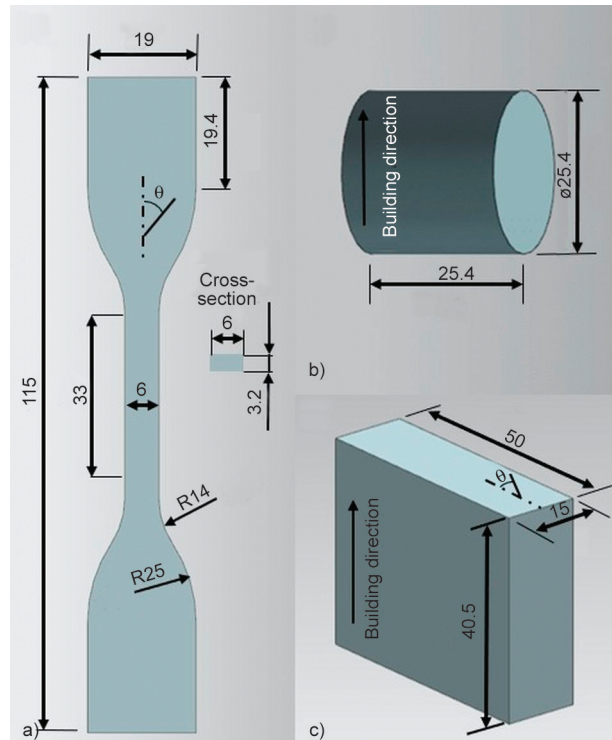


Figure 2. Schematic views of the specimen geometries. a) Tensile specimen. b) Compression specimen. c) Rectangular slab specimen with graded properties for Shore hardness measurements. All dimensions are in mm.

employed an alternating raster of $\theta = \pm 45^\circ$, as defined in Figure 2c. Other raster orientations were not considered as the primary focus of the study was on parameters that directly influence the foaming characteristics. The only exception was the grid raster type employed for the tensile specimens with varying infill ratios. At least five identical tension and compression specimens were printed for all printing parameter combinations.

The study systematically investigated the effect of nozzle temperature, layer thickness, feed rate, printing speed, and infill ratio through tension and compression tests. Table 2 summarizes the printing conditions utilized for this parametric study.

The rectangular slab specimen was printed using a nozzle temperature of 230 °C, layer thickness of 0.45 mm, printing speed of 45 mm/s, and infill ratio of 100%. The feed rate varied linearly from 20 to 100% in the build direction, according to the definition in Figure 2c.

A Zwick/Roell Z250 (ZwickRoell, Ulm, Germany) universal testing machine performed the tensile and compression tests at room temperature. The displacement rate was 5 mm/min for both cases. A Type-A hardness tester JIS (KORI SEIKI MFG, Tokyo,

Table 2. The printing conditions employed in the parametric study for tension, compression, and Shore hardness specimens.

Parameter under investigation	Range of values considered				Fixed parameters						
					ND* [mm]	NT* [°C]	LT* [mm]	FR* [%]	PS* [mm/s]	IR* [%]	IT*
NT [°C]	215	230	245	260	0.4	–	0.45	100	50	100	±45°
LT [mm]	0.2	0.35	0.5	0.7	0.6	230/245	–	100	50	100	±45°
FR [%]	100	75	50	25	0.4	230/245	0.45	–	50	100	±45°
PS [mm/s]	50	37.5	25	–	0.4	230/245	0.45	100	–	100	±45°
IR [%]	100	75	50	25	0.4	230	0.45	100	50	–	Grid
Shore hardness	Feed rate varied between 20 and 100%				0.4	230	0.45	–	50	100	±45°

*ND: nozzle diameter, NT: nozzle temperature, LT: layer thickness, FR: feed rate, PS: printing speed, IR: infill ratio, IT: infill type.

Japan) performed the Shore hardness measurements with a tip of 0.79 mm diameter.

A Nikon Eclipse E200 (Nikon, Tokyo, Japan) optical microscope imaged the specimen fracture surfaces. There was no surface preparation before imaging. An FEI Quanta 400F (FEI, Oregon, USA) scanning electron microscope (SEM) imaged selected specimens at 20 kV. Before imaging, a desktop sputter coated the specimens with 10 nm Au-Pd.

3. Results and discussion

3.1. Effect of nozzle temperature

We considered four different nozzle temperatures in the range of 215–260 °C, going beyond the recommendation by the manufacturer, 230–250 °C [32]. Figure 3 shows the tensile stress-strain data of the respective specimens. The results demonstrate the good repeatability of the measurements and the large influence of nozzle temperature on the mechanical behaviour. The tensile strength and the slope of the

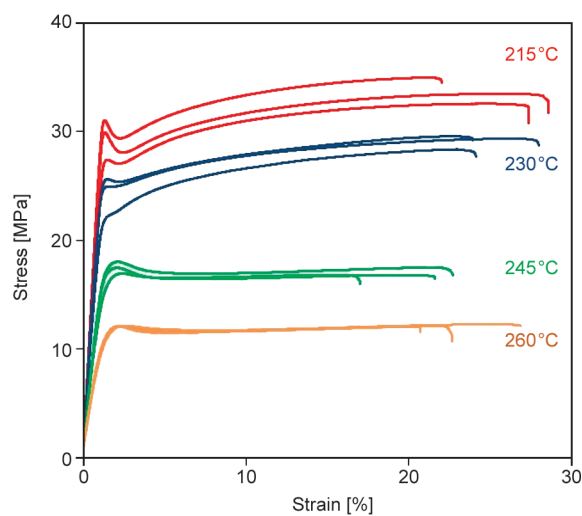


Figure 3. Representative tensile stress–tensile strain curves for specimens printed at different nozzle temperatures.

elastic response show a monotonic increase with decreasing nozzle temperature. Elongation at break remains relatively constant and does not exhibit an apparent variation.

Figure 4 shows the average mechanical properties, density, and density-specific mechanical properties as a function of nozzle temperature. Both tensile strength and elastic modulus monotonically decrease with increasing nozzle temperature. The nozzle temperature of 215 °C results in tensile strength of 33.2 MPa and an elastic modulus of 2.6 GPa. When the nozzle temperature reaches 260 °C, the strength and the modulus decrease almost by a factor of three and become 12.1 MPa, and 1.0 GPa, respectively (Figure 4a).

Elongation at break has a slightly decreasing trend with increasing nozzle temperature (Figure 4b). However, the variations are comparable to the standard deviation of the data. Density decreases monotonically with increasing nozzle temperature but at a slower rate than strength and elastic modulus.

Figure 5 shows optical microscope images of the fracture surfaces. The number density of pores increases with increasing nozzle temperature, indicating a rising extent of foaming. The fusion zones between printing lines contain fewer pores, and the fusion seems adequate, with no visible defects in either of the cases. The pores exhibit an almost perfect spherical morphology without any sign of flow-induced elongation.

Increasing nozzle temperature alters PLA's foaming characteristics. The diffusivity of the foaming agent rises with temperature and the bubble growth accelerates [36]. On the other hand, the solubility of the foaming agents usually gets lower with temperature, decreasing the number density of pores [36]. The overall effect is a rise in the porosity with temperature,

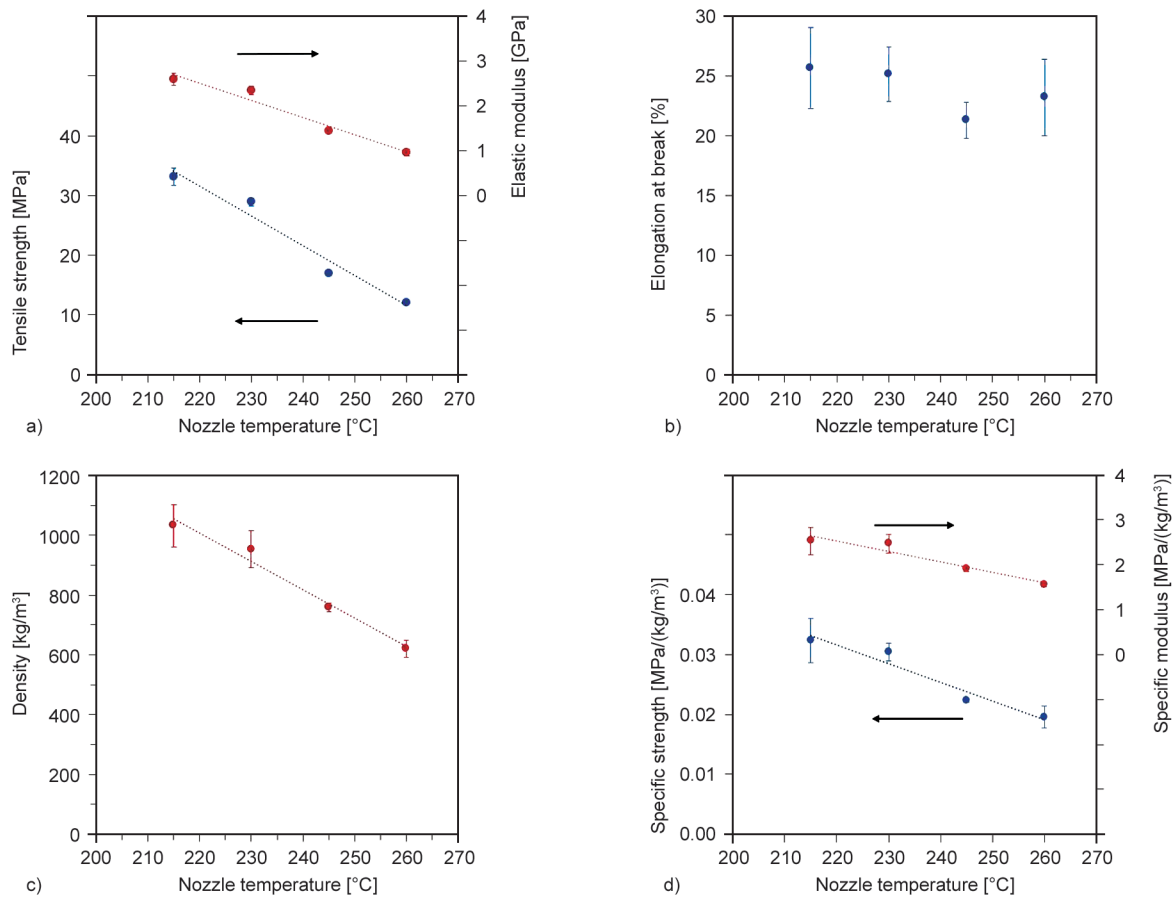


Figure 4. Effects of nozzle temperature on the density and the mechanical properties. a) Tensile strength and elastic modulus, b) elongation at break, c) density, and d) specific strength and specific modulus. The error bars represent one standard deviation.

as the increase in the bubble size is more pronounced than the decrease in the number density.

The variations in the porosity and the pore characteristics dramatically influence the mechanical properties. The density measurements (Figure 4c) and the microscope images (Figure 5) provide evidence for the monotonic rise of foaming with increasing nozzle temperature. A rising number density of pores decreases the apparent load-bearing area and reduces the strength and modulus, in agreement with the measurements. The decrease in strength is more pronounced than the elastic modulus due to the stress concentration sites introduced by the pores. A qualitative inspection of Figure 5 suggests a more rapid increase in foaming from 230 to 245 °C, which is also reflected in the measurement results presented in Figure 4.

Nozzle temperature affects the mechanical properties of non-foaming FDM-produced parts to a smaller extent. In FDM, increasing nozzle temperature increases the heat transfer to the deposition zone, which improves the quality of fusion between printed lines and layers [4, 37]. As a result, voids and gaps

that might result from poor fusion disappear, and the strength rises. However, the effect of the quality of fusion on strength is usually within 10% for 100% infill parts with quasi-isotropic raster conditions [4]. In our case, the microscope images demonstrate a good fusion between the layers even for the lowest nozzle temperature of 215 °C, eliminating the possibility of a pronounced fusion-based effect.

Lastly, nozzle temperature can also affect the printed part's crystallinity, potentially affecting the mechanical properties. For example, an increase in the nozzle temperature causes a higher cooling rate, which reduces the PLA crystallinity in PLA/PHA blend filaments [29]. However, the findings so far in the literature suggest that the crystallization-induced effects on mechanical properties are negligible in most cases. Furthermore, our DSC (data not shown here) analysis showed that the crystallinity does not vary considerably between the filament and the printed specimens for different nozzle temperatures. In addition, the specimen surfaces exhibited Fourier-transform infrared spectroscopy (FTIR) spectra that are

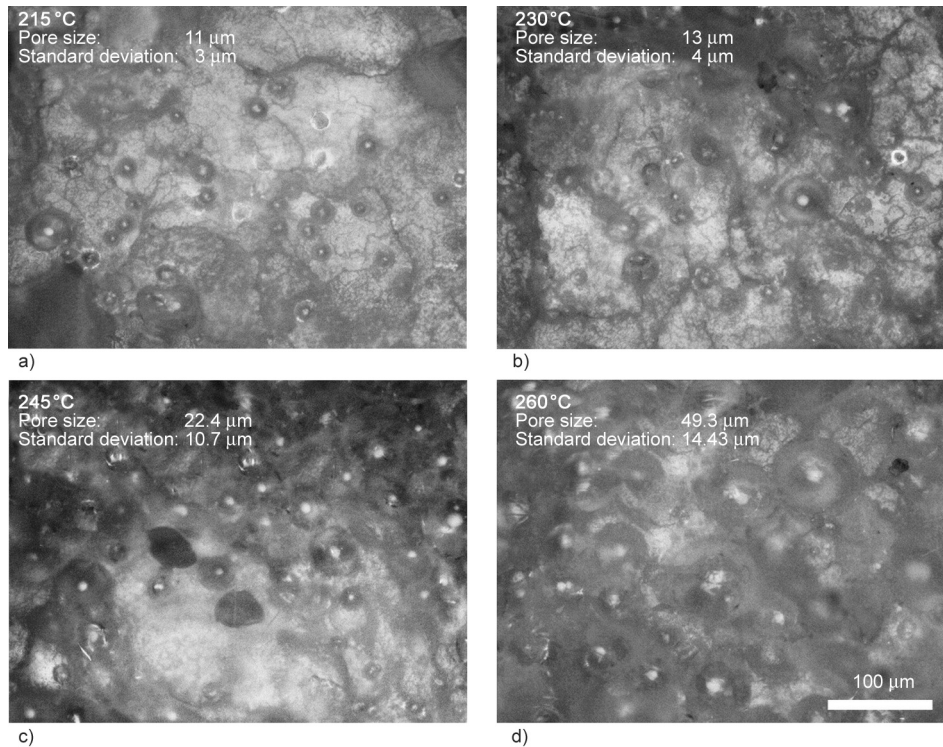


Figure 5. Optical microscope images of the printed specimens as a function of nozzle temperature. a) 215 °C, b) 230 °C, c) 245 °C, and d) 260 °C. The average pore size and its standard deviation is indicated for each case.

virtually the same as that of pure PLA, suggesting that there are no significant changes in the composition of the specimen surface (data not shown here). Therefore, we conclude that the foaming behavior is the primary cause of the observed mechanical properties variations.

As the specimens exhibit a wide range of densities, considering the specific strength and modulus values is helpful for better understanding the trends. The corresponding data in Figure 4d demonstrates that the specific strength and modulus decrease as the nozzle temperature increases and the density decreases. The drops in strength and modulus are more significant beyond 230 °C, suggesting that the pores' interaction and coalescence play a role in further weakening the porous structure [38].

3.2. Effect of filament feed rate

The filament feed rate defines the filament flow rate into the printing head. Most FDM printers automatically adjust the feed rate through their feeder mechanism to ensure continuous filling of the printing trajectory for a given nozzle diameter, printing speed, and layer thickness. The feed rate is usually defined in percentages, where 100% corresponds to the default flow rate that ensures continuous and void-free printing. While printing with conventional filaments,

the default feed rate of 100% does not need further adjustments. However, for the printing of the foaming PLA, feed rate becomes a very powerful tool to tune the extent of foaming. Figure 6 shows the four feed rates considered in this part and the corresponding flow rates calculated by measuring the total filament consumption and printing time in a build.

Figure 7 shows specimens' density and mechanical properties as a function of feed rate for two different

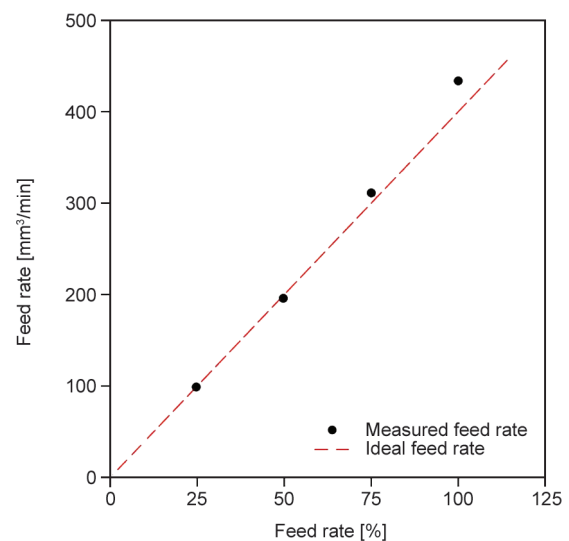


Figure 6. Relationship between the feed rate and measured filament flow rate for a nozzle diameter of 0.4 mm and a printing speed of 50 mm/s.

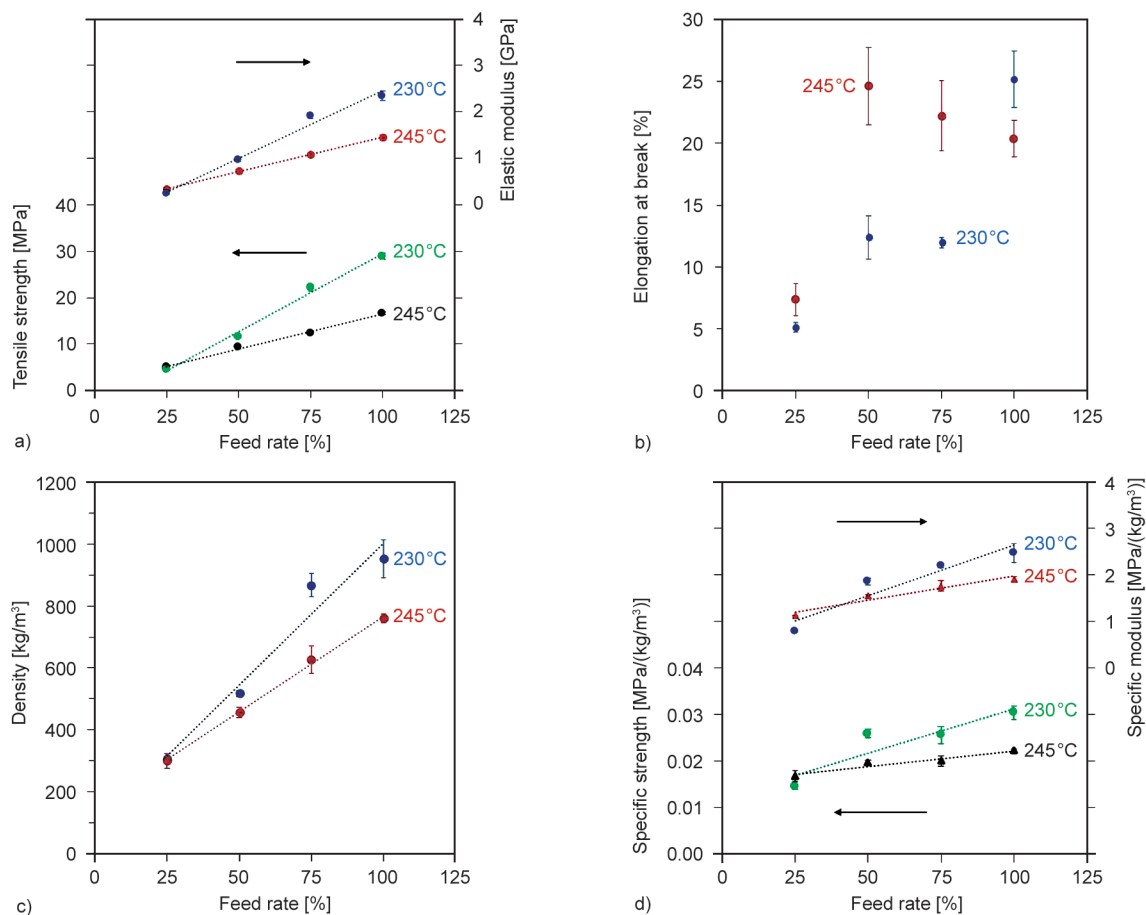


Figure 7. Effects of feed rate on the density and the mechanical properties. a) Tensile strength and elastic modulus, b) elongation at break, c) density, d) specific tensile strength and elastic modulus. Each plot shows the results for two different nozzle temperatures of 230 and 245 °C.

nozzle temperatures, namely, 230 and 245 °C. Density, tensile strength, and elastic modulus increase sharply as the feed rate increases for both cases of nozzle temperatures. For the case of 230 °C, the dependence of the properties on feed rate is more pronounced. As the feed rate increases from 25 to 100%, tensile strength increases by a factor of about 6.5, and the rise in the elastic modulus reaches almost an order of magnitude.

Elongation at break varies with feed rate differently for the nozzle temperatures of 230 and 245 °C. At 230 °C, elongation at break improves as the feed rate increases. For 245 °C, the elongation at break is around 25% for feed rates of 50% and higher and then exhibits a rapid drop to below 10% for the feed rate of 25%.

Figure 8 shows SEM images of the fracture surfaces of selected specimens printed at different feed rates. As the feed rate decreases, the number density of pores increases, and the layer interfaces start showing some gaps and defects.

Feed rate has a dramatic effect on the density and mechanical properties of the specimens. A low feed rate increases the travel time of the polymer through the hot zone and provides extra time for further gasification and porosity formation [39]. The resulting porosity reduces the printed parts' density and load-bearing capacity.

The effect of feed rate on density and mechanical properties is more severe for the nozzle temperature of 230 °C. Figure 7d shows the specific strength and modulus, indicating that even the density-normalized data depends on the nozzle temperature. For a given feed rate, 245 °C specimens show inferior specific properties. These observations agree with the adverse effect of nozzle temperature on the specific properties discussed in the previous section (see Figure 4d).

Elongation at break data shows a more complicated trend, which can be understood by considering the effect of nozzle temperature on the quality of fusion. Especially for the 50 and 75% feed rates, the nozzle temperature of 245 °C provides a considerably higher

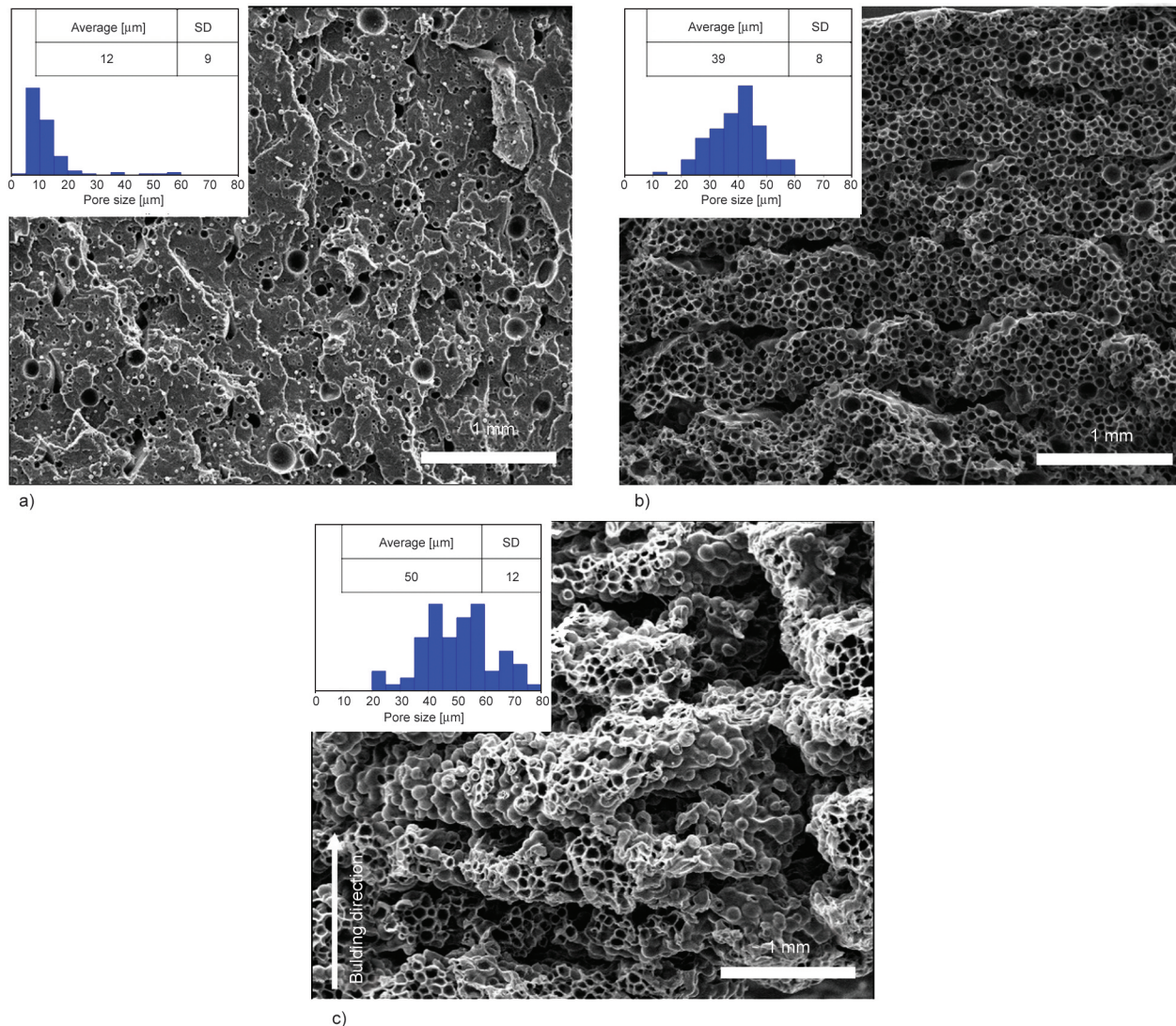


Figure 8. SEM images of the fracture surfaces of selected specimens printed by using different feed rates of a) 100%, b) 50%, and c) 25%. Nozzle temperature is 230 °C. SD: stands for standard deviation.

ductility than those of 230 °C. The higher resistance of 245 °C specimens to fracture is likely to result from the superior fusion between printing lines and layers at this temperature [40, 41]. The dependence on nozzle temperature diminishes at the lowest and highest feed rates due to the dominating effects of excess porosity and excess material flow, respectively. For example, at a feed rate of 100%, the 230 °C specimen does not exhibit any apparent lack of fusion, as shown in Figure 8a. As a result, the effect of nozzle temperature on the elongation at break becomes small.

The increasing extent of foaming with decreasing feed rate can be attributed to the hydrostatic pressures involved in the process. As the filament material goes through the heating section and the nozzle, the diameter of the polymer flow cross-section decreases almost by an order of magnitude, resulting in a pressure rise. This pressure is highest in the case of 100% feed

rate, which hinders the expansion of the gas bubbles. A decrease in the feed rate is analogous to a reduction in the flow rate of a liquid through a channel, which reduces the pressure build-up in the heated section. As a result, the gas bubbles expand more quickly, resulting in a more significant fraction of porosity.

For the wide range of feed rate values considered in this study, the print quality remained satisfactory, which makes feed rate an excellent parameter to tune the porosity on the fly. As opposed to other parameters such as nozzle temperature, layer thickness, and infill ratio, feed rate does not cause any ‘side-effects’ that alter the resolution or quality of the print.

3.3. Effect of printing speed

Printing speed refers to the velocity magnitude of the nozzle during printing. Figure 9 shows the density and mechanical properties of the specimens as a

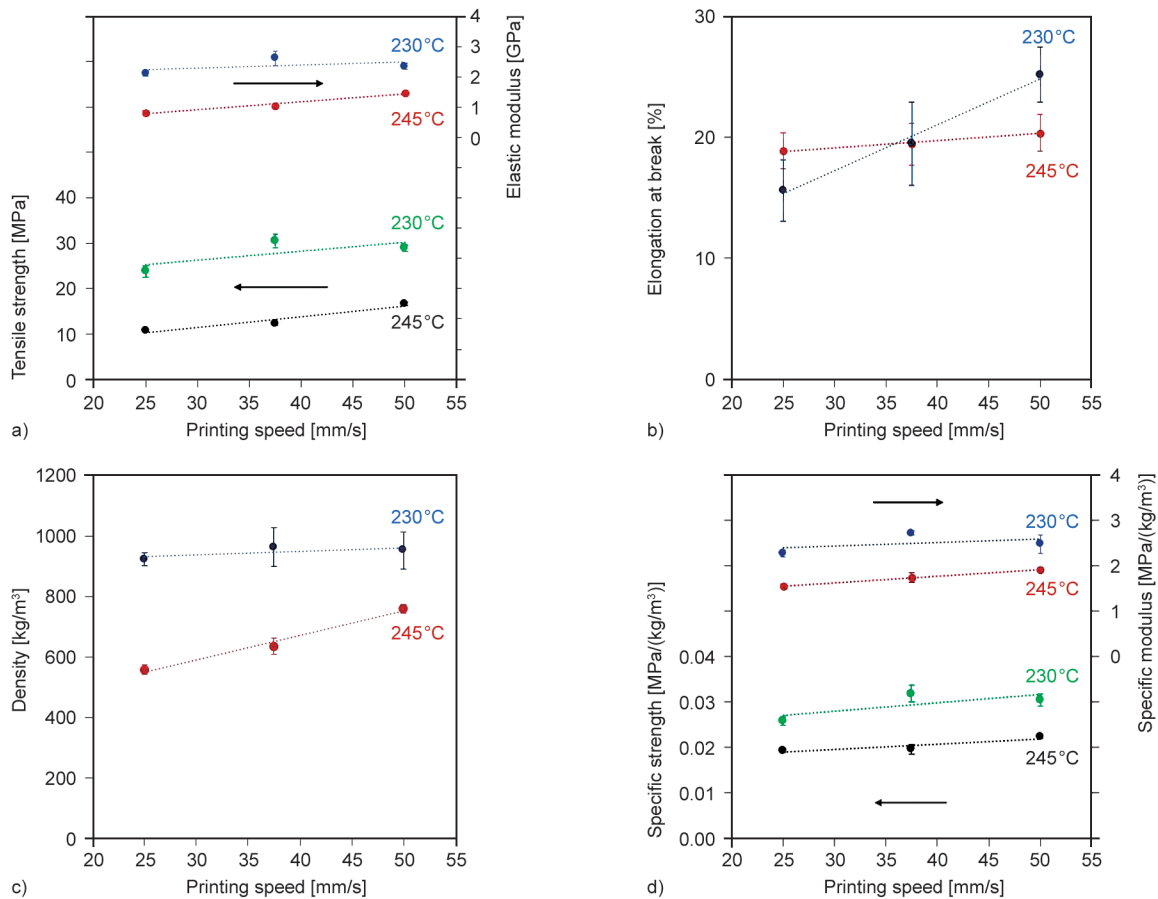


Figure 9. Effects of printing speed on the density and the mechanical properties. a) Tensile strength and elastic modulus, b) elongation at break, c) density, and d) specific tensile strength and specific elastic modulus.

function of printing speed, considered for two nozzle temperatures.

Overall, the printing speed does not significantly influence the mechanical properties. The only major trends are an increase in the density with increasing printing speed for the case of 245 °C and an increase in the elongation at break with increasing printing speed for the case of 230 °C.

As printing speed decreases, the filament stays longer in the heating section, promoting foaming and decreasing density. At 230 °C, the lower rate of the foaming reaction is insufficient to cause a strong dependence on printing speed. The small increase in elongation at break with printing speed can be explained by the slight increase in the density and accompanying reduction in the porosity, reducing the occurrence of stress concentration sites.

Printing speed is not a major parameter for tuning the foaming, which renders it useful for controlling other features. For example, the compromise between manufacturing rate and build quality can be the primary focus for optimizing the printing speed in practical applications.

3.4. Effect of infill ratio

Infill ratio is one of the most commonly varied parameters in additive manufacturing to establish a compromise between printing time, weight, and strength. A lower infill ratio implies shorter printing times and lower weight at the expense of lower strength. The resulting cellular geometry often introduces stress concentrations, leading to low elongations at break [42]. In practice, most FDM-produced parts are covered with a 100% infill shell to improve structural rigidity and provide a smooth and gapless surface for proper functionality. In this study, however, we considered tensile specimens without top and bottom shells to better understand the effect of the infill ratio. The infill pattern choice was grid (see Figure 11), one of FDM’s most commonly used patterns.

Figure 10 shows the density and the mechanical properties of specimens printed at different infill ratios. As the infill ratio increases, the density and the mechanical properties show an increasing trend. 100% infill ratio provides the highest tensile strength and elastic modulus of 22.1, and 2073 MPa, respectively. Elongation at break values are considerably

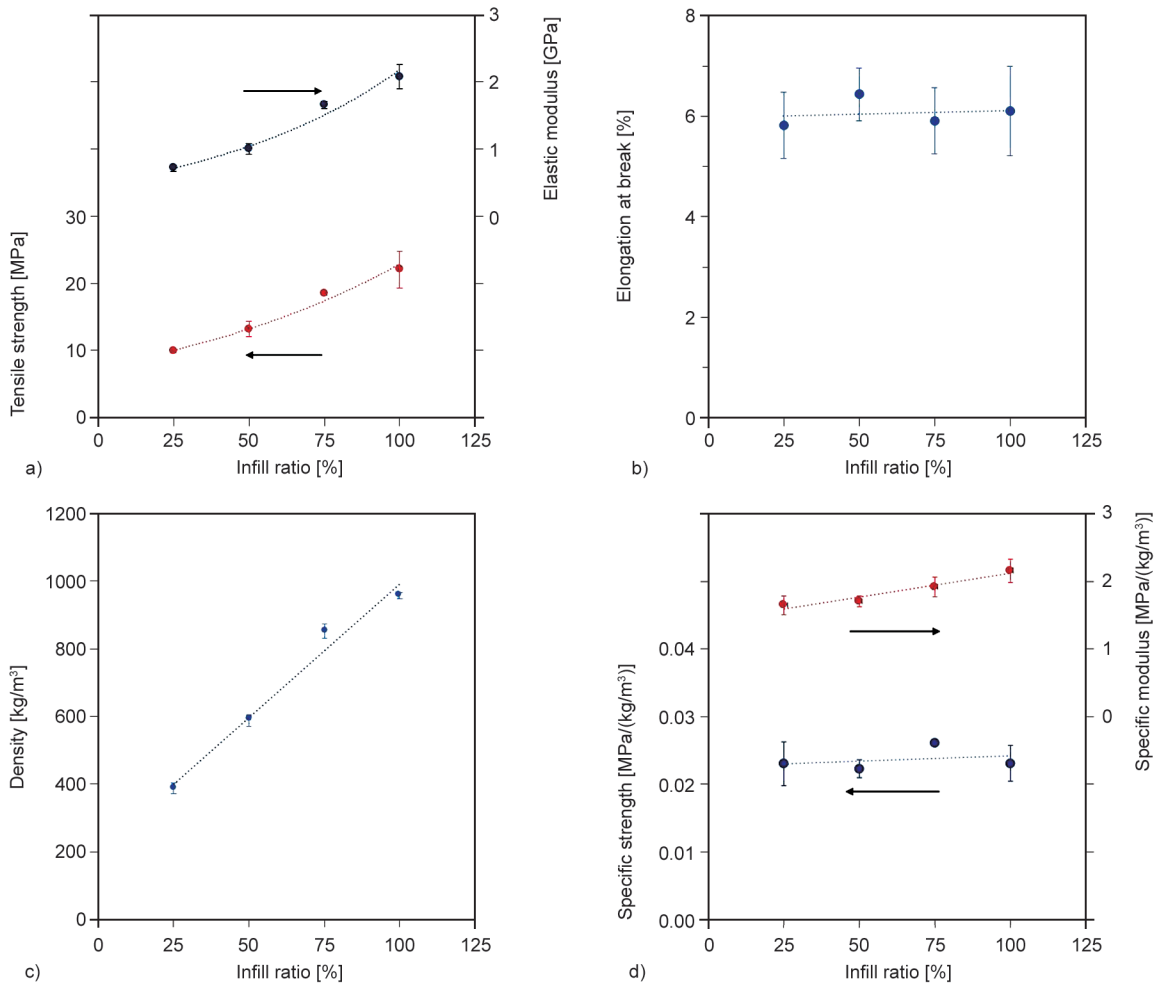


Figure 10. Effects of infill ratio on the density and the mechanical properties. a) Tensile strength and elastic modulus, b) elongation at break, c) density, d) specific tensile strength and specific elastic modulus.

lower than those measured in the previous sections, around 6% for all infill ratios.

Low elongation at break is a common feature of low infill ratio specimens. The stress concentrations due

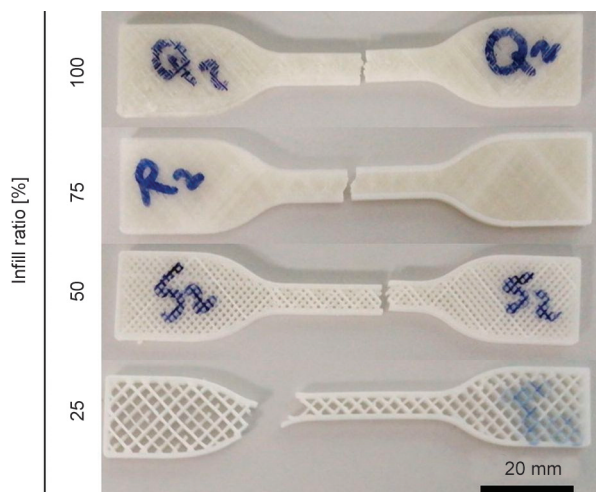


Figure 11. Photographs of selected specimens after testing with different infill ratios.

to the grid pattern are the primary reason for the premature failure. On the other hand, the 100% infill ratio specimen exhibiting a similarly low elongation requires a separate explanation. For 100% infill, the raster employed a grid pattern different from the $\pm 45^\circ$ alternating layers employed for the rest of the study. We attribute the low elongation to the grid pattern that increases the likelihood of poor fusion and defects in a solid print. Further investigation of the effect of different printing patterns can give more insight, which has been beyond the scope of this work.

3.5. Effect of layer thickness

The layer thickness has a relatively smaller effect on the mechanical properties within the range of process parameters considered in this study. The results did not show clear trends; we only provide some key values here. For the nozzle temperature of 230 °C, 0.5 mm layer thickness yielded the highest tensile strength and elastic modulus of 33.3 MPa, and

3.14 GPa, respectively. On the other hand, 0.35 mm layer thickness provided the largest elongation at break (30%). At the higher nozzle temperature of 245 °C, 0.7 mm layer thickness yielded the best results with a tensile strength of 22.5 GPa and an elastic modulus of 2.08 GPa. Changing the layer thickness did not affect the density of the specimens, irrespective of the nozzle temperature.

The results suggest that tuning the layer thickness can optimize the surface quality, dimensional accuracy, and printing time, similar to the FDM printing with conventional filaments [2, 7, 43].

3.6. Overview of the design space

Table 3 compares the results with the key properties of PLA foams produced by injection molding [11, 44] and 3D printing [8] reported in the literature. Injection-molded parts can exhibit a wide range of porosities and mechanical properties depending on the implementation of the foaming agent and the process parameters. The example data taken from our work show that the mechanical properties of FDM-produced PLA foams are comparable to those of injection-molded parts, demonstrating the technology's suitability for use in applications.

At a similar porosity level, FDM-produced specimens' tensile strength and ductility were lower than those of injection molded specimens, possibly due to the additional fusion defects that FDM introduces. As the average pore size and its variation tend to be larger for injection molded specimens [44], a direct comparison is difficult, and future work is needed in this regard.

Figure 12 summarizes all mechanical property measurements as a function of density. The figure also in-

cludes the mechanical properties of a non-foamed specimen (nozzle temperature = 200 °C) produced by the same LW-PLA filament [45] and an FDM-produced conventional pure PLA specimen [46]. This comparison shows that the pure PLA specimen from the literature provides considerably higher strength than the foamed specimens. Examining the specific strength–density curve indicates that the higher strength of pure PLA is beyond the density's contribution to strength. On the other hand, the elastic modulus of the pure PLA specimen is comparable to our specimens, suggesting that the pores and defects in the foamed specimens weaken the load-bearing capacity.

The data demonstrates the general trends in strength and modulus as a function of density that is common to all printing conditions. Tensile strength and elastic modulus increase with density (Figures 12a and 12b). The rate of increase in the mechanical properties amplifies with increasing density, and the scatter in the data widens accordingly. Specific strength also improves with density in general (Figure 12c). Especially for densities around 1000 kg/m³, specimens with similar densities can yield considerably different specific strengths, depending on the corresponding printing conditions. Overall, 230 °C nozzle temperature provides superior performance in absolute and specific strength. Tensile strength and elastic modulus are linearly proportional for most of the data, as shown in Figure 12d.

The entire data for each mechanical property follows a curve with a relatively narrow scatter, suggesting that the density, in fact, the porosity, is the primary parameter that governs the mechanical behavior of

Table 3. A comparison of the findings of this study with injection molded and FDM-produced specimens reported in the literature [8, 11, 44].

Reference	[44]	[11]	[8]	This study	
Production method	IM*	IM*	FDM	FDM	FDM
Nozzle temperature [°C]	170	180	215	230	230
Feed rate [%]	–	–	95	100	50
Infill ratio [%]	–	–	100	100	100
Mold temperature [°C]	25	10	–	–	–
Screw speed [rpm]	400	100	–	–	–
Elastic modulus [GPa]	0.91	1.46	1.89	2.34	0.96
Tensile strength [MPa]	25.1	33.6	31.2	28.9	11.5
Elongation at break [%]	43	30	–	25	12
Porosity [%]	28	–	–	24	56
Pore density [#cm ³]	0.48·10 ⁶	0.23·10 ⁸	–	0.16·10 ⁸	0.8·10 ⁶
Average pore size [µm]	90	120	–	14	40

*IM: injection molding

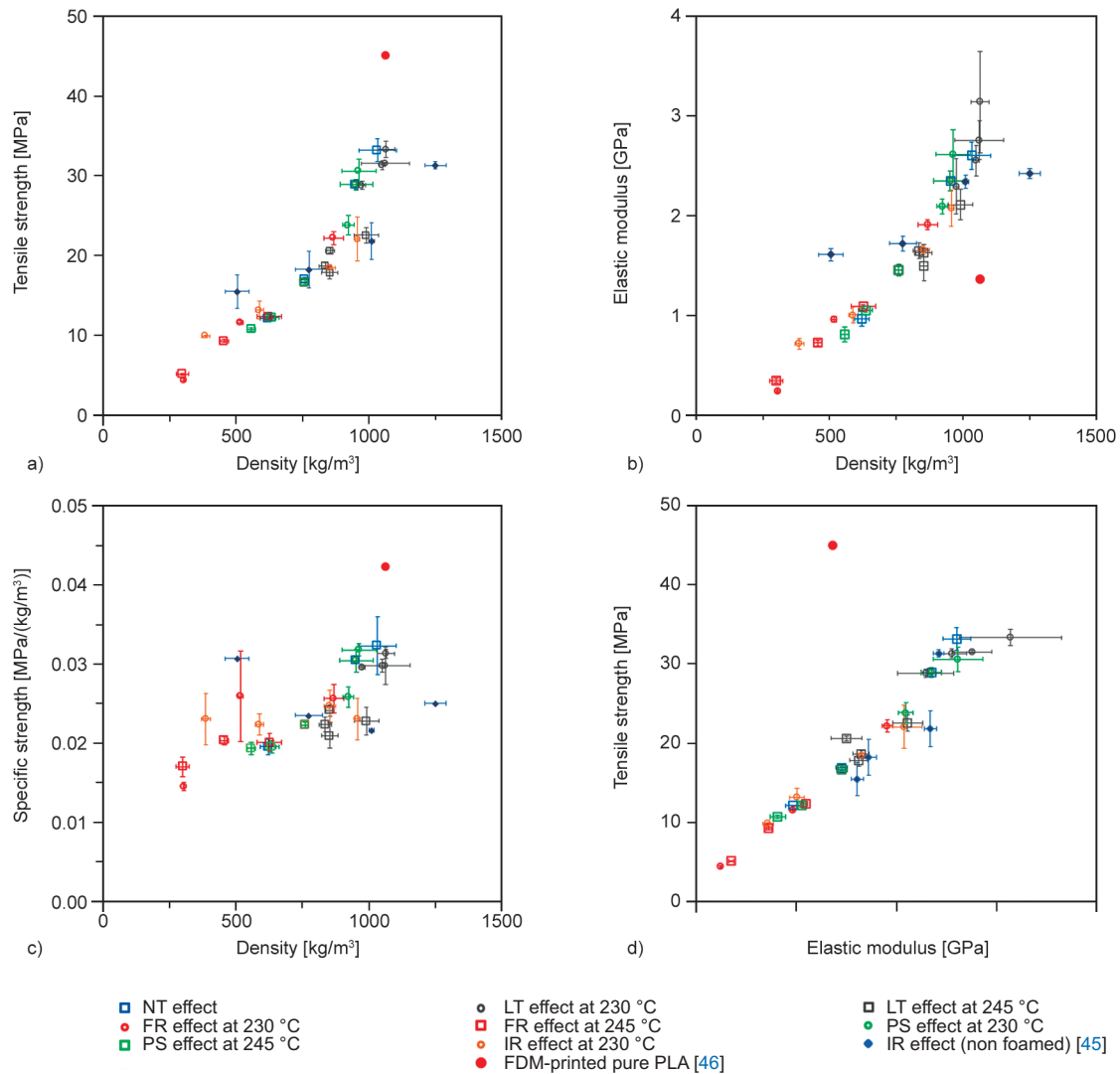


Figure 12. A summary of all mechanical property data. a) Tensile strength vs. density, b) elastic modulus vs. density, c) specific strength vs. density, and d) strength vs. elastic modulus. Each data point shows the average properties for a given combination of printing parameters. The printing parameters for non-foamed samples were nozzle temperature of 200 °C, raster angle of $\pm 45^\circ$, and layer height of 0.2 mm, and the infill ratio of the conventional PLA sample was 100% [45, 46].

the foaming PLA. In other words, the influence of process parameters on the mechanical properties is mainly through a change in the porosity. The effects of fusion defects and crystallinity are of secondary importance, supporting the previous discussion in Section 3.1.

The results show that porosity can be tuned by controlling a wide range of parameters, including nozzle temperature, feed rate, printing speed, layer thickness, and infill ratio. Most of these parameters also alter other features of the build at the same time. For example, increasing nozzle temperature improves the fusion between the layers, layer thickness affects the z-resolution of the build and the surface roughness, and printing speed would impact build quality,

manufacturing speed, and cost. Feed rate, on the other hand, only affects the porosity and does not influence the other feature significantly, making it the ideal choice for controlling the foaming. Controlling the feed rate for tuning foaming also provides the advantage of quickly adjusting the foaming spatially over the part. In contrast, on-the-fly adjustment of the nozzle temperature or the layer thickness is not as practical.

In summary, the findings suggest that 230 °C nozzle temperature is an effective value providing high specific strength. After this selection, the layer height and printing speed should be adjusted according to the requirements of the print, such as build quality and time restrictions. Then, the feed rate will provide

control over the extent of foaming. Lastly, the infill ratio and raster pattern can be used to adjust the weight of the printed part further.

As the study does not explore all possible combinations of printing parameters, the statements here are the implications of the existing data rather than conclusions, which would require a more comprehensive exploration of the entire design space. Such a future study should also investigate possible synergistic effects, such as how the impact of feed rate might change as a function of nozzle temperature and layer height.

The data for specimens with different infill ratios agree well with the porous specimens printed with 100% infill for a given density. Infill ratio tunes the density through a macroscale architected porosity, whereas the porous specimens achieve density control by foaming. The results suggest that foaming PLA printing is an excellent alternative to the conventional low-infill printing frequently used to reduce printing times, material consumption, and weight.

The Gibson-Ashby model is a useful and simple approach to predicting the mechanical properties of cellular materials and foams. The model predicts the elastic modulus and strength of the cellular structures as follows in Equations (1) and (2) [18]:

$$\frac{E_F}{E_S} = \varphi^2 \cdot \left(\frac{\rho_F}{\rho_S}\right)^2 + (1 - \varphi) \cdot \left(\frac{\rho_F}{\rho_S}\right) \quad (1)$$

$$\frac{\sigma_F}{\sigma_S} = 0.55 \cdot \left(\frac{\varphi \cdot \rho_F}{\rho_S}\right)^{1.5} + (1 - \varphi) \cdot \left(\frac{\rho_F}{\rho_S}\right) \quad (2)$$

where E is the elastic modulus, σ is the strength, and φ is a fitting parameter. Subscripts S and F refer to the fully solid and foamed specimens, respectively.

Figure 13 shows the elastic modulus and strength predictions of the Gibson-Ashby model using the properties of solid PLA from the literature [47] and compares the predictions with our data. The prediction curve exhibited a high coefficient of determination and low standard deviation, as indicated in the figures. The fitting constant, φ , is determined as 0.85 for both curves, in agreement with the literature values reported for polyurethane foams in the range of 0.8–0.85 [20, 48].

3.7. Compression testing

Compression testing of specimens provided further insight into the mechanical behavior of foaming PLA. We focused on specimens with varying feed rates, the simplest and most effective parameter to tune the porosity.

Figure 14a shows representative compressive stress-strain curves of specimens printed at different feed rates. The curves exhibit a linear-elastic regime, followed by a stress plateau and a second rise in stiffness, respectively. The slope of the elastic response and the magnitude of the stress plateau increase with increasing feed rate.

The stress-strain curves exhibit the typical characteristics of foams under compression. After the initial nearly-linear elastic response, the ligaments and surfaces surrounding the pores buckle, which reduces the load-bearing capacity. With further compression,

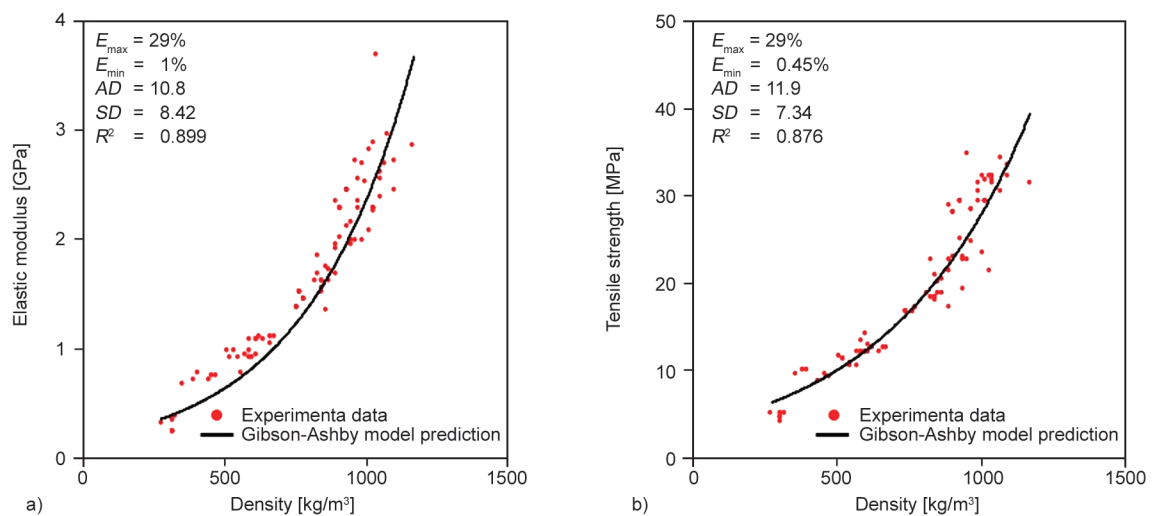


Figure 13. A comparison of all mechanical property data and Gibson-Ashby model predictions. a) Elastic modulus and b) tensile strength. E_{\max} and E_{\min} : the maximum and minimum percent difference respectively. AD : average difference. SD : standard deviation. R^2 : coefficient of determination.

buckling and collapse propagate to the remainder of the specimen at a relatively constant stress level. As the collapse of the structure nears completion, deformations in the solid zones become more pronounced, which increases the measured stiffness. As the feed rate decreases, the porosity increases, and the onset of this stiffness rise is postponed to higher compressive strains.

Figures 14b, and 14c represent the density and the compressive mechanical properties as a function of feed rate for 230 °C nozzle temperature. Compressive strength corresponds to the local peak in the stress-strain curves right after the linear deformation segment. Density, compressive strength, and elastic modulus increase rapidly by increasing the feed rate. As the feed rate increases from 25 to 75%, the elastic modulus and compressive strength increase by factors of 13.3 and 9.5, respectively.

Figure 14d shows photographs of the compression specimens after testing. 100% feed rate specimen does not show any obvious damage upon a compression

exceeding 60% strain. As the feed rate decreases to 75 and 50%, the irreversible damage becomes more pronounced. In fact, 25% specimen shows little recovery upon unloading. All specimens apart from the 100% feed rate case show some delamination-like failure. Delamination planes are perpendicular to the build direction, suggesting that the fusion between layers is weaker than the fusion between adjacent printing lines.

3.8. Shore hardness measurements

The last part of the mechanical analysis was performed on a printed rectangular block with varying porosity over its build direction to demonstrate the foaming PLA's capability to generate structures with graded morphology. Decreasing the feed rate incrementally after the completion of each layer tuned the porosity in the build direction.

Figure 15 shows the Shore hardness measurements as a function of the build length and a photograph of the specimen. Shore hardness is 54.7 for the layers

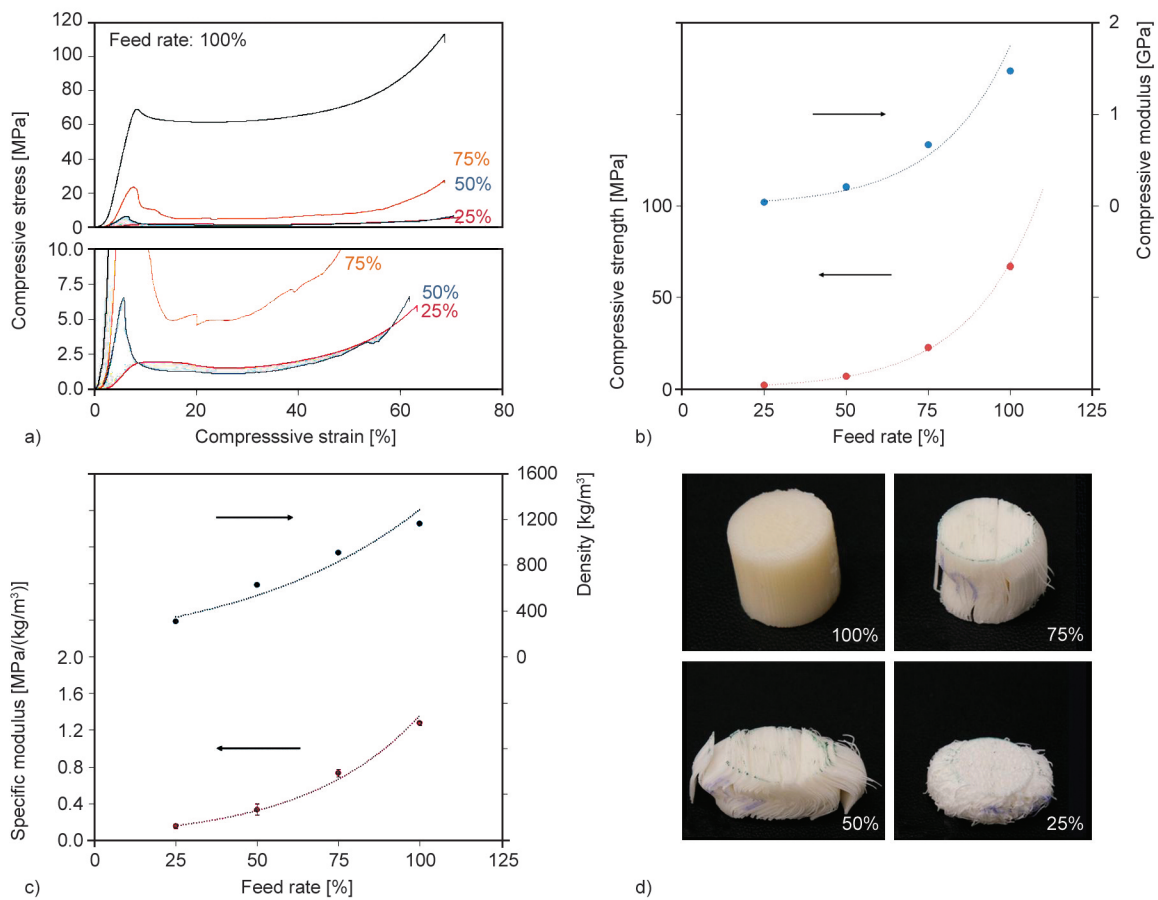


Figure 14. Effect of feed rate on the compressive mechanical properties. a) Representative compressive stress-strain curves of specimens printed using different feed rates. b) Compressive strength and elastic modulus as a function of feed rate. c) Specific elastic modulus and density as a function of feed rate. d) Photographs of compression specimens upon testing rate [%].

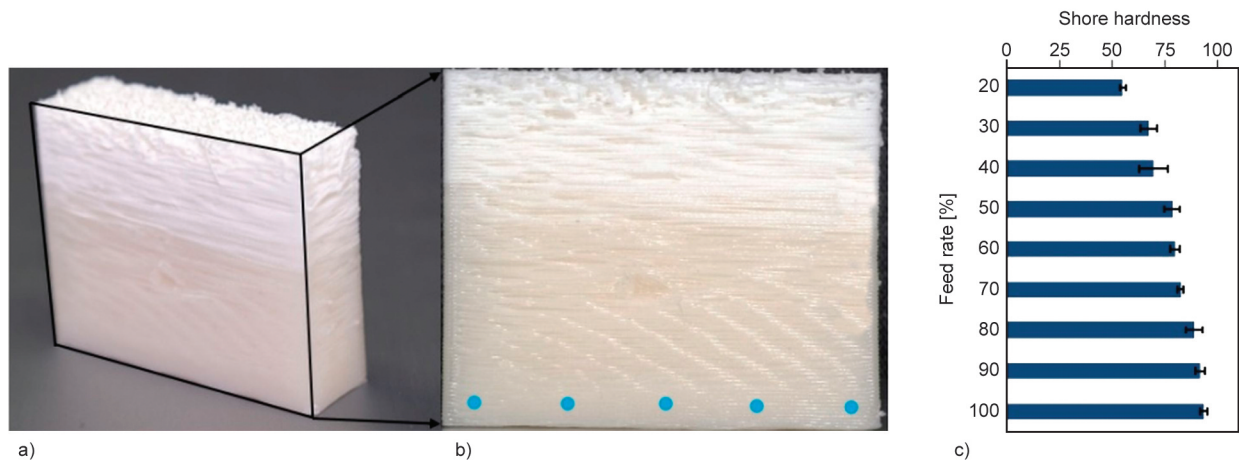


Figure 15. The Shore hardness measurements as a function of the feed rate and a photograph of the specimen. a) A photograph of the printed specimen with varying feed rates, b) front view of the specimen, where blue dots show the hardness measurement locations for the feed rate of 100% and c) Shore hardness over the thickness of the specimen. The error bar represents one standard deviation of five different measurements.

with an average feed rate of 20%, and it monotonically increases with feed rate, reaching 93.0 at a feed rate of 100%. The dependence of Shore hardness on feed rate is much smaller than those observed for tensile strength and compressive strength.

The specimen photographs suggest a reduction in the surface quality with decreasing feed rate. Further characterization of the surface properties would be necessary to implement such heterogeneous structures effectively in applications.

4. Conclusions

This study investigated the mechanical properties of 3D-printed PLA foams under different printing parameters. The nozzle temperature, feed rate, and infill ratio significantly affect the extent of foaming, density, and mechanical properties. We can summarize the findings as follows:

- Increasing the nozzle temperature from 215 to 260°C increased foaming and decreased density by 40% and strength by 60%.
- Feed rate was also effective in tuning the foaming. By only adjusting the feed rate between 25 and 100%, it has been possible to achieve strength values in the range of 5 to 40 MPa.
- Infill ratio, printing speed, and layer thickness also influenced the foaming. However, these parameters are not practical for precise control of the density and strength due to their weak influence on foaming or the complicated trends involved.

- The Shore hardness strongly varied as a function of the feed rate. Decreasing the feed rate from 100 to 20% reduced the Shore hardness from 93.0 to 54.7. Nevertheless, this variation was less pronounced than those observed for tensile strength.

Foaming filaments provide additional control over printed parts' density and mechanical properties. With the capability to spatially control these properties, foaming filaments offer new opportunities for designing compliant mechanisms, soft robotics components, and biomedical scaffolds.

Acknowledgements

This work is funded by METU BAP under Project No. GAP-302-2021-10609. We would like to thank METU Central Laboratory and Mr. Servet Şehirli for their support in the testing and characterization.

References

- [1] Zein I., Hutmacher D. W., Tan K. C., Teoh S. H.: Fused deposition modeling of novel scaffold architectures for tissue engineering applications. *Biomaterials*, **23**, 1169–1185 (2002).
[https://doi.org/10.1016/S0142-9612\(01\)00232-0](https://doi.org/10.1016/S0142-9612(01)00232-0)
- [2] Wimpenny D. I., Pandey P. M., Kumar J. L.: *Advances in 3D printing and additive manufacturing technologies*. Springer, Berlin (2017).
<https://doi.org/10.1007/978-981-10-0812-2>
- [3] Ngo T. D., Kashani A., Imbalzano G., Nguyen K. T. Q., Hui D.: Additive manufacturing (3D printing): A review of materials, methods, applications and challenges. *Composites Part B: Engineering*, **143**, 172–196 (2018).
<https://doi.org/10.1016/j.compositesb.2018.02.012>

- [4] Bakır A. A., Atik R., Özerinç S.: Mechanical properties of thermoplastic parts produced by fused deposition modeling: A review. *Rapid Prototyping Journal*, **27**, 537–561 (2021).
<https://doi.org/10.1108/RPJ-03-2020-0061>
- [5] Ben Ali N., Khlif M., Hammami D., Bradai C.: Mechanical and morphological characterization of spherical cell porous structures manufactured using FDM process. *Engineering Fracture Mechanics*, **216**, 106527 (2019).
<https://doi.org/10.1016/j.engfracmech.2019.106527>
- [6] Choi W. J., Hwang K. S., Kwon H. J., Lee C., Kim C. H., Kim T. H., Heo S. W., Kim J.-H., Lee J.-Y.: Rapid development of dual porous poly(lactic acid) foam using fused deposition modeling (FDM) 3D printing for medical scaffold application. *Materials Science and Engineering: C*, **110**, 110693 (2020).
<https://doi.org/10.1016/j.msec.2020.110693>
- [7] Sanz-Horta R., Elvira C., Gallardo A., Reinecke H., Rodríguez-Hernández J.: Fabrication of 3D-printed biodegradable porous scaffolds combining multi-material fused deposition modeling and supercritical CO₂ techniques. *Nanomaterials*, **10**, 1080 (2020).
<https://doi.org/10.3390/nano10061080>
- [8] Damanpack A. R., Sousa A., Bodaghi M.: Porous PLAs with controllable density by FDM 3D printing and chemical foaming agent. *Micromachines*, **12**, 866 (2021).
<https://doi.org/10.3390/mi12080866>
- [9] Lee S.-T., Park C. B.: *Foam extrusion: Principles and practice*. CRC Press, Ohio (2014).
- [10] Zhang X., Ding W., Chang E., Chen X., Chen J., Park C. B., Shen C.: Foaming behaviors and mechanical properties of injection-molded polylactide/cotton-fiber composites. *Industrial and Engineering Chemistry Research*, **59**, 17885–17893 (2020).
<https://doi.org/10.1021/acs.iecr.0c03348>
- [11] Zhao H., Cui Z., Sun X., Turng L.-S., Peng X.: Morphology and properties of injection molded solid and microcellular polylactic acid/polyhydroxybutyrate-valerate (PLA/PHBV) blends. *Industrial and Engineering Chemistry Research*, **52**, 2569–2581 (2013).
<https://doi.org/10.1021/ie301573y>
- [12] Dong G., Wijaya G., Tang Y., Zhao Y. F.: Optimizing process parameters of fused deposition modeling by Taguchi method for the fabrication of lattice structures. *Additive Manufacturing*, **19**, 62–72 (2018).
<https://doi.org/10.1016/j.addma.2017.11.004>
- [13] Liu W., Song H., Wang Z., Wang J., Huang C.: Improving mechanical performance of fused deposition modeling lattice structures by a snap-fitting method. *Materials and Design*, **181**, 108065 (2019).
<https://doi.org/10.1016/j.matdes.2019.108065>
- [14] Lee S.-T., Ramesh N. S.: *Polymeric foams: Mechanisms and materials*. CRC Press, Ohio (2004).
- [15] Wu G., Xie P., Yang H., Dang K., Xu Y., Sain M., Turng L. S., Yang W.: A review of thermoplastic polymer foams for functional applications. *Journal of Material Science*, **56**, 11579–11604 (2021).
<https://doi.org/10.1007/s10853-021-06034-6>
- [16] Xu J., Turng L.-S.: *Microcellular injection molding*. Wiley, New Jersey (2010).
- [17] Ykhlef N., Lafranche E.: Development of bio-based poly(butylene succinate) formulations for microcellular injection foaming. *International Journal of Material Forming*, **12**, 1009–1022 (2019).
<https://doi.org/10.1007/s12289-019-01512-4>
- [18] Gibson L. J., Ashby M. F.: *Cellular solids: Structure and properties*. Cambridge University Press, Cambridge (1997).
- [19] Kabir M. E., Saha M. C., Jeelani S.: Tensile and fracture behavior of polymer foams. *Materials Science and Engineering: A*, **429**, 225–235 (2006).
<https://doi.org/10.1016/j.msea.2006.05.133>
- [20] Ramsteiner F., Fell N., Forster S.: Testing the deformation behaviour of polymer foams. *Polymer Testing*, **20**, 661–670 (2001).
[https://doi.org/10.1016/S0142-9418\(00\)00090-8](https://doi.org/10.1016/S0142-9418(00)00090-8)
- [21] Ykhlef N., Lafranche E.: Injection-moulding of nitrogen-foamed bio-based microcellular poly(butylene succinate): Processing conditions/foam structure/flexural properties relationship. *Polymers from Renewable Resources*, **11**, 30–46 (2020).
<https://doi.org/10.1177/2041247920952653>
- [22] Clifton W., Pichelmann M., Vlasak A., Damon A., Re-Faey K., Nottmeier E.: Investigation and feasibility of combined 3D printed thermoplastic filament and polymeric foam to simulate the cortiocancellous interface of human vertebrae. *Scientific Reports*, **10**, 2912 (2020).
<https://doi.org/10.1038/s41598-020-59993-2>
- [23] Wallin T. J., Pikul J., Shepherd R. F.: 3D printing of soft robotic systems. *Nature Reviews Materials*, **3**, 84–100 (2018).
<https://doi.org/10.1038/s41578-018-0002-2>
- [24] Zhai W., Hu B., Li M., Jiang J., Zhou M.: Dimensional accuracy control and compressive property of microcellular polyetherimide honeycomb foams manufactured by an *in situ* foaming fused deposition modeling technology. *Advanced Engineering Materials*, **23**, 2001449 (2021).
<https://doi.org/10.1002/adem.202001449>
- [25] Li M., Jiang J., Hu B., Zhai W.: Fused deposition modeling of hierarchical porous polyetherimide assisted by an *in-situ* CO₂ foaming technology. *Composites Science and Technology*, **200**, 108454 (2020).
<https://doi.org/10.1016/j.compscitech.2020.108454>
- [26] Marascio M. G. M., Antons J., Pioletti D. P., Bourban P.-E.: 3D printing of polymers with hierarchical continuous porosity. *Advanced Materials Technologies*, **2**, 1700145 (2017).
<https://doi.org/10.1002/admt.201700145>

- [27] Zhou C., Yang K., Wang K., Pei X., Dong Z., Hong Y., Zhang X.: Combination of fused deposition modeling and gas foaming technique to fabricated hierarchical macro/microporous polymer scaffolds. *Materials and Design*, **109**, 415–424 (2016).
<https://doi.org/10.1016/j.matdes.2016.07.094>
- [28] Song P., Zhou C., Fan H., Zhang B., Pei X., Fan Y., Jiang Q., Bao R., Yang Q., Dong Z., Zhang X.: Novel 3D porous biocomposite scaffolds fabricated by fused deposition modeling and gas foaming combined technology. *Composites Part B: Engineering*, **152**, 151–159 (2018).
<https://doi.org/10.1016/j.compositesb.2018.06.029>
- [29] Kaygusuz B., Özerinç S.: Improving the ductility of polylactic acid parts produced by fused deposition modeling through polyhydroxyalkanoate additions. *Journal of Applied Polymer Science*, **136**, 48154 (2019).
<https://doi.org/10.1002/app.48154>
- [30] Camargo J. C., Machado Á. R., Almeida E. C., Silva E. F. M. S.: Mechanical properties of PLA-graphene filament for FDM 3D printing. *The International Journal of Advanced Manufacturing Technology*, **103**, 2423–2443 (2019).
<https://doi.org/10.1007/s00170-019-03532-5>
- [31] Camargo J. C., Machado A. R., Almeida E. C., de Almeida V. H. M.: Mechanical and electrical behavior of ABS polymer reinforced with graphene manufactured by the FDM process. *The International Journal of Advanced Manufacturing Technology*, **119**, 1019–1033 (2022).
<https://doi.org/10.1007/s00170-021-08288-5>
- [32] Colorfabb: Technical data sheet for LW-PLA filament.
- [33] ASTM D638-4: Standard test method for tensile properties of plastics – Tension (2021).
- [34] ASTM D1621: Standard test method for compressive properties of rigid cellular plastics – Compression (2016).
- [35] ASTM D2240: Standard test method for rubber property – Durometer hardness (2021).
- [36] Tsvintzelis I., Angelopoulou A. G., Panayiotou C.: Foaming of polymers with supercritical CO₂: An experimental and theoretical study. *Polymer*, **48**, 5928–5939 (2007).
<https://doi.org/10.1016/j.polymer.2007.08.004>
- [37] Bakır A. A., Atik R., Özerinç S.: Effect of fused deposition modeling process parameters on the mechanical properties of recycled polyethylene terephthalate parts. *Journal of Applied Polymer Science*, **138**, 49709 (2021).
<https://doi.org/10.1002/app.49709>
- [38] Ameli A., Jahani D., Nofar M., Jung P. U., Park C. B.: Development of high void fraction polylactide composite foams using injection molding: Mechanical and thermal insulation properties. *Composites Science and Technology*, **90**, 88–95 (2014).
<https://doi.org/10.1016/j.compscitech.2013.10.019>
- [39] Radhakrishna G., Dugad R., Gandhi A.: Morphological evaluation of microcellular foamed composites developed through gas batch foaming integrating fused deposition modeling (FDM) 3D printing technique. *Cellular Polymers*, **40**, 244–266 (2021).
<https://doi.org/10.1177/02624893211040938>
- [40] Aliheidari N., Tripuraneni R., Hohimer C., Christ J., Ameli A., Nadimpalli S.: The impact of nozzle and bed temperatures on the fracture resistance of FDM printed materials. in ‘Proceedings of Behavior and Mechanics of Multifunctional Materials and Composites. Oregon, United States’ Vol. **10165**, 1016512 (2017).
<https://doi.org/10.1117/12.2260105>
- [41] Puerta A. P. V., Fernandez-Vidal S. R., Batista M., Girot F.: Fused deposition modelling interfacial and interlayer bonding in PLA post-processed parts. *Rapid Prototyping Journal*, **26**, 585–592 (2019).
<https://doi.org/10.1108/RPJ-06-2019-0176>
- [42] Fernandez-Vicente M., Calle W., Ferrandiz S., Conejero A.: Effect of infill parameters on tensile mechanical behavior in desktop 3D printing. *3D Printing and Additive Manufacturing*, **3**, 183–192 (2016).
<https://doi.org/10.1089/3dp.2015.0036>
- [43] Nuñez P. J., Rivas A., García-Plaza E., Beamud E., Sanz-Lobera A.: Dimensional and surface texture characterization in fused deposition modelling (FDM) with ABS plus. *Procedia Engineering*, **132**, 856–863 (2015).
<https://doi.org/10.1016/j.proeng.2015.12.570>
- [44] Ameli A., Jahani D., Nofar M., Jung P. U., Park C. B.: Processing and characterization of solid and foamed injection-molded polylactide with talc. *Journal of Cellular Plastics*, **49**, 351–374 (2013).
<https://doi.org/10.1177/0021955X13481993>
- [45] Kanani A. Y., Rennie A. E. W., Abd Rahim S. Z. B.: Additively manufactured foamed polylactic acid for lightweight structures. *Rapid Prototyping Journal*, in press (2022).
<https://doi.org/10.1108/RPJ-03-2022-0100>
- [46] Soud W., Baqer I. A., Ahmed M.: Experimental study of 3D printing density effect on the mechanical properties of the carbon-fiber and polylactic acid specimens. *Engineering and Technology Journal*, **37**, 128–132 (2019).
<https://doi.org/10.30684/etj.37.4A.3>
- [47] Farah S., Anderson D. G., Langer R.: Physical and mechanical properties of PLA, and their functions in widespread applications – A comprehensive review. *Advanced Drug Delivery Reviews*, **107**, 367–392 (2016).
<https://doi.org/10.1016/j.addr.2016.06.012>
- [48] Calvert K. L., Trumble K. P., Webster T. J., Kirkpatrick L. A.: Characterization of commercial rigid polyurethane foams used as bone analogs for implant testing. *Journal of Materials Science: Materials in Medicine*, **21**, 1453–1461 (2010).
<https://doi.org/10.1007/s10856-010-4024-6>

Research article

Manufacturing and characterization of highly environmentally-friendly composites with polylactide matrix and mango kernel seed flour

Jaume Gomez-Caturla^{1*}, Diego Lascano¹, Nestor Montanes¹, Rafael Balart¹,
Franco Dominici², Debora Puglia², Luigi Torre²

¹Technological Institute of Materials (ITM), Universitat Politècnica de València (UPV), Plaza Ferrándiz y Carbonell 1, 03801 Alcoy, Spain

²Dipartimento di Ingegneria Civile ed Ambientale, University of Perugia, UdR INSTM, Strada di Pentima 4, 05100 Terni (TR) Italy

Received 7 July 2022; accepted in revised form 5 October 2022

Abstract. This work reports on the development of polylactide (PLA)/mango kernel seed flour (MKSF) composites combined with tributyrin (TBN) and triacetin (TCN) as plasticizers. Thus, wood plastic composites (WPC) are obtained by extrusion and injection-molding processes. The solubility, mechanical, morphological, thermal, colorimetric, water absorbance, flowability, and disintegrability properties are evaluated. The ductility of the PLA+MKSF composite is improved by the plasticizing effect of TBN and TCN (10 phr (parts per hundred resin) each). Elongation at break is increased from 4.4 up to 9.5 and 8.3%, respectively. The theoretical solubility analysis supports the good miscibility between PLA with TBN and TCN (relative energy difference (RED) values of 0.86 and 0.73, respectively) deduced from the mechanical performance. Field emission scanning electron microscopy (FESEM) images also corroborate the mechanical findings, where a decrease in the presence of voids in the PLA matrix suggests certain compatibility between MKSF and TBN, and TCN. Differential scanning calorimetry (DSC) and dynamic-mechanical-thermal analysis (DMTA) results show that the plasticizers decrease the glass transition temperature and the melting temperature of PLA, thus improving its ductility. Thermogravimetric analysis (TGA) results indicate that the thermal stability of the composite is slightly decreased due to the relatively high volatility of the plasticizers, while MKSF does not affect this matter. The composites exhibit excellent biodegradability, presenting more than 90% of disintegration in compost soil conditions in 12 weeks. Finally, MKSF provided the composites with a wood-like dark brown color and with high water absorbance.

Keywords: polymer composites, biodegradable polymers, mechanical properties, thermal properties, plasticizer

1. Introduction

Wood-plastic composites (WPC) have risen as an alternative for products made of wood. Those materials have a visual appearance similar to that of wood. The main difference is that they are composed of a thermoplastic polymeric matrix (such as polyethylene and polypropylene, among others), which is loaded with fillers from the wood industry (sawdust, fibres, flour) [1, 2]. In the first approach, the manufacturing

of WPC implies the incorporation of wood-based elements. However, in the last years, other fillers have been proposed as alternatives for wood-derived fillers, either lignocellulosic fillers or mineral fillers (talc, calcium carbonate, among others), or agroforestry waste flours [3, 4]. The latter have gained quite a popularity due to the significant amount of generated waste (skin, calyx, seeds) [5–7]. As a result of their low cost and abundance, the incorporation

*Corresponding author, e-mail: jaugoca@epsa.upv.es

© BME-PT

of fillers from food byproducts and agroforestry wastes has become a technical and viable solution in the plastics industry. Moreover, the materials obtained from them possess balanced properties and advantageous environmental efficiency [8]. The use of biofillers presents several advantages, such as facilitating or accelerating the disintegration of material; reducing the amount of used polymer, and the revalorization of a lignocellulosic waste, all these promoting the transition from a traditional linear economy to a circular economy and thus, remarkably reducing the carbon footprint [9, 10]. Rojas-Lema *et al.* [11] used wastes from persimmon peel to manufacture composite materials with a biopolyethylene matrix. Moreover, they studied the effect of silanization treatments and esterification with palmitic acid to enhance compatibilization between the filler and the polymer matrix. They reported interesting results compared to the conventional use of a maleic anhydride-grafted copolymer of polyethylene as a reference compatibilizer. It was also proved that this waste provided additional features to composites with polyethylene. In particular, it was observed that the persimmon peel wastes gave tremendous antioxidant activity to the polyethylene matrix. The compatibility between the polymeric matrix and the filler was also increased. The esterification with palmitic chloride treatment improved the hydrophobic behaviour of the materials, diminishing their water absorption capacity.

Tropical crops like mango have become one of the preferred products for consumers in the European market. This is because this fruit is considered exotic, has attractive colours, delicious flavour, and a comfortable odour [12]. Moreover, it presents a high nutritional value as it contains a large number of macronutrients (carbohydrates, proteins, lipids) and micronutrients (vitamins A, B, C, folic acid, and minerals), which help to prevent degenerative diseases [13]. The greatest producers in 2019 were Asia, accounting for 71.5% of the global market, followed by Africa (16%), America (12.3%), and finally Oceania, with 0.1% of the global production, according to the Food and Agriculture Organization of the United Nations. Even though the composition of mango fruit varies depending on its species, the flesh includes typically between 33–85 wt% of the total mass, resulting in a waste of 7–24 wt% of mango peel and 9–40 wt% of the kernel. The kernel contains 6–16 wt% of mango oil [14]. It has been reported that

the kernel possesses a large amount of carbohydrates and proteins (58–80 and 6–13 wt%, respectively), apart from containing oleic and stearic acids [15] and polyphenols [16].

The search to reduce the use of petrochemical polymers in the composite fabrication sector has made the development and use of renewable and biodegradable materials gain popularity in the last few years [17]. Polylactic acid (PLA) is one of the most widely used polymer matrices in environmentally friendly materials. This is because PLA monomers are obtained from the fermentation of starch-rich compounds, so the products are biodegradable in controlled compost soil conditions [18, 19].

PLA-based composites present several limitations provoked by PLA's low impact strength and toughness and, subsequently, high fragility [20]. One of the most common techniques to overcome this inconvenience is mixing PLA with more flexible polymers and/or incorporating additives (plasticizers) [21, 22]. Lascano *et al.* [21] developed a binary blend using PLA and poly (butylene succinate-*co*-adipate) (PBSA). It was observed that the ductile behaviour of the blend improved, increasing the elongation at break and impact strength from 9.23% and 2.48 kJ/m² for neat PLA, respectively, to 56% and 5.75 kJ/m² for the blend with 30 wt% of PBSA. Several natural-origin plasticizers are being utilized due to their low toxicity. Among those plasticizers are lactic acid, lactic acid oligomers (OLA), vegetal oils (VO), citrate esters, tributyrin, triacetin, and so on. Montes *et al.* [23] developed a blend made of poly(lactic acid)/poly(3-hydroxybutyrate) utilizing tributyrin as a plasticizer to produce completely natural films for food packaging applications. They observed that the incorporation of 15 wt% tributyrin increased the ductile properties of the material apart from presenting good water vapour barrier properties and certain transparency. Crystallinity was also increased. Coltelli *et al.* [24] studied the behavior of composites based on PLA and polyhydroxybutyrate plasticized with triacetin. They observed that PLA biodegradability improved thanks to the disintegration of the amorphous phase.

This work aims to develop a completely natural composite based on a polylactic acid (PLA) matrix and mango kernel seed flour (MKSF) as a biobased filler. To overcome the low intrinsic toughness of the PLA matrix, two bio-derived plasticizers were used, namely glycerol tributyrate (tributyrin) and glycerol

triacetate (triacetin). There is little literature regarding the use of mango kernel flour as a filler for polylactide. Additionally, TBN and TCN have not been widely used for plasticizing PLA wood plastic composites and never have been used in a PLA/MKSF composite. The effects of both plasticizers and the MKSF filler were evaluated through standard mechanical, thermal, and thermomechanical tests, morphology characterization, water absorption, and disintegrability under controlled compost soil characterization.

2. Materials and methods

2.1. Materials

Bio-based PLA Purapol L130 grade (min. 99% of L-isomer) was supplied by Corbion Purac (The Netherlands, Amsterdam), with a density of 1.24 g/cm³, a melt flow index of 16 g/10 min (measured at a temperature of 210 °C and a load of 2.16 kg) and a melting temperature of 175 °C.

Flour extracted from mango kernel from *Mangifera indica* L. species was used as a filler. The mango seed was dried at 65 °C for a week. The mango kernel was extracted and submitted to a milling process in a Retsch GmbH model ZM 1000 ultracentrifugal mill (Haan, Germany) with a sieve size of 25 µm and a rotation speed of 12 000 rpm. Figure 1 shows the morphology and histogram (size distribution) of the mango kernel seed flour particles (MKSF), which present an average particle diameter size of 18–20 µm.

Glycerol tributyrate (tributyrin) from ACROS Organics™ and distributed by Thermo Fisher Scientific (Geel, Belgium) (Product Code: A11830.0B) and glycerol triacetate (triacetin) from Sigma Aldrich

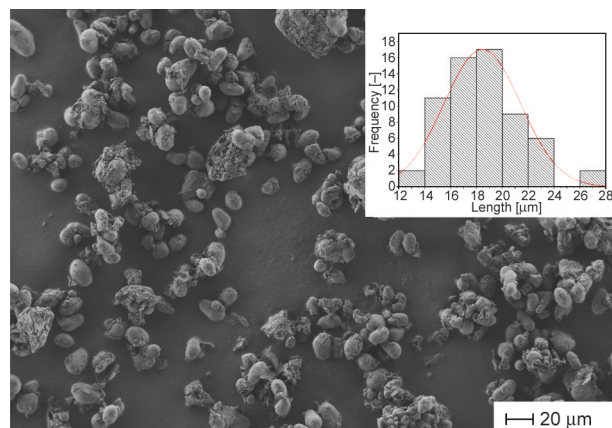


Figure 1. FESEM image of mango kernel seed flour (MKSF) particles at 150× with a marker scale of 20 µm.

(Madrid, Spain) (Product Code: 90240) were used as plasticizers. Tributyrin is 97% pure, with a density of 1.0335 g/ml and a melting point of −75 °C. Triacetin presents a purity of 99%, a density of 1.16 g/ml, and a melting point of 3 °C.

2.2. Manufacturing of PLA-MKSF composites

Prior to processing, PLA pellets and MKSF particles were dried in an air circulating oven at 65 °C for 12 hours to eliminate humidity. The compounds were formulated with a constant MKSF weight percentage of 30 wt%. Plasticizers (tributyrin and triacetin) were added directly in the extrusion process, always maintaining 10 phr (parts by weight of plasticizer per one hundred parts by weight of the PLA/MKSF base composition taking the work of Pawlak *et al.* [25]). The compounds were named using the code PLA-MKSF/XX, where XX refers to the used plasticizer, TBN for tributyrin, and TCN for triacetin. These formulations were placed in a ziplock bag for the initial mixing. Then, they were submitted to an extrusion process in a co-rotating twin-screw extruder from Dupra S.L. (Alicante, Spain). The extrusion temperature profile was 160–170–180–190 °C with a rotating speed of 20 rpm. Then, the extruded filaments were pelletized in an air-knife unit. Finally, an injection-moulding process was carried out using a Meteor 270/75 from Mateu & Solé (Barcelona, Spain). Standardized tensile test and impact strength test specimens were obtained. The injection-moulding temperature profile was 170–175–180–190 °C from the hopper to the injection nozzle, with an injection time of 5 s and a cooling time of 60 s.

2.3. Characterization of PLA-MKSF composites

2.3.1. Theoretical miscibility between PLA and the plasticizers

When studying the interaction between a polymer and a plasticizer, the solubility of both components is very useful information to consider before initiating all the experimental setups. The general solubility parameter (δ) for each component can be calculated, according to the method of van Krevelen and te Nijenhuis [26], Equation (1), which takes into account the contributions of the dispersion forces (δ_d), polar forces (δ_p), and hydrogen bonding (δ_h):

$$\delta = \delta_d^2 + \delta_p^2 + \delta_h^2 \quad (1)$$

Each one of the contributions can be calculated by Equations (2), (3), and (4):

$$\delta_d = \frac{\sum F_{di}}{V} \quad (2)$$

$$\delta_p = \frac{\sqrt{\sum F_{pi}^2}}{V} \quad (3)$$

$$\delta_h = \sqrt{\frac{\sum E_{hi}}{V}} \quad (4)$$

where F_{di} is the dispersive force contribution of the chemical groups present in the molecule, F_{pi} is the polar force contribution of the chemical groups present in the molecule, E_{hi} is the hydrogen cohesive energy contribution of the chemical groups in the molecule, and V is the molar volume of the molecule.

Considering the chemical structure and the group contribution of neat PLA and both plasticizers (tributyrin and triacetin), Table 1 gathers all the solubility components and the solubility parameter. Moreover, the parameter R_a was also calculated, which indicates the distance that exists between the solubility coordinates of the plasticizers and the ones of PLA. If R_a is zero, it is indicative of good miscibility between the polymer and the plasticizer. So, the solubility between both materials becomes poorer as the parameter R_a (the distance) increases until it surpasses a certain threshold, from which both polymer and plasticizer become incompatible. This distance relates to the polymer radius, R_0 , which defines a spherical solubility region of a polymer. The center of this sphere is determined by the three solubility contributions δ_d , δ_p , and δ_h . R_a is calculated Equation (5):

$$R_a = \sqrt{4 \cdot (\delta_{d_{plast}} - \delta_{d_{PLA}})^2 + (\delta_{p_{plast}} - \delta_{p_{PLA}})^2 + (\delta_{h_{plast}} - \delta_{h_{PLA}})^2} \quad (5)$$

Additionally, the relative energy difference (RED) was also calculated. This parameter indicates the ratio between R_a and the solubility sphere radius of neat PLA, R_0 , which is $10.7 \text{ MPa}^{1/2}$ (Equation (6)) [27]. The lower the RED parameter is, the better the affinity between the polymer and the plasticizer. When the RED value is close to 1, it means that both

elements are in the threshold of good miscibility, while values superior to 1 are indicative of poor miscibility between both elements.

$$RED = \frac{R_a}{R_0} \quad (6)$$

As it can be observed in Table 1, both tributyrin and triacetin have good miscibility for PLA, as their RED value is smaller than the unity, with both plasticizers exhibiting RED values of 0.86 and 0.73, respectively.

2.3.2. Mechanical characterization

The mechanical characterization of neat PLA and PLA-MKSF composites was carried out through tensile, impact strength, and hardness (Shore D) tests. Tensile tests were done following the ISO 527 using a universal testing machine ELIB 30 from Ibertest (Madrid, Spain), equipped with a cell load of 5 kN and a crosshead speed of 5 mm/min. Young modulus, tensile strength, and elongation at break were obtained with this test. Five specimens were tested, and their results were averaged.

The impact strength was determined through the Charpy test, using a Charpy pendulum with an energy of 6 J, from Metrotec S.A. (San Sebastian, Spain) on injection moulded rectangular unnotched samples with dimensions $80 \times 10 \times 4 \text{ mm}$ following ISO 179. Finally, Shore D hardness was measured using a durometer model 673-D from J. Bot S.A. (Barcelona, Spain), according to ISO 868. At least five samples were tested for each composite, and their corresponding parameters were averaged.

2.3.3. Morphology characterization

Morphology of fractured Charpy test samples was studied by field emission scanning electron microscopy (FESEM) using a ZEISS ULTRA 55 microscope from Oxford Instruments (Abingdon, United Kingdom). The samples were sputtered with a gold-palladium alloy in an EMITECH sputter coating

Table 1. Theoretical solubility parameters of PLA with tributyrin and triacetin plasticizers.

Material	δ_d [MPa ^{1/2}]	δ_p [MPa ^{1/2}]	δ_h [MPa ^{1/2}]	δ [MPa ^{1/2}]	R_a [MPa ^{1/2}]	RED [-]
PLA	15.33	8.44	10.98	20.66	–	
Tributyrin (TBN)	15.96	1.67	4.89	16.78	9.19	0.86
Triacetin (TCN)	16.21	2.60	6.10	17.51	7.81	0.73

SC7620 from Quorum Technologies, Ltd. (East Sussex, UK). The microscope was operated with an acceleration voltage of 1.5 kV.

2.3.4. Thermal characterization

The main thermal transitions of the PLA-MKSF composites were evaluated through differential scanning calorimetry (DSC) in a DSC 821 from Mettler-Toledo Inc. (Schwerzenbach, Switzerland). Samples weighed about 5–8 mg and were placed in 40 μ l aluminium crucibles. The samples were subjected to a thermal cycle divided into three steps: a first heating cycle from 30 to 180 °C was followed by a cooling cycle down to –50 °C and, finally, a second heating stage from –50 up to 220 °C was scheduled. The heating and cooling stages were run at a rate of 10 °C/min in a nitrogen atmosphere (66 ml/min). Parameters such as the glass transition temperature (T_g), the cold crystallization peak temperature (T_{cc}) and enthalpy (ΔH_{cc}), the melt peak temperature (T_m) and enthalpy (ΔH_m) were obtained from the second heating stage. Moreover, the degree of crystallinity (X_c [%]) was calculated Equation (7):

$$X_c [\%] = \frac{|\Delta H_m| - |\Delta H_{cc}|}{|\Delta H_m^0|} \cdot (1 - w) \cdot 100 \quad (7)$$

where ΔH_m^0 is a theoretical value representing the theoretical melt enthalpy of a fully crystalline PLA polymer, *i.e.* 93.7 J/g as reported in the literature [28], and $1 - w$ is the weight fraction of PLA.

To evaluate the thermal stability and thermal degradation of the PLA-MKSF composites and MKSF at high temperatures, thermogravimetric analysis (TGA) was carried out on a TGA1000 thermobalance from Linseis (Selb, Germany). Samples of 15–20 mg were used, which were placed in standard alumina crucibles (70 μ l). The heating cycle was established from 30 to 700 °C with a heating rate of 10 °C/min, with a nitrogen atmosphere (66 ml/min). The onset degradation temperature was estimated at a mass loss of 5% ($T_{5\%}$) in the corresponding TGA curve, while the maximum degradation rate temperature (T_{max}) was obtained from the first derivative thermogravimetric (DTG) curve.

2.3.5. Thermomechanical characterization

Dynamical mechanical thermal analysis (DMTA) was carried out in a DMA1 dynamic analyzer from Mettler-Toledo (Schwerzenbach, Switzerland), working

in single cantilever flexural conditions. Rectangular samples with dimensions 20×6×2.7 mm were subjected to a dynamic temperature sweep from –50 to 140 °C at a constant heating rate of 2 °C/min. The selected frequency was 1 Hz, and the maximum flexural deformation or cantilever deflection was set to 10 μ m.

2.3.6. Water uptake characterization

Water uptake of neat PLA and PLA-MKSF composites was characterized following ISO 62:2008. Rectangular samples of dimensions 80×10×4 mm were sunk in distilled water at room temperature for nine weeks up to saturation. The samples were extracted from the distilled water, dried with absorbent paper, and weighed; the specimens were then again immersed in the distilled water. The weighting process was made on an analytical balance model AG245 provided by Mettler-Toledo (Schwerzenbach, Switzerland) with an accuracy of 0.001 g. This process was repeated every week under the same conditions; measurements were taken in triplicate to ensure reliable results. The percentage of water absorption was calculated using Equation (8):

$$\text{Water absorption} [\%] = \frac{W_t - W_0}{W_0} \cdot 100 \quad (8)$$

where W_t [g] is the weight of the dry sample at any time, and W_0 [g] is the weight of the initial dry sample.

2.3.7. Disintegration in controlled compost soil

The degree of disintegration under composting conditions of PLA samples and PLA-MKFS composites was studied at a temperature of 58 °C and relative humidity of 55% according to ISO 20200. Samples of dimensions 25×2×1 mm were placed inside a textile mesh to facilitate their removal. Then they were buried in a controlled compost soil made of organic solids 45%, vegetable solids 40, 30% water content, and pH between 6 and 7. Samples were periodically extracted from the compost and cleaned with distilled water. Then they were dried and weighted with an analytical balance model AG245 from Mettler-Toledo (Schwerzenbach, Switzerland) with an accuracy of 0.001 g. The percentage of weight loss was calculated using Equation (9):

$$\text{Weight loss} [\%] = \frac{W_0 - W_t}{W_0} \cdot 100 \quad (9)$$

where W_0 is the initial dry weight of the sample and W_t is the weight of the sample after t burial time. All assays were carried out in triplicate to ensure accuracy and reliability.

2.3.8. Melt flow index

The melt flow index (MFI) of neat PLA and PLA-MKSF composites was determined using MFI equipment from Metrotec S.A. (San Sebastian, Spain), equipped with a 1 mm diameter nozzle. Measurements were taken using a temperature of 190 °C and an applied load of 2.16 kg, following ISO 1133. MFI measurements were done in triplicate for each composition.

2.3.9. Surface wettability and colour measurement

The wettability of the PLA and the PLA-MKSF composites was estimated by water contact angle (WCA) measurements. To this, an Easy drop FM140 goniometer supplied by Krüss equipment (Hamburg, Germany) was used. The test was carried out at room temperature with water droplets of approximately ~15 µl randomly deposited on the sample surface. The WCA was measured eight times for each droplet for each formulation, and the average values were provided.

The effect of MKSF on the colour of the PLA matrix was analysed with a colorimeter model KONICA CM-3600d Colorflex-DIFF2 from Hunter Associates Laboratory (Reston, Virginia, USA). The instrument was calibrated considering the standard white tile and a mirror unit for black. The CIELab colour scale (coordinates L^* , a^* and b^*) was recorded. L^* refers to lightness, a^* stands for the colour coordinate between red and green, and b^* represents the colour coordinate between yellow and blue. The total colour difference (ΔE_{ab}^*) was calculated by Equation (10):

$$\Delta E_{ab}^* = \sqrt{(\Delta L^*)^2 + (\Delta a^*)^2 + (\Delta b^*)^2} \quad (10)$$

where ΔL^* , Δa^* , and Δb^* are the differences between the CIELab colour coordinates of the samples and the reference colour.

3. Results

3.1. Mechanical characterization

Table 2 summarises the main values of the tensile test parameters, impact strength, and Shore D hardness of neat PLA and PLA-MKSF composites. In the case of neat PLA, high values of elastic modulus (E_t) and tensile strength (σ_t) are obtained (3848 MPa and 40.1 MPa, respectively), while a low percentage of elongation at break (ϵ_b) is obtained (4.7%). These properties are typical of PLA, being a rigid and brittle material [21]. The incorporation of MKSF leads to an increase in the stiffness and brittleness of the material. This is demonstrated by the high elastic modulus values reported, which are 35% higher than the values of neat PLA. It is also verified by a decrease in tensile strength and elongation at break of 40 and 35%, respectively, related to neat PLA. This provokes a highly brittle behavior in PLA-MKSF composites. This behaviour can be related to the low interaction between the MKSF and the surrounding PLA matrix, which generates a stress concentration effect, provoking a detriment of mechanical properties [29].

As expected, the incorporation of tributyrin (TBN) and triacetin (TCN) improves the ductile behaviour of PLA-MKSF composites. In the case of PLA-MKSF/TBN, a decrease in the tensile modulus and tensile strength of 37 and 58% can be observed, respectively. An increase in elongation at break can also be observed up to 9.5%, thus, demonstrating the plasticizing effect of tributyrin. Even though impact strength is lower than neat PLA, the PLA-MKSF composite plasticized with tributyrin has a higher impact strength than the unplasticized PLA-MKSF composite. This effect was also reported by other studies [30], with tributyrin as a plasticizer in a PLA/PHB blend. In general, it was observed how the

Table 2. Mechanical properties of PLA, PLA-MKSF composites obtained from tensile tests (elastic modulus – E_t , tensile strength – σ_t , elongation at break – ϵ_b), Shore D, impact strength.

Code	Tensile			Shore D hardness	Impact strength [kJ/m ²]
	Elastic modulus, E_t [MPa]	Strength, σ_t [MPa]	Elongation at break, ϵ_b [%]		
PLA	3848±245	40.1±3.7	4.7±0.5	63.8±1.3	33.6±3.6
PLA-MKSF	5219±27	23.9±0.9	4.4±0.6	60.8±1.3	21.7±1.5
PLA-MKSF/TBN	2424±193	16.9±0.5	9.5±0.6	61.0±1.3	27.7±1.6
PLA-MKSF/TCN	2995±199	18.7±0.6	8.3±0.7	61.7±1.2	33.1±3.1

incorporation of tributyrin provoked a reduction of the tensile strength and elastic modulus in all formulations. However, no significant changes were observed in the elongation at break.

As it occurs with the composites with TBN, the incorporation of triacetin is quite notorious regarding ductile properties. On the one hand, a decrease in the elastic modulus and tensile strength of 22 and 33% with respect to neat PLA is observed. Additionally, an increase of 77% in elongation at break is observed. In spite of this, the impact strength of the material remains quite high, with a value of 33.1 kJ/m², comparable to the impact strength of neat PLA but with a noticeable difference since ductile properties have been improved. This effect can be related to the excellent miscibility that TCN has with the PLA matrix, as it was stated in the theoretical solubility section. This phenomenon, together with the compatibility of TCN with MKSF (composed mainly of polysaccharides and protein), enhances the general plasticization effect [31]. Some studies have reported that the plasticizer embeds the surface of lignocellulosic

particles, thus making the particles slide all over the matrix [32].

Regarding Shore D hardness, it can be observed that the incorporation of MKSF provokes a slight decrease in hardness from 63.8 down to 60.8. Different plasticizers (TBN and TCN) do not significantly affect the hardness, despite a little increase. These results are similar to those reported by Gonzalez *et al.* [33], who observed that the use of maleinized linseed oil (MLO) plasticizer did not alter the hardness of the matrix. These results are in accordance with the estimated miscibility between neat PLA and tributyrin and triacetin. As the theoretical study showed good compatibility between the plasticizers and the polymer, which has been demonstrated by the good mechanical response in both cases.

3.2. Morphological characterization.

Figure 2 shows the morphology of the fracture surface of impact test samples of each one of the developed composites observed by FESEM at 1000× magnification. Figure 2a corresponds to neat PLA,

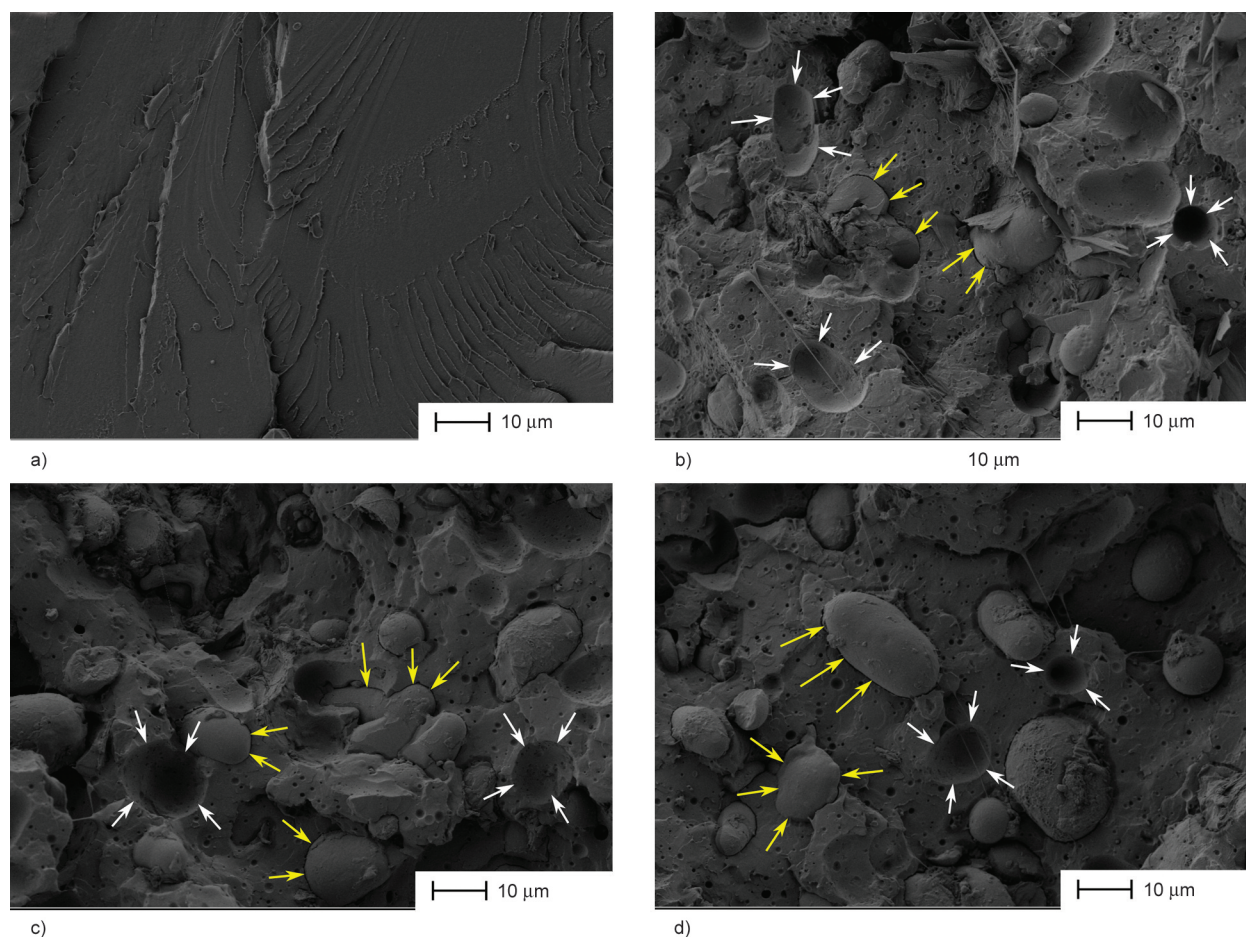


Figure 2. FESEM image of mango kernel seed flour (MKSF) particles at 1000× with a marker scale of 10 μm. a) PLA, b) PLA-MKSF, c) PLA-MKSF/TBN, d) PLA-MKSF/TCN.

which shows the typical morphology of a brittle polymer. This behaviour is detected by a smooth and flat surface, with the presence of little microcracks [21]. This perfectly matches the mechanical results observed in the previous section, where PLA exhibited an extremely low ductility (low elongation at break). In the case of Figure 2b, the morphology of PLA with the incorporation of MKSF is shown. The presence of MKSF particles is clearly seen all over the matrix, where the adhesion of the particles is undoubtedly poor, as evidenced by the presence of voids (white arrows) in the matrix surface. Pulled-out MKSF particles generate those voids during impact fracture due to the poor compatibility between PLA and MKSF [34]. Figures 2c and 2d show the FESEM morphology of the composites with tributyrin and triacetin, respectively. The concentration of voids in the PLA matrix has been observed to be reduced with respect to the unplasticized PLA/MKSF composite. This indicates an increase in the affinity between PLA and MKSF microparticles, thanks to the addition of both plasticizers, which possess ester groups that enhance interaction with MKSF through hydrogen bonds [20]. Additionally, the gap (yellow arrows) between the MKSF particles and the surrounding PLA matrix is smaller than in the unplasticized composite. This fact corroborates the increased ductile properties observed in the mechanical characterization section, especially by using triacetin, which provided an elongation at break of 9.5%.

3.3. Thermal properties of PLA-MKSF composites

Differential scanning calorimetry (DSC) was used in order to study the thermal properties of the PLA-MKSF composites. Figure 3 gathers the thermograms that correspond to the second heating cycle of neat PLA and each one of the PLA-MKSF composites. At the same time, Table 3 summarizes the main thermal parameters extracted from these thermograms. Neat PLA shows a glass transition temperature at about

62 °C, which is a typical value for this polymer, as observed by Petchwattana *et al.* [20]. The addition of MKSF into the polymer matrix decreases this value by approximately 1 °C, indicating almost negligible plasticization.

On the other hand, adding tributyrin and triacetin decreases this temperature to 40.6 and 46.4 °C, respectively. This remarkable decrease is ascribed to increased chain mobility of the amorphous phase of PLA induced by both plasticizers [20]. The addition of triacetin and tributyrin also plays a key role in the cold crystallization process. The cold crystallization peak temperature of neat PLA is located at 115.3 °C. In contrast, the addition of MKSF decreases it down to 109 °C, but, once again, the incorporation of tributyrin and triacetin plasticizers moves the cold crystallization peak temperature down to such low values of 89 and 98 °C, respectively. This decrease in cold crystallization is also ascribed to the increase in PLA chain mobility, which provokes polymer chains to rearrange more quickly to a packed structure in the presence of plasticizers. Pure PLA exhibits a melting temperature of approximately 167 °C, which is increased by the presence of MKSF up to 169 °C. This effect is typical in rigid lignocellulosic fillers, as they

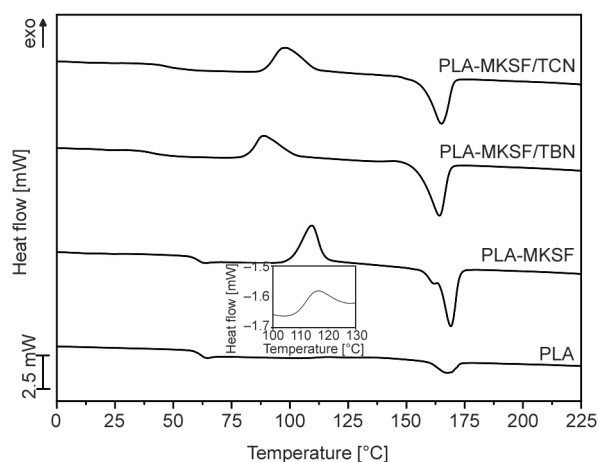


Figure 3. Differential scanning calorimetry (DSC) thermograms of neat PLA and plasticized and unplasticized PLA-MKSF composites.

Table 3. Glass transition temperature (T_g), cold crystallization peak temperature (T_{cc}), cold crystallization enthalpy (ΔH_{cc}), melting temperature (T_m), melting enthalpy (ΔH_m), and crystallinity X_c of the PLA-MKSF composites, obtained by differential scanning calorimetry (DSC).

Code	T_g [°C]	T_{cc} [°C]	ΔH_{cc} [J/g]	T_m [°C]	ΔH_m [J/g]	X_c [%]
PLA	62.4±1.2	115.3±3.5	0.7±0.1	167.1±0.2	10.1±0.1	10.1±0.5
PLA-MKSF	61.3±1.5	109.5±4.1	24.6±0.4	169.1±0.4	30.3±1.2	8.7±0.2
PLA-MKSF/TBN	40.6±2.1	88.9±3.6	19.1±1.1	164.1±1.0	30.4±1.7	17.3±0.1
PLA-MKSF/TCN	46.4±1.7	98.2±2.7	24.7±0.5	165.0±1.2	29.3±1.2	7.1±0.3

are more thermally stable than neat PLA, thus delaying the melting phenomenon.

Similarly, the addition of plasticizers follows an analogous trend to the glass transition and cold crystallization temperatures. Tributyrin and triacetin decrease T_m to 164 and 165 °C, respectively, due to higher segmental mobility [20]. Finally, the crystallinity of PLA did not suffer significant changes, presenting a value of around 10%, except for the sample with tributyrin, which showed a crystallinity of 17.3%. This increase is related to the aforementioned enhanced chain mobility, which accelerates the crystallization rate of PLA, allowing it to crystallize at a lower T_{cc} and then present a higher crystalline region.

In order to assess the thermal degradation behaviour of the composites, a thermogravimetric (TGA) analysis was carried out. Figure 4 shows the thermogravimetric (TGA) and first derivative (DTG) curves of the studied composites, whereas Table 4 gathers the main thermal parameters related to this analysis. Neat PLA exhibits a single-step degradation curve, typical of this polyester. Its onset degradation temperature ($T_{5\%}$) is drastically reduced from 365 °C down to 273 °C due to the incorporation of MKSF. This is due to the earlier decomposition of low molecular weight hemicellulose in the mango kernel seed flour [20]. A similar trend occurs with the maximum degradation rate temperature extracted from the first derivative diagram, as it decreases from 404.5 down to 322.6 °C for PLA-MKSF. This is ascribed to the inherent lower thermal degradation stability of the lignocellulosic particles of MKSF, namely hemicellulose, cellulose, lignin, and pectin [35]. This phenomenon is clearly observed in the TGA dia-

Table 4. Main thermal degradation parameters of the PLA-MKSF composites: onset degradation temperature at a mass loss of 5 wt% ($T_{5\%}$), maximum degradation rate temperature (T_{deg}), and the residual mass at 700 °C.

Code	$T_{5\%}$ [°C]	T_{deg} [°C]	Residual mass [%]
PLA	365.2±2.5	404.5±3.1	0.2±0.1
PLA-MKSF	272.7±1.2	321.1±1.3	0.2±0.2
PLA-MKSF/TBN	216.4±2.0	324.7±3.3	0.1±0.2
PLA-MKSF/TCN	204.1±1.1	321.2±1.1	0.1±0.2

grams, where the PLA mass decreases far later than in the rest of the samples. The TGA curves of the samples with tributyrin and triacetin show a two-step degradation process, which is ascribed to the initial degradation (plasticizer removal) of both plasticizers, which are more volatile than the PLA matrix [36]. In this case, the onset degradation temperature is further decreased to 218 and 203 °C for tributyrin and triacetin, respectively. This demonstrates the results observed in DSC, as both plasticizers reduce the interaction between polymer chains and increase their mobility, thus diminishing thermal stability. The maximum degradation rate temperature is also reduced to 325 and 322 °C, respectively, a decrease of approximately 20% relative to neat PLA. The residual mass of PLA-MKSF composites increases due to a higher tendency of MKSF for char formation than PLA.

3.4. Thermomechanical characterization

To assess the mechanical properties of the composites in dynamic thermal conditions, DMTA was carried out. This analysis also allows a more detailed evaluation of the glass transitions of polymers. Figure 5 shows the dynamic-mechanical thermal analysis

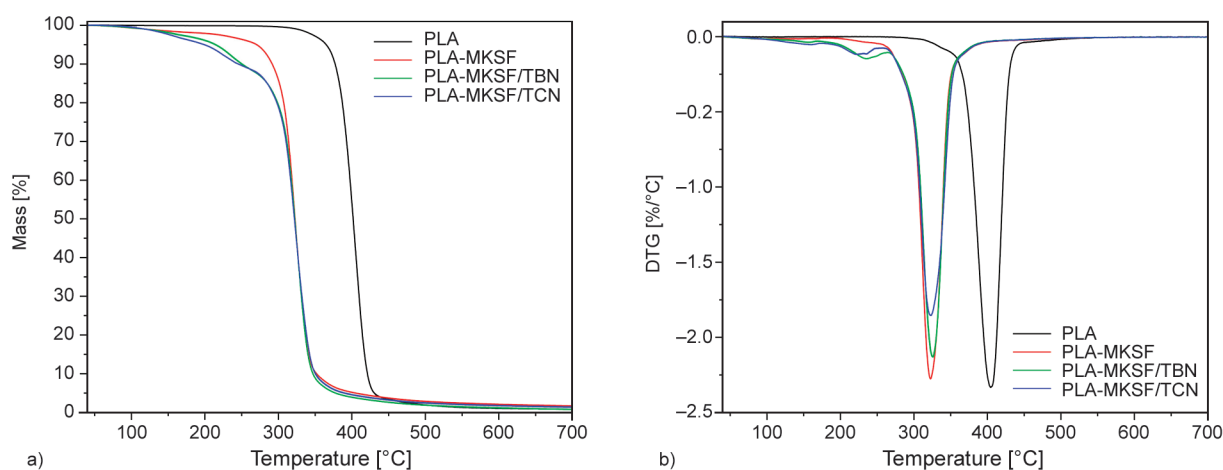


Figure 4. Thermal degradation of PLA-MKSF composites, a) thermogravimetric (TGA), and b) first derivative (DTG) of neat PLA, plasticized and unplasticized PLA-MKSF composites.

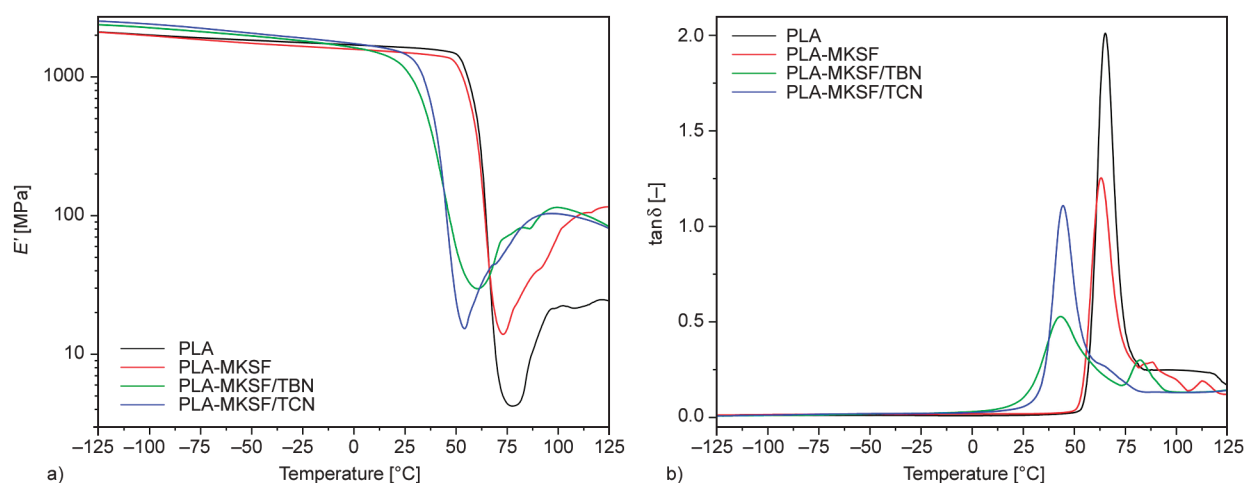


Figure 5. Plot evolution of a) the storage modulus (E') and b) the dynamic damping factor ($\tan\delta$) of the PLA-MKSF composites.

(DMTA) curves for all the PLA-MKSF composites, namely the evolution of the storage modulus (E') and the dynamic damping factor ($\tan\delta$). At the same time, Table 5 gathers the main thermomechanical parameters to be analyzed. Figure 5a shows the variation of the storage modulus, which slowly decreases in the whole temperature range until a sudden drop is detected. This drop occurs between 60 and 70 °C for neat PLA and PLA-MKSF, and between 40 and 50 °C for the plasticized PLA-MKSF composites. Those drops are related to the α -relaxation of PLA chains once the glass transition region is surpassed [37]. This is due to the plasticizing effect of TBN and TCN, which increases the mobility of PLA chains, thus reducing their stiffness in comparison with neat PLA. These changes in rigidity are registered in Table 5, where there is a significant difference between the storage modulus at 5 and 70 °C, which goes down from 1500–1700 MPa to values of 8–50 MPa, respectively. Figure 5b allows observing more precisely the glass transition temperature of the materials, which is indicated by a peak in the evolution of the dynamic damping factor ($\tan\delta$) with temperature. The glass transition temperature of neat PLA is located at approximately 65 °C, as already

observed in DSC. Adding MKSF does not provoke significant changes in its T_g , with an average value of 63 °C. On the other hand, adding the TBN and TCN plasticizers reduces the glass transition temperature to 43 and 44 °C, respectively. This is again due to the chain mobility enhancement phenomenon that both plasticizers provide. This result proves the successful plasticization of PLA and demonstrates the increase in elongation at break reported in the mechanical properties section. After the glass transition process, there is a slight rise of E' in the plasticized samples and the PLA+MKSF composite, which can also be observed in the $\tan\delta$ graph, around 80 °C. This rise is due to crystallization, as an increase in chain mobility favors the formation of crystals after the T_g [38]. This crystal formation slightly increases the stiffness of the composites, which is why E' increases a little bit at high temperatures (75 to 100 °C). This is in accordance with the DSC results, where a cold crystallization peak was recorded for the PLA+MKSF, and the TBN and TCN plasticized samples in the 75–100 °C temperature range.

3.5. Melt flow index (MFI)

Figure 6 gathers the melt flow index (MFI) for neat PLA and the PLA-MKSF composites developed in this work, measured at 190 °C with a load mass of 2.16 kg. Neat PLA presents an MFI of approximately 17 g/10 min, similar to that provided in the technical data sheet. Once the MKSF is incorporated into the PLA matrix, the melt flow index increases up to about 18 g/10 min. A similar effect was observed by Pantyukhov *et al.* [39] in polyethylene composites with lignocellulosic fibres as fillers. As expected, the

Table 5. Main dynamic-mechanical parameters of the PLA MKSF composites.

Code	E' at 5 °C [MPa]	E' at 70 °C [MPa]	T_g [°C]
PLA	1690.6±33.80	8.37±0.13	65.26±0.97
PLA-MKSF	1569.4±29.81	16.9±0.32	63.13±1.39
PLA-MKSF/TBN	1579.0±27.01	54.1±1.14	43.36±0.65
PLA-MKSF/TCN	1704.9±30.68	45.9±0.92	44.43±0.71

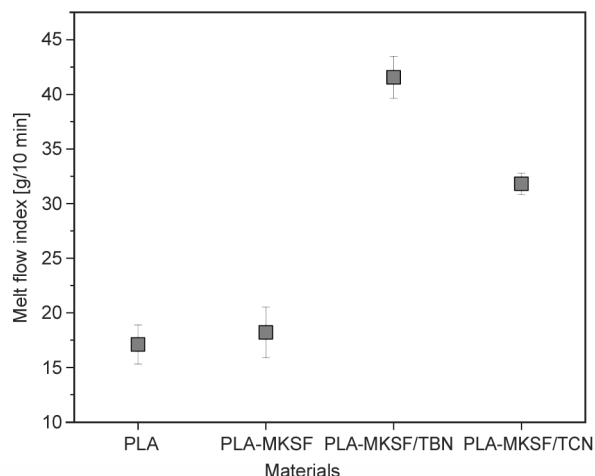


Figure 6. Melt flow index (MFI) of neat PLA and PLA-MKSF composites.

addition of tributyrin and triacetin drastically increased the MFI of the composites. This is ascribed to the enhanced chain mobility that both plasticizers provide to PLA-MKSF composites. Thus, the PLA polymer chain entanglement becomes poorer, positively affecting the composite’s flowability. The measured MFI values for PLA-MKSF/TBN and PLA-MKSF/TCN are 42.5 g/10 min and 32.5 g/10 min, respectively. This indicates that the plasticizing effect of tributyrin is stronger than that of triacetin, as it has also been demonstrated in its mechanical and thermal properties.

3.6. Visual appearance and water contact angle characterization

Visual appearance is an essential factor regarding the product’s perception by the consumer. Figure 7 shows the visual appearance of PLA-MKSF composites. At first sight, it can be seen that only the neat PLA sample shows certain transparency due to the semicrystalline nature of the polyester [40]. The incorporation of MKSF leads the samples to turn completely opaque with characteristic dark brown colours, which are especially attractive from the point of view of wood-plastic composites. Meanwhile, Table 6 gathers the $L^*a^*b^*$ colour coordinates. Neat PLA exhibited a luminance of 36.8, which is reduced to values close to

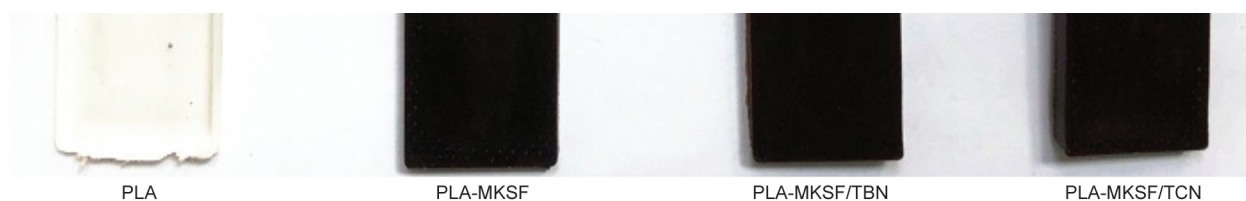


Figure 7. The visual appearance of the PLA-MKSF composites.

Table 6. Main colour parameters of the PLA-MKSF composites in terms of the CieLab colour space ($L^*a^*b^*$) and the colour difference ΔE_{ab}^* .

Code	L^*	a^*	b^*	ΔE_{ab}^*
PLA	36.8±0.3	-0.2±0.1	0.9±0.1	–
PLA-MKSF	25.8±0.3	3.1±0.1	3.5±0.1	11.7±0.3
PLA-MKSF/TBN	26.0±0.1	4.2±0.2	5.3±0.1	12.4±0.1
PLA-MKSF/TCN	26.9±0.3	4.0±0.1	5.4±0.2	11.6±0.3

26 for all the rest of the samples as a result of the incorporation of MKSF, which turns the samples into darker colours.

Regarding colour coordinates a^* and b^* , neat PLA displays very low values (–0.2 and 0.9, respectively) due to its characteristic white colour. Adding MKSF increases those values to 3.1 and 3.5, respectively. This was expected, as the observed dark brown colour is composed of red and yellow components. With the addition of tributyrin and triacetin, both values increase even more, as they provide a clearer tonality to the dark brown colour of the PLA-MKSF composite, as seen in Figure 7. The values of a^* and b^* for TBN and TCN are very close to 4 and 5, respectively, in both cases. Finally, the colour difference ΔE_{ab}^* is very similar for all three PLA-MKSF composites, giving values of approximately 12. That was expected, as the three samples presented very similar colours. A similar tonality was reported in previous work for a polypropylene matrix with mango peel wastes [41].

The water contact angle analysis gives information regarding the affinity and interaction of the studied materials with water. Figure 8 shows the contact angle of distilled water with the surface of each one of the PLA-MKSF composites developed in this study. As it can be observed, neat PLA presents a contact angle of 85°, which is characteristic of a hydrophobic polymer according to Vogler, who established the hydrophilic threshold at 65° [42]. Once MKSF is added to the polymer matrix, the contact angle considerably decreases to 75°, increasing the hydrophilicity of the polymer. This behaviour is ascribed to the polar groups contained in MKSF, mainly from

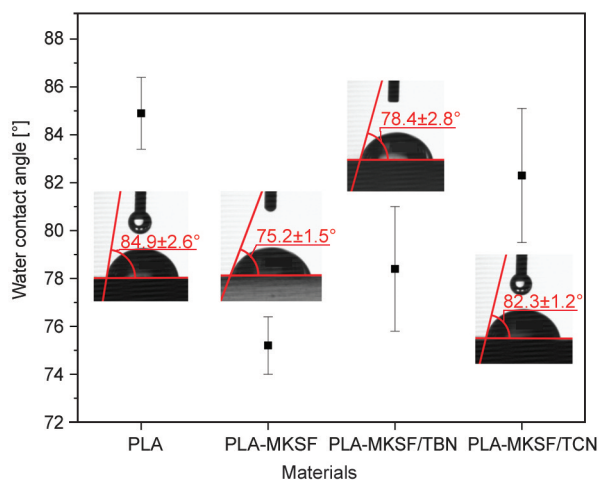


Figure 8. Water contact angle measurements of plasticized and unplasticized PLA-MKSF composites.

polysaccharides and proteins. Those molecules have a great capacity to form hydrogen bonds, thus increasing affinity towards the water and then enhancing hydrophilicity [43]. The addition of plasticizers into the PLA-MKSF composite reduces the affinity towards water, exhibiting contact angles of 78.5 and 82° for tributyrin and triacetin, respectively. Both plasticizers reduce the contact angle of neat PLA, as tributyrin and triacetin are certainly hydrophilic [44]. However, they increase the contact angle in relation to the PLA-MKSF sample. This could be due to the interaction of ester groups contained in both plasticizers with the hydroxyl groups in MKSF, thus reducing the availability of –OH functionalities in MKSF that can hydrogen-bond with water molecules.

3.7. Water uptake

The water uptake test evaluated the water absorption capacity of neat PLA and PLA-MKSF composites over 11 weeks. Figure 9 shows the evolution of the water absorption of the samples over 11 weeks in terms of the percentage of water mass absorbed in relation to the initial weight of the specimens. As expected, neat PLA presents the lowest water absorption profile, with maximum absorption of less than 1 wt%. This is the typical behaviour of a hydrophobic polymer; a similar profile was observed in previous works [37] for neat PLA. When MKSF is added into the PLA matrix, the water uptake of the composite drastically increases up to almost 12 wt% at 11 weeks of immersion in distilled water. This effect is ascribed to the presence of polar groups in the composite coming from starch, proteins, and lignin. Their characteristic

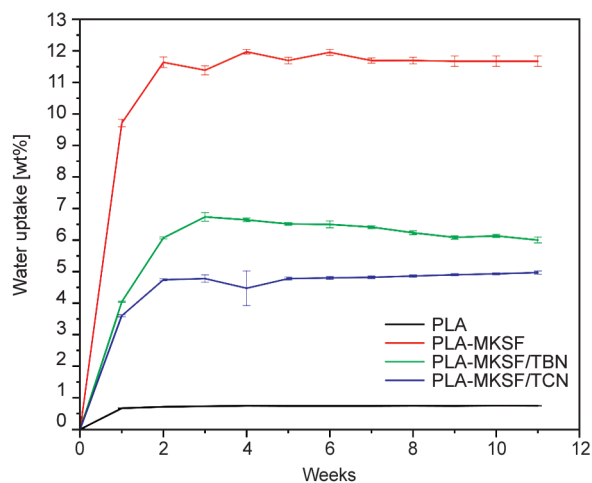


Figure 9. Water uptake evolution of the PLA-MKSF composites over 11 weeks.

functionalities provide the material with a great affinity for water, as observed in the contact angle measurements. Finally, adding tributyrin and triacetin also increases the water absorption compared with neat PLA up to 6.5 and 5 wt%, respectively. However, they decrease the water absorption capacity with respect to the PLA-MKSF composite. This decrease could be related to the interaction between carbonyl groups in both plasticizers and hydroxyl groups in MKSF, reducing the possible reaction with distilled water [45]. The sample with tributyrin seems to slightly decrease its mass over time from 4 weeks of immersion. This could be ascribed to the certain water solubility of the plasticizer in distilled water. The results presented here are in total accordance with the contact angle measurements, where tributyrin also presented a slightly higher affinity for water than triacetin.

3.8. Disintegration test

The disintegrability of the PLA-MKSF composites was assessed through the disintegration test. Figure 10 shows the disintegration profile of all the studied PLA-based samples in terms of mass loss. As can be observed, only neat PLA disintegrated at 100% (at 9 weeks). Nonetheless, the remaining specimens disintegrated up to 90% at 12 weeks, which is the objective for considering a material biocompostable [43]. Neat PLA exhibited the typical behaviour of a biodegradable polymer, fully disintegration at 9 weeks due to a hydrolytic degradation process. Once MKSF is added to the polymer matrix, the disintegration capacity decreases to 90% at 12 weeks of incubation time in compost soil.

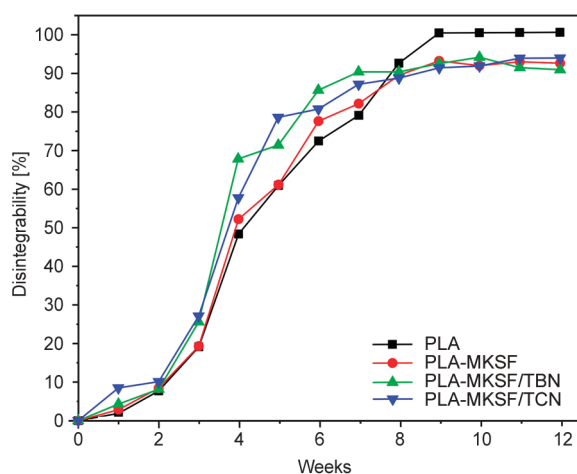


Figure 10. Disintegration profile of the PLA-MKSF specimens over 12 weeks.

Moreover, the addition of plasticizers does not significantly vary tPlease check all of the figures and tables, carefully (axes, headings, designations, lowercase or capital letters, etc.).

Please check the equations, carefully. The disintegration process. This decrease in biodegradability could be ascribed to an increase in the crystallinity of the polymer, especially in the PLA-MKSF/TBN composite. The hydrolytic degradation process occurs more easily in the amorphous regions of the polymer. Thus, the higher the crystallinity, the lower the proportion of the amorphous phase in the polymer, providing more resistance against biodegradation [37]. Nonetheless, both plasticizers do increase the disintegrability rate during the first 8 weeks. This phenomenon could be ascribed to the hydrophilic nature of TBN and TCN, which makes water absorption and diffusion through the polymer bulk in the initial phase of disintegration to be faster. This results in higher hydrolysis in the polymer chains, leading to smaller molecules (monomers and short-chain oligomers) being available for microorganisms to attack [46]. In the last weeks, the samples with MKSF seem to have a disintegrability threshold, which could correspond to the MKSF fraction left in the samples, which does not fully disintegrate.

Figure 11 gathers images that record the visual aspect of the samples all over the test. As has been aforementioned, it is observed that neat PLA is entirely disintegrated after 9 weeks, while the rest of the specimens continue to degrade until week 12, when just little remnants are left (90% of biodegradation). Moreover, neat PLA started to decompose at week 2, as demonstrated by the macrocracks that

appear in the square sample in Figure 11. In contrast, the MKSF samples start their decomposition at week 4. Thus, the results herein presented are in total accordance with the disintegration profile shown in Figure 10.

4. Conclusions

This work shows the successful development of wood plastic composites based on a polyester PLA matrix with mango kernel seed flour (MKSF) as a reinforcing agent and tributyrin (TBN) and triacetin (TCN) as plasticizers. The addition of MKSF gave the composites a characteristic dark brown color, which could prove to be interesting in replacing wood-based materials for these wood-plastic composites. Regarding their mechanical response, tributyrin and triacetin improved the ductility of the polymer matrix, increasing the elongation at break from 4.4% for the PLA+MKSF sample to 9.5 and 8.3% for PLA+MKSF/TBN and PLA+MKSF/TCN, respectively. These results matched the theoretical solubility parameters of neat PLA and the plasticizers, which were also studied, showing good compatibility between PLA, TBN, and TCN (*RED* values of 0.86 and 0.73, respectively). FESEM results also supported the mechanical properties of the composites, as well as certain compatibility effects exerted by the plasticizers over the polymer matrix and the MKSF particles. The plasticizing effect was further verified by thermal analysis, where the glass transition temperature and melting temperatures were reduced in relation to neat PLA as a result of the increased chain mobility provided by both TBN and TCN. MKSF made the affinity for water of the composite drastically increase, as was observed by means of contact angle measurements and water uptake. Both plasticizers reduced this considerably large water absorption of PLA+MKSF thanks to their bonding with MKSF particles. The thermal degradation of the composites became faster as a result of the presence of both plasticizers, again attributed to the increased chain mobility of the polymer chains ascribed to the plasticizing effect. Finally, all the composites showed a positive response towards disintegration under compost soil conditions. Disintegrating over 90% of the total mass of the samples.

All in all, these results prove that environmentally friendly wood plastic composites can be obtained from the combination of PLA, MKSF, TBN, and TCN, with enhanced ductility, good thermal stability,

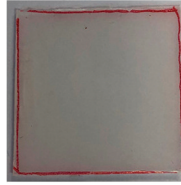
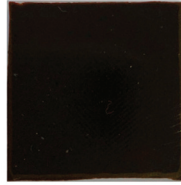

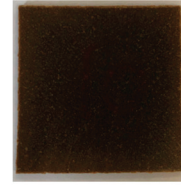

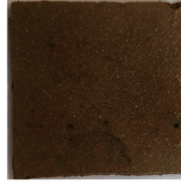


















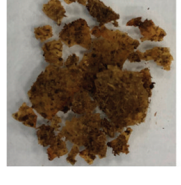



Week	PLA	PLA-mKSF	PLA-MKSF/TBN	PLA-MKSF/TCM
0				
1				
2				
3				
4				
5				
6				

Figure 11. Evolution of the visual appearance of the samples (25×2×1 mm) during the disintegration test.



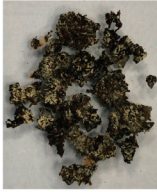



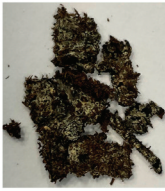
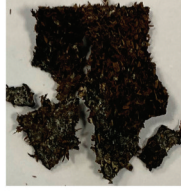

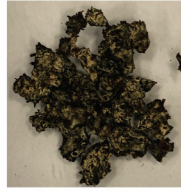






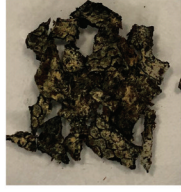



Week	PLA	PLA-mKSF	PLA-MKSF/TBN	PLA-MKSF/TCM
7				
8				
9				
10				
11				
12				

Figure 11. Evolution of the visual appearance of the samples (25×2×1 mm) during the disintegration test (continued).

and excellent biodegradability. Thus, they could be used in applications substituting wood-based products, as they present quite attractive dark brown colors.

References

- [1] Azeez A. T.: A review of wood plastic composites effect on the environment. Journal of University of Babylon for Pure and Applied Sciences, **25**, 360–367 (2017).

- [2] Siakeng R., Jawaid M., Asim M., Saba N., Sanjay M. R., Siengchin S., Fouad H.: Alkali treated coir/pineapple leaf fibres reinforced PLA hybrid composites: Evaluation of mechanical, morphological, thermal and physical properties. *Express Polymer Letters*, **14**, 717–730 (2020).
<https://doi.org/10.3144/expresspolymlett.2020.59>
- [3] Mokhena T. C., Sadiku E. R., Mochane M. J., Ray S. S.: Mechanical properties of fire retardant wood-plastic composites: A review. *Express Polymer Letters*, **15**, 744–780 (2021).
<https://doi.org/10.3144/expresspolymlett.2021.61>
- [4] Akintayo O., Olajide J., Betiku O., Ego A., Adegbesan O., Daramola O., Sadiku E., Desai D.: Poly(lactic acid)-silkworm silk fibre/fibroin bio-composites: A review of their processing, properties, and nascent applications. *Express Polymer Letters*, **14**, 924–951 (2020).
<https://doi.org/10.3144/expresspolymlett.2020.76>
- [5] Persic M., Mikulic-Petkovsek M., Slatnar A., Veberic R.: Chemical composition of apple fruit, juice and pomace and the correlation between phenolic content, enzymatic activity and browning. *LWT-Food Science and Technology*, **82**, 23–31 (2017).
<https://doi.org/10.1016/j.lwt.2017.04.017>
- [6] Mala T., Sadiq M. B., Anal A. K.: Optimization of thermosonication processing of pineapple juice to improve the quality attributes during storage. *Journal of Food Measurement and Characterization*, **15**, 4325–4335 (2021).
<https://doi.org/10.1007/s11694-021-01011-8>
- [7] Kringel D. H., Dias A. R. G., da Rosa Zavareze E., Gandra E. A.: Fruit wastes as promising sources of starch: Extraction, properties, and applications. *Starch-Stärke*, **72**, 1900200 (2020).
<https://doi.org/10.1002/star.201900200>
- [8] Haeldermans T., Samyn P., Cardinaels R., Vandamme D., Vanreppelen K., Cuypers A., Schreurs S.: Poly(lactic acid) bio-composites containing biochar particles: Effects of fillers and plasticizer on crystallization and thermal properties. *Express Polymer Letters*, **15**, 343–360 (2021).
<https://doi.org/10.3144/expresspolymlett.2021.30>
- [9] Kalita N. K., Hazarika D., Kalamdhad A., Katiyar V.: Biodegradation of biopolymeric composites and blends under different environmental conditions: Approach towards end-of-life panacea for crop sustainability. *Biore-source Technology Reports*, **15**, 100705 (2021).
<https://doi.org/10.1016/j.biteb.2021.100705>
- [10] Rojas-Lema S., Ivorra-Martinez J., Lascano D., Garcia-Garcia D., Balart R.: Improved performance of environmentally friendly blends of biobased polyethylene and kraft lignin compatibilized by reactive extrusion with dicumyl peroxide. *Macromolecular Materials and Engineering*, **306**, 2100196 (2021).
<https://doi.org/10.1002/mame.202100196>
- [11] Rojas-Lema S., Lascano D., Ivorra-Martinez J., Gomez-Caturla J., Balart R., Garcia-Garcia D.: Manufacturing and characterization of high-density polyethylene composites with active fillers from persimmon peel flour with improved antioxidant activity and hydrophobicity. *Macromolecular Materials and Engineering*, **306**, 2100430 (2021).
<https://doi.org/10.1002/mame.202100430>
- [12] Tharanathan R. N., Yashoda H. M., Prabha T. N.: Mango (*Mangifera indica L.*), ‘The king of fruits’ – An overview. *Food Reviews International*, **22**, 95–123 (2006).
<https://doi.org/10.1080/87559120600574493>
- [13] Maldonado-Celis M. E., Yahia E. M., Bedoya R., Landázuri P., Loango N., Aguillón J., Restrepo B., Guerrero Ospina J. C.: Chemical composition of mango (*Mangifera indica L.*) fruit: Nutritional and phytochemical compounds. *Frontiers in Plant Science*, **10**, 1073 (2019).
<https://doi.org/10.3389/fpls.2019.01073>
- [14] Wadhwa M., Bakshi M.: Utilization of fruit and vegetable wastes as livestock feed and as substrates for generation of other value-added products. *Rap Publication*, Bangkok (2013).
- [15] Das P. C., Sattar S., Jony M. E., Islam M. N.: Rehydration kinetics of flour from dehydrated mango kernel. *Food Research*, **2**, 474–480 (2018).
[https://doi.org/10.26656/fr.2017.2\(5\).210](https://doi.org/10.26656/fr.2017.2(5).210)
- [16] Ribeiro S., Barbosa L., Queiroz J., Knödler M., Schieber A.: Phenolic compounds and antioxidant capacity of brazilian mango (*Mangifera indica L.*) varieties. *Food chemistry*, **110**, 620–626 (2008).
<https://doi.org/10.1016/j.foodchem.2008.02.067>
- [17] Gao C., Zhang J., Zhang D., Dong Y., Wang S., Peng J., Liu Y.: Synthesis of bio-based waterborne polyesters as environmentally benign biodegradable material through regulation of unsaturated acid structure. *European Polymer Journal*, **156**, 110632 (2021).
<https://doi.org/10.1016/j.eurpolymj.2021.110632>
- [18] Garcia-Garcia D., Carbonell-Verdu A., Arrieta M. P., López-Martínez J., Samper M. D.: Improvement of PLA film ductility by plasticization with epoxidized karanja oil. *Polymer Degradation and Stability*, **179**, 109259 (2020).
<https://doi.org/10.1016/j.polymdegradstab.2020.109259>
- [19] Gürlér N., Paşa S., Alma M. H., Temel H.: The fabrication of bilayer polylactic acid films from cross-linked starch as eco-friendly biodegradable materials: Synthesis, characterization, mechanical and physical properties. *European Polymer Journal*, **127**, 109588 (2020).
<https://doi.org/10.1016/j.eurpolymj.2020.109588>
- [20] Petchwattana N., Naknaen P., Narupai B.: A circular economy use of waste wood sawdust for wood plastic composite production: Effect of bio-plasticiser on the toughness. *International Journal of Sustainable Engineering*, **13**, 398–410 (2020).
<https://doi.org/10.1080/19397038.2019.1688422>

- [21] Lascano D., Quiles-Carrillo L., Balart R., Boronat T., Montanes N.: Toughened poly(lactic acid) – PLA formulations by binary blends with poly(butylene succinate-co-adipate) – PBSA and their shape memory behaviour. *Materials*, **12**, 622 (2019).
<https://doi.org/10.3390/ma12040622>
- [22] Tejada-Oliveros R., Gomez-Caturla J., Sanchez-Nacher L., Montanes N., Quiles-Carrillo L.: Improved toughness of polylactide by binary blends with polycarbonate with glycidyl and maleic anhydride-based compatibilizers. *Macromolecular Materials and Engineering*, **306**, 2100480 (2021).
<https://doi.org/10.1002/mame.202100480>
- [23] Montes M. I., D'Amico D. A., Manfredi L. B., Cyrus V. P.: Effect of natural glyceryl tributyrates as plasticizer and compatibilizer on the performance of bio-based polylactic acid/poly(3-hydroxybutyrate) blends. *Journal of Polymers and the Environment*, **27**, 1429–1438 (2019).
<https://doi.org/10.1007/s10924-019-01425-y>
- [24] Coltelli M-B., Mallegni N., Rizzo S., Fiori S., Signori F., Lazzeri A.: Compatibilization of poly(lactic acid) (PLA)/plasticized cellulose acetate extruded blends through the addition of reactively extruded comb copolymers. *Molecules*, **26**, 2006 (2021).
<https://doi.org/10.3390/molecules26072006>
- [25] Pawlak F., Aldas M., Parres F., López-Martínez J., Arrieta M. P.: Silane-functionalized sheep wool fibers from dairy industry waste for the development of plasticized PLA composites with maleinized linseed oil for injection-molded parts. *Polymers*, **12**, 2523 (2020).
<https://doi.org/10.3390/polym12112523>
- [26] van Krevelen D. W., te Nijenhuis K.: *Properties of polymers: Their correlation with chemical structure; Their numerical estimation and prediction from additive group contributions*. Elsevier, Amsterdam (2009).
- [27] Auras R. A., Lim L-T., Selke S. E., Tsuji H.: *Poly(lactic acid): Synthesis, structures, properties, processing, and applications*. Wiley, Amsterdam (2011).
- [28] Kangalli E., Bayraktar E.: Preparation and characterization of poly(lactic acid)/boron oxide nanocomposites: Thermal, mechanical, crystallization, and flammability properties. *Journal of Applied Polymer Science*, **139**, e52521 (2022).
<https://doi.org/10.1002/app.52521>
- [29] Quiles-Carrillo L., Montanes N., Sammon C., Balart R., Torres-Giner S.: Compatibilization of highly sustainable polylactide/almond shell flour composites by reactive extrusion with maleinized linseed oil. *Industrial Crops and Products*, **111**, 878–888 (2018).
<https://doi.org/10.1016/j.indcrop.2017.10.062>
- [30] D'Amico D. A., Montes M. L. I., Manfredi L. B., Cyrus V. P.: Fully bio-based and biodegradable polylactic acid/poly(3-hydroxybutyrate) blends: Use of a common plasticizer as performance improvement strategy. *Polymer Testing*, **49**, 22–28 (2016).
<https://doi.org/10.1016/j.polymertesting.2015.11.004>
- [31] Murariu M., da Silva Ferreira A., Pluta M., Bonnaud L., Alexandre M., Dubois P.: Polylactide (PLA)–CaSO₄ composites toughened with low molecular weight and polymeric ester-like plasticizers and related performances. *European Polymer Journal*, **44**, 3842–3852 (2008).
<https://doi.org/10.1016/j.eurpolymj.2008.07.055>
- [32] Herrera N., Mathew A. P., Oksman K.: Plasticized polylactic acid/cellulose nanocomposites prepared using melt-extrusion and liquid feeding: Mechanical, thermal and optical properties. *Composites Science and Technology*, **106**, 149–155 (2015).
<https://doi.org/10.1016/j.compscitech.2014.11.012>
- [33] Gonzalez L., Agüero A., Quiles-Carrillo L., Lascano D., Montanes N.: Optimization of the loading of an environmentally friendly compatibilizer derived from linseed oil in poly(lactic acid)/diatomaceous earth composites. *Materials*, **12**, 1627 (2019).
<https://doi.org/10.3390/ma12101627>
- [34] Liminana P., Garcia-Sanoguera D., Quiles-Carrillo L., Balart R., Montanes N.: Optimization of maleinized linseed oil loading as a biobased compatibilizer in poly(butylene succinate) composites with almond shell flour. *Materials*, **12**, 685 (2019).
<https://doi.org/10.3390/ma12050685>
- [35] Mwaurah P. W., Kumar S., Kumar N., Panghal A., Attkan A. K., Singh V. K., Garg M. K.: Physicochemical characteristics, bioactive compounds and industrial applications of mango kernel and its products: A review. *Comprehensive Reviews in Food Science and Food Safety*, **19**, 2421–2446 (2020).
<https://doi.org/10.1111/1541-4337.12598>
- [36] Avolio R., Castaldo R., Avella M., Cocca M., Gentile G., Fiori S., Errico M. E.: PLA-based plasticized nanocomposites: Effect of polymer/plasticizer/filler interactions on the time evolution of properties. *Composites Part B: Engineering*, **152**, 267–274 (2018).
<https://doi.org/10.1016/j.compositesb.2018.07.011>
- [37] Terroba-Delgado E., Fiori S., Gomez-Caturla J., Montanes N., Sanchez-Nacher L., Torres-Giner S.: Valorization of liquor waste derived spent coffee grains for the development of injection-molded polylactide pieces of interest as disposable food packaging and serving materials. *Foods*, **11**, 1162 (2022).
<https://doi.org/10.3390/foods11081162>
- [38] Martin O., Avérous L.: Poly(lactic acid): Plasticization and properties of biodegradable multiphase systems. *Polymer*, **42**, 6209–6219 (2001).
[https://doi.org/10.1016/S0032-3861\(01\)00086-6](https://doi.org/10.1016/S0032-3861(01)00086-6)
- [39] Pantyukhov P., Kolesnikova N., Popov A.: Preparation, structure, and properties of biocomposites based on low-density polyethylene and lignocellulosic fillers. *Polymer Composites*, **37**, 1461–1472 (2016).
<https://doi.org/10.1002/pc.23315>

- [40] Nguyen T. L., Bedoui F., Mazeran P. E., Guigon M.: Mechanical investigation of confined amorphous phase in semicrystalline polymers: Case of PET and PLA. *Polymer Engineering & Science*, **55**, 397–405 (2015). <https://doi.org/10.1002/pen.23896>
- [41] Gomez-Caturla J., Balart R., Ivorra-Martinez J., Garcia-Garcia D., Dominici F., Puglia D., Torre L.: Biopolypropylene-based wood plastic composites reinforced with mango peel flour and compatibilized with an environmentally friendly copolymer from itaconic acid. *ACS Applied Polymer Materials*, **4**, 4398–4410 (2022). <https://doi.org/10.1021/acsapm.2c00373>
- [42] Vogler E. A.: Structure and reactivity of water at biomaterial surfaces. *Advances in Colloid and Interface Science*, **74**, 69–117 (1998). [https://doi.org/10.1016/S0001-8686\(97\)00040-7](https://doi.org/10.1016/S0001-8686(97)00040-7)
- [43] Jorda-Reolid M., Gomez-Caturla J., Ivorra-Martinez J., Stefani P. M., Rojas-Lema S., Quiles-Carrillo L.: Upgrading argan shell wastes in wood plastic composites with biobased polyethylene matrix and different compatibilizers. *Polymers*, **13**, 922 (2021). <https://doi.org/10.3390/polym13060922>
- [44] Zięba A., Drelinkiewicz A., Chmielarz P., Matachowski L., Stejskal J.: Transesterification of triacetin with methanol on various solid acid catalysts: A role of catalyst properties. *Applied Catalysis A: General*, **387**, 13–25 (2010). <https://doi.org/10.1016/j.apcata.2010.07.060>
- [45] Meskens F. A.: Methods for the preparation of acetals from alcohols or oxiranes and carbonyl compounds. *Synthesis*, **1981**, 501–522 (1981). <https://doi.org/10.1055/s-1981-29507>
- [46] Arrieta M. P., López J., Rayón E., Jiménez A.: Disintegrability under composting conditions of plasticized PLA–PHB blends. *Polymer Degradation and Stability*, **108**, 307–318 (2014). <https://doi.org/10.1016/j.polymdegradstab.2014.01.034>